technische universität
dortmund

Robustness and Variation of Low-Dimensional Signal Transmission in Topological Phases

Dissertation
zur Erlangung des akademischen Grades
eines Doktors der Naturwissenschaften
(Dr. rer. nat.)

vorgelegt von
Maik Malki

Lehrstuhl für Theoretische Physik I
Fakultät Physik
Technische Universität Dortmund

2019

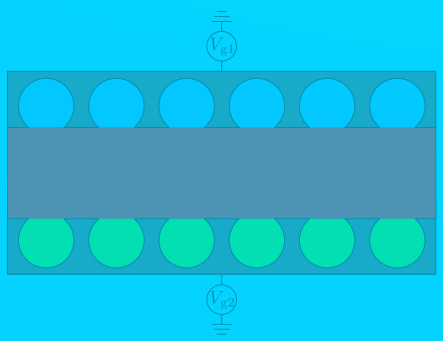

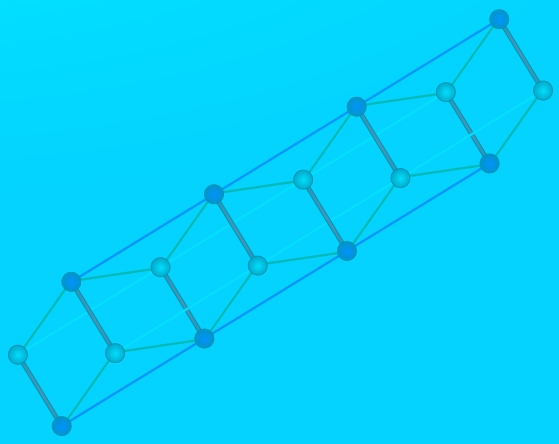

1. Gutachter: Prof. Dr. Götz S. Uhrig

2. Gutachter: Prof. Dr. Kai P. Schmidt

Datum des Einreichens der Arbeit: 31.10.2019

Kontakt zum Autor: maik.malki@tu-dortmund.de

"You can distort a football into a rugby ball with small forces. But if you want to change it into a doughnut, an object with a hole, you have to do a significant amount of violence to it."

(F. Duncan M. Haldane on 03.06.2019 at the Lindau Nobel Laureate Meeting 2019)

Abstract

This thesis investigates the variation of signal transmission in topological phases as well as their robustness in one- and two-dimensional systems. For this purpose, multiple approaches in different systems are pursued.

First, the possibility of designed modifications at the boundaries is explored in order to change the Fermi velocity at edge states of topological phases. The Fermi velocity as a quantity of the transport behavior describes the speed of signal transmission. The main idea is to hybridize local modes with dispersive edge modes in a controllable way so that the signal speed can be significantly slowed down. In the beginning, the Haldane model is modified. Thereafter, the findings are extended by the spin degree of freedom, yielding to Kane–Mele model with helical edge states. In addition, the robustness of edge states against local disorder is investigated by reconstructing the dispersion of the edge modes in the Haldane model. As a result, certain limits regarding the protection of topological edge states become apparent.

Triggered by the results for lattice systems, the central idea is carried over to the integer quantum Hall effect of a free two-dimensional electron gas. The local modes are generated by periodically aligned bays at the boundary of the sample. The Hamiltonian of a free two-dimensional electron gas subjected to a perpendicular magnetic field is approximated by a finely discretized lattice. Hence the dispersion of arbitrary periodic geometries becomes numerically accessible. The application of a gate voltage brings the weakly hybridized edge states into resonance with the Fermi energy. Therefore the Fermi velocity can be varied by up to two orders of magnitude. To extend the research approach, graphene is investigated as another possible implementation due to its special properties and the technical possibility to realize desired geometries. The numerical results indicate that possible applications such as delay lines or interferometers are feasible.

The investigation of the topological properties of triplon excitations in $BiCu_2PO_6$ reveals new insights into the bulk-boundary correspondence. $BiCu_2PO_6$ is described by frustrated quantum spin-1/2 ladders which are weakly coupled to form a two-dimensional lattice. The eigenenergies and eigenmodes of single-triplons are determined by applying deepCUTs and Bogoliubov transformations. The one-triplon dispersions are used to fit the inelastic neutron scattering data by adjusting the coupling constants. Based on that, $BiCu_2PO_6$ is shown to be the first disordered quantum antiferromagnet exhibiting a gap and a non-trivial Zak phase. Additionally the topological character of $BiCu_2PO_6$ is established by a finite winding number. Despite the bulk-boundary correspondence, no localized edge states can be found due to the absence of an indirect gap. The investigation of the Su–Schrieffer–Heeger model confirms that the disappearance of the indirect gap leads to delocalized in-gap states. In order to further explore the localization of edge states regarding the indirect gap, two-dimensional topological systems such as the Haldane model and the topological checkerboard model are investigated as well.

Finally, the investigation of the ferromagnetic Shastry–Sutherland lattices reveals the existence of topological magnon excitations. Using exact spin wave theory, finite Chern numbers of the magnon bands are determined which give rise to chiral edge states. The thermal Hall conductivity as an experimental signature of the topological phase is calculated. Various promising compounds are discussed as possible physical realizations of ferromagnetic Shastry–Sutherland lattices.

Kurze Zusammenfassung

In dieser Arbeit wird untersucht, wie man die Signalübertragung topologischer Phasen variieren kann, sowie deren Robustheit in ein- und zweidimensionalen Systemen. Zu diesem Zweck werden verschiedene Ansätze in unterschiedlichen Systemen verfolgt.

Als erstes wird die Möglichkeit untersucht, mithilfe von gezielten Modifikationen am Rand die Fermi-Geschwindigkeit von topologischen Randzuständen zu reduzieren. Die Fermi-Geschwindigkeit ist eine wichtige Eigenschaft des Transportverhaltens, welche die Geschwindigkeit bei einer Signalübertragung beschreibt. Der grundlegende Gedanke ist es, lokale Zustände kontrollierbar mit den Randzuständen in Wechselwirkung zu bringen, sodass die Geschwindigkeit des Signals maßgeblich reduziert werden kann. Als erstes wird das Haldane-Modell modifiziert. Danach werden die Erkenntnisse um den Spin-Freiheitsgrad erweitert und auf das Kane–Mele-Modell mit den helikalen Randzuständen übertragen. Anschließend wird die Robustheit von Randzuständen in Anwesenheit von lokaler Unordnung im Haldane-Modell untersucht, indem die Dispersion der Randzustände rekonstruiert wird. Die topologischen Randzuständen sind dabei nur bis zu einem gewissen Grad geschützt.

Aufgrund der aussichtsreichen Ergebnisse wird die zentrale Idee auf den ganzzahligen Quanten-Hall-Effekt eines freien zweidimensionalen Elektronengases übertragen, um sie einer Realisierung näher zubringen. Dazu wird der Rand mit periodisch angeordneten Buchten modifiziert. Der Hamiltonoperator eines freien geladenen Teilchens im elektromagnetischen Feld wird auf einem fein diskretisierten Gitter approximiert, sodass die Dispersion von beliebig periodischen Geometrien numerisch zugänglich wird. Durch das Anlegen einer Gate-Spannung können die hybridisierten Randzustände in Resonanz mit der Fermi-Energie gebracht werden, sodass die Fermi-Geschwindigkeit um bis zu zwei Größenordnungen variiert werden kann. Aufgrund seiner besonderen Eigenschaften und der technischen Möglichkeit gewünschte Geometrien herzustellen wird zur Erweiterung Graphen untersucht. Die numerischen Ergebnisse zeigen, dass mögliche Anwendungen wie Verzögerungsleitungen oder Interferometer realisierbar sind.

Die Untersuchung der topologischen Eigenschaften der Triplon-Anregungen von $BiCu_2PO_6$ führt zu neuen Erkenntnissen bezüglich der Bulk-Boundary-Korrespondenz. $BiCu_2PO_6$ wird durch frustrierte Spin-1/2-Leitern beschrieben, welche schwach miteinander gekoppelt sind und so ein zweidimensionales Gitter bilden. Durch Anwendung einer deepCUT und einer Bogoliubov-Transformation werden die Kopplungskonstanten bestimmt, indem wir die Dispersion an die Daten der inelastischen Neutronenstreuung anpassen. Darauf basierend wird gezeigt, dass $BiCu_2PO_6$ der erste lückenbehaftete, ungeordnete Quantenantiferromagnet mit einer nicht-trivialen Zak-Phase ist. Der topologische Charakter von $BiCu_2PO_6$ wird zusätzlich durch eine endliche Windungszahl bestätigt. Trotz der Bulk-Boundary-Korrespondenz konnten keine lokalisierten Zustände vorgefunden werden, was durch die Abwesenheit einer indirekten Lücke begründet wird. Zur Bestätigung dieser Hypothese wird das Su–Schrieffer–Heeger-Modell untersucht, welches zeigt, wie das Verschwinden der indirekten Lücke zu delokalisierten Zuständen innerhalb der Energielücke führt. Um die Anfälligkeit der Lokalisierung von Randzuständen im Bezug auf die indirekte Lücke weiter zu untersuchen, werden zweidimensionale topologische Systeme wie das Haldane-Modell und das topologische Schachbrett-Modell untersucht.

Abschließend zeigt die Untersuchung des ferromagnetischen Shastry–Sutherland-Gitters das Vorkommen von topologischen Magnonanregungen. Mit Hilfe der exakten Spinwellentheorie werden die nicht-trivialen Chern-Zahlen der Magnonenbänder bestimmt, die zu chiralen Randzuständen führen. Um eine experimentelle Signatur vorherzusagen wird die thermische Hall-Leitfähigkeit der topologischen Phase berechnet. Verschiedene vielversprechende Verbindungen werden als mögliche physikalische Realisierungen des ferromagnetischen Shastry–Sutherland-Gitters diskutiert.

List of Acronyms and Abbreviations

Notation	Description
BZ	Brillouin zone
deepCUT	directly evaluated enhanced perturbative continuous unitary transformation
DM	Dzyaloshinskii–Moriya
INS	inelastic neutron scattering
IPR	inverse participation ratio
IQHE	integer quantum Hall effect
LL	Landau level
NN, NNN	nearest neighbor, next-nearest neighbor
QBCP	quadratic band crossing point
QHE	quantum Hall effect
QSHE	quantum spin Hall effect
SIA	single-ion anisotropy
SOC	spin-orbit coupling
SPT	symmetry-protected topological
SSH	Su–Schrieffer–Heeger
TRS	time-reversal symmetry
1D/2D/3D	one-/two-/three-dimensional

Contents

List of Acronyms and Abbreviations **IX**

1. Introduction **1**
1.1. Outline of the thesis . . . 8
1.2. Publications . . . 9

2. Topological band theory **11**
2.1. General context . . . 11
2.2. Berry phase . . . 12
2.3. Su–Schrieffer–Heeger model . . . 17
2.3.1. Pseudo-spin representation and winding number . . . 19
2.3.2. Symmetry classification . . . 20
2.3.3. Zak phase . . . 23
2.3.4. Bulk-boundary correspondence and Thouless charge pump . . . 25
2.4. Haldane model . . . 27
2.4.1. Chern number and chiral edge states . . . 30
2.5. Kane–Mele model . . . 33
2.5.1. $\mathbb{Z}_2$ topological invariant and helical edge states . . . 34

3. Tuning of Fermi velocity **37**
3.1. Tunable edge states and their robustness towards disorder . . . 37
3.1.1. General context . . . 37
3.1.2. Tuning chiral edge states of the Haldane model . . . 38
3.1.3. Tuning chiral edge states of the Kane–Mele model . . . 40
3.1.4. Robustness of the edge states against potential disorder . . . 46
3.1.5. Conclusion . . . 56
3.2. Tunable dispersion of the edge states in the integer quantum Hall effect . . . 58
3.2.1. General context . . . 58
3.2.2. Present objective . . . 58
3.2.3. Tunable edge states in the integer quantum Hall effect . . . 60
3.2.3.1. Model and technical aspects . . . 60
3.2.3.2. Dispersions in decorated quantum Hall samples . . . 66
3.2.3.3. Tuning the Fermi velocity . . . 74
3.2.4. Conclusion . . . 79
3.3. Tunable signal velocity in the integer quantum Hall effect of graphene . . . 81
3.3.1. General context . . . 81
3.3.2. Model and method . . . 83
3.3.3. Results . . . 84
3.3.3.1. Dispersions, hybridized edge modes, and localization . . . 84
3.3.3.2. Fermi velocities for signal transmission . . . 87

3.3.4. Conclusion . . . 89

4. Topological properties of $BiCu_2PO_6$ 91
4.1. General context . . . 91
4.2. Structure and model of $BiCu_2PO_6$ . . . 92
4.3. Berry phases in bosonic systems . . . 96
4.4. Berry curvature in $BiCu_2PO_6$ . . . 98
4.5. Winding number w . . . 100
4.6. (Non-)Existence of edge states . . . 101
4.7. (De-)Localization in the Su–Schrieffer–Heeger model . . . 103
4.8. Local dynamic structure factor in $BiCu_2PO_6$ . . . 106
4.9. Conclusion . . . 109

5. Delocalization of topological edge states 111
5.1. General context . . . 111
5.2. Delocalization of edge states in the Haldane model . . . 111
5.2.1. Further insights into delocalization . . . 117
5.3. Delocalization in the topological checkerboard model . . . 120
5.4. Delocalization of chiral edge states . . . 124
5.5. Conclusion . . . 126

6. Topological magnon bands in the ferromagnetic Shastry–Sutherland model 129
6.1. General context . . . 129
6.2. Topological magnon excitations . . . 130
6.2.1. Possible compounds for realization . . . 130
6.2.2. Topological magnons . . . 132
6.2.3. Effects of interlayer couplings . . . 135
6.2.4. Thermal Hall effect . . . 138
6.3. Conclusion . . . 142

7. Summary 143

Appendix 147
A. Symmetry analysis of $BiCu_2PO_6$ . . . 147
B. Matrix representation of the bilinear Hamilton operator . . . 151
C. Symplectic product and Berry phase for bosons . . . 153
D. Numerical calculation of the Zak phase . . . 156
D.1. Exemplary calculation of the Zak phase . . . 157
E. Investigation of the localization length in the Su–Schrieffer–Heeger model 159
F. Estimation of the ground state with two classical spins . . . 162

Bibliography 165

List of Figures 183

List of Tables 185

1. Introduction

Solid-state physics is the study of macroscopic and microscopic physical properties of solids. The collective behavior of electrons in solids is very different from the behavior of electrons in unbounded atoms. Even if the fundamental particles and interactions are well-known, the emergent phenomena that arise in crystal lattices are far from being completely understood. The research results provided a large number of very important technological achievements in the last decades such as semiconductor technology, transistors, LEDs, hard disk drives, etc. A better understanding and the discovery of new materials are of great importance in developing new technologies that are more efficient and sustainable. Currently, solid-state physics focuses on new types of materials and phenomena, such as quantum materials realizing superconductivity which may become a pioneering technology in the future. Recently, a new class of quantum materials have been discovered which are characterized by topological properties. They possess an enormous potential for innovations such as quantum computing or energy efficient applications in spintronics and electronics. Topological materials have quantum mechanical properties which are protected against perturbations in a novel way due to the global nature of topological properties.

Topology is a fundamental branch of mathematics that deals with global properties of a geometrical object that are preserved under continuous deformations such as stretching, twisting or bending. The preservation is attributed to the intrinsic structure in the space of the geometrical object. The properties are characterized by discrete topological invariants that can only change stepwise through non-adiabatic processes such as tearing and/or gluing. Thus, these invariants have to exhibit an inevitable connection to the intrinsic structure and have to be preserved independent of local deformations. In this sense, two objects are topologically equivalent if the topological invariants coincide.

The genus g of an orientable surface corresponds to the number of its holes and therefore represents an intuitive example of an integer topological invariant. A doughnut and a cup have genus $g = 1$ while a football has no holes and thus $g = 0$. Hence, we can turn a doughnut into a cup through continuous deformations, but not into a football. The genus can only be changed by integer amounts by adding or removing holes. As a result, the doughnut and a football are declared to be topologically distinct geometrical objects, but a doughnut and a cup belong to the same equivalence class. Similar topological invariants are used in the following to characterize topological phases.

The discovery of the integer quantum Hall effect (IQHE) in 1980 by von Klitzing marks the beginning of an era of research on topological phases[1]. The introduction of topological concepts in order to explain the IQHE in 1983 by Thouless was a great surprise [1]. The Hall conductance in the IQHE[2] [2] changes in a step-wise manner in

[1] Note that this refers to the introduction of topological phases in condensed matter and not to the first relation of topology and physics which was made in gauge theory.

[2] Unless noted otherwise, the IQHE always refers to the conductivity of a free 2D electron gas under the influence of a strong magnetic field at low temperature.

response to a reduction of the strength of the magnetic field. This strange behavior could only be explained by the theoretical research of Thouless.

For his research results regarding the IQHE, von Klitzing was awarded the 1985 Nobel Prize in physics. Topological phenomena in solid-state physics still inspire and astonish numerous physicists. The 2016 Nobel Prize was awarded to Thouless, Haldane and Kosterlitz for their theoretical investigation of topological phase transitions and topological phases of matter. This proves the subject to be one of the most actively researched and relevant topics in physics. Throughout the last years, the number of different topological materials and phases has increased with an amazing rate.

While it is predicted that the number of topological materials will increase even more in the future [3], the increasing variety of possible topological properties can lead to confusion and misunderstandings. For this reason, I will give an introductory overview of different topological phases and specify the focus of this thesis. I will start in a very general fashion by introducing phases and phase transitions, then continue with the classification of general topological phases before presenting the framework of the thesis.

First of all, distinct phases are usually associated with different states of aggregation such as gas, liquid or solid. There also exist different phases within a given state of matter. The most prominent example is given by H_2O which can be found as water vapor, water and ice. In addition, each phase can also exist in various forms, e.g., phases of ice can be found in crystalline or amorphous forms [4]. Furthermore, crystalline forms of ice are discovered to realize 17 different phases so far [5]. All these phases are described by state parameters such as pressure and temperature and are connected by thermodynamic phase transitions. The Kosterlitz–Thouless phase transition [6, 7] represents a special case that can only be found in two-dimensional systems and is historically the first example of a topological phase transition. In contrast to common phase transitions, the Kosterlitz–Thouless transition[3] does not break any symmetry and can therefore not be described by the well-established Ginzburg–Landau theory which is based on local order parameters.

At very low temperatures close to absolute zero, material properties are determined by quantum physics and new exotic states are revealed. Such quantum materials are described as zero-temperature phases with properties which can persist even for finite temperatures. At $T = 0\,\mathrm{K}$, different phases are linked by quantum phase transitions including topological phase transitions. Quantum matter can have many different types of topological properties known as topological quantum states. They do not fit into the scheme of standard symmetry breaking phases due to their inherently global nature.

To provide an overview regarding topological properties, a schematic tree diagram is shown in Fig. 1.1. First, systems can be divided into gapped and gapless Hamiltonians, where we shall focus on the former. The system energies are theoretically described by Hamiltonians. A gapped Hamiltonian is specified for an infinitely large system where the ground state, defined as the lowest-energy state, is separated with a finite energy gap[4] from the first excited states. Otherwise the Hamiltonian is called gapless. The Hamiltonian with a finite gap can be further divided into long-range and short-range entangled phases.

The phenomena of quantum entanglement corresponds to a special kind of correlation

[3] The Kosterlitz–Thouless transition is also declared as a thermodynamic phase transition since the transition depends on temperature.

[4] An energy gap describes an energy range where no energy states exist.

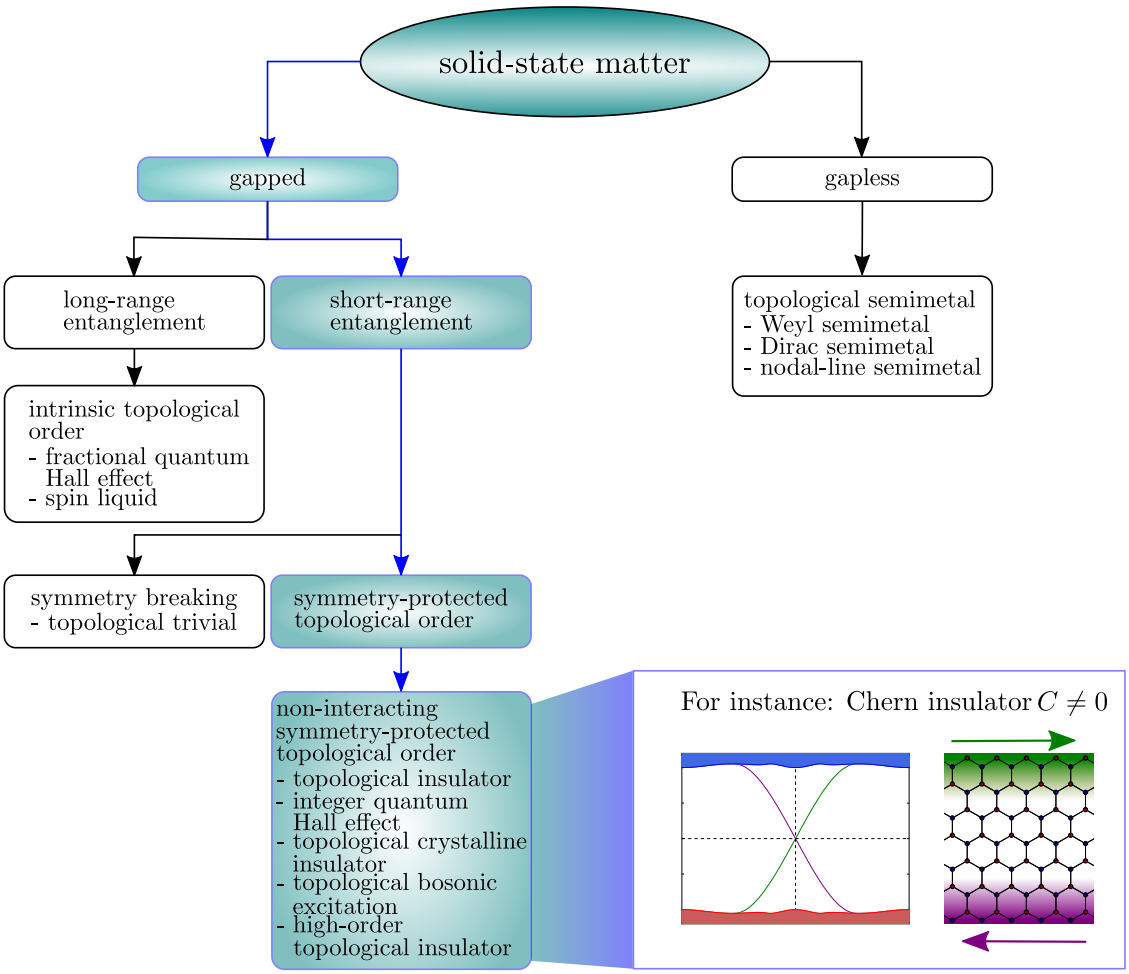

Figure 1.1: Classification of solid-state matter by basic properties. This overview serves as a guideline to locate the focus of this thesis which is highlighted in color. The assignment of the integer quantum Hall effects to non-interaction symmetry-protected topological orders are based on their used models in this thesis described in Chap. 3.

between particles. The quantum states of these particles can only be described as a whole system. Even if the particles are separated by a large distance, each particle cannot be described by a quantum state independently from the other particles. The von Neumann entropy S measures the entanglement of a quantum state and is calculated by taking the trace

$$S = -\mathrm{Tr}(\rho \ln(\rho)) \quad , \tag{1.1}$$

where ρ describes the density matrix of a quantum mechanical system. States of short-range entangled phases can always be smoothly deform into trivial product states without a quantum phase transition where the gap closes and opens. These product states are trivial since their von Neumann entropy vanishes. The smoothly deformations are allowed to break all symmetries as long as the gap remains. In contrast, ground states of long-range entangled phases [8, 9] have always a finite von Neumann entropy S as long as the gap is preserved due to the topological entanglement entropy [8, 9]. The topological

entanglement entropy is a universal constant contribution to the von Neumann entropy which characterizes the global properties of the entanglement in the ground state.

Quantum phases with an intrinsic topological order [10, 11] have finite gaps and long-range entanglements. In contrast, phases with a symmetry-protected topological (SPT) order [12, 13] have topological quantum states with a finite gap and short-range entanglements. States with intrinsic topological order are characterized by a non-trivial robust ground state degeneracy [14], long-range entanglement [8, 9] and fractionalized excitations [15, 16]. The presence of interaction is indispensable for the existence of intrinsic topological order. The description of intrinsic topological insulators therefore requires the usage of many-body theory. Distinct intrinsic topological ordered phases cannot change into each other without a phase transition. Phases of intrinsic topological order have a non-trivial topological entanglement entropy. They display many special features such as anyonic statistics [17] (non-Abelian or fractional statistics) or edge states [18] (gapless boundary excitations). Prominent examples of intrinsic topological orders are given by the fractional quantum Hall effect (QHE) [19, 20] and quantum spin liquids [21]. The IQHE can be assigned to provide short-range or long-range entanglement depending on the used definition. According to the original definition of long-range entanglement in Ref. [11], the states of the IQHE have long-range entanglement. In contrast, Kitaev's definition in Ref. [22] results that the states of the IQHE are short-range entangled.

SPT phases always have a finite energy gap with a unique ground state and specific symmetries which need to be preserved for the phase. The finite energy gap refers to the bulk properties[5] of the system. A SPT phase cannot be smoothly deformed into another phase if the energy gap and the symmetries are preserved [23]. The requirement to close the gap in order to change the phase is interpreted as a consequence of the topological nature of the system. One subtle but important difference of SPT orders to intrinsic topological orders consist in the necessary preservation of the symmetries in the SPT phases during a deformation. The importance of symmetry is also evident in the analysis of edge states. The edge states in the SPT phases are robust against local perturbations preserving the symmetry while edge states in intrinsic topological ordered phases are robust against any local perturbations. The fact that the symmetry needs to be preserved leads to the notion of "SPT phases". The eigenstates of SPT phases have only short-range entanglement, which lead automatically to a trivial topological entanglement entropy. This emphasizes the distinction from intrinsic topological order.

The SPT order can be classified in interacting systems such as the Haldane phase of odd-integer-spin chains and in non-interacting systems. Topological insulators in non-interacting fermionic systems are well-known examples of SPT phases[6] without interaction. The concept of topological insulators is chiefly used in this work.

A topological insulator differs from the known band insulators by a twisted topology due to a band inversion, i.e., the usual orbital character of the conduction band and valence band is inverted by spin-orbit coupling. The energy band structure in the bulk looks like the energy band structur of an ordinary band insulator but it possesses a non-trivial topological index similar to the genus. Thus the change of the topological index is always connected to a non-adiabatic quantum phase transitions where the gap closes

[5] The term bulk refers to volume properties of systems in contrast to boundary or interface properties. Hence, the bulk represents the translation invariant part of the system. One can think of infinite or periodic systems in all present spatial-dimensions.

[6] Note that the general notation of SPT order applies to fermionic as well as to bosonic systems.

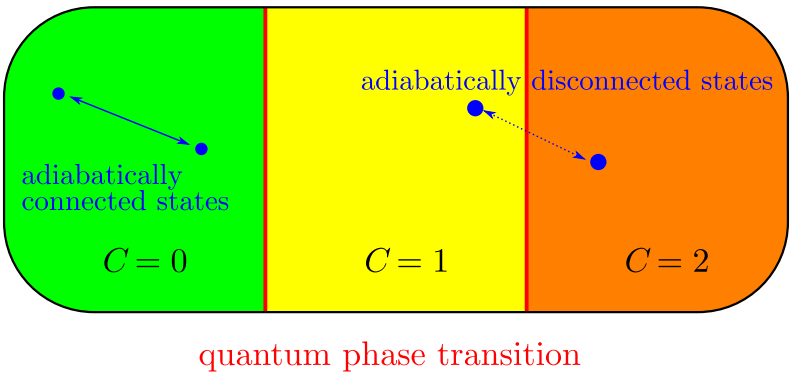

Figure 1.2: Illustration of distinct topological phases. The topological invariant is denoted by C. The phase transitions by closing and opening a gap are marked in red. All three phases share the same symmetries.

and opens as schematically shown in Fig. 1.2. However, the index of a topological insulator is not visible from its energy band structure in the bulk. The topology is deeply rooted in the eigenstates with their intrinsic phase ambiguity and not in the eigenenergies. The presence of a non-trivial topological bulk index leads to conducting topological edge states. This fact is explained by the bulk-boundary correspondence [24–27]. As a result, the topological insulator behaves like an insulator in its interior while its boundary behaves like a metal. Topological insulators have been found in several two- and three-dimensional materials [27–32]. A more detailed explanation of topological insulators is provided in Chap. 2.

The different properties and the resulting behavior of topological insulators strongly depend on the spatial-dimension as well as on the symmetries of the system. All possible classes of topological invariants for topological insulators and topological superconductors of non-interacting fermionic systems in dependence of all spatial-dimensions as well as symmetries are shown in the periodic table introduced by Kitaev [33]. All ten discrete symmetry classes are characterized by the eigenvalues of the squares of the time-reversal $\mathcal{T}$, particle-hole $\mathcal{C}$ and chiral symmetry operators $\mathcal{S}$, as pointed out by Altland and Zirnbauer [34, 35]. The symmetries are of particular importance because they reveal the framework of the phase. For instance, if the bulk system preserves time-reversal symmetry (TRS) then possible edge states in a topological phase have to fulfill the TRS as well. An excerpt of the periodic table up to three dimensions is shown in Tab. 1.1. Depending on the dimension and the symmetry, different topological edge states[7] are achievable in presence of a non-trivial topological invariant. For notational simplicity, we will henceforth use the term “edge state” for all states localized at a boundary irrespective of dimensionality.

The periodic table applies only to fermionic systems. Nonetheless, there is also a large number of possible topological phases for bosonic excitations. For instance, single-particle excitations in magnetic systems have also been observed to show topological properties. Note that such topological phases are analogous to topological insulators but they differ

[7] Edge states are often stated in the literature to be symmetry-protected. This does not implies that the phase is protected by its symmetry. It means that the symmetry must be preserved.

	class	$\mathcal{T}^2$	$\mathcal{C}^2$	$\mathcal{S}^2$	$D=1$	$D=2$	$D=3$
Wigner–Dyson	A	$-$	$-$	$-$	$-$	$\mathbb{Z}$(Haldane, IQHE)	$-$
symmetry classes	AI	$+1$	$-$	$-$	$-$	$-$	$-$
	AII	-1	$-$	$-$	$-$	$\mathbb{Z}_2$(Kane–Mele)	$\mathbb{Z}_2$
chiral	AIII	$-$	$-$	1	$\mathbb{Z}$	$-$	$\mathbb{Z}$
symmetry classes	BDI	$+1$	$+1$	1	$\mathbb{Z}$(SSH)	$-$	$-$
	CII	-1	-1	1	$2\mathbb{Z}$	$-$	$\mathbb{Z}_2$
Bogoliubov–de	D	$-$	$+1$	$-$	$\mathbb{Z}_2$	$\mathbb{Z}$	$-$
Gennes	C	$-$	-1	$-$	$-$	$2\,\mathbb{Z}$	$-$
symmetry classes	DIII	-1	$+1$	1	$\mathbb{Z}_2$	$\mathbb{Z}_2$	$\mathbb{Z}$
	CI	$+1$	-1	1	$-$	$-$	$2\,\mathbb{Z}$

Table 1.1: Overview of all possible topological insulators and topological superconductors classified by the ten symmetry classes of non-interacting fermionic Hamiltonians [36]. The classes are characterized by the spatial-dimension ($D = \{1, 2, 3\}$) and the discrete symmetries given by the time-reversal symmetry $\mathcal{T}$, the particle-hole symmetry $\mathcal{C}$ and the chiral symmetry $\mathcal{S}$ which are formulated at the level of the single-particle Hamiltonian (see Sec. 2.3.2). The absence of a symmetry is denoted by $-$. A present symmetry is indicated by the square of the symmetry operator which can be represented by $\pm\mathbb{1}$ and are denoted by ± 1. For instance, $\mathcal{T}^2 = -\mathbb{1}$ holds for half-integer spins while $\mathcal{T}^2 = +\mathbb{1}$ holds for integer spins.

due to bosonic nature which results in a different occupation of the modes[8].

Furthermore, topological crystalline insulators correspond to another variant of topological insulators. It extends the classification of topological phases by including certain crystal point group symmetries. Instead of the discrete symmetries in the Altland–Zirnbauer classification, the presence of crystalline symmetries are necessary in order to have topological characteristics. Point group symmetries such as inversion, mirror and rotation represents typical symmetries for the nature of topological crystalline insulators.

For completeness it should be mentioned that topological phases do not necessarily have a finite gap. Topological semimetals obey concepts similar to those used in topological insulators. They are also characterized by topological invariants and have special edge states. There are a number of other specific topological phases which are not mentioned here (and not shown in Fig. 1.1) for reasons of clarity. The presented phases are chosen to clearly allocate the work within the large research area of topological phases.

In this work we will focus on low-dimensional topological phases. As indicated above, the spatial-dimensions has a huge impact. Physics in low-dimensional topological phases can be very different from the behavior in three-dimensional systems. Depending on the dimension and the symmetries, one can determine different topological invariants such as the Zak phase [37], winding number [38], Chern number [39], $\mathbb{Z}_2$ index [40], etc., which will be explained in Chap. 2. In addition, the same invariant can be determined by

[8] Unlike the fermionic case, bosonic systems do not obey the Pauli principle. As a result, the term "insulators" would cause confusion since no valence and conduction bands are defined.

various methods. The preferred method depends on the studied model.

The signal transmission of topological phases is largely determined by edge modes which are attributed to a non-trivial topological invariant and the gap of the system. The term "topological phases" is used as a synonym for non-interacting SPT phases henceforth. The edge states in topological phases are commonly presented as their key property which enables energy-efficient applications. The predicted stability of edge states against disorder [41–43] and interaction [41, 42] are remarkable and the main reason why they are so interesting for technical applications. A prominent example of the robustness of edge states is the forbidden backscattering in case of TRS [42]. Thus edge states theoretically represent a perfect conductor due to the ballistic transport without dissipation. Such transport behavior for a material class is unique and promises an enormous application potential. The possibility to vary the transport behavior in a controllable way is a useful tool to create devices. In order to contribute to these topics, I followed various theoretical approaches which are briefly described in the following outline.

1.1. Outline of the thesis

The structure of the thesis is as follows:

The articles published during this PhD project are listed at the end of this chapter.

In Chap. 2, the basic concept of the Berry phase will be introduced. Afterwards, the Su–Schrieffer–Heeger model (1D, Zak phase), the Haldane model (2D, Chern number) and the Kane–Mele model (2D, $\mathbb{Z}_2$ index) are presented as fundamental examples which will greatly contribute to the understanding of the remaining work.

Chapter 3 shows the investigation how to tune the Fermi velocity in topological systems. First, the main idea is introduced and its application to electronic and spintronic systems is shown in order to achieve new application areas. Secondly, the robustness of tunable edge states is studied. The theoretical approaches in the IQHE regime of a 2D electron gas and of graphene are examined to propose experimental realizations.

The study of topological properties in $BiCu_2PO_6$ is presented in Chap. 4. A short introduction of the compound clarifies the basic framework and its peculiarities. Then, the topological characteristics are investigated. Due to the presence of a non-trivial quantized Zak phase, localized edge states are expected, but not found. The subsequent analysis reveals the importance of the indirect gap for the localization of edge states.

The delocalization of edge states is studied in detail in Chap. 5. It will be shown that the delocalization of edge states in one- as well as in two-dimensional topological systems is generically driven by the disappearance of the indirect gap.

In Chap. 6, the ferromagnetic Shastry–Sutherland model is analyzed by using exact spin-wave theory. Different compounds are proposed as possible physical realizations of the ferromagnetic Shastry–Sutherland model. The non-trivial Chern number in combination with the material properties provide excellent conditions for stable topological magnonic excitations.

Finally, in Chap. 7 main results are summarized.

In the appendix, supplementary material is provided.

1.2. Publications

This thesis comprises parts of the published and submitted manuscripts which are listed below in chronological order:

1. M. Malki and G. S. Uhrig. "Tunable edge states and their robustness towards disorder". In: Physical Review B 95.23 (2017), p. 235118. DOI: 10.1103/PhysRevB.95.235118 .

2. M. Malki and G. S. Uhrig. "Tunable dispersion of the edge states in the integer quantum Hall effect". In: SciPost Physics 3.4 (2017), p. 032. DOI: 10.21468/SciPostPhys.3.4.032 .

3. M. Malki and G. S. Uhrig. "Topological magnon bands for magnonics". In: Physical Review B 99.17 (2019), p. 174412. DOI: 10.1103/PhysRevB.99.174412 .

4. M. Malki, L. Müller, and G. S. Uhrig. "Absence of localized edge modes in spite of a non-trivial Zak phase in $BiCu_2PO_6$". In: Physical Review Research 1 (2019), p. 033197. DOI: 10.1103/PhysRevResearch.1.033197 .

5. M. Malki and G. S. Uhrig. "Delocalization of edge states in topological phases". In: Europhysics Letters 127 (2019), p. 27001. DOI: 10.1209/0295-5075/127/27001 .

6. M. Malki and G. S. Uhrig. "Tunable signal velocity in the integer quantum Hall effect of tailored graphene". In: arXiv:1909.03520 (2019) .

In addition one publication during my PhD is not covered in this thesis:

7. M. Malki and K. P. Schmidt. "Magnetic Chern bands and triplon Hall effect in an extended Shastry–Sutherland model". In: Physical Review B 95.19 (2017), p. 195137. DOI: 10.1103/PhysRevB.95.195137 .

2. Topological band theory

This chapter presents the required topological band theory within this thesis to ensure the basic notion of the following chapters. First, we give an introduction to the general context of topological insulators in Sec. 2.1. Afterwards, we will introduce the key concept of the Berry phase in Sec. 2.2. The Su–Schrieffer–Heeger model in Sec. 2.3 serves as an example to explain topological phases in one dimension. Sections 2.4 and 2.5 describe the Chern and the $\mathbb{Z}_2$ topological phase in two dimensions, respectively.

2.1. General context[1]

Quantum states of matter stand out by very astonishing features. Their energy spectra show a special structure and they are characterized by special properties of their eigenstates. In particular, unanticipated topological properties generated by eigenstates attract great interest. Since the discovery of the integer and the fractional QHE [19, 20], topological phenomena have become an important field of research in condensed matter physics. The edge states [45] occurring in the QHE are localized exponentially at the boundaries of the sample. They are protected by the topological properties of the band structure in the bulk [27]. As shown by Thouless et al. [1], the number of edge states corresponds to the Chern number ν [39, 46] of the filled electronic bands which characterizes the famous quantized Hall conductivity $\sigma_{xy} = \nu e^2/h$. The description of the QHE by topological invariants [39, 47–49] is based on the Berry phase [50].

In order to mimic the IQHE in a lattice model *without* external magnetic field, Haldane proposed the first Chern insulator [51]. In addition to nearest neighbor (NN) hopping on a honeycomb lattice, the proposed Haldane model comprises a magnetic flux which induces complex next-nearest neighbor (NNN) hopping elements while the translational symmetry is preserved. Averaged over a unit cell of the lattice the magnetic flux vanishes.

In order to realize a Chern insulator the time-reversal symmetry (TRS) must be broken. Non-trivial Chern numbers imply chiral edge states also in the absence of an external magnetic field, extending the concept of the usual QHE. In the context of topologically protected edge states the term "chiral" means that the electrons only propagate in one direction along one edge. If no magnetic field is involved this effect is called the *anomalous* QHE [52–54].

The Kane–Mele model [29, 55, 56] represents a crucial extension of the Haldane model including the spin degree of freedom. This renders the preservation of the TRS possible because one spin species realizes the time-reversed replica of the other. The Kane–Mele model was suggested to describe the effect of spin-orbit interaction on the electronic band structure of graphene in the low-energy regime, but it turned out that the spin-orbit interaction in graphene is too weak to produce noticeable effects. Nevertheless, the

[1] Parts of this section have been published in Physical Review B as regular article [44].

Kane–Mele model provides fascinating theoretical insights.

Due to the preservation of the TRS in the Kane–Mele model it cannot display a net charge current at the edges. Instead, a net spin current is possible. This phenomenon is referred to as the quantum spin Hall effect (QSHE) [57] which can be attributed to the topological $\mathbb{Z}_2$ invariant [27, 40, 56], implying helical edge states [41]. These topologically protected edge states are called "helical" because they have a spin filtering property, i.e., the spins $\uparrow$ propagate in one direction while the spins $\downarrow$ propagate in the opposite direction along the same edge. As a result, the QSHE implies a quantization of the spin Hall conductivity. Materials displaying the QSHE characterized by the $\mathbb{Z}_2$ topological invariant are referred to as $\mathbb{Z}_2$ topological insulators [29, 30].

Since the QSHE is too weak in graphene to be measurable, Bernevig, Hughes, and Zhang proposed a model [58] for the quantum spin Hall phase in HgTe quantum wells where the spin-orbit coupling (SOC) is much stronger. Soon after the theoretical proposal, the quantum spin Hall phase has been observed experimentally in a 2D HgTe/CdTe quantum well [28, 59]. Another experimental observation of the QSHE was realized in InAs/GaSb quantum wells [60, 61]. The discovered QSHE is only measured at low temperatures below 40 K. Theoretical calculations [62] predict a possible realization of the QSHE in germanium with a large energy gap corresponding to 277 K. The calculated energy gap of the low-buckled (2D lattice is buckled into three dimensions) honeycomb structure of germanium results from the stronger SOC so that this system is a candidate for detecting the QSHE at higher temperatures.

Historically, the QSHE was measured first in 2D topological insulators. A Chern insulator was considered unlikely to be realized. But very recently, progress has been achieved towards 2D Chern insulators. The first observation of the anomalous QHE was made in thin ferromagnetic Chern insulators [32, 63, 64]. It could be observed up to temperatures of a few Kelvin. Theoretical proposals indicate that Chern insulators near room temperature are possible in thin ferromagnetic Chern insulators [65] or in superlattices of gold atoms on single-vacancy graphene [66, 67].

An alternative realization has been achieved using ultracold fermionic ^{40}K atoms in a periodically modulated optical lattice [68]. The usage of ultracold fermions could implement the Haldane model in an experimental setup. A particular asset of this setup is the tunability of the physical properties.

This historically short overview only provides a first foray into the topic. To get deeper insights into the appearance of topological effects, we introduce the notion of the Berry phase.

2.2. Berry phase

The Berry phase [50, 69] is the most fundamental concept in topological band theory and serves as an essential tool to analyze topological phenomena [69]. Since its discovery in 1984, many observable effects (various Hall effects, electronic or photonic polarization, ...) of geometric origin could be described systematically with the Berry phase. Furthermore, it was recognized that the Aharononv–Bohm effect can also be understood as a Berry phase. In reverse it means that the Aharononv–Bohm effect can be interpreted as a consequence of a non-trivial gauge field. In this work, the Berry phase is mainly used as the basis to decode the topological properties of the system and for defining several

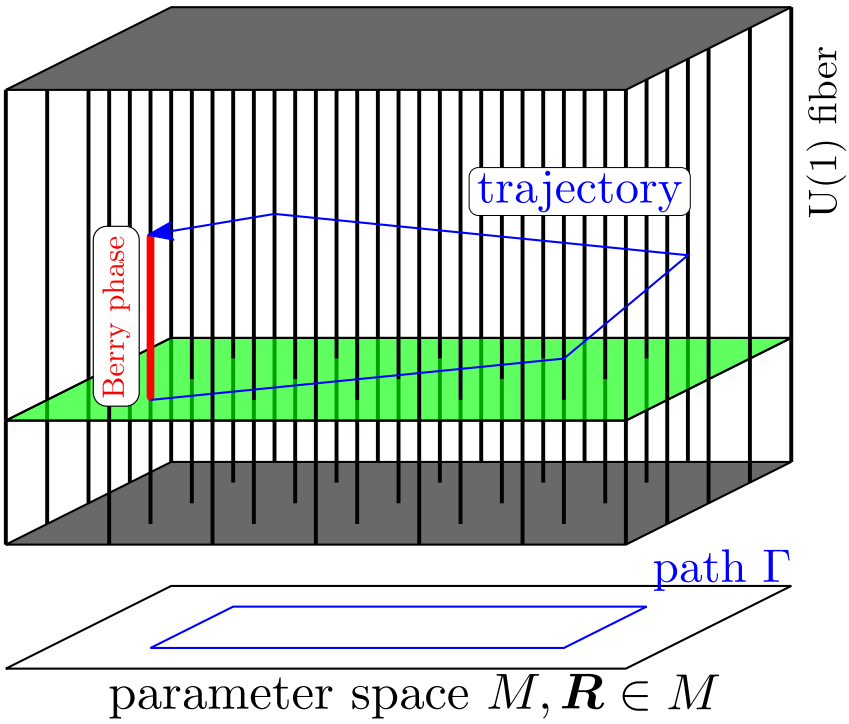

Figure 2.1: The accumulated Berry phase during an adiabatic cyclic transport in parameter space (base space). The black lines represents exemplary U(1) fibers (bundle space). The green patch corresponds to a smooth gauge choice which contains the closed path shown in blue. The parameter space drawn below corresponds only to the projection of the shown patch. During the parallel transport along the closed path the eigenstate acquires an additional quantum phase as indicated by the height of the trajectory.

topological invariants, classifying distinct topological phases.

In general, a Berry phase[2] may occur in every system under an adiabatic evolution along a cyclic process depending on a parameter set $\boldsymbol{R}$ of a general Hamiltonian $\mathcal{H}(\boldsymbol{R})$. The adiabatic theorem [71] states that if the variation of continuous parameters proceeds slow enough, a non-degenerate eigenstate remains in its instantaneous eigenstate. To this extent, one assumes that the parameter set $\boldsymbol{R}$ lies in a differential manifold M called parameter space, $\boldsymbol{R} \in M$, and that $\mathcal{H}(\boldsymbol{R})$ has non-degenerate eigenenergies E_n with a smooth behavior as a function of $\boldsymbol{R}$. Thus, eigenvalues over the manifold M form energy bands which are labeled by n. Diagonalizing the Hamiltonian in the matrix representation $H(\boldsymbol{R})$ at each $\boldsymbol{R}$

$$H(\boldsymbol{R})\,|n, \boldsymbol{R}\rangle = E_n(\boldsymbol{R})\,|n, \boldsymbol{R}\rangle \tag{2.1}$$

provides an instantaneous orthonormal basis for the parameter set $\boldsymbol{R}$. Note that the Hamiltonians in this thesis are denoted by $\mathcal{H}$ whereas the matrix representation of Hamiltonians are denoted by H. Each instantaneous eigenstate $|n, \boldsymbol{R}\rangle$ is precisely determined

[2]The Berry phase has been derived in quantum mechanics. Similar classical phases such as the Pancharatnam phase have been investigated [70].

except for a complex phase (see Fig. 2.1) which is an element of the U(1) group

$$|n, \boldsymbol{R}\rangle' = \mathrm{e}^{\mathrm{i}\varphi_n(\boldsymbol{R})} |n, \boldsymbol{R}\rangle \quad . \tag{2.2}$$

This ambiguity is called gauge freedom and leads to U(1) fiber $\{g\,|n, \boldsymbol{R}\rangle\,|g \in \mathrm{U}(1)\}$ at each $\boldsymbol{R}$. Put simply, an eigenstate is a representative of an equivalence class of vectors which are connected by a complex phase transformation. The parameter space M and the U(1) fiber at each $\boldsymbol{R}$ of the same band define a fiber bundle over the parameter space M (see Fig. 2.1). Thus each band n represents a U(1) principal fiber bundle. The next step is to define a connection between the U(1) fibers of the eigenstates in order to describe the adiabatic evolution in parameter space. The connection is used to transfer the change of the gauge phase to the associated fiber element and is necessary for the definition of the parallel transport in the U(1) principal fiber bundle [46]. A natural connection can be derived from the Schrödinger equation. To this end, the parameter sets are considered to be time-dependent quantities $\boldsymbol{R} = \boldsymbol{R}(t)$ which are parameterized by t along the closed path Γ in M: $t \in [0, T] \to \boldsymbol{R}(t) \in \Gamma$. Thus, the following equations should hold

$$\boldsymbol{R}(0) = \boldsymbol{R}(T) \quad , \quad |n, \boldsymbol{R}(0)\rangle = |n, \boldsymbol{R}(T)\rangle \quad \text{and} \quad H(0) = H(T) \quad . \tag{2.3}$$

The introduction of time is only a means to an end and not a necessary condition. Before we consider the time evolution, it is important to know that a smooth and unique gauge choice in order to remove the arbitrariness of the phases of fibers is only possible over certain parts of M also called patches. Finding a proper gauge choice for the entire parameter space is not always possible. For instance, if the system possesses a topological invariant such as a non-trivial Chern number, which is connected to a U(1) twist in the parameter space, we can only make a well-defined gauge choice for piecewise patches [27]. To this end, the parameter space M is divided into patches and the collection of patches is called the atlas of the parameter space M. The gauge transformation between the overlap of these patches are called transition function. Usually in physics, two patches ($\{O_1, O_2\} \in M$ and $O_1 \cap O_2 \neq \emptyset$) are sufficient to correctly describe the entire parameter space. For simplicity, we first assume that the closed path Γ lies completely in a single patch (see green patch in Fig. 2.1). We use the ansatz

$$|\psi(t)\rangle = \mathrm{e}^{\mathrm{i}\theta(t)} |n, \boldsymbol{R}(t)\rangle \quad \text{with} \quad t \in [0, T] \quad , \tag{2.4}$$

where $\theta(t)$ should describe the time evolution of the eigenstate $|n, \boldsymbol{R}(0)\rangle$ with the starting condition $\theta(0) = 0$. We set $\hbar = 1$ for simplicity. Inserting the ansatz Eq. (2.4) in the Schrödinger equation leads to the differential equation

$$-E_n(\boldsymbol{R}(t)) + \mathrm{i}\,\langle n, \boldsymbol{R}(t)| \frac{\mathrm{d}}{\mathrm{d}t} |n, \boldsymbol{R}(t)\rangle = \frac{\mathrm{d}}{\mathrm{d}t}\theta(t) \quad . \tag{2.5}$$

According to the adiabatic approximation[3], the solution is given by

$$\theta(t) = -\int_0^t E_n(\boldsymbol{R}(t'))\,\mathrm{d}t' + \mathrm{i}\int_0^t \langle n, \boldsymbol{R}(t')| \frac{\mathrm{d}}{\mathrm{d}t'} |n, \boldsymbol{R}(t')\rangle\,\mathrm{d}t' \quad . \tag{2.6}$$

In addition to the generic dynamical phase, the eigenstate also acquires a second phase while moving along the path, the so-called Berry phase γ_n or geometric phase

$$|\psi(t)\rangle = \mathrm{e}^{-\mathrm{i}\int_0^t E_n(\boldsymbol{R}(t'))\,\mathrm{d}t'} \mathrm{e}^{\mathrm{i}\gamma_n(t)} |n, \boldsymbol{R}(t)\rangle \quad . \tag{2.7}$$

[3] Non-adiabatic terms correspond to $\mathrm{i}\,\langle m, \boldsymbol{R}(t)| \frac{\mathrm{d}}{\mathrm{d}t} |n, \boldsymbol{R}(t)\rangle$ with $n \neq m$.

The implicit time dependence can be transformed to an explicit dependence on $\boldsymbol{R}$ leading to the expression for the Berry phase

$$\gamma_n = \mathrm{i} \int_\Gamma \langle n, \boldsymbol{R}| \nabla_{\boldsymbol{R}} |n, \boldsymbol{R}\rangle \ \mathrm{d}\boldsymbol{R} \ = \int_\Gamma \boldsymbol{A}_n(\boldsymbol{R}) \, \mathrm{d}\boldsymbol{R} \quad \text{with} \quad \gamma_n \in \mathbb{R} \tag{2.8}$$

$$\boldsymbol{A}_n(\boldsymbol{R}) = \mathrm{i} \, \langle n, \boldsymbol{R}| \nabla_{\boldsymbol{R}} |n, \boldsymbol{R}\rangle \quad . \tag{2.9}$$

This representation emphasizes the fact that the Berry phase is not a time-dependent quantity. The vector quantity $\boldsymbol{A}_n(\boldsymbol{R})$ is known as the Berry connection and represents the desired canonical connection of the local U(1) fibers of the eigenstates.

So the basic manifold is divided into overlapping patches with well-defined gauge phases. The intersections between the different patches are connected by gauge transformation which is defined by the Berry connection, see Eq. (2.10). The connection of all U(1) fiber bundle sections results in the complete U(1) fiber bundle. During the connection process, twists between the U(1) fiber sections are mediated, which defines the topological properties of the whole bundle [72]. The connection between the phases of two neighboring eigenstates described by the Berry connection can be made clear by expressing the derivative in terms of the differential quotient, so that the Berry connection depends on the eigenstate $|n, \boldsymbol{R}\rangle$ and the infinitesimally shifted eigenstate $|n, \boldsymbol{R} + \boldsymbol{\Delta}\rangle$ (Shift in parameter space $\boldsymbol{\Delta} \in M$). Moreover, it shows that the Berry connection measures the deviation of $|n, \boldsymbol{R}\rangle$ by varying the parameter set $\boldsymbol{R}$.

The Berry connection defines the parallel transport of the eigenstates in the U(1) principal fiber bundle. As a result, the Berry phase corresponds to the acquired phase relative to the initial state during a parallel transport along a closed path through the U(1) principal fiber bundle. The assumption of a closed path is necessary so that the Berry phase is gauge invariant and thus observable. Under a gauge transformation $|n, \boldsymbol{R}\rangle' \rightarrow \mathrm{e}^{\mathrm{i}\xi_n(\boldsymbol{R})} |n, \boldsymbol{R}\rangle$, the Berry connection is extended by an additional term

$$\boldsymbol{A}_n(\boldsymbol{R}) \rightarrow \boldsymbol{A}_n(\boldsymbol{R}) - \nabla_{\boldsymbol{R}} \xi_n(\boldsymbol{R}) \quad . \tag{2.10}$$

By considering a closed path, the additional contribution is restricted by

$$-\oint \nabla_{\boldsymbol{R}} \xi_n(\boldsymbol{R}) \, \mathrm{d}\boldsymbol{R} = \xi_n(R(0)) - \xi_n(R(T)) = 2\pi m \quad \text{with} \quad m \in \mathbb{Z} \tag{2.11}$$

due to the condition that $|n, \boldsymbol{R}(0)\rangle = |n, \boldsymbol{R}(T)\rangle$. Therefore the Berry phase is only changed by a multiple of 2π using a gauge transformation and can be regarded as a physically relevant observable in this way only.

A further important quantity in this context is given by the Berry curvature F_n since it has the advantage to be gauge invariant in contrast to the gauge-dependent Berry connection. The physical importance becomes clear through the possibility to observe the Berry curvature [68, 73]. In order to express the Berry phase in terms of the Berry curvature we consider a three-dimensional parameter space due to simpler mathematics and more general formulation. Using Stokes' theorem, we can recast the Berry phase by introducing the Berry field strength[4] Ω_n, where each component corresponds to an

[4] This notation is inspired by the strong similarity to electromagnetism, which can also be recast in terms of gauge theory.

expression of a Berry curvature $F_{n,jk}$:

$$\gamma_n = -\mathrm{Im} \iint \mathrm{d}\boldsymbol{S}(\nabla \times \langle n, \boldsymbol{R}| \nabla_{\boldsymbol{R}} |n, \boldsymbol{R}\rangle) \tag{2.12a}$$

$$= -\mathrm{Im} \iint \mathrm{d}\boldsymbol{S}(\langle \nabla_{\boldsymbol{R}} n, \boldsymbol{R}| \times |\nabla_{\boldsymbol{R}} n, \boldsymbol{R}\rangle) \tag{2.12b}$$

$$= \iint \mathrm{d}\boldsymbol{S}\boldsymbol{\Omega}_n \qquad \text{with} \quad \Omega_{n,i} = \varepsilon_{ijk} F_{n,jk} \tag{2.12c}$$

$$F_{n,jk} = \mathrm{i}\left(\langle \partial_{R_j} n, \boldsymbol{R}| \partial_{R_k} n, \boldsymbol{R}\rangle - \langle \partial_{R_k} n, \boldsymbol{R}| \partial_{R_j} n, \boldsymbol{R}\rangle\right) \quad . \tag{2.12d}$$

As a result, we rewrote the Berry phase as an integral of the Berry field strength/Berry curvature over the whole interior of the closed path instead of an integral of the Berry connection along the boundary. Note that the definition of the Berry phase in Eq. (2.7) requires γ_n to be completely real in order to express the Berry phase through the imaginary part of the integral. The reduction to a two-dimensional parameter space can be achieved by the restriction to a single component of Ω_n. The Berry curvature is parameter-dependent and can be of importance, even if the Berry phase vanishes.

The Berry curvature in Eq. (2.12d) is expressed by using the derivatives of eigenstates which is unsuitable for computational calculations since the derivatives generate arbitrary phases. This numerical problem can be solved through various methods, for instance by shifting the derivation from the eigenstates to the Hamiltonian. The Berry phase can thus be expressed as

$$\gamma_n = -\iint \mathrm{d}\boldsymbol{S}\, \mathrm{Im} \sum_{m \neq n} \frac{\langle n, \boldsymbol{R}| \nabla_{\boldsymbol{R}} H(\boldsymbol{R}) |m, \boldsymbol{R}\rangle \times \langle m, \boldsymbol{R}| \nabla_{\boldsymbol{R}} H(\boldsymbol{R}) |n, \boldsymbol{R}\rangle}{(E_m(\boldsymbol{R}) - E_n(\boldsymbol{R}))^2} \quad . \tag{2.13}$$

First, this formula does not depend on the gauge of $|n, \boldsymbol{R}\rangle$ or $|m, \boldsymbol{R}\rangle$ and can therefore be applied in numerical calculations. The representation of γ_n in Eq. (2.13) gives further insights into the Berry phase. It shows that the Berry phase can be interpreted as an interaction between the dispersion band $|n, \boldsymbol{R}\rangle$ and the remaining dispersion bands $|m, \boldsymbol{R}\rangle$. The sum of the Berry curvatures $F_{n,jk}$ over all bands n cancels out, so that $\sum_n F_{n,jk} = 0 \,\forall\, j, k$ holds. Furthermore, a degenerate eigenstate from a closed gap would cause a singularity which can lead to a quantum phase transition. Degenerate energy bands are also general possible (multiband case) and lead to the slightly different expression of non-Abelian Berry phases [74].

The generalization to the multiband case extends each Berry connection component into a square matrix of dimension equal to the number of unseparated bands. The non-Abelian Berry connection $\mathcal{A}_{mn,j}$ [75] is defined as

$$\mathcal{A}_{mn,j} = \mathrm{i} \langle m, \boldsymbol{R}| \partial_{R_j} |n, \boldsymbol{R}\rangle \tag{2.14}$$

and the non-Abelian Berry curvature $\mathcal{F}_{mn,jk}$ is given by

$$\mathcal{F}_{mn,jk} = F_{mn,jk} - \mathrm{i}\left[\mathcal{A}_j, \mathcal{A}_k\right]_{mn} \quad . \tag{2.15}$$

In this thesis, we focus on topological quantum materials which can be described by the framework of the band theory of solids. A further simplification is the assumption of translation symmetry due to a Bravais lattice. The investigation of topological properties

with a lack of translational invariance proves to be difficult using band theory and is part of current research. Particularly, the investigation of disorder effects on topological phases is of significance due to the prediction of their stability against disorder.

The translational invariance allows the definition of a momentum $\boldsymbol{k}$. In presence of a crystalline structure[5] the solution of the stationary Schrödinger equation $H(\boldsymbol{k})\,|\psi(n,\boldsymbol{k})\rangle = E_n(\boldsymbol{k})\,|\psi(n,\boldsymbol{k})\rangle$ can be written in the form $|\psi(n,\boldsymbol{k})\rangle = \mathrm{e}^{\mathrm{i}\boldsymbol{k}\boldsymbol{r}}\,|n,\boldsymbol{k}\rangle$ according to Bloch's theorem, where $\boldsymbol{r}$ corresponds to the position operator. The eigenstates $|n,\boldsymbol{k}\rangle$ and eigenvalues $E_n(\boldsymbol{k})$ of the Bloch Hamiltonian $H(\boldsymbol{k}) = \mathrm{e}^{\mathrm{i}\boldsymbol{k}\boldsymbol{r}} H \mathrm{e}^{-\mathrm{i}\boldsymbol{k}\boldsymbol{r}}$ define the band structure. Thus the parameter space is specified as the momentum $\boldsymbol{k}$ of the first Brillouine Zone (BZ), $\boldsymbol{R} \hat{=} \boldsymbol{k}$. The restriction of the momentum space to the first BZ leads to a closed manifold identified as a d-dimensional torus T^d.

The classification of different topological phases for quantum materials are handled by defining invariants, which are usually expressed as integrals of some geometric quantities like the Berry phase over the whole parameter space. Topological invariants are global properties so that the complete parameter space is required to obtain a quantized quantity. In this sense, the accumulated Berry phase along a path that goes around the BZ is suitable for defining an invariant. The definition, application and consequences of the used topological invariants in this work are exemplified with fundamental models in the following sections.

2.3. Su–Schrieffer–Heeger model

The Su-Schrieffer–Heeger (SSH) model [76, 77] represents the most basic non-trivial topological system in one dimension. Originally, it was introduced to describe the conducting polymer polyacetylene. The Peierls distortion in polyacetylene leads to a bipartite sublattice structure with an alternating tunnel coupling strength. At half filling, the system represents a Peierls insulator due to the dimerization. Particularly, the choice between the two possible dimerizations has huge consequences because the two different realization are topologically distinct (see Fig. 2.2 (b) and (c)) for finite systems with even number of sites.

The presented SSH model describes the spinless fermion hopping[6] by an effective 1D tight-binding model, providing a simple two-band model for the bulk system. The topologically protected zero-energy modes emerging for the boundary in the topological phase are associated to a non-trivial invariant in the bulk. In this section, we will perform bulk and boundary calculations of the SSH model and elucidate their connection. Systems in one dimension have more than one topological quantity in one symmetry class. We will examine the two most important topological quantities in 1D: the Zak phase and the winding number.

The single-particle Hamiltonian is given by

$$\mathcal{H}_{\mathrm{SSH}} = \sum_i \left(v c^\dagger_{i,\mathrm{B}} c_{i,\mathrm{A}} + w c^\dagger_{i+1,\mathrm{A}} c_{i,\mathrm{B}} \right) + \mathrm{h.c.} \tag{2.16}$$

[5] The IQHE for the free 2D electron gas has no crystalline structure. Nonetheless, the IQHE can approximately be described by square lattice models and has a lot in common with topological insulators. For further information see Sec. 3.2.

[6] For simplicity, the spin degree of freedom is neglected.

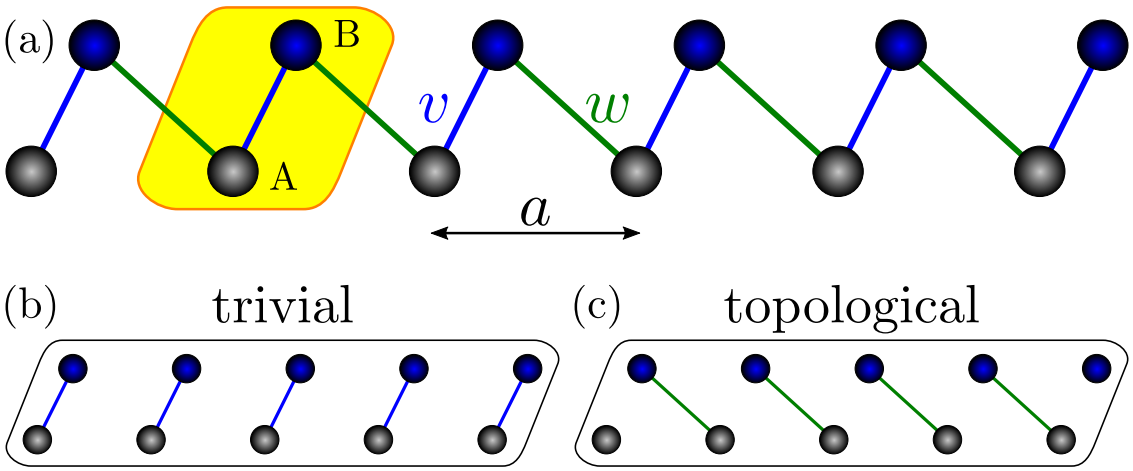

Figure 2.2: (a) Illustration of the lattice structure of the SSH model. Sublattice A (B) is shown as gray (blue) dots. The staggered hopping amplitudes are composed of intracell hoppings v (blue lines) and intercell hoppings w (green lines). The yellow shaded area highlights the two-site unit cell. The corresponding lattice constant a is depicted by a black arrow. (b)-(c) Fully dimerized limits of a finite SSH chain with even number of sites. The trivial case ($w = 0$) consists of disconnected intracell dimers. The topological case ($v = 0$) exhibit dimers between neighboring unit cells. Thus each end of the chain provides one isolated site corresponding to the topological zero-mode.

where $c_{i,\alpha}$ and $c_{i,\alpha}^\dagger$ are, respectively, the fermionic annihilation and creation operators at site $\alpha \in \{\mathrm{A}, \mathrm{B}\}$ of unit cell i. The average tunneling strengths v and w are real and non-negative. The lattice and coupling structure are shown in Fig. 2.2(a). In order to investigate the bulk system, we consider periodic (Born–von Kármán) boundary conditions. Thus we are able to apply a discrete Fourier transformation leading to

$$\mathcal{H} = \sum_{k \in \mathrm{BZ}} \begin{pmatrix} c_{k,\mathrm{A}}^\dagger, & c_{k,\mathrm{B}}^\dagger \end{pmatrix} H(k) \begin{pmatrix} c_{k,\mathrm{A}} \\ c_{k,\mathrm{B}} \end{pmatrix} \tag{2.17}$$

$$\text{with} \quad H(k) = \begin{pmatrix} 0 & v + w\mathrm{e}^{-\mathrm{i}k} \\ v + w\mathrm{e}^{\mathrm{i}k} & 0 \end{pmatrix} \quad , \tag{2.18}$$

where the lattice constant a is set to unity. The resulting bulk dispersion is described by

$$E_n(k) = \pm\sqrt{v^2 + w^2 + 2vw\cos(k)} \quad \text{with} \quad n \in \{1, 2\} \quad . \tag{2.19}$$

The two bands remain separated as long as $v \neq w$ holds and the energy gap is $\Delta = 2|v - w|$. The condition $v = w$ defines the transition point between both phases and describes a conducting phase. The Peierls distortion is preferably realized since the staggering of the hopping amplitudes ($v \neq w$) lowers the energy of the occupied states. Note that the choice between the two unit cell configurations is arbitrary in the bulk. The change between the two unit cells equals exchanging v and w. The swapping of both hopping parameters v and w does not affect the energy eigenvalues in the bulk. In contrast, the eigenstates in the bulk are significantly changed since a trivial phase is swapped to a topological phase or vice versa. Since the impact is restricted to the eigenstates or the

pseudo-spin representation, the consequences are not so obvious and have to be shown by additional calculations. This is illustrated in the following sections.

The investigation of a finite chain with open boundary conditions clearly shows a difference in the energetic spectrum by exchanging v and w. The two limiting cases depicted in Fig. 2.2 (b) and (c) illustrate the different phases of the system. The case $w = 0$ corresponds to a trivial fully dimerized chain, while at $v = 0$ the system hosts additional uncoupled sites at the ends of the chain. These uncoupled sites lead to in-gap states at zero energy. They are fittingly referred to as zero-modes which are localized at the boundary of the chain. Furthermore, they are also called end states or edge states and their emergence is linked to a topological invariant. These zero-modes are of special importance due to their unique characteristics such as being topologically protected and exponentially localized at the boundary[7]. In order to predict zero-modes in the SSH model and to clarify their occurrence, we perform further bulk calculations to determine their topological origin.

2.3.1. Pseudo-spin representation and winding number

The representation of the Hamiltonian with a pseudo-spin provides an intuitive access to determine topological invariants. The key idea is that the pseudo-magnetic field contains the information about the topological invariant. Therefore the calculation of the eigenstates is not necessary. To begin with, the matrix representation of the Hamiltonian must be expressed in a compact notation

$$H(k) = d_0(k)\mathbb{1} + \boldsymbol{d}(k)\boldsymbol{S} \quad , \tag{2.20}$$

where a pseudo-magnetic field $\boldsymbol{d}(k) \in \mathbb{R}^3$ couples to a pseudo-spin $\boldsymbol{S} = (S_x, S_y, S_z)^\top$ in the SU(2) matrix representation. The spin matrices fulfill the commutator relation $[S_i, S_j] = \mathrm{i}\varepsilon^{ijk}S_k$. The energy offset is described by $d_0(k)$. This energy offset is neglected for the determination of the topological invariant since it does not affect the eigenstates. The total spin S is fixed by the number of bands which is equal to the multiplicity $(2S+1)$. The eigenvalues are given by

$$\omega_n = n|\boldsymbol{d}(k)| \quad , \tag{2.21}$$

where $n = -S, \ldots, S$. If $|\boldsymbol{d}(k)| \neq 0$ holds for the complete BZ, the bands are separated.

The usual two-band Hamiltonian such as the one of the SSH model leads to the use of the spin-1/2 representation with the well-known Pauli matrices $\{\sigma_x, \sigma_y, \sigma_z\}$. For this case, $\boldsymbol{S} = \frac{1}{2}\boldsymbol{\sigma}$. The factor $1/2$ in this special case is usually absorbed into the factor $\boldsymbol{d}$. The Pauli matrices with the unit matrix form a complete basis and can therefore always be applied to two-band models. For more than two bands, the matrix representation of the spin does not cover the whole matrix space so that the pseudo-spin representation is not generically applicable.

The next step depends on the dimension of the parameter space. In this section, the one-dimensional BZ is the interval from $-\pi$ to π. By exploring the SSH model as an example, we recognize that the winding number can classify the topological quantity of a one-dimensional system. For the SSH model, the Hamiltonian can be rewritten by using

$$\boldsymbol{d}(k) = \big(v + w\cos(k), w\sin(k), 0\big) \quad . \tag{2.22}$$

[7] The wave function of an edge state reaches into the bulk with an exponentially decaying tail.

Generally, the endpoint of the pseudo-magnetic field $\boldsymbol{d}(k)$ as a function of the wave number k forms a closed loop due to the periodicity of the BZ, if k is varied from 0 to 2π. The vector $\boldsymbol{d}(k)$ is restricted to the d_x-d_y-plane, wherein $\boldsymbol{d}(k)$ describes a circle centered at $(v, 0)$. The topological invariant of a loop restricted to a plane around a reference point, mostly the origin, is designated as the winding number ν. The winding number $\nu \in \mathbb{Z}$ corresponds to the total number of times that the loop winds around the reference point. Thus the model with $v > w$ has a trivial winding number $\nu = 0$ and $v < w$ corresponds to the topological phase with $\nu = 1$. The sign of the winding number is negative if the curve loops clockwise. The continuous deformations of the loop by changing v and w do not change the winding number unless we pass the point $v = w$ where the gap closes. An alternative choice of the unit cell with (B, A) instead of (A, B) would swap the meaning of v and w as intracell and intercell hoppings, respectively. Thus the trivial phase and the topological phase are swapped because then $v > w$ corresponds to $\nu = 1$.

The winding number ν can be formulated in several variants. According to the SSH model, the winding number can be calculated by

$$\nu = \frac{1}{2\pi} \oint \left(\hat{\boldsymbol{d}}(k) \times \frac{\mathrm{d}}{\mathrm{d}k} \hat{\boldsymbol{d}}(k) \right) = \frac{1}{2\pi} \oint \frac{d_x(k)\,\mathrm{d}d_y(k) - d_y(k)\,\mathrm{d}d_x(k)}{d_x^2(k) + d_y^2(k)} \quad . \tag{2.23}$$

The hat indicates unit vectors. A winding number can only be defined if the loop is restricted to plane such as in the case of the SSH model where $d_z(k) = 0$ holds. This requirement is closely related to the chiral symmetry and is treated in the following subsection.

2.3.2. Symmetry classification

All single-particle fermionic systems describing topological insulators and topological superconductors can be classified by their spatial-dimension and their discrete symmetries, see Tab. 1.1. All possible cases are divided into ten different symmetry classes. The symmetry of the system is characterized by $\mathcal{T}^2$, $\mathcal{C}^2$ and $\mathcal{S}^2$, where $\mathcal{T}$, $\mathcal{C}$ and $\mathcal{S}$ represent the time-reversal, particle-hole and chiral symmetry operators, respectively. According to Wigner's theorem [78], all symmetry operations are unitary or anti-unitary transformations in the Hilbert space. The Hamiltonian is symmetric with respect to O if the Hamiltonian commutes with the symmetry operator

$$[\mathcal{H}, O] = 0 \quad . \tag{2.24}$$

The basic transformation properties of the matrix representation of a single-particle Hamiltonian $H(k)$ as well as the consequences for the energy $E(k)$ can be taken from the overview in Tab. 2.1. A detailed consideration of the symmetries can be found in the work by Chiu et al. [38]. In the following, we want to explain the key points of symmetries by using the SSH model.

The TRS reverses the arrow of time $t \to -t$. If particles retrace their motion by inverting the arrow of time, then this indicates that the system preserves the TRS. The example of a charge particle in an external magnetic field which breaks the TRS is well-known. The time-reversal operator $\mathcal{T}$ is anti-unitary[8]. Depending whether the particles are characterized as having spin or not, different representations of $\mathcal{T}$ are used.

[8] Anti-unitary operators $\mathcal{A}$ do not support eigenvalues [27]. In contrast, $\mathcal{A}^2$ has to be unitary and can be classified by their eigenvalues.

time-reversal	$\mathcal{T}H(k)\mathcal{T}^{-1} = \quad H(-k)$	$E_i(k) = \quad E_i(-k)$	$\mathcal{T}^2 = \pm\mathbb{1}$
particle-hole	$\mathcal{C}H^{\top}(k)\mathcal{C}^{-1} = -H(-k)$	$E_i(k) = -E_j(-k)$	$\mathcal{C}^2 = \pm\mathbb{1}$
chiral	$\mathcal{S}H(k)\mathcal{S}^{-1} = -H(\quad k)$	$E_i(k) = -E_j(\quad k)$	$\mathcal{S}^2 = \quad \mathbb{1}$
inversion	$\mathcal{I}H(k)\mathcal{I} = \quad H(-k)$	$E_i(k) = \quad E_i(-k)$	$\mathcal{I}^2 = \quad \mathbb{1}$

Table 2.1: Overview of important discrete symmetry properties of single-particle Hamiltonians. Each row shows the required Hamiltonian transformation, the resulting effects on the energy dispersion and squares of the symmetry operators, respectively.

The time-reversal operator $\mathcal{T}$ of spinless particles in the position space representation is given by the complex-conjugation operator, $\mathcal{T} = \mathcal{K}$ [27]. The representation of $\mathcal{T}$ for particles with spin should also flip the spin angular momentum. This is accomplished by a π-rotation around the y-axis in the S_z-representation so that $\mathcal{T} = \mathrm{e}^{-\mathrm{i}\pi S_y}\mathcal{K}$. Furthermore, note that $\mathcal{T}^2 = +\mathbb{1}$ for integer-spin and $\mathcal{T}^2 = -\mathbb{1}$ for half-integer spin. This fact is of fundamental importance for the derivation of Kramers theorem which will be discussed in Sec. 2.5.

The particle-hole symmetry is also known as charge conjugation, hence the notation $\mathcal{C}$, it swapes all particles with their corresponding anti-particles. As a result, all possible charges are reversed. The charge conjugation operator has to be an anti-unitary operator [36]. Similar to $\mathcal{T}$, $\mathcal{C}^2 = +\mathbb{1}$ holds for integer spin while half-integer spin yields $\mathcal{C}^2 = -\mathbb{1}$.

The chiral symmetry can be understood as the combination $\mathcal{S} = \mathcal{T}\mathcal{C}$. Nonetheless, the chiral symmetry is important for a complete classification of all phases. Even if both symmetries $\mathcal{T}$ and $\mathcal{C}$ are broken, their combination can still be preserved. The chiral symmetry operator $\mathcal{S}$ is unitary and Hermitian [38], thus $\mathcal{S}^2 = \mathbb{1}$ holds.

An alternative representation of the chiral symmetry operator is based on orthogonal sublattice projectors

$$P_\alpha = \sum_i |i,\alpha\rangle \langle i,\alpha| \quad , \tag{2.25}$$

where α represents the sublattice index (internal degree of freedom), here $\alpha \in \{\mathrm{A},\mathrm{B}\}$. Hence, it is also called sublattice symmetry. The sublattice symmetry $\mathcal{S}$ requires that no couplings between sites of the same sublattice are allowed ($P_\alpha H P_\alpha = 0$, $P_\alpha P_\beta = 0$ for $\alpha \neq \beta$). This also includes on-site potentials which would break the chiral symmetry see for instance the staggered on-site potentials in the Rice–Mele model [79]. The presence of chiral symmetry leads to a symmetric energy spectrum. Using the basis of eigenstates of the chiral symmetry operator results in a block off-diagonal matrix representation [38]

$$H = \begin{pmatrix} 0 & D \\ D^\dagger & 0 \end{pmatrix} \quad . \tag{2.26}$$

The SSH model obviously preserves the chiral symmetry since only hoppings between sublattices A and B are present. For a bipartite Hamiltonian as in the SSH model we can find a general relation to reproduce the projectors on sites A and B by using $\mathcal{S}$

$$P_\mathrm{A} = \frac{1}{2}(\mathbb{1} + \mathcal{S}); \qquad P_\mathrm{B} = \frac{1}{2}(\mathbb{1} - \mathcal{S}); \qquad \mathcal{S} = P_\mathrm{A} - P_\mathrm{B} = \sigma_z \quad . \tag{2.27}$$

The diagonal form of $\mathcal{S}$ indicates that the matrix representation is expressed in the basis of eigenstates with respect to $\mathcal{S}$. Thus, without loss of generality, we conclude from the definition of chiral symmetry that $d_z(k) = 0$ which is necessary to define winding numbers. If $d_z \neq 0$, the loop is not confined in the d_x-d_y-plane so that no clear definition of winding around the origin is given. As a result, if chiral symmetry is broken, we can move from the topological phase to the trivial phase without going through a gap-closing-and-opening transition. This fact illustrates the classification as a symmetry-protected topological phase.

From the perspective of energy, we can also clarify the role of the symmetry conservation and the gap-closing-and-opening transition with respect to the protected zero energy states and the topological bulk invariant. As long as the chiral symmetry is preserved, we can calculate the winding number and hence a topological invariant for the bulk. Furthermore, the chiral symmetry implies that each eigenstate $|n, \boldsymbol{k}\rangle$ with energy E_n has an associated partner eigenstate $\mathcal{S}\,|n, \boldsymbol{k}\rangle = |\tilde{n}, \boldsymbol{k}\rangle$ with energy $E_{\tilde{n}} = -E_n$. Only the zero-modes can be their own partner $\mathcal{S}\,|n, \boldsymbol{k}\rangle = |n, \boldsymbol{k}\rangle$ for $E_n = 0$. These states only emerge at the interface of topologically distinct phases. Therefore, zero-modes are considered as topologically protected since moving away from $E = 0$ requires additional states at the same interface in order to fulfill the chiral symmetry. This can only be done by a gap-closing-and-opening transition. Otherwise, one has to break chiral symmetry. As a result, the edge states are robust as long as the chiral symmetry and the bulk gap are preserved.

The block off-diagonal representation in Eq. (2.26) can be used to give a general definition of the winding number [38]

$$\nu = \frac{1}{2\pi \mathrm{i}} \int_0^{2\pi} \mathrm{d}k \mathrm{Tr} \left[\frac{\mathrm{d}}{\mathrm{d}k} \log(D) \right] = \frac{1}{2\pi \mathrm{i}} \int_0^{2\pi} \mathrm{d}k \mathrm{Tr} \left[D^\dagger \frac{\mathrm{d}}{\mathrm{d}k} D \right] \quad . \tag{2.28}$$

The representation in block off-diagonal form is a generic feature of the chiral symmetry. For clarity, we consider the case of a two-band model such as the SSH model, where the block off-diagonal matrix D becomes one-dimensional with $D = d_x(k) + \mathrm{i}d_y(k)$. Hence, by regarding the off-diagonal element as a complex function $D = |D| \exp^{\mathrm{i}\Phi}$, the winding can be expressed by using the logarithm function which is equivalent to Eq. (2.23) [80]. The generalize formula in Eq. (2.28) can always be applied to calculate the winding number since it only requires the chiral symmetry and works with or without the pseudo-spin representation. Furthermore, the definition in Eq. (2.28) can be extended to define a winding number in a three-dimensional parameter space [36].

The inversion symmetry $\mathcal{I}$ is a spatial symmetry that reverses the position $r \to -r$. Inverting twice has no effect: $\mathcal{I}^2 = \mathbb{1}$. The inversion symmetry operator $\mathcal{I}$ is unitary and Hermitian[9]. In the case of energetically separated bands, the inversion symmetry relates the eigenstates of the same band at k and $-k$:

$$H(k)\,|u(k)\rangle = E(k)\,|u(k)\rangle \tag{2.29}$$

$$H(-k)\mathcal{I}\,|u(k)\rangle = E(k)\mathcal{I}\,|u(k)\rangle \quad . \tag{2.30}$$

[9] We refer to the inversion symmetry operator $\mathcal{I}$ as the operator acting only on internal degrees of freedom. For completeness, we mention that the inversion symmetry changes the sign of plane waves and Bloch states leading to the inversion of momentum $k \to -k$.

Thus the energy is degenerate $E(k) = E(-k)$ and for the eigenstates the relation

$$|u(-k)\rangle = \mathrm{e}^{\mathrm{i}\Phi}\mathcal{I}\,|u(k)\rangle \tag{2.31}$$

applies. At the time-reversal invariant momenta $\Lambda_i = \{0, \pi\}$, the additional phase can only be real and is denoted as the parity η

$$\mathcal{I}\,|u(\Lambda_i)\rangle = \eta\,|u(\Lambda_i)\rangle \quad \text{with} \quad \eta = \pm 1 \quad . \tag{2.32}$$

For instance the transformation symmetry operator in the SSH model is given by $\mathcal{I} = \sigma_x$ which fulfills $\mathcal{I}H(k)\mathcal{I} = H(-k)$. The investigation of the parities in the topologically distinct phases of the SSH model indicates a certain relation to the invariant of the system. The trivial phase $w < v$ provides the same parity $+1$ at $k = \{0, \pi\}$. In contrast, the sign of the parity in the topological phase $w > v$ differs since the parities are given by $\eta_0 = +1$ and $\eta_\pi = -1$. Thus we see that the parities are related to a topological invariant of the system which is known as the Zak phase and is described in the following subsection.

2.3.3. Zak phase

As explained in Sec. 2.2, topological properties originate from the eigenstates of the system. The calculation of the winding number as a topological invariant is based on a matrix representation of the Hamiltonian and therefore does not require the explicit calculation of the eigenstates. However the definition of the winding number uses the off-diagonal representation which is given in the basis of eigenstates of the chiral symmetry operator. This fact shows that the topological origin of the winding number is related to the eigenstates. In this section, we consider the Zak phase as a possible topological invariant which is based on the eigenstates of the system.

The Zak phase γ_n [37] is defined by integrating the Berry connection over the one-dimensional BZ

$$\gamma_n = \mathrm{i}\int_0^{2\pi} \langle n, k|\,\partial_k\,|n, k\rangle\,\mathrm{d}k \quad . \tag{2.33}$$

Thus, the Zak phase corresponds to the Berry phase accumulated along the closed 1D path. The path is closed due to the periodicity of the 1D BZ. Note that the 1D BZ is a special case since it cannot be interpreted as the boundary of an interior. As a result, the Zak phase must be calculated from the Berry connection.

In the presence of chiral or inversion symmetry, the Zak phase is quantized to 0 or π [37], where the trivial phase corresponds to 0 and π corresponds to a topological phase. In this cases, the quantized Zak phase can be regarded as a $\mathbb{Z}_2$ topological invariant. The calculation of the Zak phase in inversion symmetry systems can be simplified by considering the parity at 0 and π. The Zak phase corresponds to π if the sign of the parity changes.

The chiral symmetry is not intrinsically given in polyacetylene because the NNN hopping violates the chiral symmetry ($d_z \neq 0$). This prevents a well-defined winding number, but the Zak phase still remains quantized due to the preserved spatial symmetry of inversion with respect to the center of a bond [81]. This emphasizes that the quantization of the Zak phase can also be guaranteed by additional symmetries besides the chiral symmetry.

We rephrase the SSH model using the Pauli matrices ($H(k) = d_0(k)\sigma_0 + \boldsymbol{d}(k)\boldsymbol{\sigma}$, $E_\pm = d_0(k) \pm d(k)$). Then we express the two eigenstates as

$$|+\rangle = \frac{1}{\sqrt{2d(d+d_z)}} \begin{pmatrix} d_z + d \\ d_x - \mathrm{i}d_y \end{pmatrix} \quad , \qquad |-\rangle = \frac{1}{\sqrt{2d(d-d_z)}} \begin{pmatrix} d_z - d \\ d_x - \mathrm{i}d_y \end{pmatrix} \quad . \tag{2.34}$$

The Berry connection is then given by

$$A_\pm = \mathrm{i} \langle \pm | \, \partial_k \, | \pm \rangle = \frac{-1}{2d(d \pm d3)} (d_2 \partial_k d_1 - d_1 \partial_k d_2) \quad . \tag{2.35}$$

Using Eq. (2.22) and integrating over the one-dimensional BZ leads to 0 for $v > w$ and to π in the case of $v < w$.

In order to determine numerically the Zak phase correctly we need to consider the gauge freedom by calculating the eigenstate at each k. The diagonalization routine results eigenstates with arbitrary gauge phases which prevents the correct determination of the derivative. Thus a gauge invariant formula is required. Due to the closed loop in one dimension, it is appropriate to express the Zak phase as a Wilson loop based on a discretized BZ

$$\gamma_n = -\mathrm{Im} \sum_{i=0}^{N-1} \ln \left(\langle n, k_i | n, k_{i+1} \rangle \right) \mod 2\pi \quad , \tag{2.36}$$

which is gauge invariant. The discretization of the BZ is described by $k_i = 2\pi i/N$ with $i = 0, 1, \ldots, N-1$, where we set the lattice constant to unity. More details of the numerical determination is given in App. D.

The comparison between the Zak phase and the winding number reveals that each invariant has its own advantages and disadvantages. Both invariants coincide in some models where each invariant corroborate the topological properties of the system. Generically, there are also models with only one topological non-trivial invariant. The winding number is only applicable in the presence of a chiral symmetry which can hardly be defined for higher-dimensional problems. Furthermore, the usage of the pseudo-spin representation for the determination of the winding number is only possible in special cases. The Zak phase does not rely on chiral symmetry and can therefore be considered as the more general invariant. However, the Zak phase cannot be used to determine non-trivial invariants in 1D with an even number as for instance a system with winding number $\nu = 2$. Consequently, both methods complement each other very well to cover many possible scenarios.

A further notable topic in this context is the direct relation between the Berry phase and the modern theory of electric polarization [82, 83]. Electric polarization and magnetization are the two fundamental electromagnetic properties of solid matter. The charge separation in insulating materials is denoted as dielectric polarization. In this context, we focus on one-dimensional lattices. From the polarization we recognize that the Zak phase is quantized to 0 or π in presence of inversion symmetry.

The description of localized charges using Wannier states allows one to define a polarization in each unit cell. Thus, based on the dipole picture the polarization in 1D can be expressed as [84]

$$q \langle w(j) | \, x \, | w(j) \rangle = \frac{q\mathrm{i}}{2\pi} \int_{-\pi}^{\pi} \mathrm{d}k \, \langle n, k | \, \partial_k \, | n, k \rangle + qj \quad , \tag{2.37}$$

where the unit cell number is denoted by j and the electrical charge by $q = -|e|$. The lattice constant is set to unity. The centers of the Wannier charge densities are equally spaced. The first contribution in Eq. (2.37) is proportional to the Zak phase which corresponds to a uniform displacement creating a dipole moment in each unit cell. Therefore the accompanying bulk electric polarization is described by

$$P_{\text{electric}} = q \langle w(0)| x |w(0)\rangle = \frac{q\mathrm{i}}{2\pi} \int_{-\pi}^{\pi} \mathrm{d}k \langle n,k| \partial_k |n,k\rangle = \frac{q\gamma_n}{2\pi} \quad . \tag{2.38}$$

In the case of inversion symmetry, $P_{\text{electric}} = \{0, e/2\}$ [85] so that the Wannier charge center is situated at the respective lattice sites (no polarization, $P_{\text{electric}} = 0$) or between them (maximal polarization, $P_{\text{electric}} = e/2$). If $P_{\text{electric}} = \{0, e/2\}$ is inserted in Eq. (2.38), we see that the Zak phase is quantized to $\gamma = \{0, \pi\}$, respectively.

One key insight gained by modern polarization theory is the fact that only the difference in polarization has a physical meaning since only the change can be observed experimentally [86]. This polarization change is determined by the evolution of the bulk current j_n [69] given by

$$\Delta P_n = \int_0^T \mathrm{d}t j_n = -\frac{e}{2\pi} \int_0^T \int_{\text{BZ}} F_{n,kt} \, \mathrm{d}t \, \mathrm{d}k \quad , \tag{2.39}$$

which can be expressed by the Berry phase. To this end, we assume that change is periodic in time where T denotes one period. Note that the corresponding two-dimensional parameter space is made of a one-dimensional BZ and the periodicity in time. For a cyclic adiabatic evolution of the system the transported charges is quantized since it is performed by a charge pump, which shall be explained in the next subsection. The topological charge pump performed in a finite strip requires the presence of edge states and is closely related to the bulk-boundary correspondence of 2D Chern insulators. The number of transported particles and the topological invariant of 2D Chern insulators are both determined by the Chern number.

2.3.4. Bulk-boundary correspondence and Thouless charge pump

The edge states appearing at the ends of a finite chain are attributed to the topological invariants in the bulk. The relationship between the topological bulk invariants and the edge states in a finite system is described by the bulk-boundary correspondence [26, 45]. There are several formulations of the bulk-boundary correspondence. Here we will give a first insight by considering the SSH model as an example for the bulk-boundary correspondence in one dimension.

The edge state on the right hand side of a finite chain is restricted to one specific sublattice due to chiral symmetry, see Fig. 2.2(c). The difference between the edge states of both sublattices $N_{\text{A}} - N_{\text{B}}$ at one side of the chain is equal to the topological invariant [80]. So for $v > w$ no edge states can be found and for $v < w$ one edge state can be found.

The SSH model represents a special case of a one-dimensional topological insulator since a different choice of the unit cell is equivalent to swapping v and w. Thus an alternative choice can predict a trivial phase instead of a topological phase. However, the difference between both phases realizing different dimerizations results in π independent

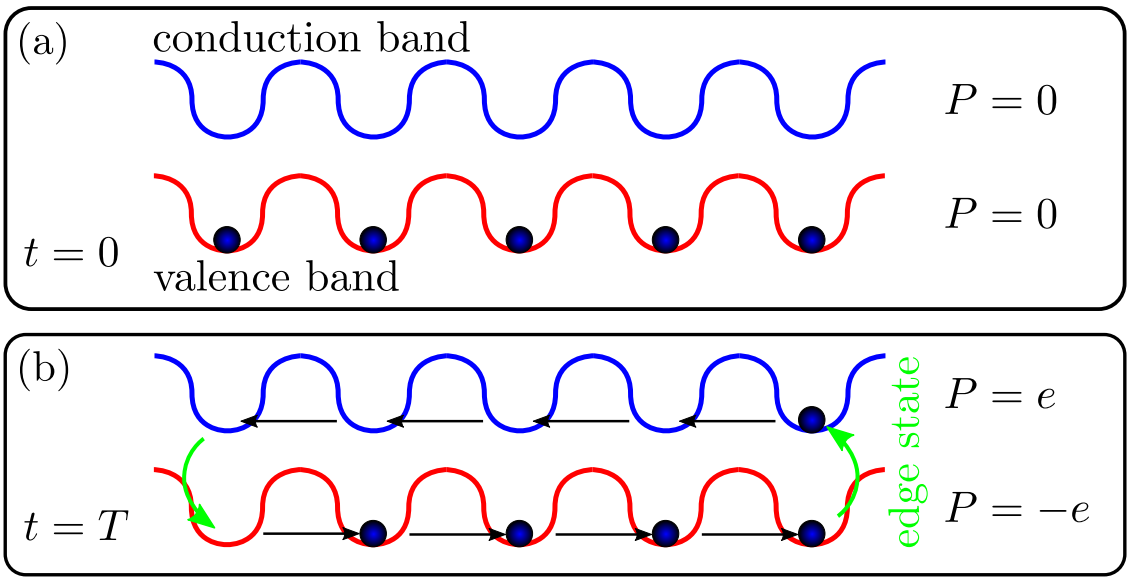

Figure 2.3: (a) Initial occupation of the time-periodic open confining potential in the valence and conduction bands. (b) Final occupation after a full pump cycle. The electron state at the end of the system is pumped into the conduction band by crossing the band gap using the edge states.

from the initial configuration. Thus the topology of the SSH model is measured through investigating the phase shift by swapping both coupling strengths [87].

The Thouless charge pump [88, 89], also known as the adiabatic charge pump, can be seen as a topological pump in one dimension, where an integer number of particles is transported across the complete system in every cycle. The one-dimensional system will be driven cyclically in time t so that the parameter space becomes two-dimensional (momentum space k and time t). Note that the polarization change in Eq. (2.39) presents a Thouless pump since the polarization is changed by transporting charged particles.

The integer number of particles transported is determined by the topology of the time-driven bulk-momentum Hamiltonian $H(k,t)$. The quantization due to the topological origin makes the transport unique and robust to perturbations. Hence, new applications are feasible such as the redefinition of the ampere in metrology [90, 91]. The Thouless charge pump requires a classification by a Chern number based on the particular parameter space given by

$$C_n = \frac{1}{2\pi} \int_0^T \int_{\mathrm{BZ}} F_{n,kt} \, \mathrm{d}k \, \mathrm{d}t \quad , \tag{2.40}$$

which determines the integer number of pumped particles along the chain. The non-trivial Chern numbers results in time-dependent edge states for a finite chain $E(t)$. The dispersion of these edge states are similar to the dispersion of the edge states $E(k_x)$ in a finite strip of a 2D Chern insulator as shown in Fig. 2.7 in the next section.

The charge pump works as a conveyor belt in one direction for the valence band and conveyor belt in the other direction for the conduction band. We consider the example of a confining potential periodic in time with one low-energy and one high-energy state similar to a two-band model. The system is initialized by occupying all-low energy dips,

see Fig. 2.3. After one period, a single electron has been transported from left to right as defined in a Thouless pump. Hence, we reached the polarized phase. At the right edge, the former electron is pumped from the valence to the conduction band. This is only possible by the appearance of edge states crossing the band gap during one periodic cycle. In the conduction band everything is reversed, so that the edge state appears at the left side. This behavior is well realized in the time-dependent Rice–Mele model

$$\mathcal{H}_{\text{time RM}} = \sum_i (v(t) c^\dagger_{i,\mathrm{B}} c_{i,\mathrm{A}} + w(t) c^\dagger_{i+1,\mathrm{A}} c_{i,\mathrm{B}} + \text{h.c.}) + u(t)(c^\dagger_{i,\mathrm{A}} c_{i,\mathrm{A}} - c^\dagger_{i,\mathrm{B}} c_{i,\mathrm{B}}) \quad (2.41)$$

$$\text{with} \quad u(t) = \sin(2\pi t/T), \quad v(t) = 1 + \cos(2\pi t/T), \quad w(t) = 1 \quad , \quad (2.42)$$

where u is the coupling in a staggered on-site potential. The charge pumping cycle only applies if the Chern number is non-trivial and requires the presence of edge states. Hence, it clearly emphasizes the close relation between the non-trivial topological invariant and the occurrence of edge states which is described by the bulk-boundary correspondence.

A topological Thouless pump may be realized by tuning the magnetic flux of a two-dimensional quantum Hall system. This prominent example is known as Laughlin's pump argument [92, 93] which elucidated the quantization of the Hall conductance in the IQHE. The characterization of a Thouless charge pump and the energetic time-evolution of edge states during a pump have many features in common with the two-dimensional topological Chern systems which will be examined more closely in the following section.

2.4. Haldane model

Historically, the Haldane model [51] was the first model studied with a topological non-trivial parameter regime where finite Chern numbers occur. In 1988, Haldane theoretically proposed a fermionic tight-binding model on a two-dimensional honeycomb lattice as a counterpart to the IQHE without an external magnetic field. Hence, the discrete translational symmetry of the honeycomb lattice can be preserved. In contrast, the lattice model of the IQHE known as the Harper–Hofstadter model [94, 95] shows only a reduced magnetic translation symmetry.

Due to its simple nature the Haldane model can be found in introductory lectures and is often applied in proof-of-principle studies. Thus, this chapter fulfills two purposes. On the one hand, the presentation of the model elucidates the general properties of topological Chern insulators in two dimensions. On the other hand, the Haldane model is later employed for proof-of-principle investigations in Sec. 3.1 and Sec. 5.2.

The single-particle Hamiltonian of the Haldane model in second quantization is described by

$$\mathcal{H}_{\text{Hal}} = t \sum_{\langle i,j \rangle} c^\dagger_i c_j + t_2 \sum_{\langle\langle i,j \rangle\rangle} \mathrm{e}^{\mathrm{i}\nu_{ij}\phi} c^\dagger_i c_j + M \sum_i \varepsilon_i c^\dagger_i c_i \quad , \quad (2.43)$$

where c_i annihilates and $c^\dagger_i$ creates a fermionic particle at site i. The Haldane model has no spin degree of freedom. The corresponding honeycomb lattice with a unit cell highlighted in green is shown in Fig. 2.4(a). The two sites within one unit cell are denoted by A and B.

The Hamiltonian comprises two different hopping elements. The real-valued hopping between NN sites corresponds to the standard tight-binding hopping on a honeycomb

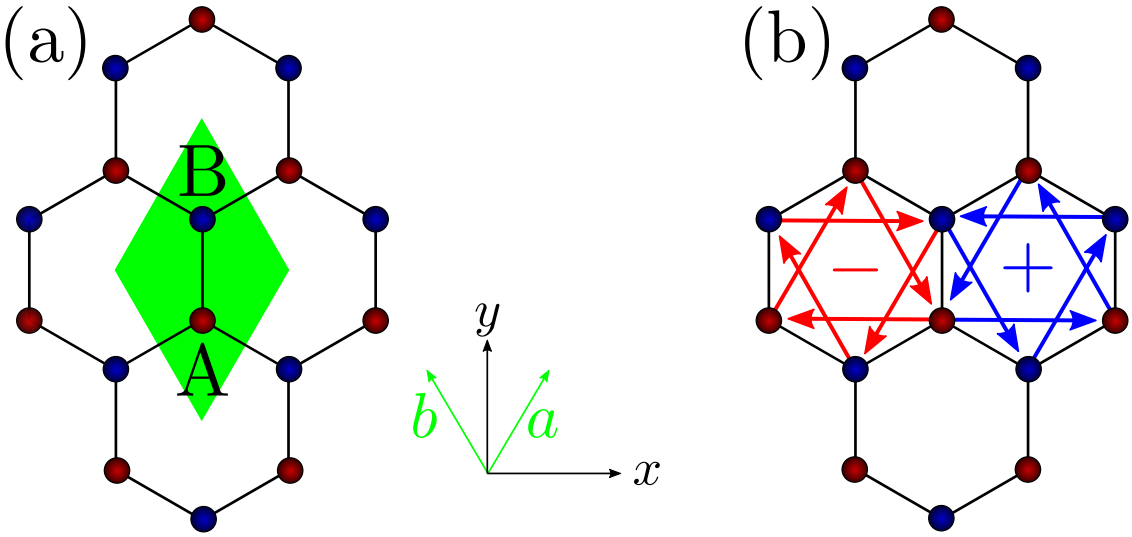

Figure 2.4: (a) Schematic sketch of the honeycomb lattice and a unit cell highlighted in green. The sublattice A is shown in red while the sublattice B is shown in blue. (b) Illustration of the t_2 hopping elements as well as the corresponding sign convention.

lattice. It leads to the famous Dirac cones in the energy dispersion. The crossing points of these cones (pinch point) are designated as Dirac nodes. The linear dispersion around a Dirac node is associated with massless Dirac fermions. This term already describes the low-energy electronic properties of graphene in sufficient detail.

The complex hopping element between NNN sites added by Haldane lifts the degeneracy at the Dirac cones and generates a mass term, so that the system receives its topological properties. The notation $\langle i, j\rangle$ denotes a pair of NN sites while $\langle\langle i, j\rangle\rangle$ denotes a pair of NNN sites. The hopping parameter t is real-valued and serves as an energy unit henceforth. The combination of the positive real parameter t_2 and the phase ϕ determines the complex NNN hopping element. The phase must not be a real number so that $\phi \neq \{0, \pi\}$ in order to break the TRS. This can be seen easily, since the time-reversal operator $\mathcal{T}$ of spinless particles reverses the complex phase. Breaking the TRS is a fundamental requirement to achieve the topological Chern phase as indicated in the periodic table of topological insulators.

The convention for the sign of the phase can be described by

$$\nu_{ij} = \mathrm{sgn}(\hat{d}_1(ij) \times \hat{d}_2(ij))_z = \pm 1 \quad , \tag{2.44}$$

where the intermediate site i' between site i to site j serves to define $\hat{d}_{1/2}(ij)$. The unit vector $\hat{d}_1(ij)$ points from i to i' whereas the unit vector $\hat{d}_2(ij)$ points from i' to j. All complex hopping elements from the sites of one unit cell are shown in Fig. 2.4(b). All positive phases $+\phi$ are displayed in blue while the negative phases $-\phi$ are shown in red. The creation of such a t_2 hopping can be realized by a magnetic flux configuration [68].

The inversion symmetry of the honeycomb lattice is violated if the sites within the unit cell are not equivalent. This is exactly what the on-site term does, because $\varepsilon_i = 1$ at site A and $\varepsilon_i = -1$ at site B. As a result, the breaking of the inversion symmetry opens a finite gap at the pinch point of the Dirac cones leading to massive Dirac particles. In

contrast to t_2 the on-site element leads only to trivial phases of band insulators which are adiabatically connected to the atomic limit. These has been experimentally observed in boron nitride, where the two sites in the unit cell of the hexagonal lattice structure show different occupation.

In order to investigate the properties in the bulk, we consider the Fourier transform of Eq. (2.43) which is given by

$$\mathcal{H}_{\text{Hal}} = \sum_{\boldsymbol{k}} \begin{pmatrix} c^\dagger_{\boldsymbol{k},\text{A}}, & c^\dagger_{\boldsymbol{k},\text{B}} \end{pmatrix} \begin{pmatrix} H_{11} & H_{12} \\ H_{21} & H_{22} \end{pmatrix} \begin{pmatrix} c_{\boldsymbol{k},\text{A}} \\ c_{\boldsymbol{k},\text{B}} \end{pmatrix} \tag{2.44a}$$

$$H_{11} = \quad M + t_2 \left[\mathrm{e}^{\mathrm{i}\phi} \left(\mathrm{e}^{-\mathrm{i}\boldsymbol{k}\boldsymbol{r}_a} + \mathrm{e}^{\mathrm{i}\boldsymbol{k}\boldsymbol{r}_b} + \mathrm{e}^{\mathrm{i}\boldsymbol{k}(\boldsymbol{r}_a - \boldsymbol{r}_b)} \right) + \mathrm{e}^{-\mathrm{i}\phi} \left(\mathrm{e}^{\mathrm{i}\boldsymbol{k}\boldsymbol{r}_a} + \mathrm{e}^{-\mathrm{i}\boldsymbol{k}\boldsymbol{r}_b} + \mathrm{e}^{\mathrm{i}\boldsymbol{k}(\boldsymbol{r}_b - \boldsymbol{r}_a)} \right) \right] \tag{2.44b}$$

$$H_{22} = -M + t_2 \left[\mathrm{e}^{-\mathrm{i}\phi} \left(\mathrm{e}^{-\mathrm{i}\boldsymbol{k}\boldsymbol{r}_a} + \mathrm{e}^{\mathrm{i}\boldsymbol{k}\boldsymbol{r}_b} + \mathrm{e}^{\mathrm{i}\boldsymbol{k}(\boldsymbol{r}_a - \boldsymbol{r}_b)} \right) + \mathrm{e}^{\mathrm{i}\phi} \left(\mathrm{e}^{\mathrm{i}\boldsymbol{k}\boldsymbol{r}_a} + \mathrm{e}^{-\mathrm{i}\boldsymbol{k}\boldsymbol{r}_b} + \mathrm{e}^{\mathrm{i}\boldsymbol{k}(\boldsymbol{r}_b - \boldsymbol{r}_a)} \right) \right] \tag{2.44c}$$

$$H_{12} = t \left(1 + \mathrm{e}^{\mathrm{i}\boldsymbol{k}\boldsymbol{r}_a} + \mathrm{e}^{\mathrm{i}\boldsymbol{k}\boldsymbol{r}_b} \right) = H^*_{21} \quad , \tag{2.44d}$$

where the translation vector are

$$\boldsymbol{r}_a = a \left(\tfrac{\sqrt{3}}{2}, \quad \tfrac{3}{2} \right) \quad \text{and} \quad \boldsymbol{r}_b = a \left(-\tfrac{\sqrt{3}}{2}, \quad \tfrac{3}{2} \right) \quad . \tag{2.45}$$

The lattice constant is denote by a. The Dirac nodes are given at

$$\boldsymbol{K} = \frac{2\pi}{3a} \left(\tfrac{1}{\sqrt{3}}, \quad 1 \right) \quad \text{and} \quad \boldsymbol{K'} = \frac{2\pi}{3a} \left(-\tfrac{1}{\sqrt{3}}, \quad 1 \right) \quad . \tag{2.46}$$

The Taylor expansion of the Haldane Hamiltonian around the Dirac nodes to linear order are described by

$$H(\boldsymbol{K} + \boldsymbol{q}) = -3t_2 \cos(\pi) + \frac{3}{2} t (q_x \sigma_x + q_y \sigma_y) + (M - 3\sqrt{3} t_2 \sin(\phi)) \sigma_z \tag{2.47a}$$

$$\text{and} \quad H(\boldsymbol{K'} + \boldsymbol{q}) = -3t_2 \cos(\pi) - \frac{3}{2} t (q_x \sigma_x - q_y \sigma_y) + (M + 3\sqrt{3} t_2 \sin(\phi)) \sigma_z \quad , \tag{2.47b}$$

where the Pauli matrices are denoted by $\{\sigma_x, \sigma_y, \sigma_z\}$. Both symmetry breaking terms lift the Dirac cones, generating massive Dirac fermions as shown in Fig. 2.5. A mass term based on the graphene tight-binding model corresponds to a term proportional to σ_z, since it lifts the degeneracy at the Dirac nodes. Breaking the inversion symmetry leads to a trivial phase whereas breaking the TRS can lead to a topological phase. This can be elucidated by considering the mass term and the expected edge modes for finite systems. Edge modes are already present in the NN hopping model for Graphene due to the finite Zak phase for finite strips [96]. These edge modes are influenced by the mass terms as illustrated in Fig. 2.5. The inversion symmetry breaking term is momentum independent so that it couples with the same sign on both Dirac cones. Thus one edge state connect the lifted Dirac nodes at the same side of the gap and therefore are attributed to a trivial phase. The Haldane mass term has different sign at different Dirac nodes. As a result, the edge modes connect the lifted Dirac nodes by crossing the gap which is attributed to a topological phase. Hence, both terms compete to set the phase properties. The change between the trivial and the topological phase is determined by a gap-closing-and-opening

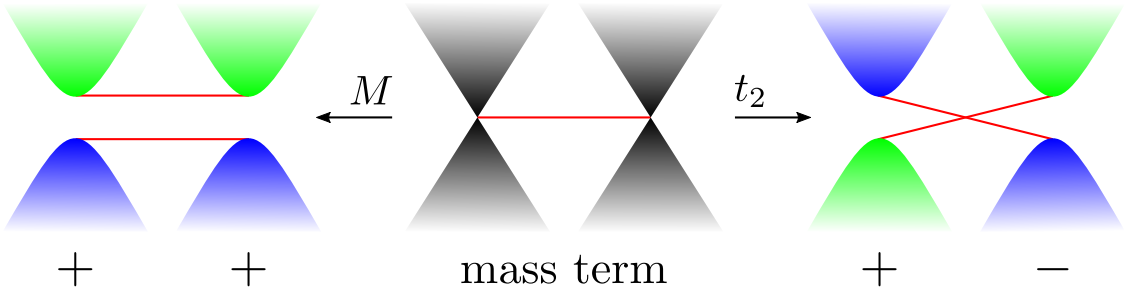

Figure 2.5: Schematic illustration of the mass term in honeycomb lattices. The filled areas indicate the continua of the bulk states. The edge modes are depicted by red lines. The signs indicate examples of mass terms at the Dirac nodes.

transition. Due to the preserved C_3 point group symmetry, the condition for a closed gap in the Haldane model is determined at the two different Dirac nodes which is given by

$$M = 3\sqrt{3}t_2 \sin(\phi) \quad \text{or} \quad M = -3\sqrt{3}t_2 \sin(\phi) \quad . \tag{2.48}$$

These two relations reproduce the transition lines in the known phase diagram of the Haldane model with three phases, see Fig. 2.6. The distinct gapped topological phases are classified by the Chern number, the topological invariant of the Haldane model, which will be explained in the next subsection.

2.4.1. Chern number and chiral edge states

The Chern numbers is used as a topological invariant of two-dimensional systems and can be expressed in many ways. Basically, the Chern number is the accumulated Berry phase along the boundary of the two-dimensional BZ in units of 2π. A non-trivial Chern number stems from the fact that it is impossible to find a smooth and unique gauge phase over the whole BZ. The obstruction to have a global defined gauge is connected to the obstruction to apply Stokes' theorem over the whole BZ [27]. Hence different phase conventions are made to different patches. Now we can apply Stokes' theorem to all patches, so that the Chern number is given by the Berry curvature integrated over the complete BZ[10]

$$C_n = \frac{\gamma_n}{2\pi} = \frac{1}{2\pi} \int_{\mathrm{BZ}} F_{n,xy}(\boldsymbol{k}) \, \mathrm{d}k_x \, \mathrm{d}k_y \quad . \tag{2.49}$$

In reverse it means that if the Stokes' theorem applies for the whole BZ with one patch, the system has a trivial Chern number. The required gauge transformations at the overlapping patches are essential for non-trivial Chern number which are encoded in the different Berry curvatures. Thus the Chern number can also be expressed as the winding number of the transition function between the well-defined gauge patches [27, 72].

The analytical determination of the Chern number is rarely feasible. For this reason a numerical approximation is indispensable. The Chern number or, more precisely, the

[10] Note that this notation is meant to comprise all required patches to cover the whole BZ.

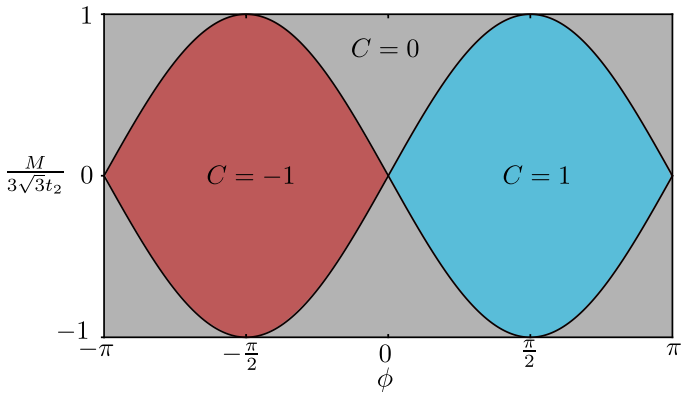

Figure 2.6: The phase diagram of the Haldane model. The given Chern numbers C refer to the lower band. The colors indicate topologically distinct phases.

Berry curvature can be numerically calculated by the formula [97]

$$F_{n,\alpha\beta} = \lim_{\Delta k_\beta \to 0} \lim_{\Delta k_\alpha \to 0} \frac{-1}{\Delta k_\alpha \Delta k_\beta} \mathrm{Im} \log\Big(\langle u_{n,\boldsymbol{k}} | u_{n,\boldsymbol{k}+\Delta\boldsymbol{k}_\alpha} \rangle \langle u_{n,\boldsymbol{k}+\Delta\boldsymbol{k}_\alpha} | u_{n,\boldsymbol{k}+\Delta\boldsymbol{k}_\alpha+\Delta\boldsymbol{k}_\beta} \rangle \cdot \langle u_{n,\boldsymbol{k}+\Delta\boldsymbol{k}_\alpha+\Delta\boldsymbol{k}_\beta} | u_{n,\boldsymbol{k}+\Delta\boldsymbol{k}_\beta} \rangle \langle u_{n,\boldsymbol{k}+\Delta\boldsymbol{k}_\beta} | u_{n,\boldsymbol{k}} \rangle \Big) \quad . \tag{2.50}$$

This formula is a discretized lattice version of the Berry curvature and handles the arbitrary gauges produced in the numerical diagonalization. This can easily be seen by noting that each state occurs twice in Eq. (2.50), as a bra and as a ket state. So an arbitrary gauge transformation at any point in the BZ does not have any effect due to the mutual cancellation of phase changes. This is the same as in Eq. (2.36).

The Chern invariant is always an integer number $C_n \in \mathbb{Z}$. For instance, the phase diagram of the Haldane model in Fig. 2.6 contains three different phases [27, 51]. The trivial phase with $C_n = 0$ is shown with a gray shaded area. The semimetal phase correspond to the transition lines which are marked by black lines and are described in Eq. (2.48). The topological Chern phases with $C_n = \pm 1$ are displayed by red and blue shaded areas, respectively.

The investigation of the Berry curvature in presence of TRS explains why the nontrivial Chern numbers are only achievable if TRS is broken. The presence of TRS in a spinless system for instance leads to

$$F_{ij}(\boldsymbol{k}) = -F_{ij}(-\boldsymbol{k}) \quad . \tag{2.51}$$

Hence, the Chern number has to vanish since the Berry curvature has a point symmetry with respect to the origin. Therefore, breaking TRS is required to get a finite Chern number. This coincides with the general fact that the inversion of time changes the sign of the Chern invariant. Breaking TRS can be done for instance by an external magnetic field or by introducing magnetic order.

A further possibility to determine the Chern number is based on the pseudo-spin representation as introduced in Sec. 2.3.1. All Hamilonians of two-band models can be expressed by Pauli matrices. Thus knowing the pseudo-magnetic field vector is enough to calculate the Chern number even without calculating the eigenstates. Contrary to the

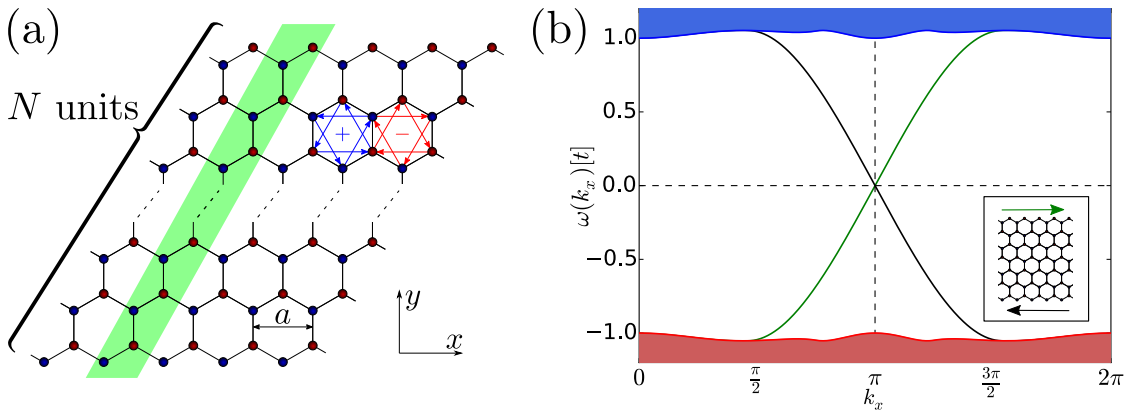

Figure 2.7: (a) Sketch of a finite strip geometry of a honeycomb lattice. The green shaded area highlights a unit cell in x-direction. (b) Dispersion of the edge states with $t_2 = 0.2t$ and $\phi = \pi/2$. The right-moving edge state is depicted in green while the left-moving is shown in black. The filled areas indicate the continua of the bulk states.

winding number in one-dimension, the builded manifold for the endpoint of the pseudo-magnetic field vector has to completely enclose the origin in order to obtain a non-trivial topological index. The Chern number is thus expressed as a winding number[11] of the form [99, 100]

$$C_n = \frac{1}{2\pi} \int_{\mathrm{BZ}} n\hat{\boldsymbol{d}}(\boldsymbol{k}) \left[\frac{\partial \hat{\boldsymbol{d}}(\boldsymbol{k})}{\partial k_y} \times \frac{\partial \hat{\boldsymbol{d}}(\boldsymbol{k})}{\partial k_x} \right] \mathrm{d}k_x \, \mathrm{d}k_y \quad , \tag{2.52}$$

where $\hat{\boldsymbol{d}}(\boldsymbol{k}) = \boldsymbol{d}(\boldsymbol{k})/d(\boldsymbol{k})$ is a normalized vector and $n = -S, \ldots, S$ is determined by the pseudo-spin S. The Berry curvature is given by

$$F_{n,ij} = n\varepsilon_{xyz} \hat{d}_x \partial_{k_i} \hat{d}_y \partial_{k_j} \hat{d}_z \quad . \tag{2.53}$$

According to the bulk-boundary correspondence, gapless conducting states called edge states have to occur in the Chern phase of gapped band structures if boundaries are introduced. The boundaries separate the Chern phase from the vacuum which can be seen as a trivial phase of matter. So in order to change the topological invariant there must exist a gap-closing-and-opening mechanism which is accomplished by the edge states. Such edge states were discovered for the first time at the interface between the IQHE regime and the vacuum [93]. A finite strip geometry[12] as shown in Fig. 2.7(a) provides two boundaries to the vacuum. As a consequence, calculating the dispersion on a finite strip leads to two one-dimensional edge states which are localized on different edges and propagating in different directions as shown in Fig. 2.7(b), where the lattice constant a is set to unity. An edge state that propagates only in one direction at one edge is called as chiral.

[11] This equation shows the close relation of the Chern number to the skyrmion number [98, 99].
[12] Note that the lattice constant a alternatively specifies the distance between NNN sites. This is done for the sake of simplicity.

2.5. Kane–Mele model

The introduction of the Kane–Mele model was a very important step towards finding realistic models which describe topological insulators. The Kane–Mele model was proposed to describe the QSHE of graphene [55]. The QSHE results from a $\mathbb{Z}_2$ topological invariant [56] and thus the corresponding materials are called $\mathbb{Z}_2$ topological insulators. The Kane–Mele model is known as the first example of a $\mathbb{Z}_2$ topological insulator. The crucial extension to more realistic models is achieved by including the spin degree of freedom, which allows new scenarios of gap opening. The topological character of the system is attributed to the spin-orbit interaction term. Like the Haldane model, the Kane–Mele model represents a very important conceptual model which is often used in proof-of-principle studies.

The model developed by Kane and Mele comprises two copies of the Haldane model due to the extension to the spin degree of freedom. One Haldane model describes the spin-↑ electron while the spin-↓ electron part is a time-reversed replica of the spin-↑ model. Thus, the TRS is preserved which leads to a variety of important consequences. The central point is that the preserved TRS is also capable of possessing topological features which are more likely to be realized in actual materials. The spin-orbit interactions preserve the TRS and induce the topological character by inverting bands [31]. In general, the SOCs are described by terms of the form $\sum_{i,j} c_{ij}\sigma_i k_j^{2n+1}$ with $n \in \mathbb{N}_0$. Applying the $\mathcal{T}$-operator does not affect the coupling

$$\mathcal{T}\sigma_i k^{2n+1} = -\sigma_i(-1)^{2n+1}k^{2n+1} = \sigma_i k^{2n+1} \quad . \tag{2.54}$$

The Kane–Mele Hamiltonian reads

$$\mathcal{H}_{\mathrm{KM}} = t\sum_{\langle i,j\rangle\alpha} c_{i\alpha}^\dagger c_{j\alpha} + \mathrm{i}t_2 \sum_{\langle\langle i,j\rangle\rangle\alpha\beta} \nu_{ij} c_{i\alpha}^\dagger \sigma_{\alpha\beta}^z c_{j\beta} + \mathrm{i}t_\mathrm{r} \sum_{\langle i,j\rangle\alpha\beta} c_{i\alpha}^\dagger (\sigma_{\alpha\beta}\times \hat{d}_{ij})_z c_{j\beta} \quad . \tag{2.55}$$

The NNN hopping does not break TRS or a spatial symmetry of the graphene lattice. Thus, in general, it will be present in graphene, though it may be very weak.

As shown in the previous section, we can perform a Fourier transformation of the Hamiltonian as a preparatory step to calculate dispersion and eigenstates. The matrix representation can be divided into two block matrices

$$H_{\mathrm{KM}}(k) = \begin{pmatrix} H_\uparrow(\boldsymbol{k}, \phi = \pi/2) & 0 \\ 0 & H_\downarrow(\boldsymbol{k}, \phi = -\pi/2) \end{pmatrix} \quad , \tag{2.56}$$

where the 2×2 matrices $H_\uparrow$ and $H_\downarrow$ are defined in the previous section in Eq. (2.45). The spin-orbit term couples the momentum with the spin so that the mass term changes sign for different Dirac nodes or different spin states, respectively. As a result, the novel massive Dirac fermions maintain the TRS.

In contrast to the quantized Hall conductivity in the Haldane model, the Kane–Mele model shows a quantized spin Hall conductivity upon applying an electric field, where the two spin channels counterpropagate. But the quantization of the spin Hall conductivity is only valid if the spin S^z is conserved. Often, the Rashba coupling [101] is present which mixes both spin alignments and as a consequence the quantization of the spin Hall conductivity is not preserved. As a result, the spin Hall conductivity decreases while the quantum spin Hall state is still preserved [55, 56].

2.5.1. $\mathbb{Z}_2$ topological invariant and helical edge states

The topological character of $\mathbb{Z}_2$ topological insulators in two dimensions cannot be identified by a Chern number because the Chern number vanishes automatically if TRS is present. This results from the fact that the integrated Berry curvatures is equal to zero due to the relation

$$F_{ij,\uparrow}(\boldsymbol{k}) = -F_{ij,\downarrow}(-\boldsymbol{k}) \quad . \tag{2.57}$$

Therefore the classification of the $\mathbb{Z}_2$ topological insulators requires a different topological invariant. The definition of the $\mathbb{Z}_2$ topological invariant is also based on the Berry phase.

The consequences of the TRS is fundamental to understanding the properties and characteristics of the $\mathbb{Z}_2$ topological phase. As a result of the time-reversal invariant Hamiltonian, all eigenstates are at least doubly degenerate. If an eigenstate $|n,\uparrow,\boldsymbol{k}\rangle$ has the energy $E(\boldsymbol{k})$, then the time-reversed state $\mathcal{T}\,|n,\uparrow,\boldsymbol{k}\rangle = |n,\downarrow,-\boldsymbol{k}\rangle$ is also an eigenstate with the same energy $E(-\boldsymbol{k})$. This important constraint is described by Kramers theorem [102]. As a result, the dispersion have crossing points at the time-reversal invariant momenta ($\boldsymbol{k} = -\boldsymbol{k}$). The Kramers pairs at the time-reversal invariant momenta of edge states are named Kramers doublets and are of special interest since they are related to the topological $\mathbb{Z}_2$ invariant by the bulk-boundary correspondence. An even number of Kramers doublets is assigned to a trivial insulator, whereas an odd number of Kramers doublets is assigned to a $\mathbb{Z}_2$ topological insulator [40].

The $\mathbb{Z}_2$ topological invariant can be formulated in many different ways [40, 56, 103–105], each with its own insights and relation to the topological origin. One possible mathematical formulation is based on the idea of the impossibility to define a gauge for the parameter space similar to the Chern number.

Since the conservation of TRS generically implies $C = 0$, one is always able to find a global gauge. Consistently, Stokes' theorem is valid for the complete BZ with one patch which leads to a Chern number equal to zero. The key idea for the definition of a $\mathbb{Z}_2$ topological invariant is the impossibility to globally define a Kramers pair with one patch. So in order to define a $\mathbb{Z}_2$ topological invariant it is important to cut the BZ into two halves so that the time-reversal momenta $\boldsymbol{k}$ and $-\boldsymbol{k}$ are found in different halves which are denoted by $\tau_{1/2}$. Thus the parameter space is reduced by half. If we follow this basic approach, the formula [40, 105] describing the $\mathbb{Z}_2$ invariant is given by

$$\nu = \frac{1}{2\pi}\left[-\int_{\tau_{1/2}} \mathrm{d}\tau F + \oint_{\partial\tau_{1/2}} \mathrm{d}\boldsymbol{l}\boldsymbol{A}\right] \mod 2\pi \quad , \tag{2.58}$$

where the Berry curvature as well as the Berry connection are required. Numerically, the formula for the $\mathbb{Z}_2$ invariant can be discretized similarly to the discretized Chern number calculation [105].

In the case of spin S^z conservation, the $\mathbb{Z}_2$ topological invariant can be simplified to the spin Chern number, where each spin alignment has the Chern number $C_\uparrow$ or $C_\downarrow$, respectively. The sum of both vanishes, but the difference

$$\nu = \frac{1}{2}(C_\uparrow - C_\downarrow) \tag{2.59}$$

is a valid definition of the invariant [106, 107].

An alternative and equivalent formula to Eq. (2.58) is based on the sewing matrix. The sewing matrix B is defined as

$$B_{nm} = \langle u_{m,\downarrow,-\boldsymbol{k}} | \, \mathcal{T} \, | u_{n,\uparrow,\boldsymbol{k}} \rangle \quad . \tag{2.60}$$

The concept of the sewing matrix is useful for $\mathbb{Z}_2$ topological insulators since it relates the eigenstate at $\boldsymbol{k}$ and spin-$\uparrow$ with the time-reversed eigenstate at $-\boldsymbol{k}$ and spin-$\downarrow$. Thus it contains the phase factor differences between eigenstates. The formula [55, 56, 104] based on the sewing matrix can be written as

$$\nu = \prod_i \frac{\sqrt{\mathrm{Det}[B(\Lambda_i)]}}{\mathrm{Pf}[B(\Lambda_i)]} \quad , \tag{2.61}$$

where Λ_i denotes the time-reversal invariant momenta and Pf corresponds to the abbreviation of a pfaffian. A great advantage of this formula is that it applies to $\mathbb{Z}_2$ topological insulators in $D = 1, 2, 3$, with the only difference regarding the dimensions is given by the number of Λ_i. The flip side is that the practical calculations of the pfaffian may be more difficult.

A further simplification is also given if a inversion symmetry is present. Similar to one dimension, all time-reversal invariant momenta Λ_i possess a parity with eigenvalues $\eta = \pm 1$. The parity at each Λ_i is a product over all occupied Kramers doublets

$$\delta_i = \prod_{m=1}^{N} \eta_{2m}(\Lambda_i) \tag{2.62}$$

and the $\mathbb{Z}_2$ invariant is thus given by the product of all δ_i [104]

$$(-1)^\nu = \prod_i \delta_i \quad . \tag{2.63}$$

The $\mathbb{Z}_2$ topological phase leads to helical edge states. The edge states in the Kane–Mele model have a close relation to the ones in the Haldane model. By considering each spin state on its own, the spin-$\uparrow$ has chiral edge states attributed to the Chern number $C_\uparrow = 1$, whereas the spin-$\downarrow$ has antichiral (counterclockwise direction) edge states due to the Chern number $C_\downarrow = -1$. The combination of both edge states leads to helical edge states crossing at the time-reversal invariant momentum $k = 0$ or $k = \pi$ (k corresponds to the momenta along the boundary). Despite the fact that the two edge states at the same edge are counterpropagating, no backscattering [42] is allowed due to time-reversal invariance[13]. Hence, the crossing point remains stable and no gap between the edge states arises. The helical edge states remain robust even if the spin S^z is not conserved, like in the presence of a Rashba coupling. As long as the Rashba term does not close the bulk energy gap, the topological edge modes are still present.

Due to the topological origin the edge states remain extended and stable even in the presence of strong disorder and avoid Anderson localization. As a result, a ballistic transport is expected at $T = 0\,\mathrm{K}$.

[13] Backscattering is forbidden between edge states of one Kramers pair. However, backscattering between an even number of Kramers pairs can open a gap. Thus an even or odd number of Kramers pairs belongs to distinct phases. An odd number of Kramers pairs indicates a non-trivial $\mathbb{Z}_2$ invariant while an even number corresponds to a trivial invariant.

3. Tuning of Fermi velocity

Parts of this chapter have been published in Physical Review B and SciPost as regular articles [44, 108]. A third manuscript has been submitted for publication [109]. I have wrote substantial parts of these manuscripts. Furthermore, I created all figures and calculated all the data shown.

3.1. Tunable edge states and their robustness towards disorder

3.1.1. General context

Due to their topological protection, edge states can carry currents without dissipation and they are protected against disorder to some extent, see below. This robustness makes them attractive for applications. With this long-term goal in mind, we set out to study the influence of controllable external parameters on the signal transmission of topological edge states as well as the effect of non-controllable features such as disorder. First, we choose the Fermi velocity v_F as the measurable quantity of interest in order to gain understanding which is complementary to the existing literature. We emphasize that the Fermi velocity does not influence the widely studied DC conductivity which is not the quantity of interest in our study, in contrast to the majority of theoretical studies in the literature, see for instance Refs. [110, 111].

The Fermi velocity is a key quantity in transport behavior, representing the group velocity of a transmitted charge or spin signal. Thus, we aim at tuning the Fermi velocity which quantifies how fast a signal is transmitted. A previous observation in the kagome lattice [112] revealed that the Fermi velocity depends on the chosen precise shape of the edge. Further investigations in the Haldane model [113] showed that the Fermi velocity can be influenced strongly by decorating one edge of the honeycomb lattice. We extend this observation by considering decoration of both edges.

Next, we transfer the idea of decoration to the Kane–Mele model, i.e., to helical edge states. An explicit Rashba coupling [101] and its effect on the Fermi velocity is also studied. The decoration of the edges of the Kane–Mele model leads to a tunable spin-dependent Fermi velocity which suggests the applicability of tunable transmission speeds in spintronics [114, 115].

Finally, we study the influence of local disorder on the edge states. Since edge modes are linked to non-trivial topological invariants, it is assumed that they are protected against disorder. However, various experiments show that the signatures of topological phases are much more prominent in high-purity samples [29] than in samples of lower quality. Thus, we intend to investigate the influence of disorder by explicit calculations. For simplicity, we study the robustness of the chiral edge states in the Haldane model on the honeycomb lattice.

Local disorder breaks the translational invariance. We define a transition probability by calculating the modulus squared of the overlap between the wave functions of the edge

modes in the disordered system with the ones in the clean system. The maximization of this quantity is used to reconstruct the momenta of the edge states. The dependence of the transition probability on the width and the length of the system as well as on the strength of the local disorder is examined. We find that the disorder may not exceed certain thresholds in order to preserve the characteristic transport properties of the edge modes.

3.1.2. Tuning chiral edge states of the Haldane model

For the sake of completeness, we recap results for decorated edges in the model without spin [113]. The results are important for the comparison with the results in the modified and extended models with spin. Moreover, they serve as reference for the disordered Haldane model which we investigate in Sec. 3.1.4.

The complete Hamiltonian of the model can be divided into two contributions

$$\mathcal{H} = \mathcal{H}_{\text{strip}} + \mathcal{H}_{\text{decor}} \tag{3.1a}$$

with

$$\mathcal{H}_{\text{strip}} = t \sum_{\langle i,j \rangle} c_i^\dagger c_j + t_2 \sum_{\langle\langle i,j \rangle\rangle} \mathrm{e}^{\mathrm{i}\nu_{ij}\phi} c_i^\dagger c_j \tag{3.1b}$$

$$\mathcal{H}_{\text{decor}} = \sum_{i,\gamma} \left[\lambda_\gamma \left(c_{d(i)}^\dagger c_i + c_i^\dagger c_{d(i)} \right) + \delta_\gamma c_{d(i)}^\dagger c_{d(i)} \right] \quad . \tag{3.1c}$$

The corresponding honeycomb lattice with decorated edges is shown in Fig. 3.1. The Hamiltonian in Eq. (3.1b) has been described in Sec. 2.4. The lattice constant a shown in Fig. 3.1 is set to unity. The hopping parameter t serves as energy unit henceforth.

The Hamilton operator $\mathcal{H}_{\text{decor}}$ of the decorating sites consists of two parts. One part describes the additional sites at the top whereas the other part describes the bottom sites ($\gamma \in \{\mathrm{t}, \mathrm{b}\}$). If the outermost sites of the undecorated honeycomb lattice are denoted by j, the adjacent decorating sites are labeled $d(j)$. The hopping elements between the outermost sites and the attached decorating sites are modified by the factor λ_γ. Generically, we consider an attenuation so that $0 \leq \lambda_\gamma \leq t$ holds. The on-site energy of the decorating sites is denoted by δ_γ. It can be thought to be generated by a gate voltage which changes the electric potential of the decorating sites [113].

The phase diagram of the Haldane model on a bulk honeycomb lattice without boundaries can be found in Sec. 2.4 [27, 51]. Calculating the dispersion on a finite strip of the system, see Fig. 3.1, provides the chiral edge states. Coupling the decorating sites to the honeycomb strip does not alter the topological characteristics of the system. The phase ϕ is set to $\pi/2$ in order to maximize the gap. To create rather flat energy bands we set $t_2 = 0.2t$ as in Ref. [113]. The Fermi level is set to $\varepsilon_{\mathrm{F}} = 0$.

To illustrate the impact of the modification we calculate the dispersion of both edge modes and compare it to the dispersion in the undecorated Haldane model. In the following, we investigate a strip of finite height in y-direction whereas the strip is infinitely extended in x-direction, see Fig. 3.1. Due to the translational symmetry in x-direction, the wave number k_x represents a good quantum number. At fixed k_x, one obtains a $(2N + 2) \times (2N + 2)$ one-particle matrix which can be diagonalized numerically. The

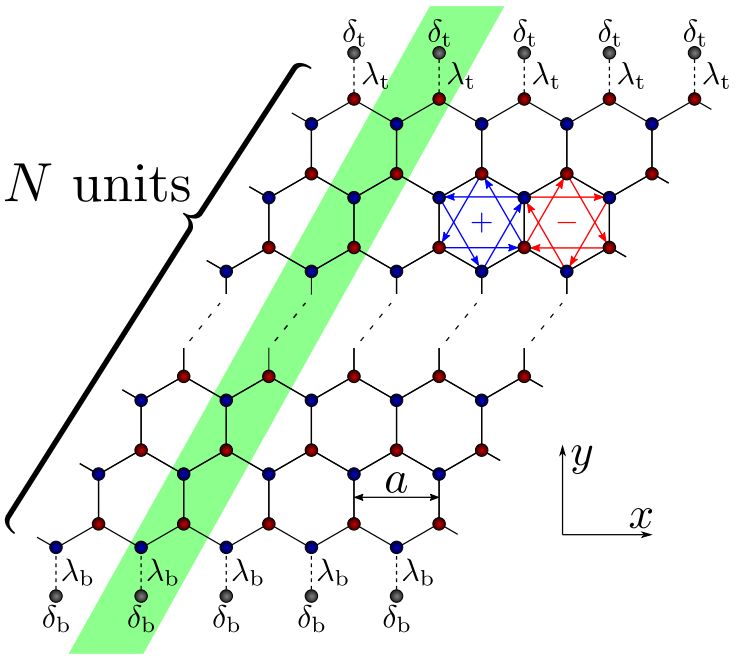

Figure 3.1: Sketch of a strip in the honeycomb lattice with NN hopping (black bonds). The green area displays a unit cell in the x-direction which consists of $2N + 2$ sites including the decorating sites. The honeycomb with blue arrows illustrates the complex hopping elements to NNN sites with phase $+\phi$ while the honeycomb with red arrows illustrates the hopping elements with phase $-\phi$, see Eq. (2.44). The top and the bottom edge are decorated by additional sites which are coupled weakly ($|\lambda_\gamma| \leq |t|$) to the bulk sites. These decorating sites are subjected to a local potential δ_γ. The index γ takes the value t (top) or b (bottom).

dispersive modes within the gap of the bulk Haldane model are the edge modes. Due to their exponential localization at the edges, their dispersion converges quickly upon increasing the number N of units in the unit cell. The calculations are based on strips with $N = 60$ units which turns out to be sufficiently wide.

An example of a dispersion with different parameters for both edges is shown in Fig. 3.2. The filled areas represent the continua stemming from bulk modes for all possible values of k_y. Our main focus lies on the investigation of the edge modes with energies between the lower band edge of the upper continuum (blue shading) and the upper band edge of the lower continuum (red shading).

Upon coupling the decorating sites to the honeycomb strip, i.e., $\lambda_\gamma \neq 0$, the dispersions of the edge modes display an "avoided crossing" (or "level repulsion") due to the hybridization with the local modes from the decorating sites. In the case of small values of λ, see right mover in Fig. 3.2, the edge states have a rather flat band. Increasing λ leads to a stronger repulsion between the edge modes near the zone boundary $k_x = \pi$ so that the dispersion acquires stronger momentum dependence, see left mover in Fig. 3.2.

Besides the coupling λ_γ, the decorating sites can be influenced by the local potentials δ_γ. Increasing the local energy of the decorating sites counteracts the hybridization because the tendency of an electron to visit the decorating sites is decreased if these sites differ

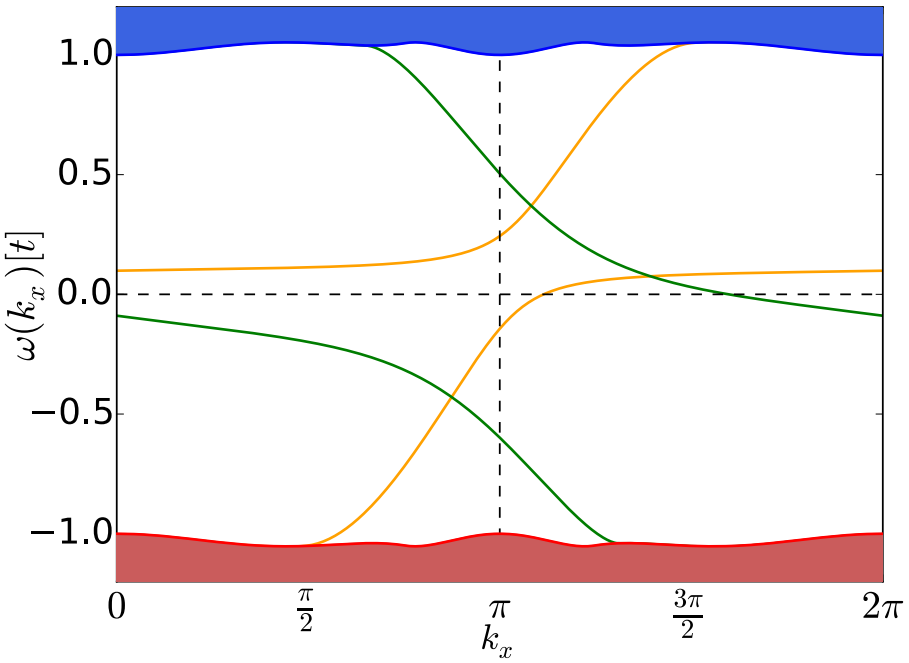

Figure 3.2: Dispersion of the edge states in the decorated Haldane model with $t_2 = 0.2t$, $\phi = \pi/2$, $\lambda_\mathrm{t} = 0.2t$, $\delta_\mathrm{t} = 0.1t$, $\lambda_\mathrm{b} = 0.6t$, and $\delta_\mathrm{b} = -0.1t$. The right-moving edge state marked in orange is located at the top edge while the left-moving edge state marked in green is located at the bottom edge. The filled areas indicate the continua of the bulk states. The Fermi velocities $v_\mathrm{F} = \partial\omega/\partial k_x|_{\varepsilon_\mathrm{F}}$ of both edges modes are independent of each other.

in energy from the bulk sites. In this way, the decorating sites can be smoothly switched off. Then, the Fermi velocity converges to the Fermi velocity $v_{\mathrm{F}0}$ without decoration.

The dependence of the Fermi velocity on the parameters of the decorated model was studied quantitatively for a single decorated edge [113]. To prove the independence of the chiral edge modes explicitly we calculated the Fermi velocity of both edges while tuning parameters of only one edge. The Fermi velocity of the unaltered edge remains unaffected to the tenth digit. We stress that the relative coupling λ_γ and the local potential δ_γ provide control parameters to tune the Fermi velocity of the edge mode independently of the other edge mode. Furthermore, different decorations at top and bottom edges enable us to realize different Fermi velocities $v_{\mathrm{F},\gamma}$ so that the velocities become direction-sensitive.

3.1.3. Tuning chiral edge states of the Kane–Mele model

Here, we investigate the impact of decorated edges on the helical edge states of the Kane–Mele model which includes the spin degree of freedom in such a fashion that it preserves the TRS. The Hamiltonian reads

$$\mathcal{H} = \mathcal{H}_\mathrm{strip} + \mathcal{H}_\mathrm{decor} \tag{3.2a}$$

with

$$\mathcal{H}_{\text{strip}} = t \sum_{\langle i,j\rangle\alpha} c^\dagger_{i\alpha} c_{j\alpha} + \mathrm{i}t_2 \sum_{\langle\langle i,j\rangle\rangle\alpha\beta} \nu_{ij} c^\dagger_{i\alpha} \sigma^z_{\alpha\beta} c_{j\beta} + \mathrm{i}t_\mathrm{r} \sum_{\langle i,j\rangle\alpha\beta} c^\dagger_{i\alpha} (\sigma_{\alpha\beta} \times \hat{d}_{ij})_z c_{j\beta} \tag{3.2b}$$

and

$$\mathcal{H}_{\text{decor}} = \sum_{i,\gamma,\alpha} \left[\lambda_\gamma \left(c^\dagger_{d(i)\alpha} c_{i\alpha} + c^\dagger_{i\alpha} c_{d(i)\alpha} \right) + \delta_\gamma c^\dagger_{d(i)\alpha} c_{d(i)\alpha} \right] \tag{3.2c}$$

on the honeycomb lattice similar to the decorated Haldane model from the previous section, see Fig. 3.1. In the Kane–Mele model, each site can host two electrons with a spin quantum number denoted by $\alpha, \beta \in \{\uparrow, \downarrow\}$. The Hamilton operator of the strip contains three contributions. The first term describes the usual tight-binding hopping t between NN sites. As before, the hopping parameter t is real and used as the energy unit.

Kane and Mele [55] argued that the second hopping term $\propto t_2$ is induced by spin-orbit interaction. The hopping parameter t_2 is real and the sign depends on the NNN sites i and j as given by ν_{ij} defined in Eq. (2.44). The NNN term is closely related to the NNN hopping in the Haldane model. Considering each spin specie separately, the corresponding Hamiltonian with NN and NNN hoppings violates the TRS. It equals the Haldane Hamiltonian at $\phi = +\pi/2$ for $S^z = +1/2$ and at $\phi = -\pi/2$ for $S^z = -1/2$. The Kane–Mele model comprises two decoupled Haldane models with opposite phases. Since the time-reversal transformation $T = \exp(-\mathrm{i}\pi S^y)K$ maps one onto the other, their combination preserves the TRS [27].

The last term in $\mathcal{H}_{\text{strip}}$ proportional to t_r describes a Rashba term [55, 101] which can also result from SOC in the presence of a perpendicular electric field or a certain interaction with a substrate. The Rashba coupling preserves the TRS such as all types of spin-orbit couplings. The hopping element parameter t_r of the Rashba term is real. The Rashba term violates the conservation of the total S^z component so that the two Haldane models for $S^z = \pm 1/2$ are coupled for $t_\mathrm{r} \neq 0$.

The Hamiltonian of the decorating sites at the edge is chosen to be spin-independent for simplicity, similar to the decoration of the Haldane model. So the notation will be the same except that an additional index is used to denote the spin.

The topological phases of the Kane–Mele model are classified by a $\mathbb{Z}_2$ invariant [40, 105], see Eq. (2.58). The phase diagram of the bulk Kane–Mele model including the Rashba coupling is known [27, 56]. We detect the presence of helical edge states by calculating the dispersion on a strip of finite width as before.

First, we set the Rashba coupling to zero so that our results can be directly linked to the results for the decorated Haldane model. For $\lambda_\gamma = \delta_\gamma = 0$, the original Kane–Mele model on a strip is retrieved. The corresponding Hamiltonian consists of two decoupled Haldane Hamiltonians, each of which displays its own chiral edge states. The chiral edge states of the spin-$\uparrow$ part move in opposite direction to the chiral edge states of the spin-$\downarrow$ part because the phase of their NNN hopping element is opposite. The two chiral edge states with opposite spins constitute a pair of counterpropagating edge modes at each edge. As shown in the previous section, the top edge can be modified independently of the bottom edge. This also holds true for the Kane–Mele model. Therefore, we only consider the decoration of the top edge in the following for brevity.

In the Kane–Mele model, the Fermi velocities of the edge modes are spin-dependent. Except for this difference, one can carry over the basic considerations that we developed

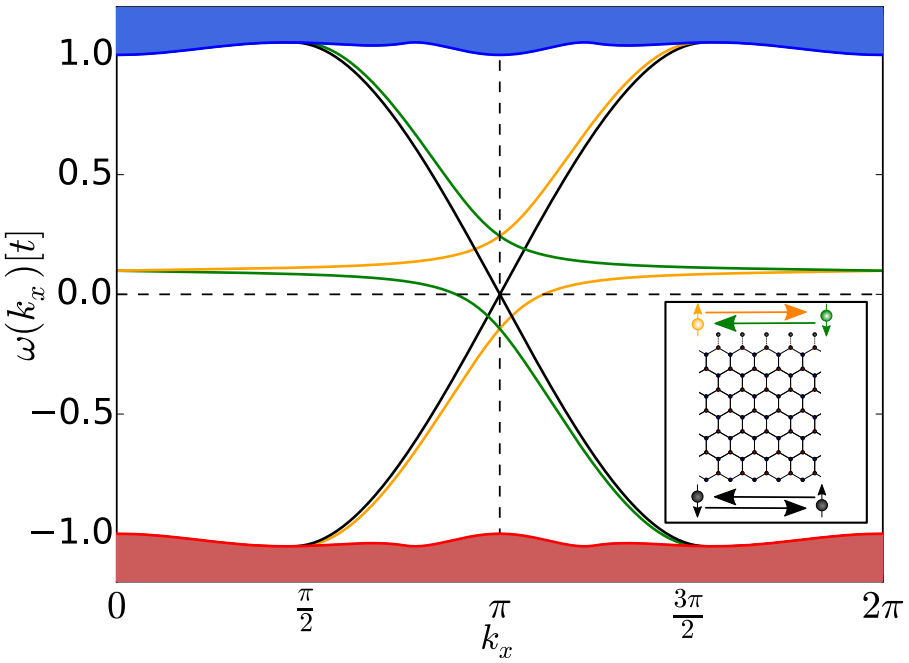

Figure 3.3: Dispersion of the edge states in the Kane–Mele model with $t_2 = 0.2t$, $\lambda_\mathrm{t} = 0.2t$, and $\delta_\mathrm{t} = 0.1t$. The filled areas indicate the continua of the bulk states. The edge states located at the top edge are shown in color. The spin-↑ mode propagating to the right is marked in orange while the spin-↓ mode counterpropagating to the left is marked in green. The dispersions of the edge states at the lower boundary are displayed in black. The schematic sketch in the inset clarifies the assignments.

for the decorated Haldane model. Figure 3.3 illustrates this point. The helical edge states of the bottom edge are the same edge states as in an undecorated Kane–Mele strip because the bottom edge is undecorated. The dispersions of the modes at the top edge displays the effect of the 'avoided crossing' combined with a certain shift of the dispersion due to the local potential. This is in line with the results for the Haldane model.

Due to TRS, the dispersions display two mirror planes at the momenta invariant under time-reversal: $k_x = 0$ and $k_x = \pi$, respectively. This property is based on Kramers theorem [102]. Kramers theorem predicts crossing points of the counterpropagating edge states at time-reversal invariant momenta. These Kramers doublets are robust against time-reversal symmetric perturbations. The hybridization of the edge modes with the local modes at the top edge leads to one Kramers doublet located at $k_x = 0$ and one additional Kramers doublet at $k_x = \pi$ (3 Kramers doublet for the top edge mode and 1 Kramers doublet for the bottom edge mode). The number of Kramers doublets at one edge is odd as usual in the topologically non-trivial phase because it is related to the $\mathbb{Z}_2$ topological invariant [29].

The inclusion of a finite Rashba coupling $t_\mathrm{r} \neq 0$ violates the S^z-conservation and the two Haldane models hybridize. The Rashba coupling alone without the imaginary NNN hopping does not lead to a topologically non-trivial phase [27], which means that the imaginary NNN hopping is indispensable for the anomalous QSHE in the Kane–Mele model. But the Rashba coupling reduces or enhances the bulk gap and influences the

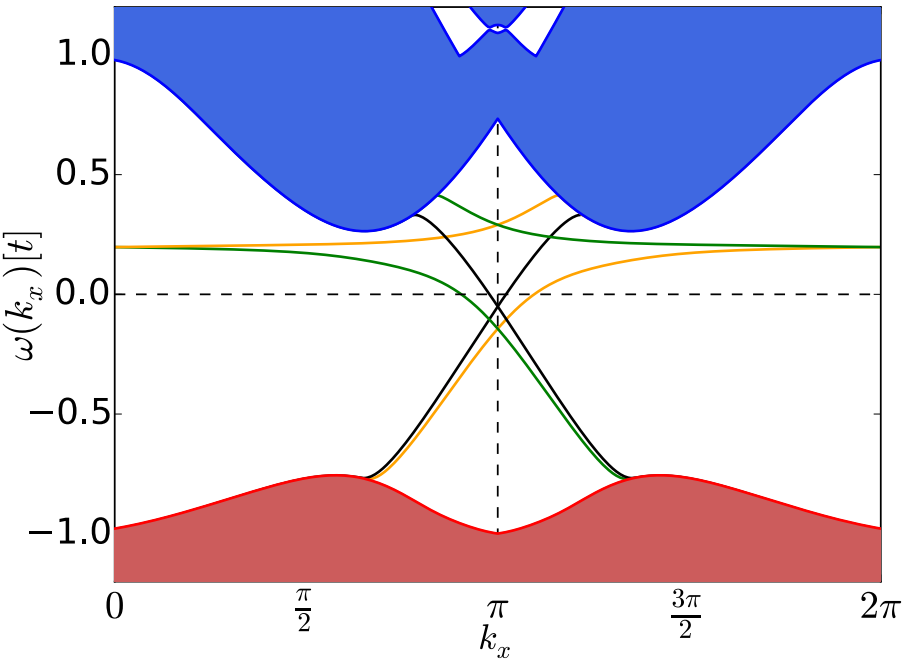

Figure 3.4: Dispersion of the edge states in the Kane–Mele model at finite Rashba coupling at $t_2 = 0.2t$, $t_\mathrm{r} = 0.8t$, $\lambda_\mathrm{t} = 0.2t$, and $\delta_\mathrm{t} = 0.2t$. The filled areas indicate the continua of the bulk states. The edge states located at the top edge are shown in color. The spin-↑ mode propagating to the right is marked in orange while the spin-↓ mode counterpropagating to the left is marked in green. The dispersions of the edge states at the lower boundary are displayed in black.

edge states in this way. An exemplary dispersion of the helical edge states in the Kane–Mele model is depicted in Fig. 3.4 where the Rashba coupling t_r is chosen fairly large in order to show its influence on the bulk and on the edge states. For not too large values of the Rashba coupling the qualitative features of the bulk and of the helical edge states remain unaltered.

The counterpropagating edge modes forming a Kramers pair still cross each other as long as the TRS is preserved and the bulk gap does not close. If the gap is reduced by tuning t_r the bulk states repel the edge modes. The effect can be seen in Fig. 3.4 where the energies of the Kramers pair at the bottom edge are shifted downwards away from the upper continuum which is displayed in blue. As a result, v_F can increase or decrease upon switching on the Rashba coupling as shown in Fig. 3.5. Since the particle-hole symmetry is broken by the Rashba coupling the inclusion of the local potentials at the decorating sites is no longer symmetric so that the effect of a negative potential differs from the one of a positive potential. Even the sign of the effect can change.

In a system preserving TRS the addition of a finite amount of unpolarized charge at one edge does not lead to a net charge current because the two counterpropagating modes compensate in charge due to their equal Fermi velocities. In order to create a net charge current the TRS must be broken. One possible way to do so is to include a spin-dependent decoration. This can be accomplished for example by proximity-induced ferromagnetic exchange at the interface with a magnetic insulator [116]. To demonstrate this basic idea,

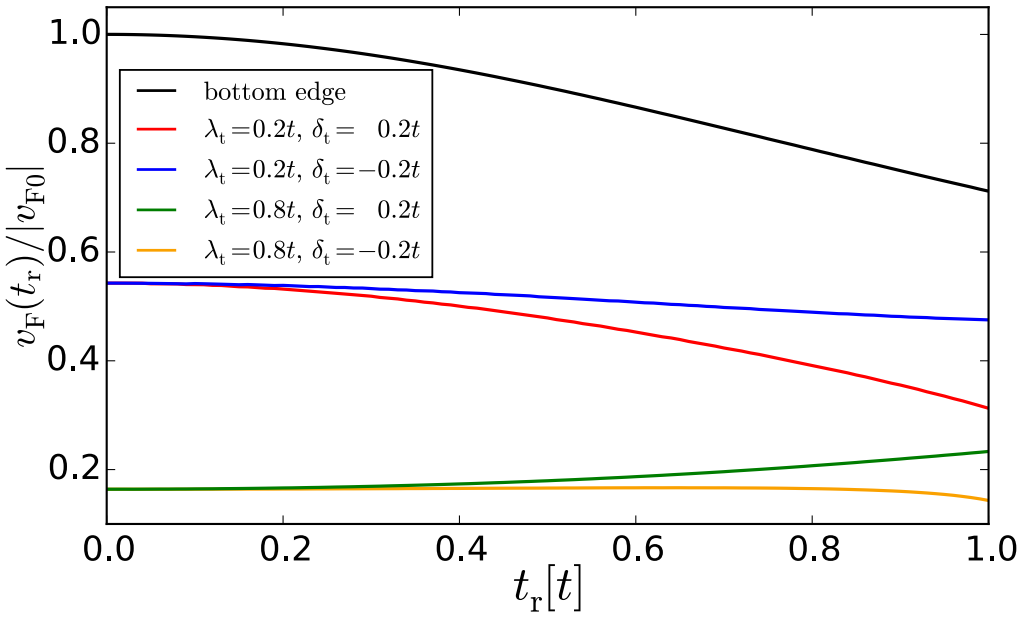

Figure 3.5: Fermi velocity $v_\mathrm{F} = \partial\omega/\partial k_x|_{\varepsilon_\mathrm{F}}$ of the right-moving edge modes in the Kane–Mele model relative to the original v_F0 without decorated edges vs. the Rashba coupling t_r at $t_2 = 0.2t$ for various decorations of the top edges and undecorated bottom edges.

we replace $\mathcal{H}_\mathrm{decor}$ by

$$\mathcal{H}_\mathrm{decor} = \sum_{i,\gamma,\alpha} \left[\lambda_\gamma \left(c^\dagger_{d(i)\alpha} c_{i\alpha} + c^\dagger_{i\alpha} c_{d(i)\alpha} \right) + \delta_\gamma c^\dagger_{d(i)\alpha} \sigma^z_{\alpha\alpha} c_{d(i)\alpha} \right] \quad . \tag{3.3}$$

The change relative to Eq. (3.2c) is that the local potential depends on the Pauli matrix σ_z. To illustrate the difference to the previous decoration we depict the resulting dispersions in Fig. 3.6(a) keeping all other parameters as before. Due to the spin-dependent decoration of the top edge the corresponding Kramers doublets no longer exist since the crossing points are not located at the time-reversal invariant momenta. Furthermore, the counterpropagating edge modes do not cancel each other out. Hence, a net charge and spin current is possible.

Another possible way to break the TRS is to split the two spin states by adding a ferromagnetic exchange field

$$\mathcal{H}_\mathrm{FMX} = h_z \sum_{i,\alpha} (c^\dagger_{i\alpha} \sigma^z_{\alpha\alpha} c_{i\alpha} + c^\dagger_{d(i)\alpha} \sigma^z_{\alpha\alpha} c_{d(i)\alpha}) \tag{3.4}$$

to the decorated model in Eq. (3.2a). In contrast to the previous example, the exchange field is present at all sites. This can be realized by magnetic doping [117–119]. For vanishing Rashba coupling $t_\mathrm{r} = 0$, the influence of the exchange field can be easily understood by regarding the Kane–Mele model as two decoupled decorated Haldane models of which the chemical potentials are shifted in the opposite directions. Kramers doublets no longer exist, see Fig. 3.6(b).

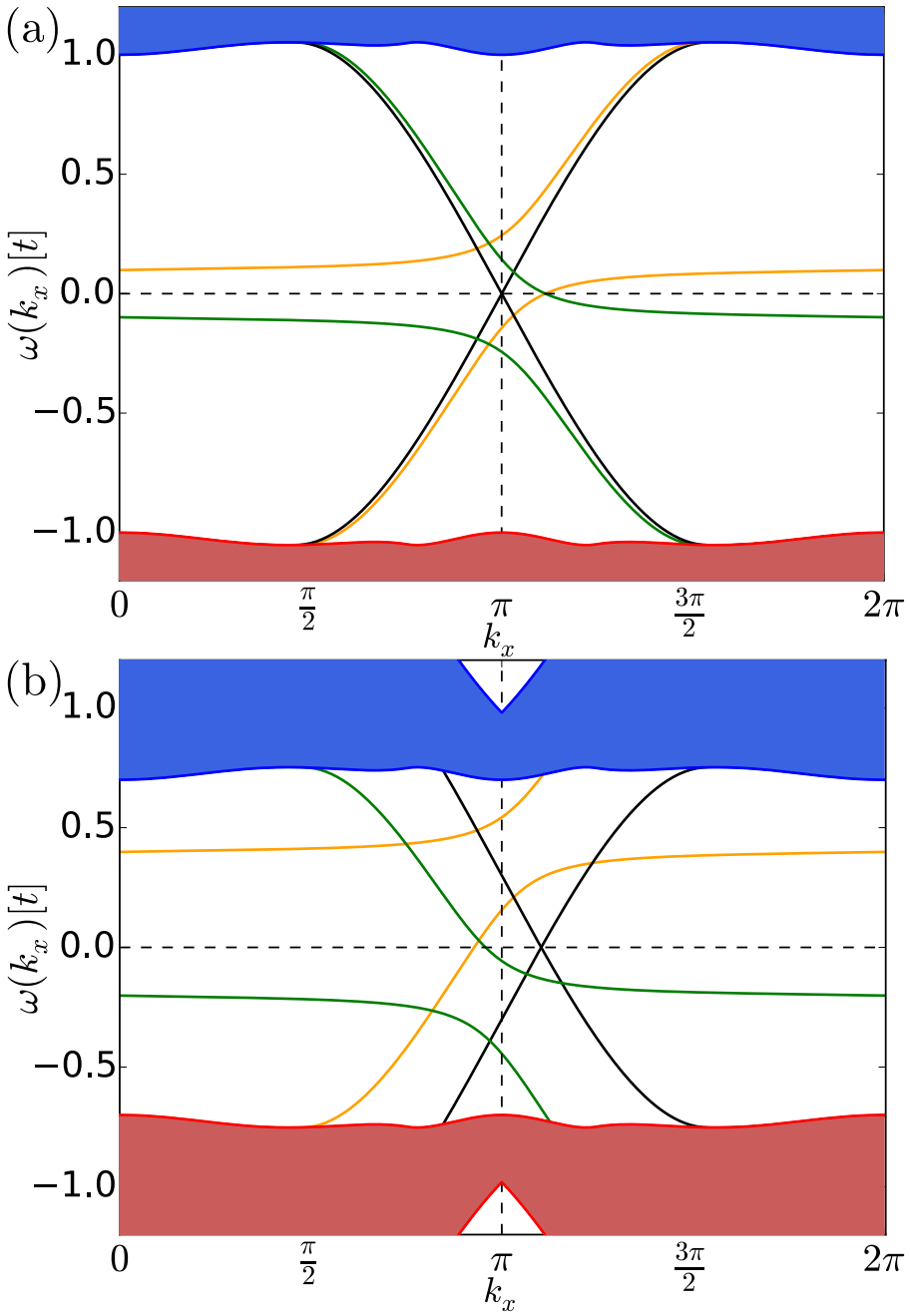

Figure 3.6: (a) Dispersions of the edge states in the Kane–Mele model at $t_2 = 0.2t$, $t_\mathrm{r} = 0$ described in Eq. (3.2b), $\lambda_\mathrm{t} = 0.2t$, and $\delta_\mathrm{t} = 0.1t$ described in Eq. (3.3). The filled areas indicate the continua of the bulk states. The edge states located at the top edge are shown in color. The spin-↑ mode propagating to the right is marked in orange while the spin-↓ mode counterpropagating to the left is marked in green. The dispersion of the edge states at the lower boundary are displayed in black. (b) Dispersions of the edge states in the Kane–Mele model with $t_2 = 0.2t$, $t_\mathrm{r} = 0$, $\lambda_\mathrm{t} = 0.2t$, $\delta_\mathrm{t} = 0.1t$ described in Eq. (3.2a), and $h_z = 0.3t$ in Eq. (3.4).

3.1.4. Robustness of the edge states against potential disorder

So far, we analyzed how an important transport property of the edge states, the Fermi velocity, can be controlled by tuning parameters. But there are also uncontrollable properties of a solid-state system. For instance, imperfections of all kinds such as impurities, defects or vacancies in the lattice structure can never be fully excluded. We cannot consider them exhaustively here, but we aim at a first study of the robustness of edge states to disorder. To this end, we consider random disorder in the local potentials.

The edge states emerge as a result of the discontinuity of topological invariants at the edges of a system. Since a topological invariant is a global property of the bulk system, it is expected that the edge states are protected as long as the disorder does not change the global properties of the bulk system. We want to study this explicitly. To this end, we investigate the Haldane model (3.1b) on a finite strip of the honeycomb lattice as shown in Fig. 3.7. We consider a strip of N_x columns of a finite width of N_y units so that there are $2N_xN_y$ sites. We add a random local potential at each site to the Haldane model (3.1b) to simulate the disorder. The random energies are taken from a continuous uniform distribution in the interval $[-\sqrt{3}\sigma, \sqrt{3}\sigma]$, where σ is the standard deviation. This is the control parameter for the strength of the local disorder. We also investigated random local potentials which are normally distributed, but the results with respect to the reconstruction do not differ fundamentally.

The translation symmetry in the x-direction is no longer preserved due to disorder. In order to establish a link to the system without disorder we continue to consider periodic boundary conditions. By diagonalizing the $(2N_yN_x) \times (2N_yN_x)$ matrix encoding hopping and local energies we obtain the eigenenergies. The corresponding eigenvectors cannot be classified directly according to their momenta k_x. The eigenstates are given in spatial representation by

$$|\psi\rangle = \sum_{x,y} c(x,y)\,|x,y\rangle \quad , \tag{3.5}$$

where x and y correspond to the discrete coordinates of the lattice sites. In order to map the eigenstates of the disordered system to the eigenstates of the clean system we express the edge states, right- and left-moving ones, of the clean system in real space. Denoting the wave function of such an edge state by $|\psi_{\mathrm{cl}}\rangle\,(k_x)$ leads to

$$\begin{aligned} |\psi_{\mathrm{cl}}\rangle\,(k_x) &= \sum_{y} d(k_x,y)\,|k_x,y\rangle \\ &= \sum_{x,y} d(k_x,y)\frac{\mathrm{e}^{-\mathrm{i}k_x x}}{\sqrt{N}}\,|x,y\rangle \quad . \end{aligned} \tag{3.6a}$$

In comparison to the representation (3.5) we deduce

$$c_{k_x}(x,y) = d(k_x,y)\frac{\mathrm{e}^{-\mathrm{i}k_x x}}{\sqrt{N}} \quad . \tag{3.6b}$$

The possible momenta are given by $k_x = 2\pi n_x/N_x$ with $n_x = \{0,1,\ldots,N_x-1\}$.

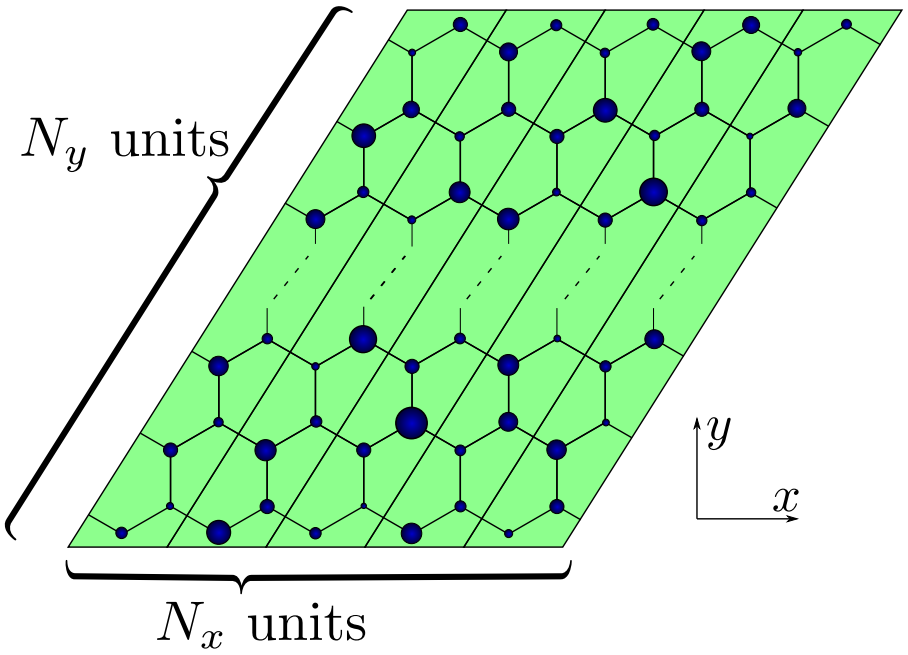

Figure 3.7: Sketch of a finite strip of honeycomb lattice consisting of N_x columns of finite width of N_y units. Each column is enclosed by thin black lines. The different sizes of the dots illustrate the random local potentials of a disordered configuration.

In order to assign a momentum k_x to an energy of an edge state of the disordered system, we search for the largest overlap with a clean edge mode, i.e., we maximize $\left|\langle\psi|\psi_{\mathrm{cl}}\rangle\right|^2(k_x)$ by varying k_x. The momentum k_x which maximizes this overlap is the one assigned to the eigenstate of the disordered system. The overlap can be interpreted as a transition probability and is calculated by

$$\left|\langle\psi|\psi_{\mathrm{cl}}\rangle\right|^2(k_x) = \left|\sum_{x,y} c^*(x,y)c_{k_x}(x,y)\right|^2 \quad . \tag{3.7}$$

Following this procedure, we reconstruct the dispersion of the edge state in the BZ as shown in Fig. 3.8 for $\sigma = 0.1t$. Typically, we consider a system of $N_y = 50$ and $N_x = 21$ leading to $2N_yN_x = 2100$ eigenenergies from which we select the energies corresponding to the edge state by maximizing the transition probability (3.7). The dispersions of the edge modes of the clean system computed from the infinite strip ($N_x = \infty$) are shown as solid lines for the sake of comparison. To test the maximization of the transition probability we assign momenta to eigenstates computed for a finite clean system. The results are depicted by black diamonds in Fig. 3.8 and match the continuous lines perfectly as it has to be. The yellow circles display the eigenenergies at the assigned momenta in a disordered system with $\sigma = 0.1t$. They are still located close to the solid lines, but do not lie perfectly on them due to the effects of disorder.

We conclude that the qualitative features of the edge states are indeed robust against disorder. The gaplessness of the edge modes is preserved as was to be expected from the topological protection. But also the quantitative aspects are not drastically altered by disorder, at least as long as the disorder strength is not too large.

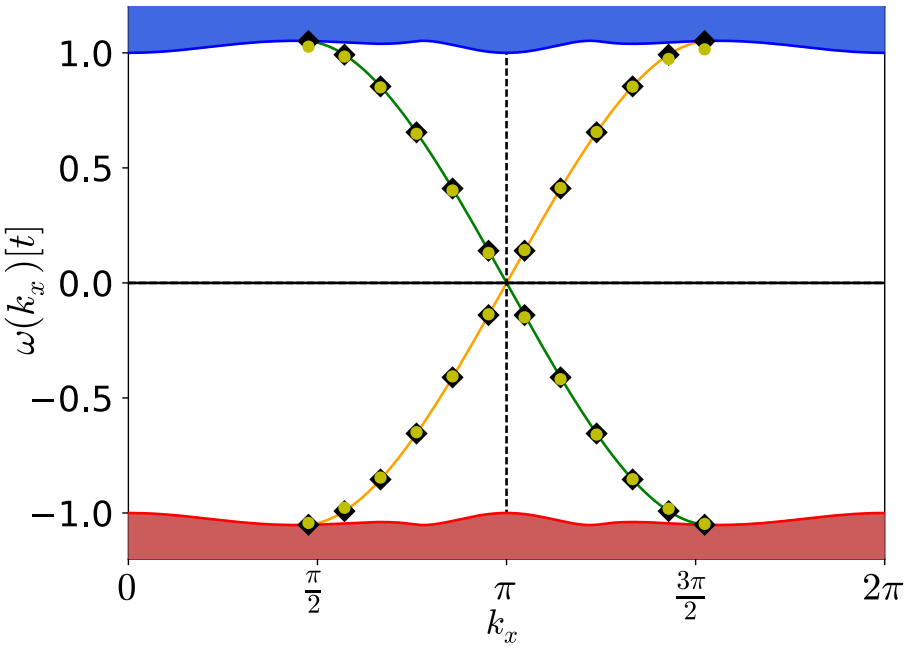

Figure 3.8: Dispersion of the edge states with $t_2 = 0.2t$ and $\phi = \pi/2$ of the Haldane model. The filled areas indicate the continua of the bulk states. The right-moving edge state marked in orange is located at the top edge while the left-moving edge state marked in green is located at the bottom edge. The symbols indicate the energies of eigenstates of which the momenta are determined from maximizing the transition probability in (3.7). The black diamonds are calculated for a clean system with $N_y = 50$ and $N_x = 21$ while the yellow circles result from a disordered system with $\sigma = 0.1t$.

An important point to study is the influence of the disorder on the bulk gap. If the bulk gap becomes small or even vanishes the topological properties disappear. Increasing disorder reduces the bulk gap. Note that a high number of draws from a normal distribution usually leads to (at least) one value which deviates strongly from the mean value. Thus, in the strict sense, the energy gap would always closed by disorder. To this end, we favor the uniform distribution. An estimate for the reduction of the bulk gap can be derived by assuming that the disorder strength σ behaves similarly to an on-site inversion-symmetry breaking term $\varepsilon_i M c_i^\dagger c_i$. Here ε_i takes the values ± 1 depending on whether site i belongs to one sublattice or to the other. The energy gap Δ of the bulk system decreases upon increasing M. Similarly, Δ decreases upon increasing σ as we illustrate in Fig. 3.9 where the lower band edge $\omega_{\text{unoc}} = \Delta/2$ of the unoccupied states and the upper band edge $\omega_{\text{occu}} = -\Delta/2$ of the occupied states are shown. The difference between the two black lines depicts the bulk gap as a function of M according to $\Delta = 2|M \pm 3\sqrt{3}t_2 \sin\phi|$ [51, 72, 119]. The symbols show the corresponding energies in the disordered sample determined in the following way. For the lower band edge we compute the minimum energy of the eigenstates which *cannot* be assigned to an edge mode of the clean system. Similarly, the upper band edge is determined from the maximum energy of the eigenstates which *cannot* be assigned to an edge mode of the clean system. Of course, this way of determining the bulk gap in the disordered system is a heuristic one and not mathematically rigorous. But the comparison to $\omega_{\text{occu}}(M)$ and $\omega_{\text{unoc}}(M)$

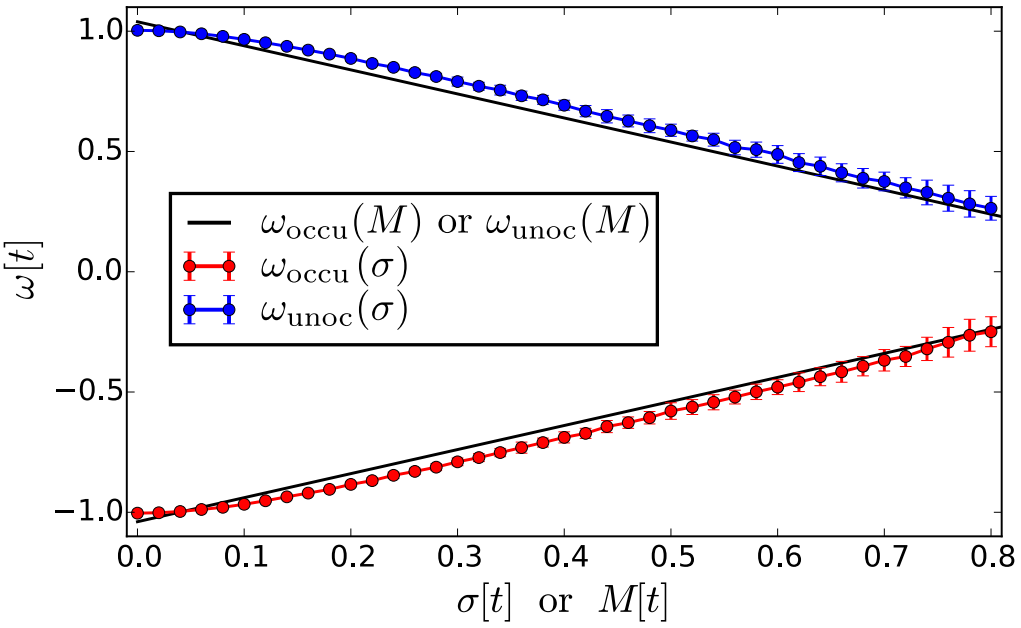

Figure 3.9: The lower band edge of the conduction band (blue) and the maximum energy of the valence band (red) vs. the disorder strength σ in a system with $N_y = 50$ and $N_x = 21$. The energies are averaged over 60 randomly chosen configurations. The error bars represent a standard deviation. The black lines show the band edges in a clean system as a function of a local inversion-symmetry breaking term $\propto M$, see main text.

shows good agreement so that we conclude that the estimate works very well.

The energy gap disappears at $M = 3\sqrt{3}t_2 \sin\phi$ [51, 72, 119]. Thus, the estimate predicts that the topological properties will definitely cease to exist for a disorder strength

$$\sigma \approx 3\sqrt{3}t_2 \sin\phi \quad . \tag{3.8}$$

We stress that the decreasing bulk gap reduces the energy interval in which the edge mode can be identified. Concomitantly, the interval in momentum k_x in which the edge mode can be identified is reduced as well.

Next, we study how well the edge mode can be identified close to the bulk continua. Figure 3.10 displays the transition probability $\left|\langle\psi|\psi_{\mathrm{cl}}\rangle\right|^2(k_x)$ of the edge states in the BZ. The vertical dashed lines indicate the thresholds where the edge modes enter the bulk continua, i.e., where the energies of the edge modes exceed the estimated bulk gap. It is obvious that around $k_x = \pi$ the transition probability between the edge modes in the disordered system and in the clean system is large. Thus, in particular for low disorder, the identification of the edge mode works reliably. For increasing disorder, the overlap decreases gradually. Approaching the band edges at fixed disorder strength, i.e., approaching the dashed line, the overlap decreases rapidly and a clear identification of the edge modes becomes more and more difficult until it becomes impossible. This data shows the breakdown of the edge modes under the influence of disorder. Clearly, there are limits to the topological protection, even though the feature of a vanishing energy of the edge modes persists as required by the bulk-boundary correspondence.

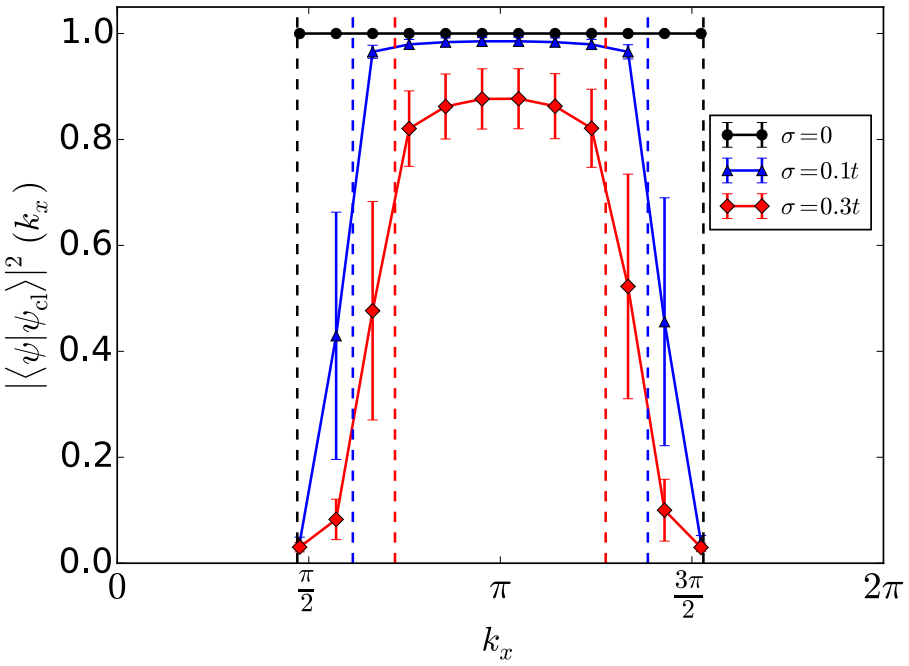

Figure 3.10: Transition probability $|\langle\psi|\psi_{\mathrm{cl}}\rangle|^2(k_x)$ of the right-moving edge state averaged over 50 random configurations in a system with $N_y = 50$ and $N_x = 21$ as a function of the momentum k_x. The error bars indicate the standard deviation. The dashed lines indicate at which momenta the energy of the edge mode enters the bulk continua.

The quantitative behavior of $|\langle\psi|\psi_{\mathrm{cl}}\rangle|^2(k_x)$ as a function of σ is studied in Fig. 3.11(a). The transition probability decreases upon increasing σ. If the energy of the edge mode in the clean system is far away from the band edges of the continua (red curve, diamond symbols) the transition probability decreases more slowly than if its energy is close to one of the continua (green curve, circle symbols).

In Fig. 3.11(b) we depict the dependence of the complete energy spectrum on the disorder strength. The modes assigned to the two momenta shown in Fig. 3.11(a) are highlighted by the two lines. There are regions where the eigenenergies are dense, corresponding to the continua. The energies between the two dense regions at low and at high energies belong to the edge modes. The energies assigned to the two momenta evolve upon increasing σ. At some value of σ, which is specific for the momentum k_x of the mode, they enter the bulk continuum. The corresponding values of σ are indicated approximately by vertical dashed lines in both panels of Fig. 3.11. Beyond these disorder strengths one can no longer decide whether the modes are true edge modes or whether they belong to the continuum states.

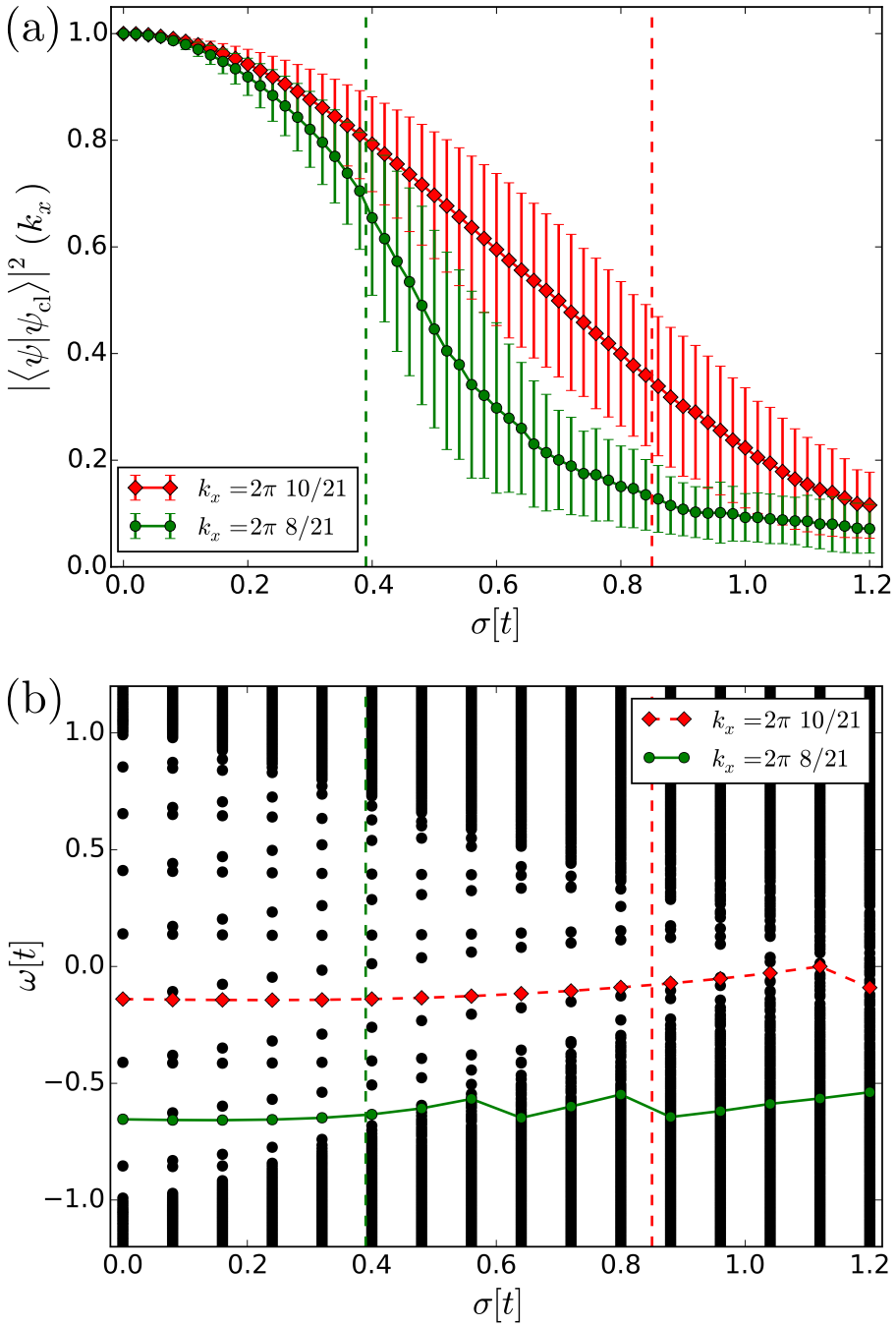

Figure 3.11: (a) Transition probability $|\langle\psi|\psi_{\mathrm{cl}}\rangle|^2\,(k_x)$ at two values of k_x for the right-moving edge state as a function of the disorder strength σ in a system with $N_y = 50$ and $N_x = 21$. The probability is averaged over 50 configurations. The error bars represent the standard deviation. The dashed lines depict where the edge modes enter the continuum of the bulk states. (b) Complete energy spectrum for an exemplary configuration. The energies highlighted in color correspond to the two values of k_x displayed in (a).

Yet even beyond the dashed lines the transition probability is large enough to assign energies to the momenta k_x. But it happens that the assigned energies jump, as can be

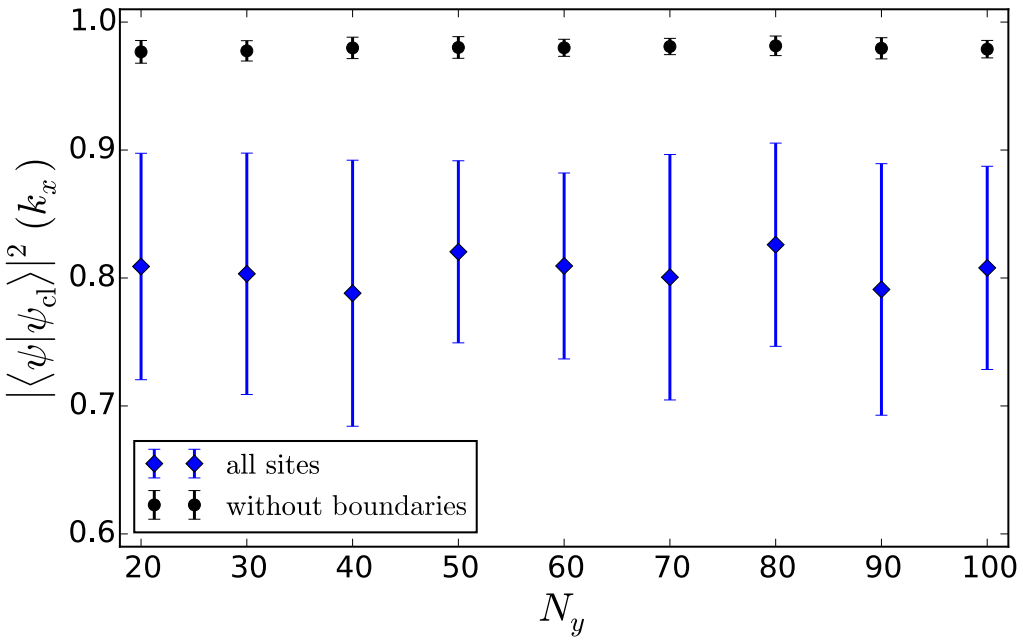

Figure 3.12: Transition probability $|\langle\psi|\psi_{\mathrm{cl}}\rangle|^2$ at $k_x = 2\pi\,8/21$ as a function of the width N_y of the strip of the Haldane model with $t_2 = 0.2t$, $\phi = \pi/2$, and a length of $N_x = 21$. The probability is averaged over 50 configurations for $\sigma = 0.1t$. The error bars represent the standard deviation. The effect of local disorder on all sites is shown by blue diamonds. The black circles depict the effect if disorder is only present in the bulk, but not at the edges. As to be expected, the edge modes are much less influenced in this case.

seen for $k_x = 2\pi\,8/21$ where kinks occur beyond the dashed line. This indicates that the assignment energy $\leftrightarrow$ momentum based on the transition probability is no longer reliable.

Next, we address the dependence of the modes on the width N_y and the length N_x of the system. Larger N_y increases the width of the strip. Since the edge modes are localized at the boundaries, increasing the width separates them more and more and makes them independent of each other. We focused on wide enough strips anyway so that the edge modes are essentially independent of N_y. This is supported clearly by Fig. 3.12. The width N_y of the strip plays no important role once it is large enough. Furthermore, Fig. 3.12 shows that $|\langle\psi|\psi_{\mathrm{cl}}\rangle|^2$ crucially depends on the characteristics of the edges. The edge states are exponentially located at the boundaries. Thus we exclude the effects of local disorder onto the two outermost sites in the consideration without boundaries as depicted by black circles. If the edges are unaffected by the local disorder, the transition probability takes significantly larger values than in the case where all sites are subjected to random potentials as shown by blue diamond.

Increasing the length N_x of the system has a pronounced effect on the transition probability as shown in Fig. 3.13. Note the logarithmic scale of the y-axis. Though the numerical data for the transition probability $|\langle\psi|\psi_{\mathrm{cl}}\rangle|^2\,(k_x)$ is a bit noisy, it agrees well with an exponential dependence

$$|\langle\psi|\psi_{\mathrm{cl}}\rangle|^2\,(k_x) \propto \exp(-\gamma(\sigma)N_x) \tag{3.9}$$

where the rate γ depends on the disorder strength. Naturally, the overlap decreases more

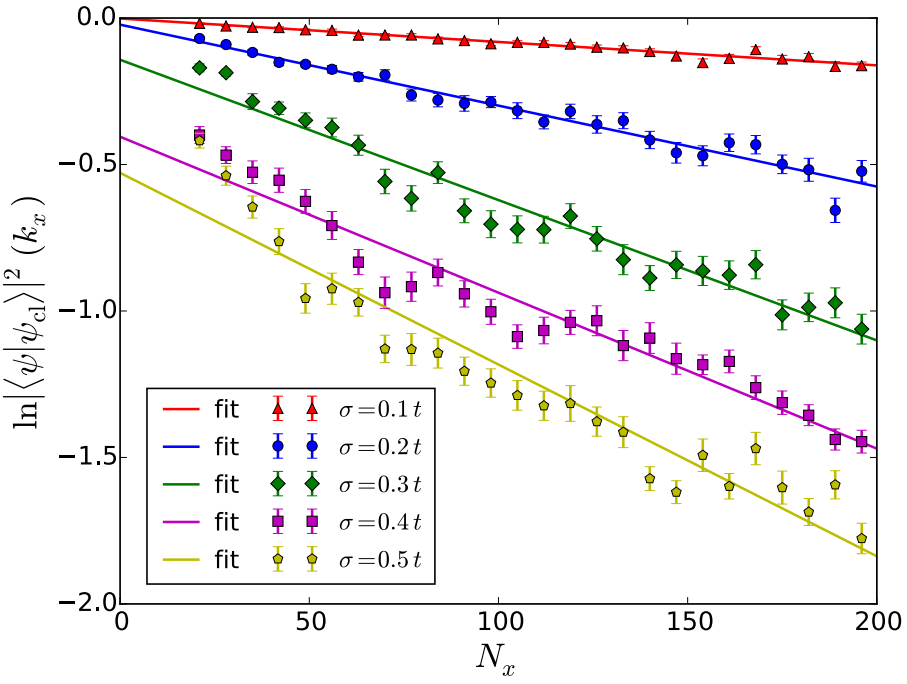

Figure 3.13: The logarithm of the transition probability at the momentum $k_x = 2\pi\,10/21$ vs. the length N_x of the system at $t_2 = 0.2t$, $\phi = \pi/2$, and the width $N_y = 20$. The transition probability is averaged over 50 random configurations for various disorder strengths σ. The error bars represent the standard deviation.

rapidly if the disorder strength is larger.

The observed dependence on N_x can be understood as follows. Let us view a system of given length N_x to be formed by concatenating a number r of short subsystems of length n_x with $N_x = r \cdot n_x$. If the subsystems are still long enough, the physics inside of each of them is only negligibly influenced by the boundaries between them. Then, the transition probability of the total system is given by the product of all the transition probabilities of the subsystems

$$\left|\langle\psi|\psi_{\mathrm{cl}}\rangle\right|^2(N_x) = \prod_{j=1}^{r} \left|\langle\psi|\psi_{\mathrm{cl}}\rangle\right|^2(n_x, j) \quad . \tag{3.10}$$

On average, the transition probabilities of all the subsystems are the same so we denote them by $p_{\mathrm{sub}} < 1$. Thus we have

$$\left|\langle\psi|\psi_{\mathrm{cl}}\rangle\right|^2(N_x) = p_{\mathrm{sub}}^r \tag{3.11a}$$

$$= \exp(-\tilde{\gamma} r) = \exp(-\gamma N_x) \tag{3.11b}$$

where we set $p_{\mathrm{sub}} = \exp(-\tilde{\gamma})$ and $\gamma = \tilde{\gamma}/n_x$.

Inspecting Fig. 3.13 reveals that the exponential decay does not apply for short systems, but only beyond a certain minimum length. Thus, the above argument is only approximately true because the assumption of negligible influence of the boundaries is not perfectly justified for short systems. Thus a linear fit $a - \gamma\,N_x$ of the logarithm of

σ	a	γ
0.1	-0.00174 ± 0.00458	0.00080 ± 0.00004
0.2	-0.02261 ± 0.01491	0.00276 ± 0.00012
0.3	-0.14242 ± 0.02713	0.00479 ± 0.00023
0.4	-0.40515 ± 0.03240	0.00532 ± 0.00027
0.5	-0.52846 ± 0.04800	0.00654 ± 0.00040

Table 3.1: Fitted values of the linear fits $\ln \left|\langle\psi|\psi_{\mathrm{cl}}\rangle\right|^2 (N_x) \approx a - \gamma\, N_x$ in Fig. 3.13. Fit values and errorbars are determined by a least-squares fitting technique.

$\left|\langle\psi|\psi_{\mathrm{cl}}\rangle\right|^2 (N_x)$ as shown in Fig. 3.13 works well, but the offset a is not zero in contrast to what our simple argument suggests in Eq. (3.11b). The fitted values are given in Tab. 3.1.

Finally, we study the effect of disorder on the edge mode at a decorated edge. It has been advocated that the decoration and a tunable gate voltage shifting the potential at the edges render the realization of tunable, direction-dependent delay lines possible [113]. If we recall the extension to the Kane–Mele model, a dependence on the spin is also possible. This makes the fundamental idea interesting for spintronics as well. But for all applications the robustness towards imperfections is decisive. This motivates the investigation of disorder.

The purpose of the decoration is to reduce the Fermi velocity by design, i.e., to introduce fairly flat regions in the dispersion. This implies that there are many eigenstates of very similar energies. From perturbation theory it is known that such systems are susceptible to generic perturbations such as disorder. We investigate a system of size $N_y = 50$ and $N_x = 21$ with a decorated upper boundary. Since the decorating sites are not excluded from disorder we also add a random local potential to the additional sites. In the reconstruction of the dispersion of the edge modes we require a certain minimum transition probability in order to obtain a reliable mapping between momenta and eigenstates. From the above results for systems of the considered size we set this threshold to 0.3, cf. Figs. 3.10 and 3.11. For weak disorder the successfully reconstructed dispersion is displayed in Fig. 3.14(a).

For stronger disorder, a complete reconstruction of the dispersion of the edge states turns out to be impossible, see Fig. 3.14(b). For instance for $\sigma = 0.1t$, the eigenstates with energies within the flat dispersion in the center of the gap cannot be mapped reliably to the corresponding momenta because their overlap falls below the threshold. As expected from our perturbative argument, the states in the flatter regions of the dispersion are not robust against disorder.

For a complete understanding, we also studied the case without disorder at the decorating sites. This is a realistic scenario if the technique which creates the decorating sites is a different one from the one growing the bulk. Clearly, this kind of disorder has much less detrimental effects on the edge modes, see for instance Fig. 3.12. The edge modes are rather localized at the decorating sites so that they are less exposed to disorder. This holds in particular for the states with rather flat dispersion because they differ only slightly from the completely local states on the decorating sites. For instance the same configuration as used in Fig. 3.14(b) can be reconstructed up to much stronger disorder $\sigma = 0.5t$ if the disorder is restricted to the bulk.

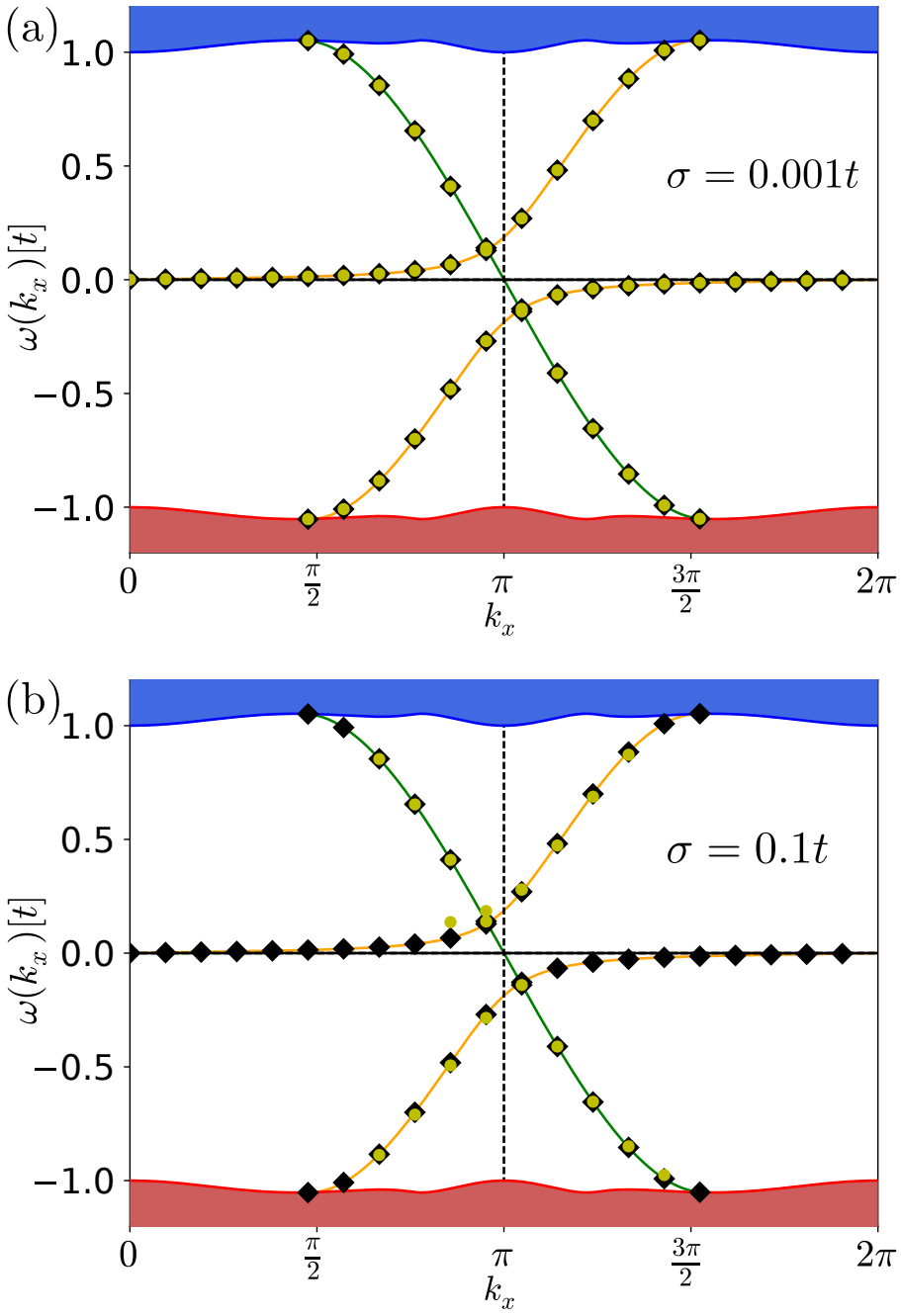

Figure 3.14: Dispersion of the edge states in a decorated system with $t_2 = 0.2t$, $\lambda_t = 0.2t$, and $\phi = \pi/2$. The filled areas indicate the continua of bulk states. The right-moving edge state marked in orange is located at the top edge while the left-moving edge state marked in green is located at the bottom edge. For reference, the black diamonds depict the reconstructed dispersion in the clean system with $N_y = 50$ and $N_x = 21$ while the yellow circles depict the reconstructed dispersion for $\sigma = 0.001t$ in panel (a) and for $\sigma = 0.1t$ in panel (b). Note that in panel (b) the flat part of the dispersion could not be reconstructed because the transition probabilities fall below the required 0.3 threshold.

Note that the above observations do not contradict the general idea of topological protection because there are modes at arbitrarily small energies. But for transmitting signals one needs a clearly defined dispersion $\omega(k_x)$ which yields the group velocity $\partial\omega/\partial k_x$. If this is not the case, as we found here for stronger disorder, we presume that the system is not suitable for applications requiring signal transmission. This sets certain limits to the general idea of topological protection which should not be misunderstood as a guarantee that dispersion and group velocity are well-defined.

3.1.5. Conclusion

We concentrated on the Fermi velocity of the edge states of topologically non-trivial fermionic lattice systems. The Fermi velocity is the group velocity with which signals can be transmitted through the edge states. Hence, it determines the speed of signal transmission. If it can be tuned it can be used to influence the time that signals need to cross the sample. In this way, the tunability of the edge states can be used to create delay lines based on interference, see Ref. [113]. Thus it is a measurable quantity which is very important for transport behavior, but it is different from DC conductivity studied previously [110, 111].

In Sec. 3.1.2, we analyzed the decorated Haldane model. The Fermi velocity is direction-dependent if the different edges are decorated and tuned independently. We discussed the effects that various parameters of the decoration have on the properties of the edge states, most notably on their dispersion.

In Sec. 3.1.3, the results for the spinless Haldane model were extended to the spinful Kane–Mele model. In this model, the dispersions of the edge modes depend on the combination of direction and spin. The model as a whole does not break TRS. For each right (or left)-moving spin-↑ mode there is a left (or right)-moving spin-↓ mode with equal energy. The full control of the dispersions and their dependence on direction and spin *separately* can be achieved by realizing spin-dependent exchange couplings at the edges. Candidates for the realization of such terms in the Hamiltonian are the proximity effect of a ferromagnet in hybrid structures or magnetic doping in the bulk of the system. In addition, we studied the effect of Rashba coupling.

In Sec. 3.1.4, we addressed the effect of disorder on the edge states as motivated by the fundamental paradigm of topological effects that the edge states are particularly robust against any kind of perturbation. For clarity, we performed this study for the spinless Haldane model. Indeed, the existence of gapless states at the edges is guaranteed by topological protection. But there is no guarantee for the preservation of a well-defined dispersion of the edge modes. Thus, the transport properties are likely to be influenced significantly by disorder.

We reconstructed the dispersion of the edge modes in disordered systems by comparing them with the edge modes of the clean system. The transition probability between the edge state in the clean system and the one in the disordered system served as a criterion to identify the momenta. In this way, one can link the eigenstates in the disordered systems to certain momenta and re-define a dispersion. The approach works very well for edge states of which the energy is far away from the continua. But if the energies approach the band edges, the mapping becomes ambiguous so that its application is no longer reliable. Thus, for stronger disorder only small parts of the original dispersions can be reconstructed. Increasing the disorder even further eventually destroys the edge

modes completely. In addition, we established an approximate formula for the reduction of the bulk gap due to disorder in the Haldane model.

Furthermore, we clarified how the transition probability depends on the width and the length of the system under study. The width does not have a significant impact once the sample is wide enough so that the two edge modes do not interact anymore. Increasing the length leads to an exponential decrease of the transition probability.

In the concluding Sec. 3.1.4, we addressed the robustness of the edge states at decorated edges which allow us to design small and tunable Fermi velocities. Applying the reconstruction procedure we could cope with small disorder strengths. But we found our expectation confirmed that the flat regions of the dispersions are particularly susceptible to perturbations. We conclude that in order to realize and to apply the ideas of tunable group velocities one has to resort to clean samples or, at least, to samples where the decorating sites are not subjected to disorder. The edge modes displaying a large dispersion and staying away from the band edges of the bulk modes are those which are most robust to disorder.

Further studies are necessary in order to investigate the influence of other kinds of disorder or imperfections. On the one hand, it is conceivable that spatially correlated disorder is less harmful to the edge modes than the completely local one we studied here. The edge modes may flow around smoother regions of disorder or imperfections, for example on the surface of a topological insulator, see Refs. [110, 120]. On the other hand, imperfections such as vacancies can behave like a local infinite potential, i.e., having very drastic effects on the edge modes. Extending such investigations to other kinds of systems displaying topological phases constitutes another broad field of research. For instance local spin-flip disorder caused by magnetic impurities could also destroy the $\mathbb{Z}_2$ topological phase or their helical edge states. A reconstruction of helical edge states in spite of local spin-flip disorder are also possible using the same procedure.

These findings are an initial step to understand the basic hybridization mechanism to tune the Fermi velocity of chiral or helical edge states. The natural next step is to investigate the application in experimentally achievable topological states. The site-specific control of Chern insulators on lattices is a tremendous challenge to experimental realization. Thus, it suggested itself to use the well-established IQHE for the same purpose. The IQHE of a free two-dimensional electron gas corresponds to the first observed topological phase. Over time, the samples became cleaner and cleaner and the theoretical understanding of the topological properties in the IQHE is very advanced. To this end, we consider that the IQHE is a possible candidate for application.

3.2. Tunable dispersion of the edge states in the integer quantum Hall effect

3.2.1. General context

Subjecting a two-dimensional electron gas at low temperature to a strong perpendicular magnetic field results in the well-known quantization of the transverse conductivity $\sigma_{xy} = \nu e^2/h$ with $\nu \in \mathbb{N}$ which is called IQHE [19]. The remarkably high precision with which the integer quantum Hall conductivity can be measured is attributed to its relation to topological invariants [1, 39, 45, 47, 48, 121]. Shortly after the discovery of the integer quantum Hall effect (IQHE) another topological effect was measured and dubbed the fractional QHE [15, 20] since Hall plateaus appear at fractional filling factors ν. The discovery of the integer and fractional QHEs triggered a steadily growing interest in topological phenomena in condensed matter physics.

The IQHE is a single-particle phenomenon [92, 93]; no interaction between the electrons needs to be taken into account, which facilitates its understanding. In the bulk, the interpretation of the IQHE is that the filling factor ν equals the total Chern number of the filled Landau bands. This Chern number is a topological invariant [39, 47, 48] related to the fundamental Berry phase [50]. This warrants the high precision of resistance measurements fulfilling Ohm's law without any non-linear corrections [47, 49].

A closer understanding is gained if one realizes that the actual charge currents are carried by gapless edge states [45] which cross the Fermi level. They have to exist at the boundaries because of the bulk-boundary correspondence [27]. The number of gapless edge states corresponds to the Chern number ν [1]. Each of these edge states can be seen as a single-channel conductor [122] propagating only in one direction along the edge. Therefore they are called chiral edge states. They allow for adiabatic transport [123] because backscattering is forbidden, which makes such transport particularly interesting for applications.

3.2.2. Present objective

For clarity, we focus here on the IQHE and do not take the spin into account, which is left to future research. The topological protection of the chiral edge states and the complete suppression of backscattering in these edge states suggests that the chiral edge states enable robust applications. Calibrating resistance standards to extremely high precision is certainly a wonderful example [124]. Yet, in the present study we want to trigger research on *further* applications. To this end, we investigate the Fermi velocity v_F occurring in the chiral edge states in the IQHE.

The key idea is to modify the edges by decorations such that local levels are created which are brought into weak contact with the dispersive edge modes. The ensuing hybridization leads to a weakly dispersing mode of which the Fermi velocity can be tuned by changing the energy of the local modes. If the local levels are in resonance with the edge modes the sketched mechanism is at work and a low Fermi velocity appears. If the modes are out-of-resonance, the hybridization is ineffective and the edge states remain strongly dispersive. The tuning of the local decorated edge modes can be achieved by gate voltages.

As pointed out in the general context, tunable Fermi velocities pave the way to inter-

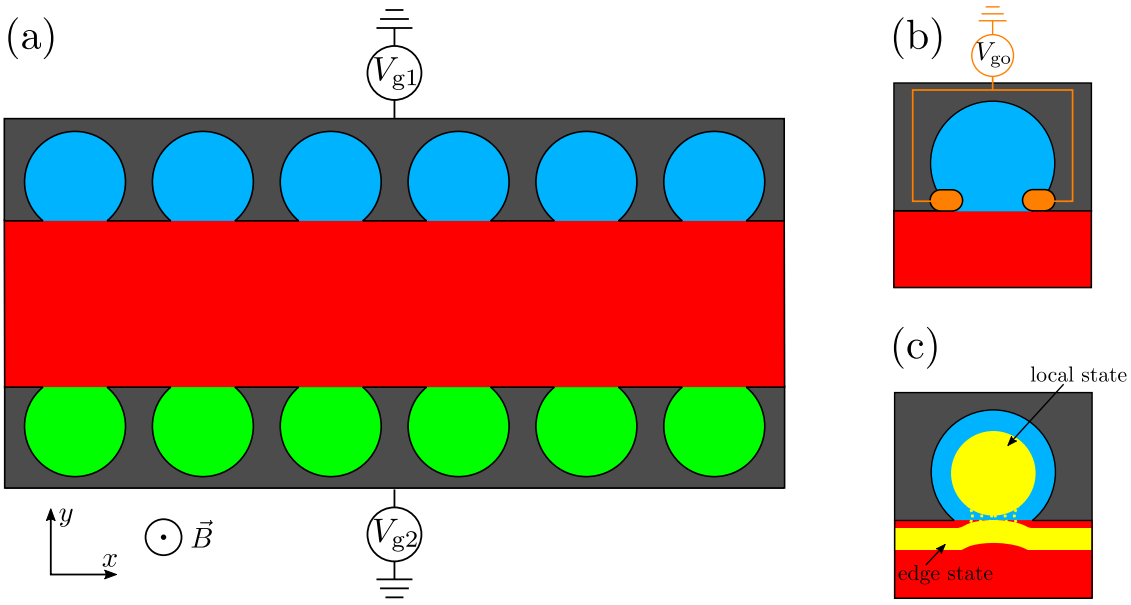

Figure 3.15: (a) Proposal for a decorated quantum Hall sample with tunable Fermi velocity. A perpendicular magnetic field puts the two-dimensional electron gas into the quantum Hall phase. Two independent gate voltages V_{g1} and V_{g2} change the potential of the blue bays at the upper boundary and of the green bays at the lower boundary, respectively. The grey area is inaccessible to the electrons. (b) The size of the opening of the bays to the bulk 2D electron gas can be controlled by a gate voltage V_{go}. (c) The size of the opening controls the degree of hybridization of the local mode within the bays and the edge mode in the 2D bulk.

esting applications such as delay lines or interference devices. Unfortunately, the lattice systems known so far cannot yet be tailored on the nanoscale to render the experimental verification of the theoretical proposal possible. So far, solid state systems postulated by density-functional theory can be envisaged to realizations in the future [53, 65, 66]. Alternatively, intricate optical lattices may make proof-of-principle realizations of tunable Fermi velocities possible [68, 125]. Yet, the search for different realizations is called for. In particular, the high standard of designing nanostructures in semiconductor systems suggests to look at such systems for the realization of tunable dispersions of edge states.

This brings us back to the IQHE which is based on a semiconducting interface generating a two-dimensional electron gas and a perpendicular magnetic field. If one is able to tailor the boundaries of the 2D electron gas in a way that corresponds to the decoration of 2D lattice models, tunable Fermi velocities become possible. Indeed, it has been proposed that attaching bays to the boundaries of a Hall sample allows us to generate local modes in the bay [113]. If they are slightly opened to the 2D bulk a weak hybridization is realized and the physics established so far for lattice systems should carry over to the IQHE. The basic geometry is sketched in Fig. 3.15.

Currently, it is possible to implement bays in the submicrometer range in IQHE samples. For instance, a single-electron source has been realized by coupling a quantum dot to a 2D electron gas via quantum point contacts and a gate voltage setting the dot potential [126]. An additional gate voltage at the quantum point contacts is used to control

the transmission, see Fig. 3.15(b), so that the hybridization can be tuned as indicated in Fig. 3.15(c). If such a coupled quantum dot is repeated periodically, the geometry in Fig. 3.15(a) is obtained. This setup will be studied in the following as an exemplary model for the realization of tunable Fermi velocities in the IQHE.

Below, we present calculations showing that the Fermi velocity v_F can be tuned by adding periodically arranged bays to an integer quantum Hall sample. In Sec. 3.2.3.1 we specify the model Hamiltonian describing the IQHE and the numerical approach to compute the edge states and their dispersion. Sec. 3.2.3.2 illustrates step by step how the spectrum of the decorated IQHE is structured. In particular, we focus on the effects of the hybridization between the modes in the bays and the edge modes because this is the mechanism altering the Fermi velocities. The results for tuned Fermi velocities are presented in Sec. 3.2.3.3. Finally, Sec. 3.2.4 collects our findings and provides an outlook.

3.2.3. Tunable edge states in the integer quantum Hall effect

3.2.3.1. Model and technical aspects

The present work is designated to illustrate the tunability of the Fermi velocity at a proof-of-principle level. For the sake of clarity, we assume that upper and lower boundaries are sufficiently far away from each other so that the edge states localized at the boundary do not influence each other. Practically, this means that the magnetic length $\ell_B = \sqrt{\hbar/|e|B}$ is significantly smaller than the width L_y of the quantum Hall sample, i.e., the external magnetic field must be large enough. Then it is not necessary to study a system of which both boundaries are decorated. Hence, we focus here on a sample with quadratic bays at the upper boundary, but no decoration at the lower boundary which is kept smooth. The precise shape of the bays does not matter for our proof-of-principle calculations. Within the colored areas shown in the panels of Fig. 3.16 the electrons can move freely. Their dynamics is only governed by their kinetic energy. The boundaries are supposed to be infinitely hard-walls as indicated by thick black lines.

Applying a perpendicular magnetic field in z-direction, see panel (a) in Fig. 3.16, is incorporated in the usual way by minimal coupling

$$\boldsymbol{p} \to \boldsymbol{p} - q\boldsymbol{A} \quad , \tag{3.12}$$

where the charge reads $q = -|e|$ and $\boldsymbol{A}$ is the magnetic vector potential. No electron-electron interactions are considered so that the full Hamilton operator reads

$$\mathcal{H} = \frac{1}{2m}\left(\boldsymbol{p} - q\boldsymbol{A}\right)^2 \quad , \tag{3.13}$$

where m is the (effective) mass of the electrons. The electrons are confined to the x-y-plane; we do not consider their spin degree of freedom. This can be justified because the two spin species $\uparrow$ and $\downarrow$ are decoupled in the perpendicular magnetic field [127, 128].

Due to the translational invariance in the x-direction a Landau gauge is particularly appropriate. We choose the Landau gauge in x-direction $\boldsymbol{A} = B(-y, 0, 0)^\top$ with $B \geq 0$, so that the momentum k_x remains manifestly conserved. This leads to the continuum

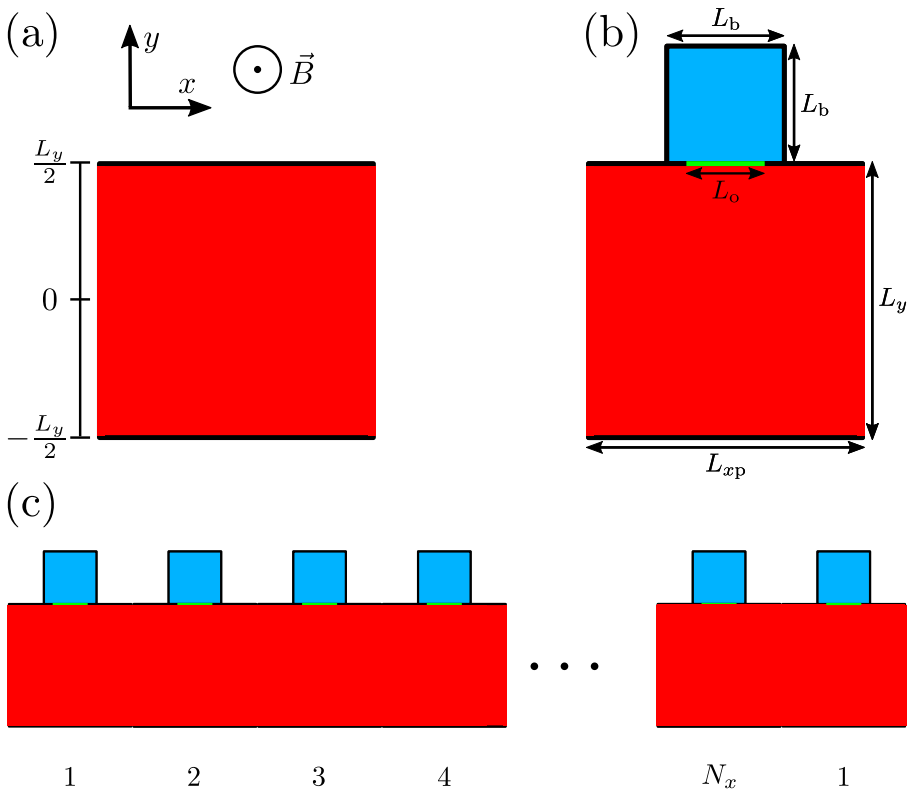

Figure 3.16: Sketch of the considered geometries of increasing complexity. Panel (a) displays the standard IQHE sample without any decoration of the boundaries; its width is denoted by L_y and its total length by L_x. Periodic boundary conditions in x-direction are assumed. Panel (b) shows the unit cell with a bay considered where the dimensions of the bay and the coupled bulk are given. Note the opening of the bay shown in green; its width is denoted by L_o. The total sample consists of N_x such unit cells as shown in panel (c) so that $L_x = N_x L_{x\mathrm{p}}$.

Hamilton operator

$$\mathcal{H}_\mathrm{bulk} = \frac{\hbar^2}{2m}\left[\left(-\mathrm{i}\frac{\partial}{\partial x} + \frac{qB}{\hbar}y\right)^2 - \frac{\partial^2}{\partial y^2}\right] \tag{3.14a}$$

$$= \frac{m\omega_\mathrm{c}^2}{2}\left(y + \mathrm{i}\ell_B^2\frac{\partial}{\partial x}\right)^2 - \frac{\hbar^2}{2m}\frac{\partial^2}{\partial y^2} \tag{3.14b}$$

in real space where we use the definition of the cyclotron frequency $\omega_\mathrm{c} = |e|B/m$ and the magnetic length $\ell_B = \sqrt{\hbar/|e|B}$. It is implied that x and y take only values in the colored regions of the panels in Fig. 3.16 unless stated otherwise.

3.2.3.1.1. Bulk system

Solving the Hamiltonian (3.14b) in the case of a bulk system without any boundaries leads to the famous Landau levels (LLs) with quantized energy values [129]

$$E_n = \hbar\omega_\mathrm{c}\left(n + 1/2\right), \; n \in \mathbb{N} \quad . \tag{3.15}$$

The corresponding wave functions are plane waves in x-direction and Gaussians multiplied by Hermite polynomials in y-direction

$$\psi(n, k_x, y) = C\mathrm{e}^{-(y-y_0)^2/2\ell_B^2} H_n((y-y_0)/\ell_B)\mathrm{e}^{\mathrm{i}k_x x} \quad , \tag{3.16}$$

because the Hamiltonian corresponds to shifted harmonic oscillators in y-direction. The wave functions are normalized by C, H_n is the nth Hermite polynomial, and $y_0 = k_x\ell_B^2$ determines the center of the wave function $\psi(n, k_x, y)$ in y-direction. These facts about the bulk Landau levels will be helpful in understanding the more complicated situations and serve as reference. Below, we consider more and more details of the actual model depicted in Fig. 3.16(c).

3.2.3.1.2. Sample of finite width L_y

Next, we consider a sample as shown in Fig. 3.16(a), i.e., of finite width in y-direction, but with translational invariance along x due to periodic boundary conditions. A numerical treatment is required which we introduce here. It is chosen flexible enough to be extended subsequently to the decorated sample including the bays.

For simplicity we set the effective electron mass $m = 1$, Planck's constant $\hbar = 1$, and use B henceforth for $|e|B$. As a result, the cyclotron frequency and the magnetic length are simplified to

$$\omega_\mathrm{c} = B \quad \text{and} \quad \ell_B = \sqrt{\frac{1}{B}} \quad . \tag{3.17}$$

We use ω_c as the energy unit henceforth. The resulting bulk Hamiltonian reads

$$\mathcal{H}_\mathrm{bulk} = \frac{1}{2}\left[\left(\frac{y}{\ell_B^2} + \mathrm{i}\frac{\partial}{\partial x}\right)^2 - \frac{\partial^2}{\partial y^2}\right] \quad . \tag{3.18}$$

As displayed in Fig. 3.16(a) the boundary conditions in y-direction imply $V(y) = \infty$ for $|y| \geq L_y/2$, where V denotes to the hard-wall confining potential. We use the same Landau gauge as before in the bulk system. In x-direction, we exploit the translational invariance using the plane wave ansatz

$$\psi(x, y) = \exp(ik_x x)\psi(y) \quad . \tag{3.19}$$

This leads to the Hamilton operator which acts on $\psi(y)$

$$\mathcal{H}_\text{undec. con.} = \frac{1}{2}\left[\left(\frac{y}{\ell_B^2} - k_x\right)^2 - \frac{\partial^2}{\partial y^2}\right] \tag{3.20}$$

with $|y| \leq \frac{L_y}{2}$. We tackle this problem by discretizing the y coordinate using a mesh with distance a between the points. It is understood that a is much smaller than any other physical length scale in the system, i.e., ℓ_B and L_y because we intend to describe the continuum limit as closely as possible. The resulting model resembles a tight-binding model, but we emphasize that its discrete character is just due to the approximate treatment of the continuum. We make sure that the discretization mesh is always fine enough so that the results are close to the continuum values.

To this end, the second derivative is approximated by the difference quotient

$$\frac{\partial^2\psi(y)}{\partial y^2} \approx \frac{1}{a^2}\left[-\frac{1}{12}\psi(y-2a) + \frac{4}{3}\psi(y-a) - \frac{5}{2}\psi(y) + \frac{4}{3}\psi(y+a) - \frac{1}{12}\psi(y+2a)\right]. \quad (3.21)$$

This formula cannot be applied to values of y which are close to a boundary because the values $\psi(y+a)$ and $\psi(y+2a)$ may not exist, see Fig. 3.17. In fact, if y_{bdry} is the value right at the boundary (red site partly in the shaded area in Fig. 3.17), then $\psi(y_{\text{bdry}}) = 0$ holds due to the hard-wall boundary condition and one does not need a term at y_{bdry}. What is needed is an approximation of the second derivative at $y_{\text{bdry}} - a$ for which $\psi(y_{\text{bdry}} + a)$ is required. One could simply omit this term, but this omission would introduce an error of the order of a with respect to the continuum situation which we intend to approximate. Hence, we exploit that $\psi(y_{\text{bdry}}) = 0$ and that a continuous function can be approximated by its Taylor expansion around y_{bdry}. In linear order this implies $\psi(y_{\text{bdry}} + a) \approx -\psi(y_{\text{bdry}} - a)$ which leads to the last term in Eq. (3.22), where we used the symbol $b(y) = y_{\text{bdry}} - a$ for the value of y adjacent to the boundary. This improves the results by one order in a, especially at the important edges of the sample. Thus the discretized Hamiltonian expressed in second quantization including the improvements at the boundaries reads

$$\begin{aligned}\mathcal{H}_{\text{undec. dis.}} = \sum_y \Bigg[&\frac{1}{2}\left(\left(\frac{y}{\ell_B^2} - k_x\right)^2 + \frac{5}{2a^2}\right) c^\dagger_{y,k_x} c_{y,k_x} - \frac{2}{3a^2} c^\dagger_{y+a,k_x} c_{y,k_x} \\ &+ \frac{1}{24a^2} c^\dagger_{y+2a,k_x} c_{y,k_x} + \text{h.c.}\Bigg] - \frac{1}{24a^2} c^\dagger_{b(y),k_x} c_{b(y),k_x} \quad , \end{aligned} \quad (3.22)$$

where c_{y,k_x} ($c^\dagger_{y,k_x}$) annihilates (creates) an electron with wave vector k_x in x-direction at coordinate y.

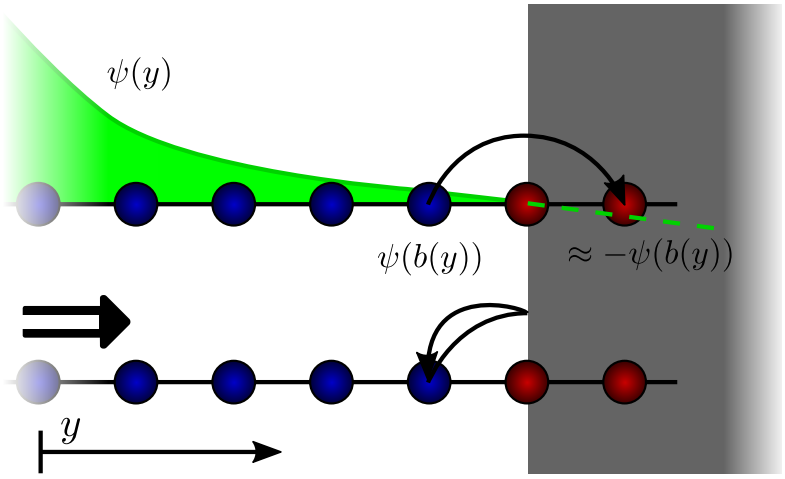

Figure 3.17: Illustration of the approximation used in the immediate vicinity of a boundary in order to improve the approximation of the continuous system by a discretized one, see main text.

In this way, we can very accurately compute eigenenergies of the plain quantum Hall sample as a function of k_x. In particular, we obtain the wanted dispersion of the edge states. The level of complexity is illustrated by Fig. 3.18 where the discretization meshes are shown. The calculation for the plain sample without any decoration only requires to discretize the y-axis, shown in Fig. 3.18(a), because the other spatial dependence is fully captured by the plane wave ansatz (3.19). The ensuing numerical calculation can be performed very efficiently because only a relatively small number of sites is required. But in order to be able to later include the bays as shown in Fig. 3.18(d), we first recalculate the sample without bays by considering the mesh in panel (b).

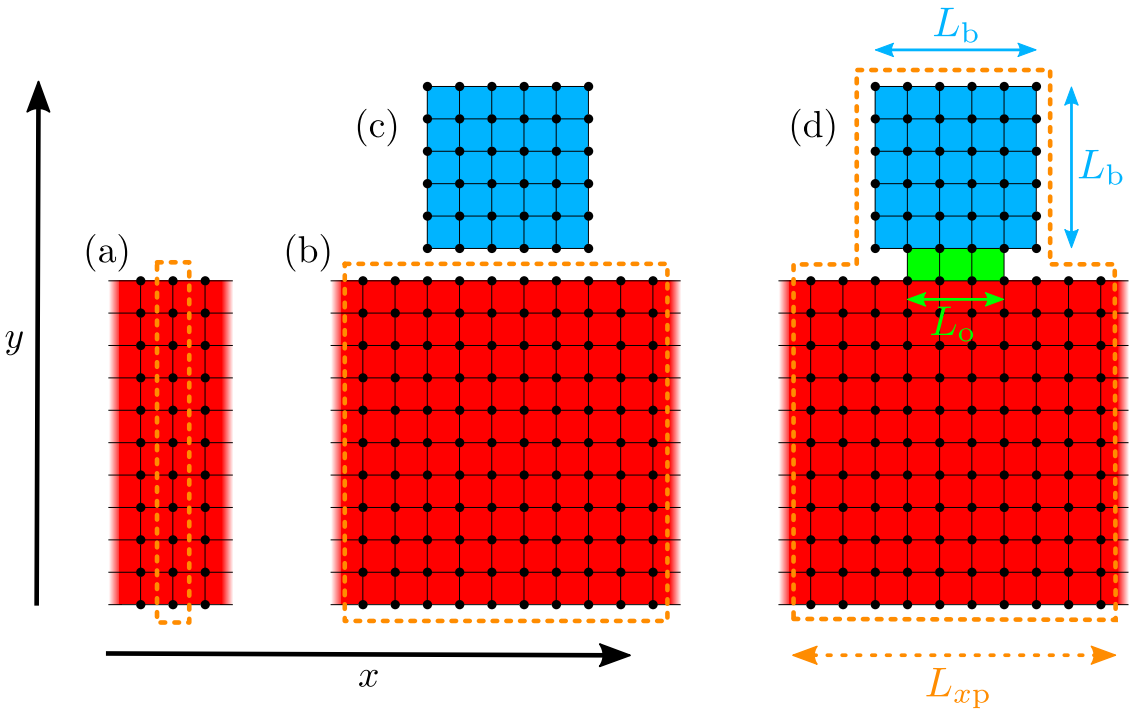

Figure 3.18: Sketches of the meshes used to capture the physics of the quantum Hall sample with and without bays. The strip geometry (a) and the rectangular geometry (b) are used to describe the sample without bays. The decoupled bay (c) is considered to compute the energy spectrum of the isolated bay as reference for the coupled system shown in panel (d). The orange dashed lines indicate the respective unit cells.

3.2.3.1.3. Fully discretized samples

Enlarging the unit cell as shown in panel Fig. 3.18(b) leads to the continuum Hamilton operator

$$\mathcal{H}_{(\mathrm{b})} = \frac{1}{2}\left(\frac{y^2}{\ell_B^4} + 2\mathrm{i}\frac{y}{\ell_B^2}\frac{\partial}{\partial x} - \frac{\partial^2}{\partial x^2} - \frac{\partial^2}{\partial y^2}\right) \tag{3.23}$$

with the periodic condition for the wave function

$$\psi(x + L_{x\mathrm{p}}, y) = \exp(ik_x L_{x\mathrm{p}})\psi(x, y) \quad . \tag{3.24}$$

We stress that this condition allows us to determine the value of k_x only up to multiples of $2\pi/L_{x\mathrm{p}}$, as usual if an enlarged unit cell in real space is considered.The corresponding BZ is reduced.

In the approximate discretized system the first order derivatives are expressed by using the central ratios of finite differences up to fourth order accuracy

$$\frac{\partial\psi(x,y)}{\partial x} \approx \frac{1}{a}\left[\frac{1}{12}\psi(x-2a,y) - \frac{2}{3}\psi(x-a,y) + \frac{2}{3}\psi(x+a,y) - \frac{1}{12}\psi(x+2a,y)\right] \quad (3.25)$$

wherever possible. Close to a hard-wall boundary the value $\psi(x+2a,y)$ is not known because it refers to sites outside of the considered domain. Then this term is simply omitted. The improvement used for the second derivative based on the mirroring explained in Fig. 3.17 cannot be used at hard-walls in x-direction because the resulting correction terms would be local densities with imaginary prefactors spoiling the hermiticity of the Hamiltonian.

Thus, the Hamiltonian $H_{(\mathrm{b})}$ is discretized in both directions. Expressed in second quantization it is given by

$$\begin{aligned}\mathcal{H} = \sum_{x,y}\Bigg[&\frac{1}{2}\left(\frac{y^2}{\ell_B^4} + \frac{5}{a^2}\right)c^\dagger_{x,y}c_{x,y} - \frac{2}{3a^2}c^\dagger_{x,y+a}c_{x,y} + \frac{1}{24a^2}c^\dagger_{x,y+2a}c_{x,y} + \frac{\mathrm{i}2By}{3a}c^\dagger_{x+a,y}c_{x,y}\\ &-\frac{\mathrm{i}By}{12a}c^\dagger_{x+2a,y}c_{x,y} + \mathrm{h.c.}\Bigg] - \frac{1}{24a^2}c^\dagger_{x,b(y)}c_{x,b(y)} - \frac{1}{24a^2}c^\dagger_{b(x),y}c_{b(x),y}\end{aligned} \quad (3.26)$$

where x and y run over the discrete sites within the colored areas in Fig. 3.18. The very last term occurs at hard-wall boundaries in x-direction, i.e., treating the bays, improving the second derivatives. The periodicity condition (3.24) carries over to

$$c_{x+L_{x\mathrm{p}},y} = c_{x,y}\mathrm{e}^{\mathrm{i}k_xL_{x\mathrm{p}}} \quad (3.27)$$

in second quantization.

The Hamiltonian (3.26) can be used to calculate numerically the spectrum for any shape of the integer quantum Hall sample. We employ it below to consider the finite strip without bays first, cf. Fig. 3.18(b), and isolated bays, cf. Fig. 3.18(c), for reference purposes. Finally, we pass to the coupled system, cf. Fig. 3.18(d). Then, we also have to include the effect of the gate voltages, see Fig. 3.15. The gate voltage V_{go} controls the size of the opening. This is implemented in our calculation by the choice of the geometry, i.e., by the value of L_{o}. Since we only consider bays at the upper boundary, there is no V_{g2} to be studied. The gate voltage V_{g1} is implemented by the Hamiltonian part

$$\mathcal{H}_{\mathrm{bays}} = -\sum_{x,y\in\ \mathrm{bays}} V_{\mathrm{g1}}c^\dagger_{x,y}c_{x,y} \quad (3.28)$$

where we incorporated the value of the charge into V_{g1}, i.e., we use V_{g1} for $|e|V_{\mathrm{g1}}$.

For small values of a the Hamiltonian (3.26) corresponds to very large, though sparsely populated matrices. We do not need all eigenvalues because we focus on the energies of the lowest LL up to about the third LL. In particular, the high-lying eigenvalues are strongly influenced by the discretization and hence they are meaningless for the underlying continuum model. In order to handle the diagonalization within given intervals of the

spectrum for large sparse matrices efficiently we employ the FEAST eigenvalue solver. The FEAST algorithm [130] uses the quantum mechanical density matrix representation and counter integration techniques to solve the eigenvalue problem within a given search interval. Now, we are in the position to calculate the dispersion of the lowest eigenstates and thus the Fermi velocities being the derivatives of the dispersion at the Fermi level.

3.2.3.2. Dispersions in decorated quantum Hall samples

So far, we analyzed the LLs in the bulk, see Sec. 3.2.3.1.1, and we introduced the approximate Hamiltonians to describe hard-wall boundaries of varying shapes, see Sec. 3.2.3.1.2 and Sec. 3.2.3.1.3. Here we present the results for geometries of increasing complexity. First, we address the strip geometry, i.e., the sample without any bays. Then, we study the isolated bays before we address the full coupled system, cf. Fig. 3.18. For clarity, we focus on the lowest LLs.

3.2.3.2.1. Strip geometry

In the case of a hard-wall confining potential in y-direction, i.e., $V(y) = \infty$ for $|y| > L_y/2$, one still expects to find eigenvalues and eigenstates bearing similarities to the bulk solutions. For instance, the eigenfunctions exponentially localized in the middle of the strip are barely influenced by the hard-wall confining potential. Hence they closely resemble the bulk functions (3.16) and their energies are exponentially close to the bulk LLs (3.15), see also below.

Moreover, the lowest eigenfunctions localized right at the boundary, i.e., $k_x = \pm L_y/2\ell_B^2$, equal the eigenfunction of the second LL with $n = 1$. This is so because the zero of the antisymmetric wave functions coincides with the boundary [131] as is well-known from the textbook problem in quantum mechanics of a parabolic potential cut off at its apex by an infinite potential. Thus, the antisymmetric Hermite polynomials are solutions which satisfy the boundary condition where they are localized. The influence of the other boundary is exponentially small if $\ell_B \ll L_y$ which is the limit we presuppose. These special points are used to verify the accuracy of the calculations based on the discretized model Hamiltonian in comparison to the continuum solutions, see Fig. 3.20.

For the discretized description to approximate the continuum efficiently in y-direction, the distance a between sites must be small enough to capture the dependence of the Hermite polynomials (3.16) on y. We use the wave function in Eq. (3.16) in order to determine the root mean square length

$$\left\langle (y - y_0)^2 \right\rangle^{1/2} = \ell_B \sqrt{n + 1/2} \quad . \tag{3.29}$$

Since $H_n(y)$ has n zeros on the root mean square length $\ell_B\sqrt{n+1/2}$ we arrive at the constraint

$$a \ll \ell_B \frac{\sqrt{n+1/2}}{n+1} \approx \frac{\ell_B}{\sqrt{n+1}} \quad . \tag{3.30}$$

In x-direction the wavelength set by $2\pi/k_x$ determines an upper limit on a so that we have to claim

$$a \ll \frac{2\pi}{k_x} \quad . \tag{3.31}$$

While (3.30) needs to be fulfilled in all our calculations, (3.31) is not required in the solution of (3.22), i.e., if the system in Fig. 3.18(a) is considered, but only if the fully discretized model introduced in Sec. 3.2.3.1.3 is considered.

In addition to these numerical requirements, we argued that we want to consider the case where the edge states at upper and at lower boundaries do not interfere. This requires

$$\ell_B\sqrt{n+1/2} \ll L_y \tag{3.32}$$

on physical grounds. The left hand side[1] is the root mean square of the spatial extension of the nth LL in y-direction. We focus on the lowest bands anyway so that $n = 0$ and $n = 1$ are the relevant cases. For concreteness, we henceforth use the values $\ell_B = 1\mu$m, $a = 0.01\ell_B$ and $L_y = 10\ell_B$. These values are in accordance with the above considerations for numerical accuracy and independence (up to exponentially small corrections) of the edge states.

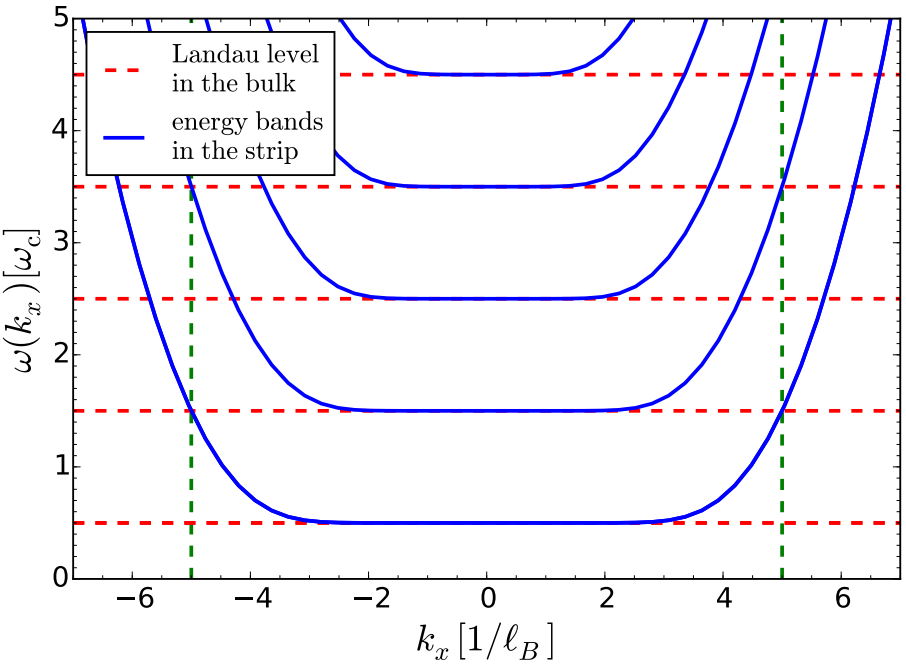

Figure 3.19: The blue curves show the dispersions of the LLs of a strip of finite width L_y, see Fig. 3.15(a). The red dashed lines indicate the equidistant energy spectrum of the LLs in the bulk. The vertical dashed lines are located at $k_x = \pm L_y/2\ell_B^2$ indicating the states which are localized at the upper and lower boundaries of the sample.

Considering the mesh in y-direction depicted in Fig. 3.18(a) we obtain the results (blue solid curves) shown in Fig. 3.19 where they are compared to the bulk results (3.15) (red dashed lines). Clearly, for small wave vectors one obtains flat bands agreeing very well with the bulk LL. Deviations occur only in the tenth digit of the eigenenergies. This is so because k_x determines the position of the harmonic oscillator in y-direction, cf. Eq. (3.16). Closer to the boundaries, an upturn in energy occurs because the electrons influenced by the vicinity of the hard-wall. As pointed out above, the lowest level right at the boundary

[1]The Eq. (3.32) in the article [108] is stated incorrectly.

acquires the energy of the LL at $n = 1$ because its wave functions correspond to half a harmonic oscillator [131]. This relation is fulfilled up to the fifth digit thanks to the improved treatment of the second derivative at the boundary, see Fig. 3.17.

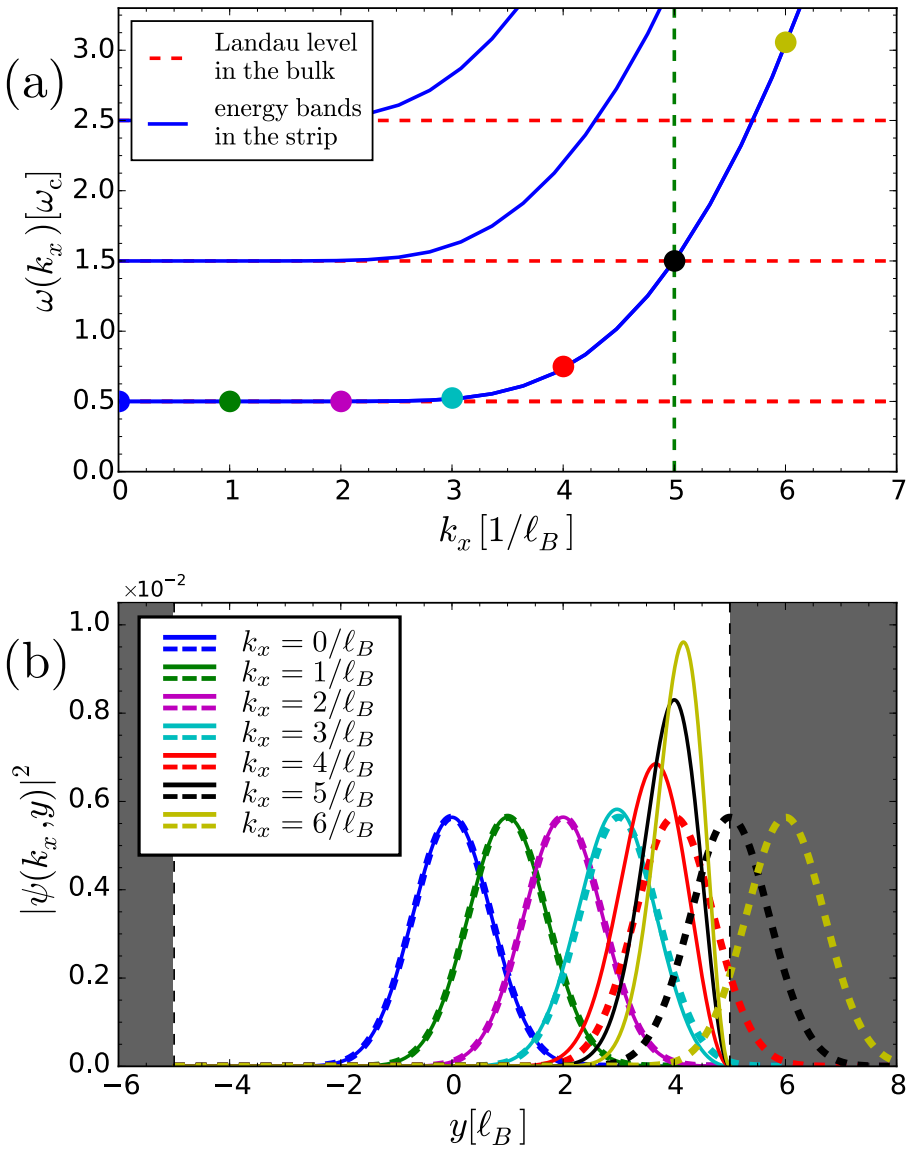

Figure 3.20: (a) Zoom of the dispersion bands in the IQHE. The vertical dashed green line is located at $k_x = L_y/2\ell_B^2$ marking the boundary of the sample. The colored dots indicate the eigenenergies of the corresponding wave functions. (b) Probability densities $|\psi(k_x, y)|^2$ of these eigenmodes are depicted by sold lines. The dashed lines in the same color shows the probability densities in absence of the boundary.

The gradual change of the wave functions upon increasing k_x is illustrated in Fig. 3.20. The colored dots in panel (a) indicate the energies and the k_x-values of the wave functions which are depicted in panel (b) by solid lines of the same color. The dashed lines of the same color display the corresponding eigenfunctions in the bulk which remain of Gaussian shape throughout. Note the increase of the peak of the eigenfunctions in the

strip geometry upon approaching the boundary (sequence red → black → yellow) because the electron cannot enter the hard-wall.

3.2.3.2.2. Rectangular geometry

Next, we pass to the fully discretized model (3.26) for the sample without bays, see Fig. 3.18(b). This describes the same physics as the calculation in the previous subsection. Still, we present exemplary results in Fig. 3.21 for two reasons. The first one is to illustrate that this calculation indeed reproduces the results obtained previously on the mesh shown in Fig. 3.18(a) with sufficient accuracy. Comparing the results from mesh (a) with those from mesh (b) in Fig. 3.18 we find that their eigenenergies agree up to the fifth digit. Note, that the calculation for mesh (a) requires to deal with a vector space of dimension of the order of 1000 while the calculation for mesh (b) requires to deal with a vector space with dimension of the order of 10^6.

The second reason is to obtain results for the undecorated sample, i.e., without bays, as reference for the subsequent complete analysis. The main point is that the reduction of the translational invariance by considering the enlarged rectangular unit cell in real space of length $L_{x\mathrm{p}}$ leads to a reduced BZ scheme in k_x-space. The backfolded branches of the dispersion are shown in panel (b) of Fig. 3.21. Since there is no real, physical reduction of the translational symmetry the backfolded branches display level crossings at the boundaries and elsewhere which are preserved as long as the physical translational symmetry is preserved. Hence the backfolded branches can be unfolded again to yield the extended zone scheme displayed in panel (a) of Fig. 3.21. This shows the same results presented in Figs. 3.19 and 3.20, as were obtained directly by the previous calculation based on the mesh in Fig. 3.18(a).

For clarity, we consider a quantum Hall sample of finite length in Fig. 3.21. The length of the unit cell in real space is given by $L_{x\mathrm{p}}$ and we fix the total number of these cells to $N_x = 50$. Of course, this value can easily be changed if needed. Hence, there are N_x different momenta k_x in the reduced zone scheme. They are multiples of $2\pi/N_x L_{x\mathrm{p}}$ lying in the interval $[-\pi/L_{x\mathrm{p}}, \pi/L_{x\mathrm{p}}]$.

We want to focus on the filled lowest LL, i.e., filling factor $\nu = 1$. Due to the upturn of the lowest level upon approaching the boundaries of the sample, this filling factor requires to occupy all states with energies just below the flat region of the second lowest level, see panel (a) of Fig. 3.21. However, in order to exclude any spurious effects of the energy levels of the second lowest LL we set the Fermi level to a value slightly below the flat band of the Landau level $n = 1$, namely to $\varepsilon_{\mathrm{F}} = 1.4\omega_{\mathrm{c}}$ as indicated by the green dashed line in Fig. 3.21. This allows us to distinguish unambiguously between occupied and unoccupied levels. This procedure helps to identify our quantity of interest, the Fermi velocity, i.e., the derivative of the dispersion with respect to k_x at the Fermi level. The ensuing minor deviation of the filling factor ν from 1 is macroscopically irrelevant for large values of L_y.

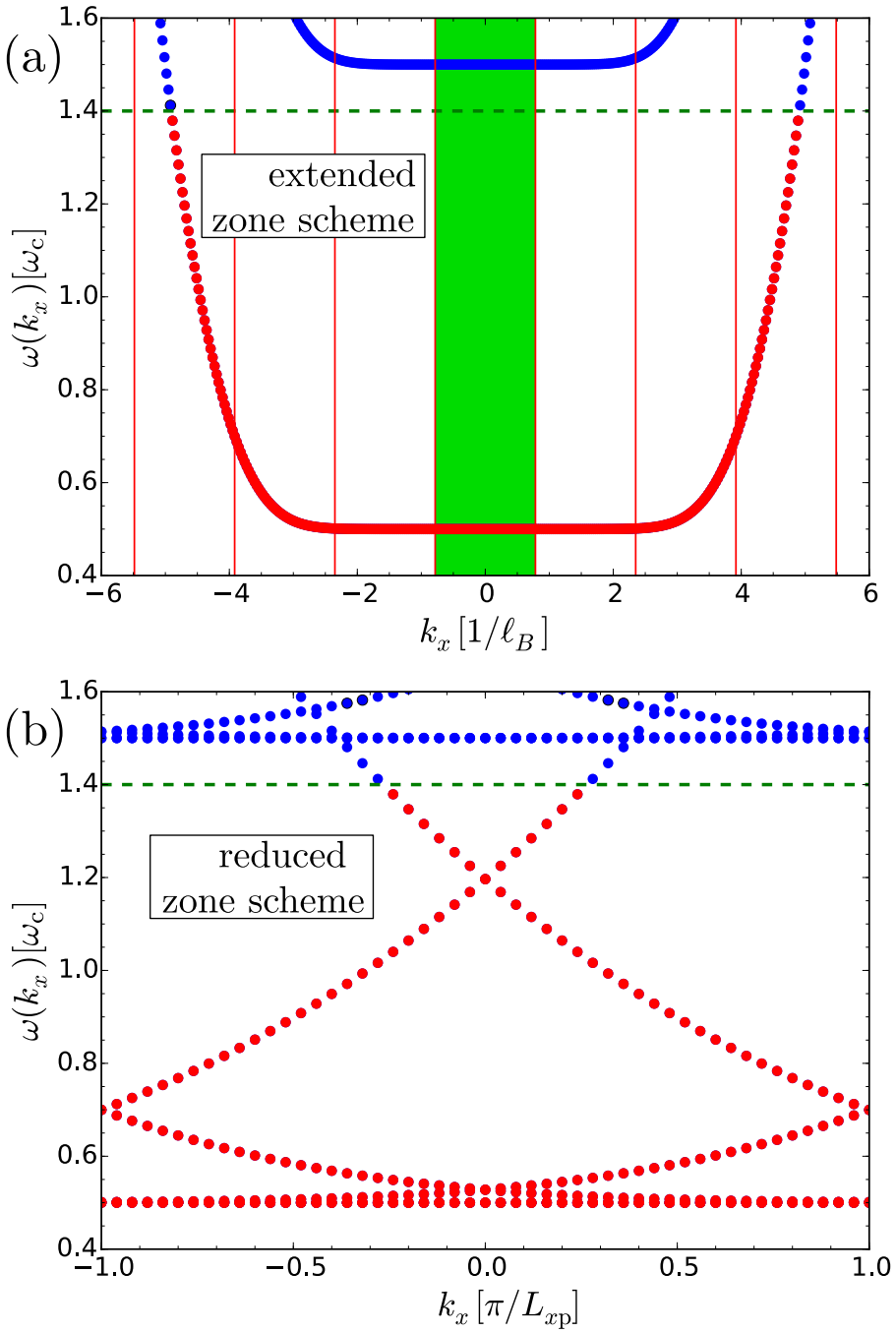

Figure 3.21: (a) Zoom of the lowest eigenenergies in the extended zone scheme for $L_y = 10\,\mu m$ and $L_{xp} = 4.01\,\mu m$ (The deviation from $4\,\mu m$ is only due to the discretization). Red symbols correspond to occupied states while blue symbols represent unoccupied states. The horizontal dashed green line indicates the chosen Fermi energy. The thin vertical red lines show boundaries of the corresponding reduced zone scheme. By backfolding the energies into the green shaded area one obtains the representation of the reduced zone scheme which is shown in (b).

3.2.3.2.3. Isolated bays

Before dealing with the complete system with bays coupled to the quantum Hall sample we determine the energy spectrum of isolated bays for later comparison. Note that we choose to consider quadratic bay for calculational simplicity. The underlying physics does not require a particular shape of the bay so that samples decorated with circular bays are expected to show the same physics at somehow modified quantitative parameters.

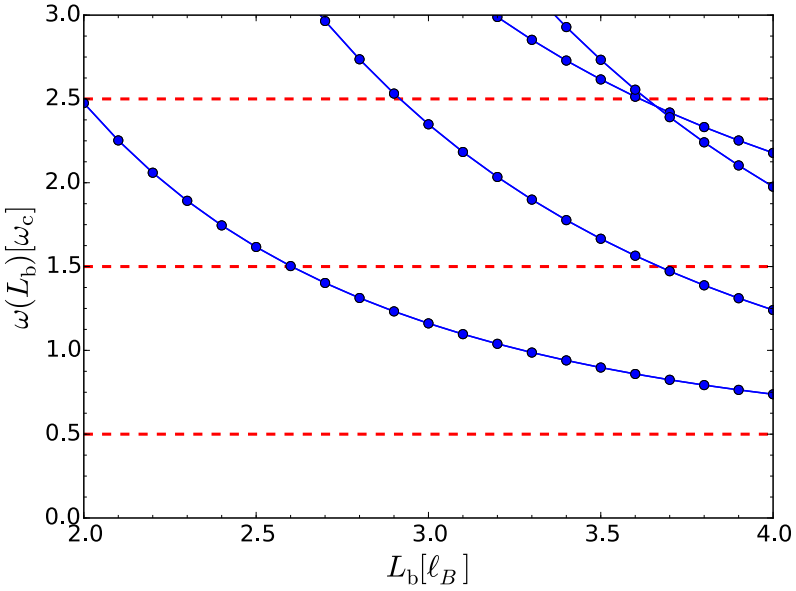

Figure 3.22: Discrete energy spectra of decoupled, i.e., isolated bays as a function of their size L_b are rendered by blue solid lines and blue symbols. The horizontal red dashed lines indicate the equidistant LLs in the bulk for comparison.

For considering the isolated bays we deal with the mesh shown in Fig. 3.18(c). The calculated energy spectrum as a function of the length L_b is plotted in Fig. 3.22. Having the classical cyclotron picture of circular electronic orbits in mind we choose $L_\mathrm{b} = 2\ell_B$ as starting value. No smaller bay would allow for a classical circular orbit. As expected the energies are larger than the bulk Landau energies because the confinement due to the bays restricts the motion of the electrons. Accordingly, increasing L_b lowers the energies because enlarging the bays reduces the influence of the confining potential.

The lowest eigenenergy of the bay reaches the energy gap between the two lowest LLs at a bay size of $L_\mathrm{b} \approx 2.6\ell_B$. Using the gate voltage V_g1 to shift the energies in the bays relative to the rest of the sample offers a possibility to tune a local mode in resonance to an edge mode. We will discuss this in more detail in the next subsection.

Adding the decoupled bay to the unit cell, i.e., considering the model shown in panels (b) and (c) of Fig. 3.18 without any coupling, yields the eigenenergies provided in Sec. 3.2.3.2.2 plus the eigenenergies of the bays which do not disperse at all (not shown). They appear as flat modes if plotted against k_x due to their completely local nature in real space.

3.2.3.2.4. Quantum Hall sample with coupled bays

Now, we pass to the fully decorated sample where the bays are coupled to the 2D electron gas in the strip, i.e., we consider the mesh in Fig. 3.18(d). We switch on the coupling between the bays and the strip by gradually increasing the opening L_o from zero to the maximum value L_b. The energy spectra are computed and tracked to understand how the coupling influences the eigenstates in general and the edge modes in particular.

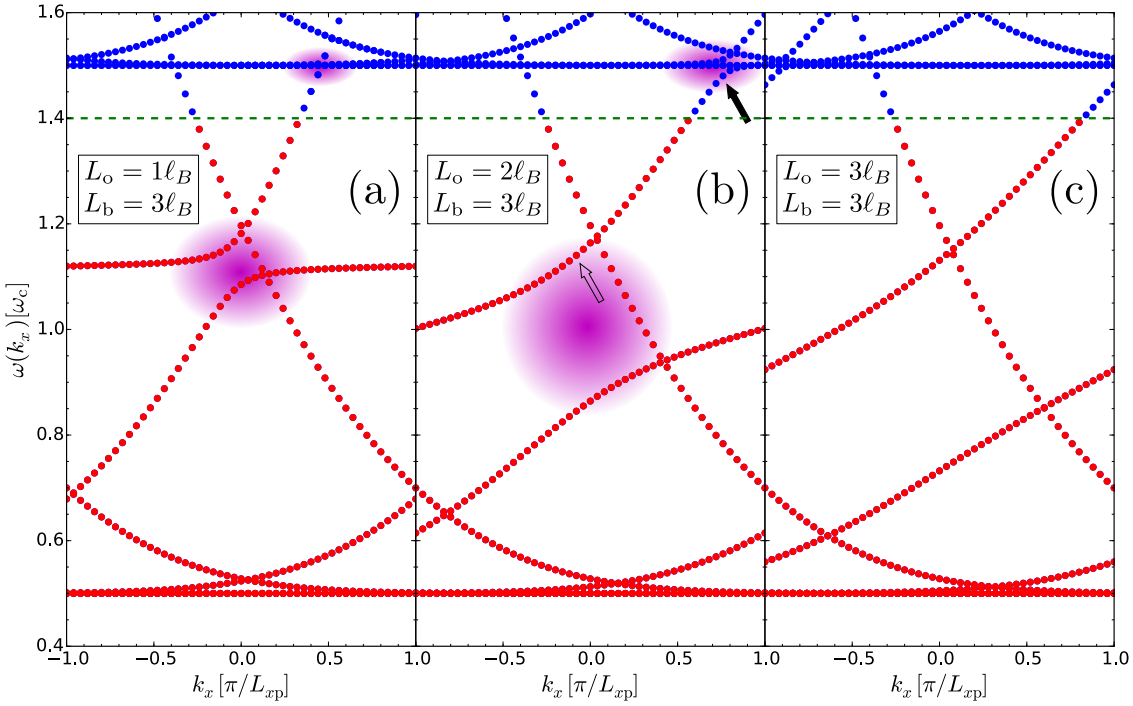

Figure 3.23: Energy spectra of the lowest eigenstates of a quantum Hall sample with $L_y = 10\,\mu\mathrm{m}$, $L_{x\mathrm{p}} = 4.01\,\mu\mathrm{m}$, and $\ell_B = 1\,\mu\mathrm{m}$. Panel (a) shows the case of weakly coupled bays because the opening L_o is small. Panel (b) shows a moderate coupling while in panel (c) a rather strong coupling is shown because the opening L_o is increased step by step. Red symbols correspond to occupied states while blue symbols depict unoccupied states; the dashed horizontal green line indicates the chosen Fermi level. The shaded areas highlight the locations of two avoided crossings due to the hybridization of local and dispersive modes. The arrows point to the eigenmodes whose probability density is shown in Fig. 3.24.

To this end, we depict three representative cases with openings $L_\mathrm{o} = \{1\ell_B, 2\ell_B, 3\ell_B\}$ and a bay size of $L_\mathrm{b} = 3\ell_B$ in Fig. 3.23. They represent the cases of weak, moderate, and strong coupling of the bays. Upon coupling the bays to the quantum Hall sample, i.e., for $L_\mathrm{o} \neq 0$, the eigenstates of the bays and the strip start to merge. Energy crossings of local modes from the bays with dispersive edge modes in absence of any coupling turn into avoided crossings once the bays and the strip are coupled. This represents a clear fingerprint of the level repulsion.

Inspecting the three panels, one realizes that only the right moving edge modes are influenced by the coupling of the bays. Only their energies depend on the degree of coupling, i.e., on the size L_o of the opening. The left moving modes are spatially separated

because they are localized at the other boundary of the sample without decoration. Hence they are influenced only exponentially weakly.

A nice example of level repulsion between a (formerly) local bay mode and a dispersive, right-moving edge mode is seen in panel (b) of Fig. 3.23 around $k_x = 0$. The relevant area is shaded in violet in panels (a) and (b). An example of a corresponding wave function is shown in panel (a) of Fig. 3.24. In panel (c) of Fig. 3.23 the avoided crossing is still present but hardly discernible because the energies are already very different due to the strong coupling. In fact, panel (a) shows the character of an avoided level crossing most clearly because the coupling of the bays is still small and hence the hybridization between the bay modes and the strip modes is still small and the repelling levels are still close to each other.

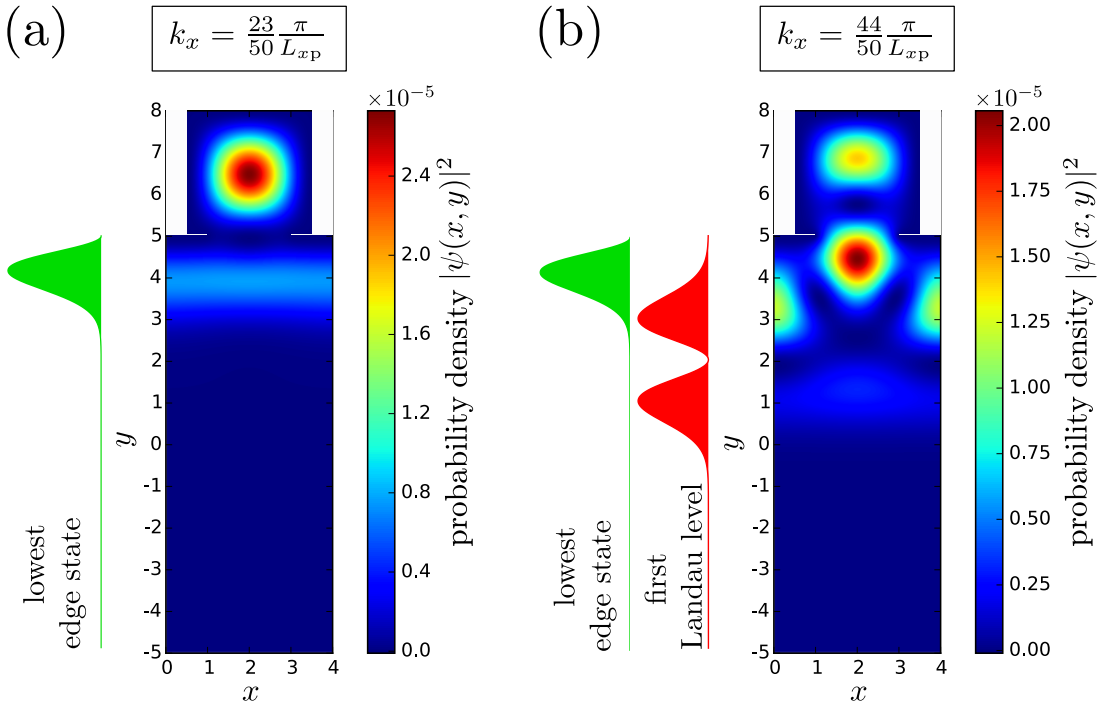

Figure 3.24: Probability density $|\psi_n(x,y)|^2$ of two eigenstates influenced by the different avoided crossings. Panel (a) shows the hybridization between the edge state of the LL $n = 0$ with the local mode in the bay. The energy and momentum of this state are indicated in panel (b) of Fig. 3.23 by the open arrow. Panel (b) shows the weak hybridization of the edge state with the second LL $n = 1$ mediated by the local mode in the bay. The energy and momentum of this state are indicated in panel (b) of Fig. 3.23 by the filled arrow. The parameters of the geometry are $L_y = 10\,\mu\mathrm{m}$, $L_{x\mathrm{p}} = 4.01\,\mu\mathrm{m}$, $L_\mathrm{b} = 3\,\mu\mathrm{m}$, $L_\mathrm{o} = 2\,\mu\mathrm{m}$, and $\ell_B = 1\,\mu\mathrm{m}$.

Another, less obvious and thus surprising, origin of avoided level crossings between dispersive edge modes and local modes results from the breaking of the translational invariance and the concomitant backfolding. This mechanism induces hybridization between local LLs and edge modes. An example is indicated by a shaded area in panel (a) at $k_x \approx 0.4\pi/L_{x\mathrm{p}}$ and in panel (b) at $k_x \approx 0.8\pi/L_{x\mathrm{p}}$ of Fig. 3.23. Clearly, the effect is weaker than the hybridization of edge modes and local bay modes. This is so because

the coupling of edge modes and local LLs is a second order effect in the coupling of the bays to the strip. Thus bay modes hybridize only indirectly in this phenomena, see also panel (b) of Fig. 3.24 where an exemplary wave function is shown. Similar effects were also found in the IQHE where different edge modes start to mix with one another due to the breaking of the translational symmetry by a step potential [132].

To support the interpretations given above, we plot the probability density $|\psi(x,y)|^2$ for eigenstates from the two avoided level crossings in Fig. 3.24. Panel (a) shows a state built from an edge mode and a local mode from the bays; its position in the energy spectrum is indicated by a open arrow in panel (b) of Fig. 3.23. Clearly, the two constituents, the edge mode and the local mode in the bay, can be seen.

Panel (b) of Fig. 3.24 shows a state built from an edge mode, a local mode from the bays, and the next higher LL $n = 1$; its position in the energy spectrum is indicated by a filled arrow in panel (b) of Fig. 3.23. Here, three states are mixed and contribute to the eigenstates as can be discerned nicely. The contribution of the local mode in the bay is much smaller than in the case shown in panel (a) because it contributes only as a intermediat state in the second order effect providing a coupling of the other two modes.

3.2.3.3. Tuning the Fermi velocity

In the previous sections we developed a detailed understanding of the energy spectra of quantum Hall samplse decorated with bays. Our ultimate goal is to study whether and how the Fermi velocity v_F can be tuned in such a decorated quantum Hall sample. We highlight that the Fermi velocity v_F represents the group velocity of the coherent quantum mechanical propagation of electronic wave packets. It cannot be seen as classical propagation of electrons along the (longer) boundaries of the bays, see below. Here we present quantitative results for the Fermi velocity and its dependence on the parameters of the model.

First, we examine the dependence of v_F on the size of the bays by increasing L_b for maximally opened bays, i.e., for $L_\mathrm{o} = L_\mathrm{b}$. The results are shown in panel (a) of Fig. 3.25. For maximally opened bays, the dispersions display no flat region because the strong level repulsion induces sizable momentum dependencies for most modes, see panel (c) of Fig. 3.23. Thus no strong dependence of the Fermi velocity for maximally opened bays is expected in accordance with panel (a) of Fig. 3.25. The complex interplay of many hybridizing levels makes it impossible to predict parameters for which v_F takes its minimum value. However, the comparison of panel (a) in Fig. 3.25 with Fig. 3.22 reveals that the Fermi velocity is indeed influenced when the local mode in the bay approaches the Fermi level, here $1.4\omega_\mathrm{c}$, which is the case around $L_\mathrm{b} = 2.6\ell_B$. Note that the Fermi velocity is generally reduced, roughly by a factor 2, once the local modes have come down in energy so that they reach the Fermi level.

The next parameter varied is the opening L_o of the bay. Panel (b) of Fig. 3.25 shows the results for various bay sizes. Note that the opening cannot exceed the size of the bay, hence the curves stop at $L_\mathrm{o} = L_\mathrm{b}$. All curves follow the general trend that the Fermi velocity is lowered upon increasing the hybridization between local modes in the bays and the dispersive edge modes. This is achieved by increasing the opening L_o. An approximate reduction by a factor of 2 occurs once the local energy levels from the bay come down in energy, i.e., for large enough L_b. This reduction is not very impressive. In addition, the geometry is fixed once the sample is grown and cannot be tuned on the fly.

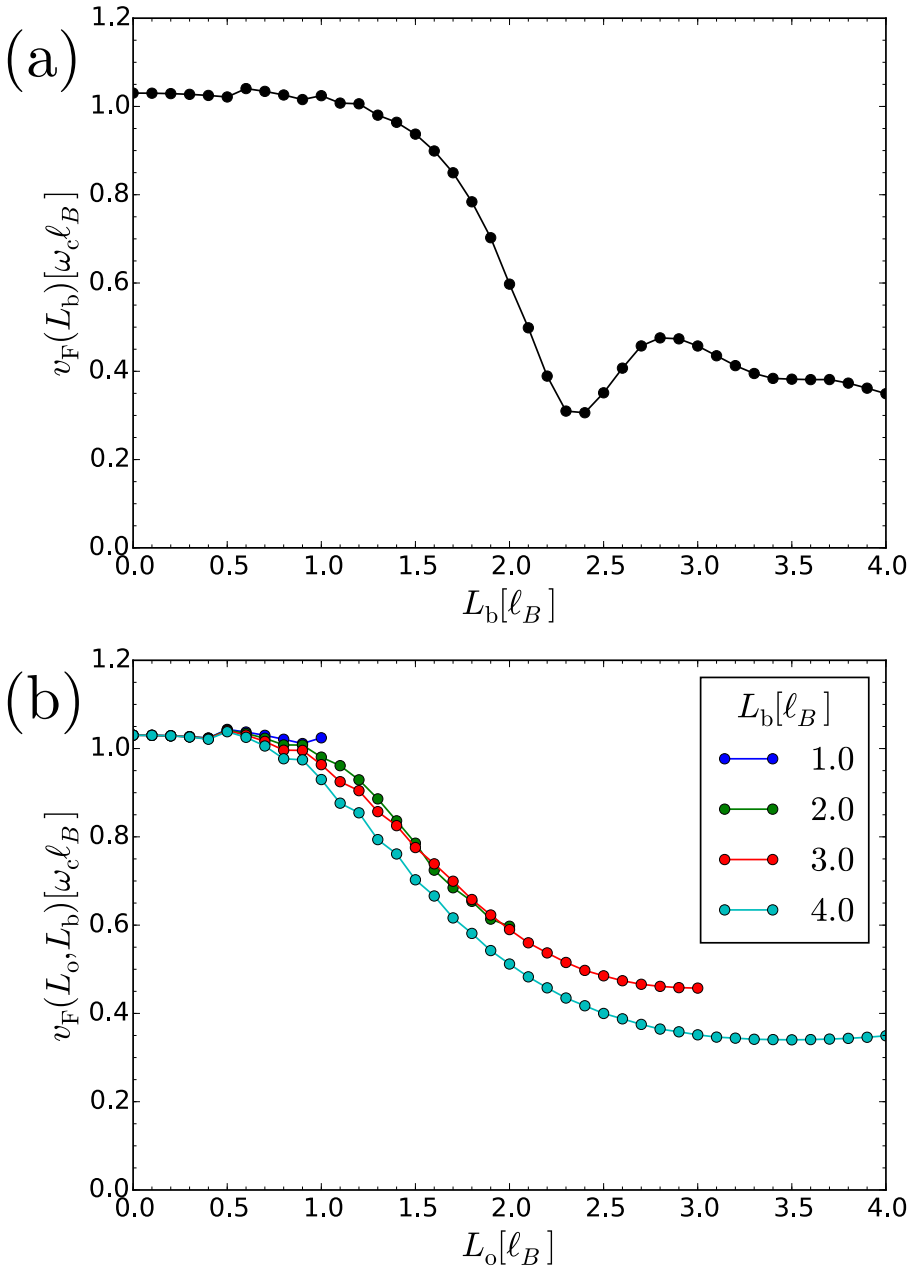

Figure 3.25: (a) Fermi velocity v_F of the right-moving modes as a function of the bay size L_b with $L_y = 10\,\mu\mathrm{m}$, $L_{x\mathrm{p}} = 4.01\,\mu\mathrm{m}$, $\ell_B = 1\,\mu\mathrm{m}$, and $L_\mathrm{o} = L_\mathrm{b}$. (b) Fermi velocity v_F as a function of the opening L_o of the bays for various bay sizes L_b with $L_y = 10\,\mu\mathrm{m}$, $L_{x\mathrm{p}} = 4.01\,\mu\mathrm{m}$, and $\ell_B = 1\,\mu\mathrm{m}$.

The last investigated dependence of v_F on a geometric parameter is the dependence on the distance between the bays, i.e. the size $L_{x\mathrm{p}}$ of the decorated unit cell, see Fig. 3.16. One could imagine that a certain resonance phenomenon occurs for special values of $L_{x\mathrm{p}}$. Generally, we expect that the influence of the decorating bays decreases upon increasing $L_{x\mathrm{p}}$ because the fraction of decorated boundary decreases. Explicit results are shown in Fig. 3.26. Again, the dependence of v_F is rather weak. The expected trend that a

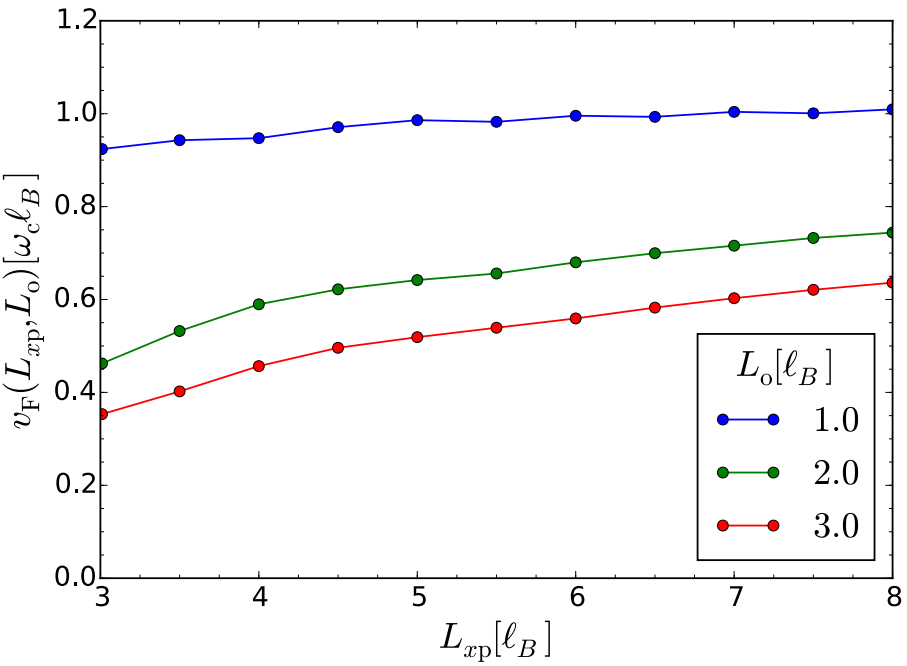

Figure 3.26: Fermi velocity v_{F} as a function of the distance between the bays, i.e., $L_{x\mathrm{p}}$ illustrated in Fig. 3.16, for various bay openings L_{o} with $L_y = 10\,\mu\mathrm{m}$, $L_{\mathrm{b}} = 3\,\mu\mathrm{m}$, and $\ell_B = 1\,\mu\mathrm{m}$.

larger $L_{x\mathrm{p}}$ reduces v_{F} less is clearly confirmed because the Fermi velocity approaches its undecorated value of about $\omega_{\mathrm{c}}\ell_B$ upon increasing $L_{x\mathrm{p}}$. At small values of $L_{x\mathrm{p}}$ we retrieve a reduction by a factor 2. But no resonance phenomena at particular values of the interbay distance are found. We attribute this to the fact that none of the local modes in the bay is truly in resonance with the edge modes.

In order to identify a suitable tuning parameter we revisit the results gained for lattice models [44, 113]. Three ingredients are important for sizable changes of the Fermi velocity: (i) the local and the dispersive modes must be in (or close to) resonance. (ii) There must be a parameter to tune and to detune this resonance. (iii) The coupling of the modes should be rather small so that they are sensitive to being or not being in resonance.

Translating these conclusions back to the IQHE, it appears that we have to use the gate voltage V_{g1} to control the resonance between the local modes in the bays and the dispersive edge modes. It is obvious that one can shift the bay modes by changing V_{g1}. An additional asset is that this can be done on the fly so that one possesses a true control knob for the speed of signal transmission and hence for the delay time which can be tuned while the signal processing is going on.

The opening of the bays should not be large because the coupling and hence the hybridization of the local and the dispersive modes should be rather weak. Thus we choose the rather small value $L_{\mathrm{o}} = \ell_B$ in Fig. 3.27. In this figure, we plot the dependence of the Fermi velocity on the gate voltage. For most values, the Fermi velocity does not deviate strongly from its value of about $\omega_{\mathrm{c}}\ell_B$ in a sample without bays. But if the energy levels of the local modes in the bays approach the dispersive edge mode at the Fermi level they resonate and lead to an avoided level crossing. In the region of the avoided level crossing

the local mode and the dispersive one mix, so that the formerly steep crossing of the dispersion through the Fermi level becomes flat. Hence the Fermi velocity is considerably suppressed. Note that the resulting resonance dips of v_F are rather narrow and can easily be used to (de)tune the velocity by moderate changes of the applied external gate voltage. In this fashion, changes of the Fermi velocity by factors 10 to 100 should be realizable, similar to what was found in lattice models [44, 113].

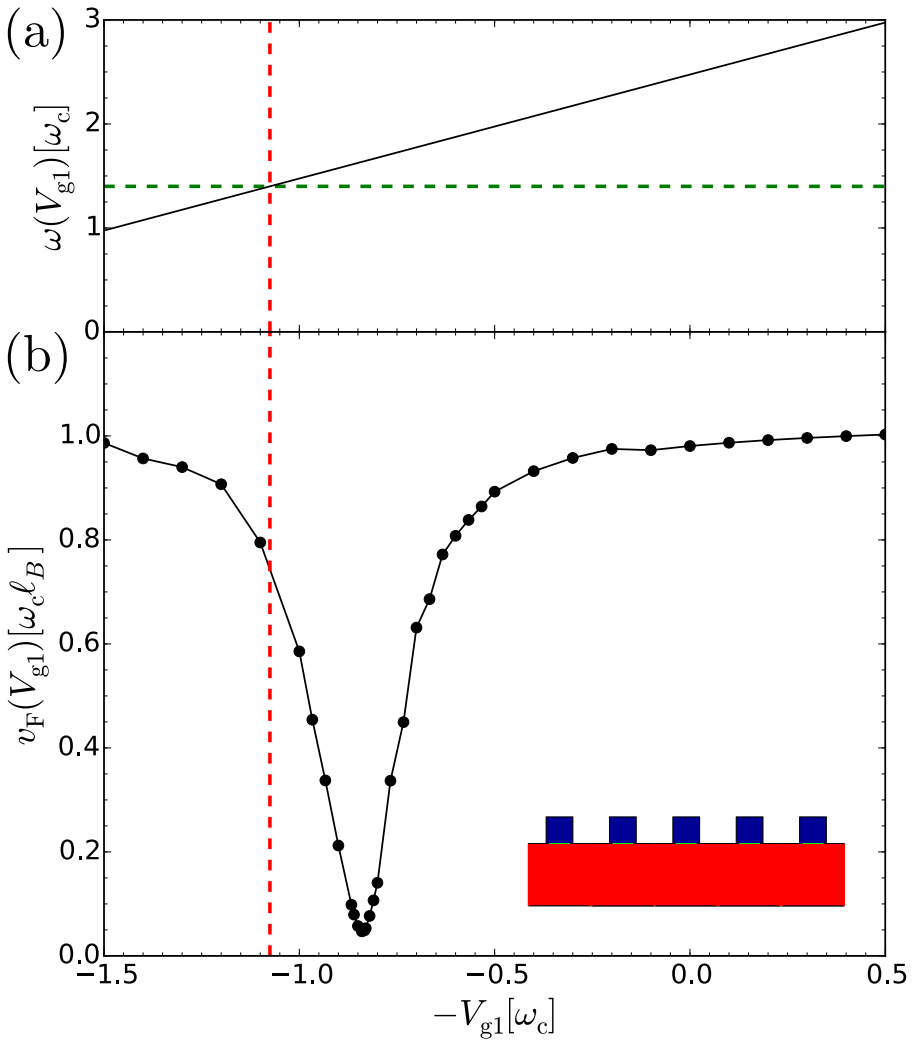

Figure 3.27: (a) The horizontal dashed line shows the set Fermi level while the slanted solid lines depict the energy level in the isolated bays shifted by the gate voltage. The vertical red line is a guide to the eye to link the resonance visible in panel (a) to the strong response in panel (b). Note that it does not predict the minimum precisely due to the level repulsion. (b) Fermi velocity v_F as a function of the gate voltage V_{g1} for $L_\mathrm{b} = 2\,\mu\mathrm{m}$, $L_y = 10\,\mu\mathrm{m}$, $L_{x\mathrm{p}} = 4.01\,\mu\mathrm{m}$, $L_\mathrm{o} = 1\,\mu\mathrm{m}$, and $\ell_B = 1\,\mu\mathrm{m}$.

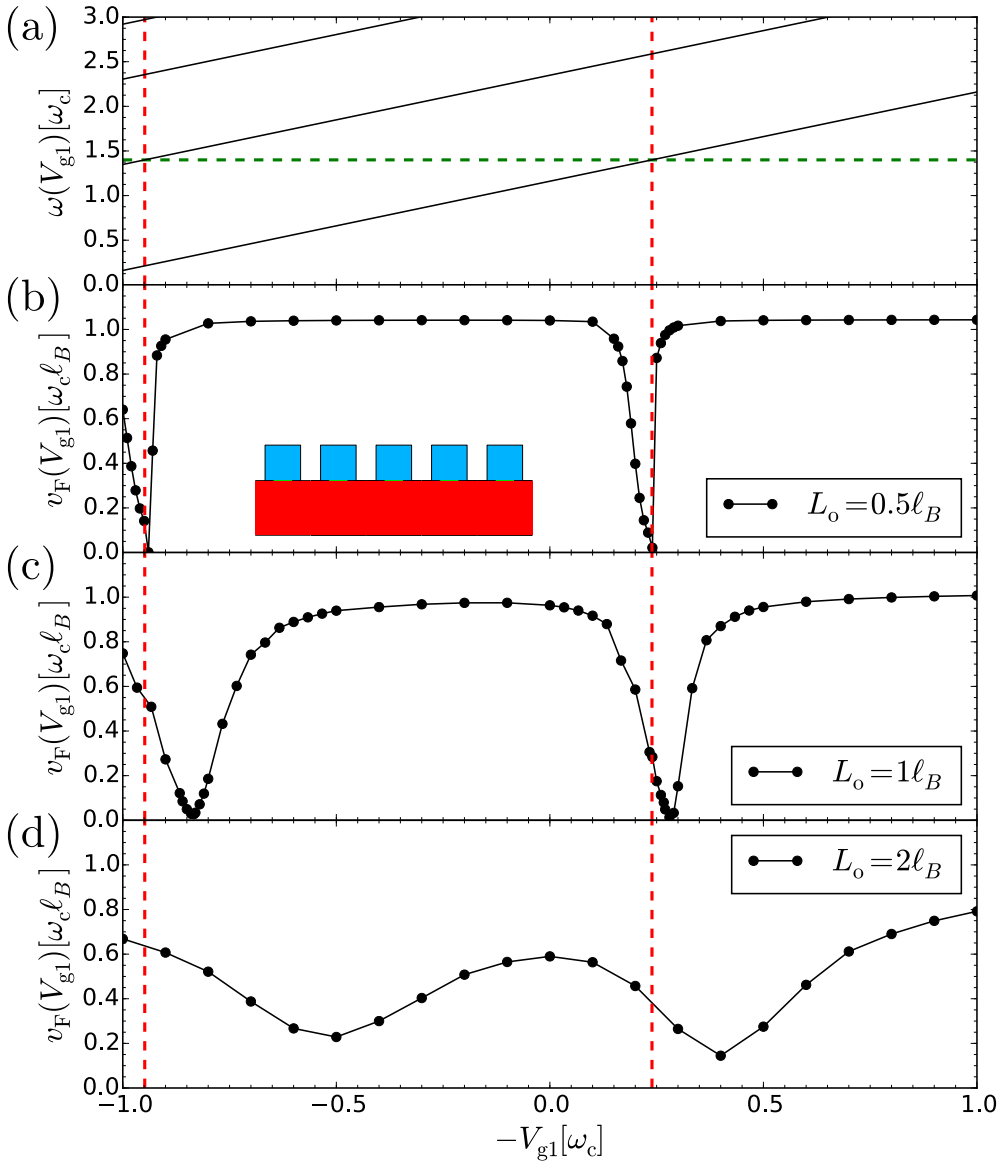

Figure 3.28: (a) The horizontal dashed line shows the Fermi level while the slanted solid lines depict the energy levels in the isolated bays shifted by the gate voltage. The vertical red lines are guides to the eye to link the resonance visible in (a) to the strong response in the panels below. Note that it does not predict the minimum precisely due to the level repulsion. (b)-(d) Fermi velocity v_F as a function of the gate voltage V_{g1} for $L_b = 3\,\mu m$, $L_y = 10\,\mu m$, $L_{xp} = 4.01\,\mu m$, $\ell_B = 1\,\mu m$, and the three different values of L_o as indicated.

Comparing Figs. 3.27 and 3.28, one realizes the similarities of the curves. The width of the resonance dips is comparable if the openings L_o are the same, cf. Fig. 3.27 and panel (c) of Fig. 3.28.

Figure 3.28 illustrates very clearly that larger openings lead to significantly broader dips which are less deep. In return, smaller openings and thus less strongly coupled bays lead to narrower dips with significantly lower residual Fermi velocity at the minimum.

This minimum value of v_F depends on how flat the dispersion of the hybridized modes is as determined by the coupling strength: weaker coupling implies a better localization for the hybridized modes with flatter dispersion. Flatter modes allow for sharper dips down to lower residual values of the Fermi velocity. Note that the reduction of the Fermi velocity can reach a factor of 100 for narrow bay openings. A classical interpretation of slower propagation due to the longer path along the boundaries of the bays would explain a factor 3.75 at best for $L_\mathrm{o} = 0.5\,\mu\mathrm{m}$. The longer path due to the included bay at the upper boundary of the unit cell corresponds to 15 µm whereas the path without the bay is 4 µm. Thus the factor 3.75 describes the extension of the path.

The positions of the resonance dips depend on the energy levels of the modes in the bay so that the bay size influences them strongly. In the smaller bays studied in Fig. 3.27, the lowest bay level lies above the Fermi level so that the gate voltage has to bring it down in order to observe resonance. In the larger bays, studied in Fig. 3.28, the lowest bay level lies below the Fermi level with the second lowest above it. So Fig. 3.28 shows that several dips may occur, even for different signs of the gate voltages. All in all, it appears that the precise position of the dips is not at the resonance with the energy levels of the decoupled bays, but at slightly higher values of the gate voltage. We attribute this to the hybridization with all the LLs including a downward shift of the local energy modes due to level repulsion from the high-lying LLs.

3.2.4. Conclusion

Topologically protected edge states possess many appealing properties. Still, avenues towards applications have not been established. The recent proposal of tunable Fermi velocities in Chern insulators and spinful topological insulators for the realization of delay lines and interference devices is a step in this direction. The purpose of the present study was to show that no lattice models are required, but that semiconductor samples with decorated boundaries show the same phenomena. This finding represents a substantial step forward towards realization because of the extremely high standard of designing and growing nanostructures for semiconductor devices.

We analyzed the dependence of the dispersion of the edge states in decorated quantum Hall samples on various parameters. The geometry of the sample defines the energy levels and partly the degree of coupling between the decorating bays and the bulk of the two-dimensional sample. Yet the geometric parameters do not allow for a fine-tuning of the Fermi velocity, let alone quick changes of it in the course of signal processing.

But gate voltages can achieve the wanted tunability. First, we found that the local levels in the bays should be close in energy to the Fermi level in the bulk of the quantum Hall sample so that the gate voltage applied to the bays does not need to shift them to a large extent. Second, the coupling between the bays and the rest of the sample should be rather weak to have rather narrow and deep dips in the Fermi velocity if the local modes are tuned into resonance to the dispersive edge states. Then, the fundamental mechanism of mode mixing and level repulsion leads to weakly dispersive eigenmodes crossing the Fermi level. This represents the key phenomenon for tunability.

Changes by up to two orders of magnitude appear possible. In our calculations, the degree of coupling is a geometric parameter. In practice, we propose to make it tunable as well by additional gate electrodes which modify the width of the bay openings, cf. Ref. [126].

The calculations are based on discretizing the sample in real space and mapping it to a tight-binding type of model. For fine enough meshes, reliable results valid for the continuum case are obtained as we could verify by comparison to analytic bulk solutions. We increased the complexity of the considered geometry step by step in order to gain a reliable understanding of the occurring physical phenomena. The approach is flexible enough to be adapted to various geometries. We considered quadratic bays, but any other shape is possible as well, however only quantitative changes are expected. Here the focus was on a proof-of-principle calculation to show that the anticipated physics indeed takes place in the IQHE.

In view of experimental realizability, some aspects must be kept in mind. First, the neglected interaction between the electrons can lead to the formation of certain charge modulations at the boundary. On the one hand, it is established that compressible and incompressible stripes form close to the boundaries [133]. The incompressible stripes may hinder the propagation of signals. On the other hand, if the filling is tuned just below filling factor $\nu = 1$, we expect that this effect is avoided because no incompressible stripes are formed at the edges. The final clarification, however, can only be reached by an experimental study.

For concreteness, we showed calculations for $\ell_B = 1\,\mu\text{m}$. This value corresponds via $B = \hbar/(e\ell_B^2)$ to a magnetic field of 0.66 mT and to an electron density of $3.2 \cdot 10^7 \text{cm}^{-2}$. Both values are very small compared to the values in generic quantum Hall setups which have magnetic fields and electron densities higher by about a factor of 10^4 [19, 124, 131]. Thus, for realization one has to look for systems with high mobility at much smaller electron densities or to make the geometric structures of the sample smaller. For instance, a factor 5 in linear dimensions yields a factor 25 in the electron density and in the magnetic field.

An interesting alternative to standard semiconductors is the IQHE in graphene. The relation between the magnetic length ℓ_B and the magnetic field is the same [134–138], but the relevant electron density n is measured relative to electron density of the semimetal so that small values are easily realized. Due to the linearity in ε_F of the density-of-state one has $n \propto \varepsilon_\text{F}^2$. Furthermore, due to the perfect lattice structure a high mobility can be expected. So the promising aim is to create non-trivial boundaries with bays on the scale of 10 to 1000 nm in graphene. This will be investigated in the next section.

In conclusion, an experimentally realizable topological phase, the IQHE, allows for tunable Fermi velocities if its edges are appropriately decorated. Gate voltages can serve as control parameters for tuning. These findings should encourage further research to realize such systems at the laboratory level to ultimately pave the way towards real devices.

As an outlook, we want to emphasize that the presented findings can be extended in several ways as has been done for lattice models [44]. The detrimental effects of disorder can be included to study the robustness of the observed effects. Such investigations will help to understand with which accuracy an experimental realization has to be grown in order to be able to observe the predicted effects. Without doubt, this constitutes an essential step toward applications.

Second, our findings can be extended to spinful models without conceptual difficulties. If the spin is subjected to spin-orbit coupling, the chiral edge modes will generically become helical modes. This opens up the promising field for applications in spintronics, for instance realizing switchable spin diodes.

3.3. Tunable signal velocity in the integer quantum Hall effect of graphene

3.3.1. General context

Non-trivial topological properties of condensed matter systems are believed to represent a valuable resource for various purposes. The key idea is that topological properties are protected so that they are not destroyed by small changes of the system. Hence they are robust against imperfections and unwanted effects. This has led to the most spectacular application of a topological insulator: the IQHE has become the international gauge standard for resistance measurements, see Ref. [124] and references therein. Apart, however, from this very important application there has been little application of topological properties so far. We are aware of three-dimensional topological insulators used as thermoelectric elements [139, 140].

In the previous section we advocated the IQHE of a 2D electron gas for Fermi velocity engineering. Indeed, it is possible to obtain tunable signal velocities in two-dimensional electron gases subjected to a perpendicular magnetic field [108]. Still, there are challenges opposing an immediate realization: modifying the edges by periodically aligned bays with the required precision on small length scales of 100 nm represents a tremendous challenge to sample design. Larger length scales are easier to realize, but the characteristic length $\ell_B^2 = h/(e|B|)$ must match the geometric scales so that larger length scales require smaller magnetic fields. At first sight, this seems easy to realize, but the mobilities in the two-dimensional electron gases are not high enough to allow for the observation of the IQHE at low magnetic fields. The present disorder is too detrimental for low electron densities.

For this reason, we advocate to explore alternative routes and it is natural to look for other systems displaying an IQHE. Graphene and related compounds are obvious candidates. Graphene is widely known for its special electronic properties [141, 142] and its extraordinary structure. It represents an isolated single sheet of graphite [143, 144] and as such realizes a two-dimensional allotrope of carbon. The low-energy band structure of graphene comprises two Dirac cones distinguished by different locations in the BZ. Thus, electrons near the Fermi level have a linear dispersion relation and therefore behave like massless relativistic particles. Theoretically, low-energy electrons are described by the Dirac equation [145, 146] where the speed of light is replaced by the Fermi velocity $v_\mathrm{F} \approx 10^6\,\mathrm{m/s}$ [147, 148]. Engineering this important parameter has been realized already by varying the substrate [147].

Subjecting graphene to a strong magnetic field at low temperatures leads to the formation of relativistic LLs. As a result, one can observe an unconventional IQHE [141, 149]. The Hall conductivity in graphene appears at half-integer values: $\sigma_{xy} = \pm 4e^2/h(|n|+1/2)$. The four-fold degeneracy given by valley and spin degeneracy yields the prefactor 4. Comparing $\sigma_{xy}(B)$ with the IQHE of a non-relativistic two-dimensional electron gas, the offset 1/2 can be attributed to the single LL with energy $E_0 = 0$ [149]. This LL is intrinsically half-filled so that one half contributes to the valence band and causes the half-integer conductivity. Due to cleaner samples and more precise measuring instruments the IQHE can be detected down to small external magnetic fields as low as $\approx 0.1\,\mathrm{T}$ owing to a very high electron mobility [150]. The unique properties of graphene open up many new possibilities for basic research and technical applications, especially in electronics [142, 151] and spintronics [152, 153].

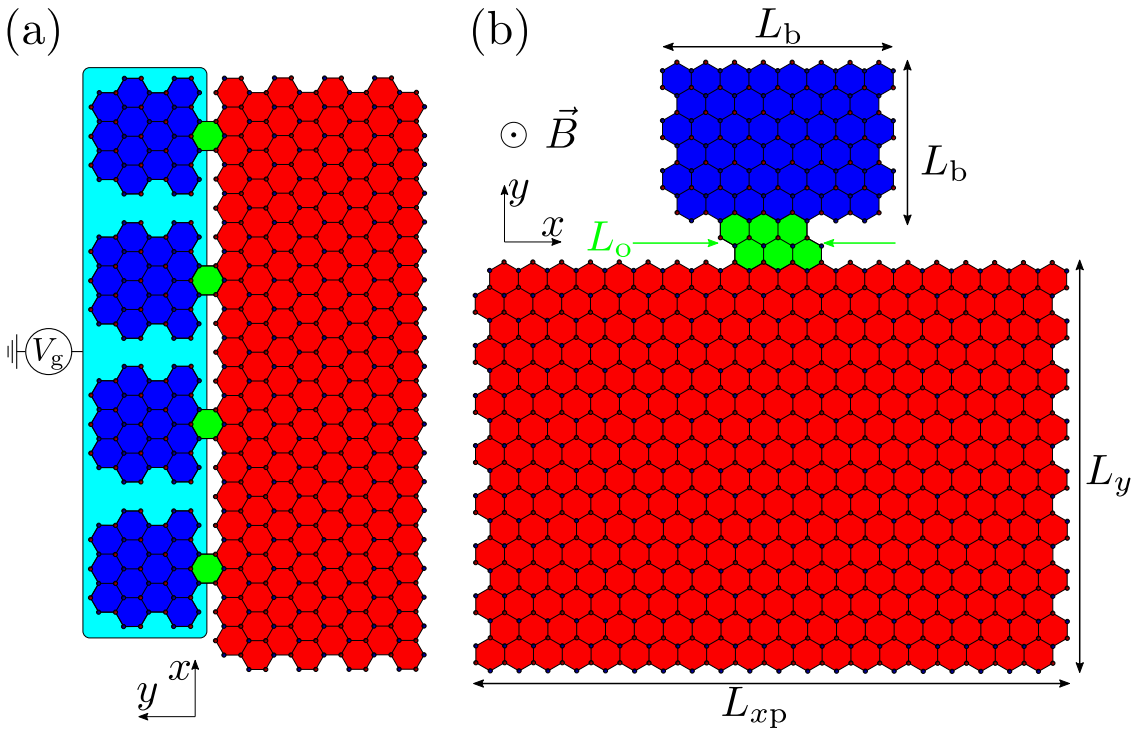

Figure 3.29: (a) Tailored strip of graphene proposed for tunable Fermi velocities. A magnetic field perpendicular to the sheet of graphene induces the IQHE. The sample has periodically aligned bays illustrated here by the zoom with 4 bays. The gate voltage V_g is applied only to the bays highlighted in blue. The red area corresponds to the bulk of the strip and the green area to the opening between the bulk and a bay. (b) Schematic sketch of a single unit cell with the notation for the linear dimensions of the bays and the strip. The total number N_x of unit cells determines the total length of the sample $L_x = N_x L_{x\mathrm{p}}$.

Our central proposal is to use graphene (or a related system) as IQHE system with accurately tailored edges in order to realize a tunable signal velocity v_F. In our view, there are several advantages of graphene as basis material over two-dimensional electron gases in semiconductors: (i) the high mobility allows one to reach the IQHE even at low magnetic fields (≈ 0.1T [150]); (ii) the possibilities to modify the edges in a reproducible and accurate way are larger; (iii) the energy separations between the lowest LLs ($n < 3$) are much larger due to the relativistic dispersion so that the IQHE in graphene can be observed for lower magnetic fields and higher temperatures [154]. So we expect that the tunability of the Fermi velocity v_F in the edge modes will be feasible in the near future.

The key challenge is to tailor the edges such that periodically arranged bays are weakly coupled to the chiral edge states, see Fig. 3.29(a). Due to the weak coupling controlled by the width of the opening of the bays the local modes in the bays hybridize with the dispersive edge modes. This hybridization leads to coupled modes with very little dispersion, hence very low Fermi velocity. By applying gate voltages to adjust the chemical potential or the local potential of the bays the Fermi velocity is tuned: choosing the external parameters such that the edge mode is in resonance with the local bay modes

reduces the Fermi velocity drastically.

The rest of this section is set up as follows. First, we introduce the model describing the edge states and the LLs of graphene. Next, we discuss the geometry of the studied samples. The main part shows the resulting dispersions and the tunability of the Fermi velocity in the edge states controlled by gate voltages as external control parameters. Finally, we conclude by summarizing and discussing possible applications.

3.3.2. Model and method

The electronic properties of graphene in the vicinity of the Fermi energy are well reproduced by a fermionic tight-binding model. Due to the negligible contribution of the spin degree of freedom and of interactions we consider spinless fermions in the Hamiltonian

$$\mathcal{H} = t \sum_{\langle i,j \rangle} c_i^\dagger c_j - V_\mathrm{g} \sum_{i \in \mathrm{bay}} c_i^\dagger c_i \quad . \tag{3.33}$$

We focus on zero temperature so that the chemical potential μ is identical to the Fermi energy ε_F. All states up to μ are occupied while the states above μ are empty. The relevant Fermi velocity is the derivative of the dispersion at the Fermi energy. A pair of NN is denoted by $\langle i, j \rangle$. The tight-binding parameters are the NN hopping $t = 2.8\,\mathrm{eV}$ and the lattice constant $a = 0.142\,\mathrm{nm}$ [148].

In order to obtain the quantum Hall state in graphene, we apply an external perpendicular magnetic field $\boldsymbol{B}$. This leads to the formation of LLs [155, 156] with energies at

$$E_n = \mathrm{sgn}(n)\sqrt{2e\hbar v_\mathrm{F}^2 B|n|} = \mathrm{sgn}(n)\sqrt{\frac{9t^2a^2}{2\ell_B^2}|n|} \quad . \tag{3.34}$$

The second equation stems from $\hbar v_\mathrm{F} = 3/2ta$ and the definition of the magnetic length $\ell_B = \sqrt{h/|eB|} \approx 25.65564/\sqrt{B}$ nm, where the value of the magnetic field B is inserted in units of Tesla. The non-linear spacing between the LLs results from the relativistic behavior of the electrons near the Dirac points. The magnetic length plays the same role as in the IQHE in the two-dimensional electron gas [108, 136]. It sets the scale for the diameter of the circular motion of the electrons due to the Lorentz force. In order for the decoration of the edges by bays to have an appreciable effect, the geometric dimensions of the bays must be of the order of this magnetic length.

The magnetic field B is included in the tight-binding model by the Peierls substitution attributing Aharonov–Bohm phases [157] to the hopping processes

$$t \to t \exp\left(\mathrm{i}e/\hbar \int_{r_1}^{r_2} \boldsymbol{A}\mathrm{d}\boldsymbol{r}\right) \quad , \tag{3.35}$$

where the start and the end site of the hopping process are denoted by r_1 and r_2, respectively. The evolution of the Dirac cones to rather flat LLs has been exhaustively studied and discussed by Delplace and Montambaux [136]. In order to keep translational invariance in the x-direction, see Fig. 3.29(a), we employ the Landau gauge $\boldsymbol{A} = B(-y, 0, 0)^\top$. Thus, the momentum k_x is a good quantum number in the calculations.

The numerical analysis is facilitated by a small system size, i.e., the number of sites in the extended unit cell, see Fig. 3.29(b), should be rather small so that the dimension of the resulting eigenvalue problem remains tractable. For the experimental realization,

however, it is advantageous to consider rather large extended unit cells. In the following, we briefly discuss these constraints, the employed numerical methods, and justify our choice of parameters.

The tight-binding Hamiltonian (3.33) comprises only on-site terms and NN hoppings. Hence, its very large matrix representing the Hamiltonian is mostly populated by zero entries and may therefore be encoded as a sparse matrix. The signal transmission is primarily determined by the properties at the Fermi energy ε_F. Undoped graphene is a semi-metal with $\varepsilon_\mathrm{F} = 0$. The states at higher energies hardly influence the low-energy dynamics. So we focus on the low LLs up to the third one, i.e., with $|n| < 4$. As before, the eigenvalue solver FEAST [130] is used to constrain the considered interval of the energy spectrum. Based on the calculated eigenenergies the Fermi velocity as derivative of the dispersion at the Fermi energy is straightforwardly approximated by the ratio of finite differences. We assume periodic boundary conditions in x-direction with 50 unit cells. This implies a sufficiently fine discretization of the BZ to identify energy crossings and avoided crossings.

The experimental constraints consist in the limitations in accurately tailoring the strips of graphene with the desired structure at the edges, i.e., with the periodic structure of bays, while maintaining a high mobility to realize the quantum Hall state. The bay pattern can be made by electron beam lithography [158, 159] or by anisotropic etching techniques [160]. It appears that creating bays of the size of 100 nm can be done without major problems. In our calculations we assume quadratic bays for simplicity. The precise shape of the bays does not matter for the qualitative results although it will have an influence on the quantitative details. The size of the bays and especially the length of the bay opening L_o to the bulk of the strip, see Fig. 3.29(b), are crucial for the dispersions of the modified edge states. To keep the example transparent, we aim at a small number of low-lying levels in the bays so that the relevant number of states which may hybridize can be easily tracked. This implies $L_\mathrm{b} \approx \ell_B$ and favors small magnetic fields (100 mT with $\ell_B \approx 81$ nm). These considerations define the framework for the numerical results in the next subsection.

3.3.3. Results

3.3.3.1. Dispersions, hybridized edge modes, and localization

In Fig. 3.30, three representative cases are depicted: uncoupled ($L_\mathrm{o} = 0\ell_B$), weakly coupled ($L_\mathrm{o} = 0.1\ell_B$), and moderately coupled ($L_\mathrm{o} = 0.5\ell_B$) bays. The magnetic field is set to $B = 0.25$ T which corresponds to a magnetic length of $\ell_B \approx 51$ nm. The definitions of the various lengths are displayed in Fig. 3.29(b). They are given by: $L_{x\mathrm{p}} = 3\ell_B \approx 153$ nm, $L_y = 6\ell_B \approx 306$ nm, $L_\mathrm{b} = 2\ell_B \approx 102$ nm and $L_\mathrm{o} = \{0, 0.1, 0.5\}\ \ell_B \approx \{0, 5, 26\}$ nm. The width of the strip L_y is chosen large enough so that the two counter-propagating edge states at the opposite edges do not overlap. This implies that both edges can be modified independently of each other. For clarity, we exploit this simplifying fact and modify only the upper edge while the lower edge remains a bare zigzag edge. The chosen bay size L_b should be experimentally realizable. The condition $L_{x\mathrm{p}} > L_\mathrm{b}$ ensures that the bays are separated from one another. Decreasing the distance between the bays by changing $L_{x\mathrm{p}}$ increases the impact on the dispersion of edge states due to the altered fraction of the decorated boundary to the total boundary. The three values for the opening L_o lead

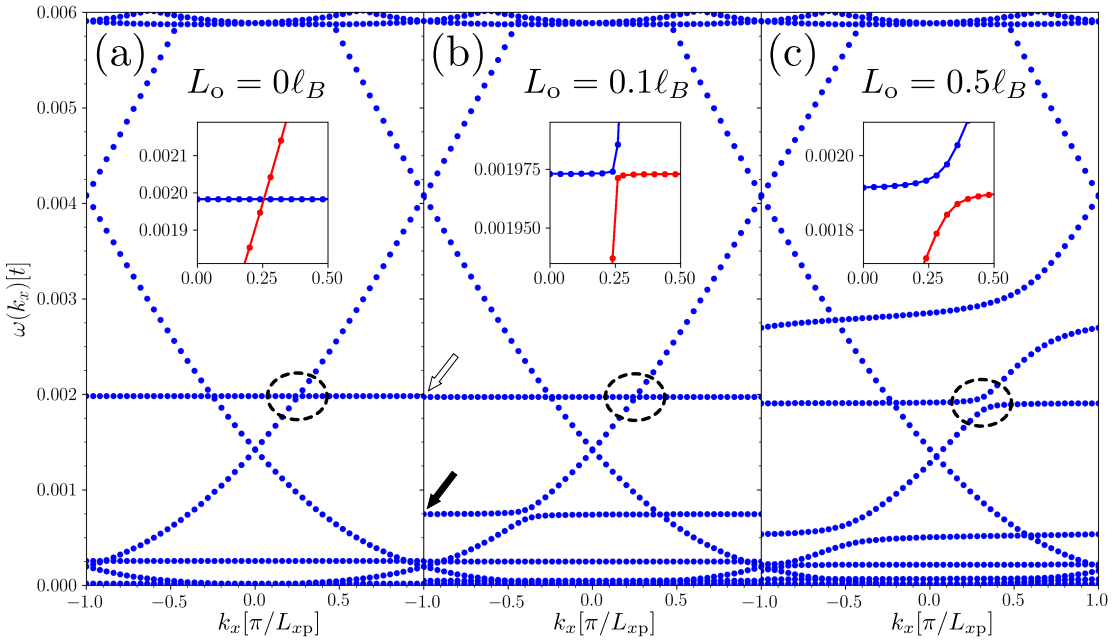

Figure 3.30: Dispersions of the lowest positive eigenenergies in graphene in the IQHE at $B = 0.25\,\mathrm{T}, L_{xp} = 3\ell_B \approx 153\,\mathrm{nm}$, $L_y = 6\ell_B \approx 306\,\mathrm{nm}$, $L_b = 2\ell_B \approx 102\,\mathrm{nm}$, and $L_o = \{0, 0.1, 0.5\}\ell_B \approx \{0, 5, 26\}$ nm. Panels (a)-(c) show the cases of uncoupled, weakly coupled, and moderately coupled bays, respectively. Crossings evolve into avoided crossings due to the hybridization of both modes. The dashed ellipses mark a location where this happens. The insets zoom into the evolution of the avoided crossings at $k_x = \pi/(4a)$, where the two dispersion branches are highlighted in blue and red.

to three different degrees of hybridization. As a rule of thumb, a wider opening corresponds to a larger hybridization. The effect is discernible in the dispersions in Fig. 3.30. For the sake of clarity, we display the dispersions up to the first LL so that only two counter-propagating edge states need to be taken into account.

Panel (a) in Fig. 3.30 shows the uncoupled case where the usual LLs and their related edge states are distinct from the local states. The LLs are essentially flat and turn upwards where their wave functions approach the edges of the strip. In contrast, the eigenstates of the modes in the bays are completely local, hence completely flat as a functions of the wave vector k_x. Thus, edge states and local modes show crossings, see inset of Fig. 3.30(a). Due to the extended unit cell comprising one bay, the edge states are backfolded into the reduced BZ scheme [44] as discussed in Sec. 3.2.3.2.2. Since the dispersion is symmetric with respect to the k_x-axis, we only show the positive eigenenergies. When the coupling of the bays to the bulk of the strip is switched on, i.e., $L_o \neq 0$, see panels (b) and (c) in Fig. 3.30, the edge states mix with the local states. We observe that the crossings turn into avoided crossings with the bay modes due to level repulsion, see for instance the encircled regions marked by dashed ellipses. Increasing the opening further and further results in a stronger and stronger level repulsion so that the former local modes become more and more dispersive.

Much to our surprise, in addition to the local states of the bays other almost local

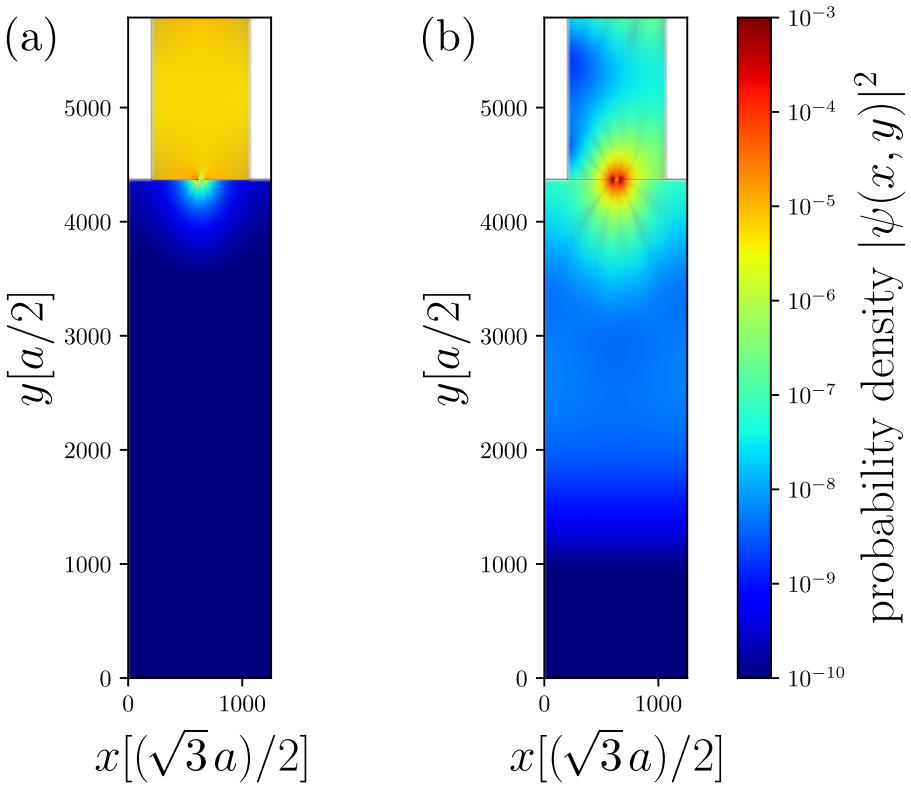

Figure 3.31: Probability densities $|\psi_n(x,y)|^2$ of two almost local eigenstates at $k_x = 0$. Clearly, these modes are localized in two different regions. Panel (a) shows the local mode stemming from the bay, whereas panel (b) shows the local mode localized in the opening of the bay. The corresponding eigenstates are indicated by open (mode from bay) and filled (mode in opening) arrows in panel (b) of Fig. 3.30. The parameters of field and geometry are $B = 0.25\,\mathrm{T}$, $L_{xp} = 3\ell_B \approx 153\,\mathrm{nm}$, $L_y = 6\ell_B \approx 306\,\mathrm{nm}$, $L_\mathrm{b} = 2\ell_B \approx 102\,\mathrm{nm}$, and $L_\mathrm{o} = 0.1\ell_B \approx 5\,\mathrm{nm}$.

states appear upon opening the bays. Such local states have not been observed in the IQHE of the non-relativistic two-dimensional electron gas [44]. Investigating the probability density of the eigenstates at $k_x = 0$ reveals the location of the unexpected modes. In Fig. 3.31 we display the probability densities of the two states with the energies highlighted by arrows in panel (b) of Fig. 3.30. Figure 3.31(a) clearly shows the density of the local state from the bays marked in Fig. 3.30(b) by the open arrow: it is almost entirely localized within the bay and leaks only weakly into the bulk of the strip. In contrast, Fig. 3.31(b) clearly shows a strong localization in the opening. This is the density of the additional local state marked in Fig. 3.30(b) by the filled arrow. Obviously, the opening gives rise to additional localization. Hence, the added sites in the opening, see green area of Fig. 3.29(b), contribute to the spectra similarly to the effect of the bay sites. Independent of the origin of the almost local states, both hybridize with the edge modes at the same energy. The additional state hybridizes more strongly as expected since it is localized in the opening very close to the bulk of the strip while the mode from within the bay leaks only weakly into the bulk. The hybridization of both local modes leads to a reduced Fermi velocity.

3.3.3.2. Fermi velocities for signal transmission

In order to tune the Fermi velocity of the edge state at the upper edge of the strip of graphene we have to change the derivative of its dispersion at the Fermi level. To do so, two ways suggest themselves in particular. The most transparent one is to change the Fermi energy, i.e., the chemical potential, such that the Fermi level lies in a rather flat region of the edge state dispersion. This can be achieved by a gate close to the total strip of graphene [141]. Alternatively, one may conceive a control of the energy level of the bays alone. This can be achieved by a voltage applied to an appropriate gate close to the edge of the strip, see Fig. 3.29(a). Undoubtedly, other ways of tuning can be devised as well. Below we present results for both approaches to show that tuning of the Fermi velocity is possible.

Figure 3.32 depicts the Fermi velocity as a function of the chemical potential. Panel (a) and (b) correspond to the case of weakly and moderately coupled bays, respectively, of which the dispersions are displayed in Fig. 3.30. The Fermi velocity in the weakly coupled case shows three deep dips. The two extremely narrow and steep dips can be attributed to the hybridization with two local levels from the isolated bays. The energetic position of these local levels is indicated by vertical red lines in the two panels. The closeness of the steep dips to these lines emphasizes our interpretation of their physical origin. The slight shifts of the dips relative to the red lines result from the energy shift due to level repulsion. This is supported by the fact that the shift is larger for panel (b) which refers to bays with a wider opening and hence stronger level repulsion. The broader dips (one in panel (a) and two in panel (b)) are related to the additional local states localized in the openings, see Fig. 3.31(b). The fact that these dips are broader is explained by the vicinity of these states to the bulk of the strips implying a stronger hybridization with the edge mode.

By tuning μ into these dips, the Fermi velocity can be reduced by orders of magnitude. In particular for narrow bay openings a strong reduction can be achieved. For instance, v_F in panel (a) of Fig. 3.32 at $\mu \approx 2\,\mathrm{meV}$ is reduced by a factor of ≈ 65000 from its value without tailored edges, i.e., without bays, see green curve in Fig. 3.32. Increasing the bay opening leads to a broadening and a shift of the dips, see Fig. 3.32(b). Thus for moderately coupled case, v_F at $\mu \approx 8\,\mathrm{meV}$ is reduced by a factor of ≈ 20. Furthermore, a wider opening possesses more low-lying energy modes so that the number of dips is increased. If the chemical potential is out-of-resonance with local modes, the reduction of the Fermi velocity is insignificant. This is particularly true for narrow openings where there is no significant difference between the green and the blue line out-of-resonance.

Tuning the bay potential V_g leads to similar results even though changing this gate voltage does not simply shift the local modes relative to the bulk modes. Still, significant changes of the Fermi velocity can be realized as illustrated in Fig. 3.33 for which we assume a generic Fermi energy $\varepsilon_\mathrm{F} = 0.0005t = 1.4\,\mathrm{meV}$ in the regime of doped graphene. The finite value of the Fermi energy is necessary to be in the dispersive regime of the edge states. In order to realize a substantial reduction of the Fermi velocity, the local states must be brought into resonance with the edge states. This tuning of the bay potential results in similar dips of the Fermi velocity as the tuning of the chemical potential μ. Negative values of V_g lift the bay spectrum up in energy so that they come into resonance with the edge state, resulting in a steep dip.

In contrast, a positive gate voltage V_g decreases the energy of the additional local

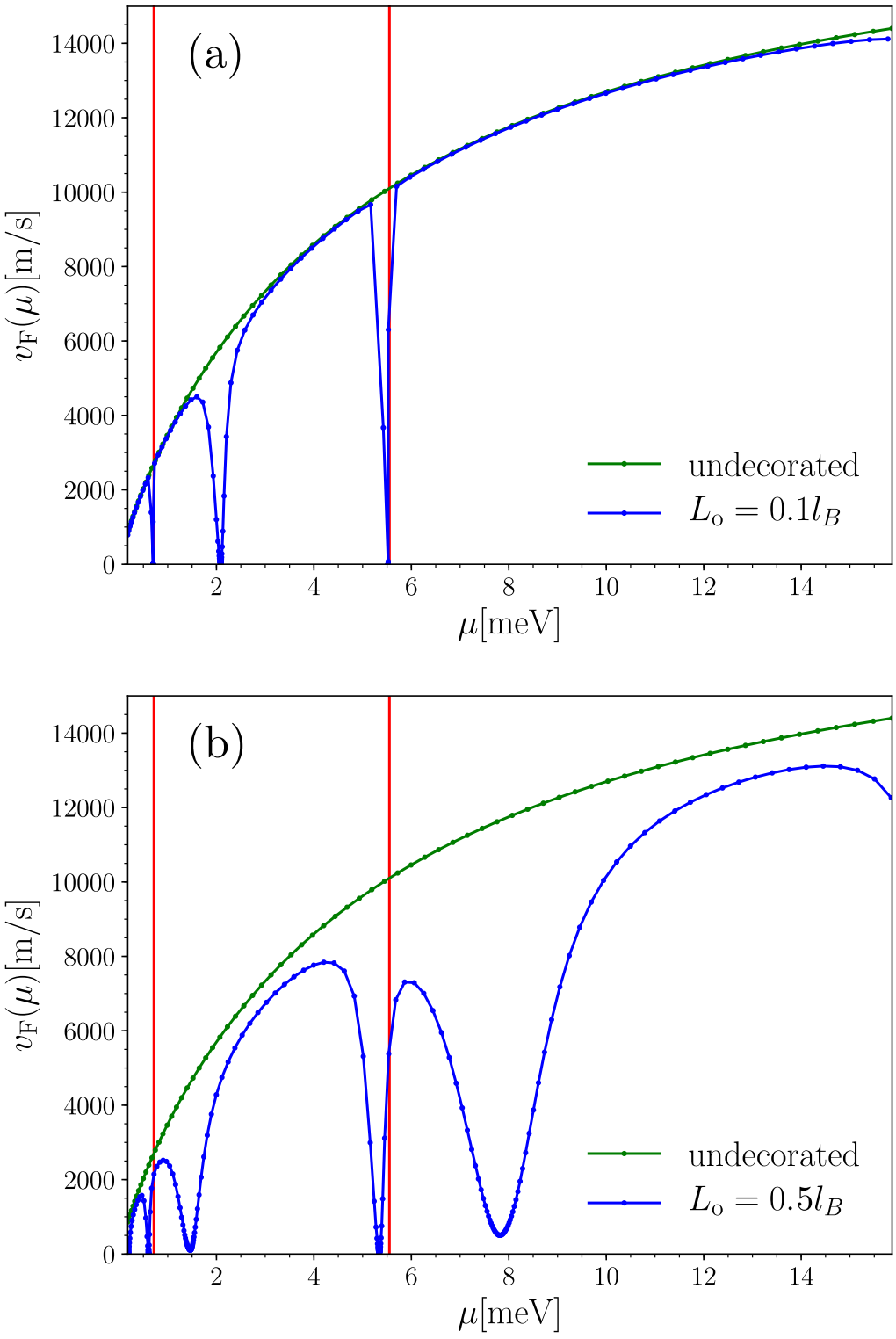

Figure 3.32: Fermi velocity v_{F} of the right-moving edge states localized at the upper edge as a function of the chemical potential μ equivalent to the Fermi energy. Panels (a) and (b) show the weakly and moderately coupled cases $L_{\mathrm{o}} = \{0.1, 0.5\}\ell_B \approx \{5, 26\}$nm, respectively. The other parameters are $B = 0.25\,\mathrm{T}, L_{x\mathrm{p}} = 3\ell_B \approx 153\,\mathrm{nm}$, $L_y = 6\ell_B \approx 306\,\mathrm{nm}$, $L_{\mathrm{b}} = 2\ell_B \approx 102\,\mathrm{nm}$. The red lines are guides to the eye to link the resonance estimated from the uncoupled bay spectrum shown in Fig. 3.30(a).

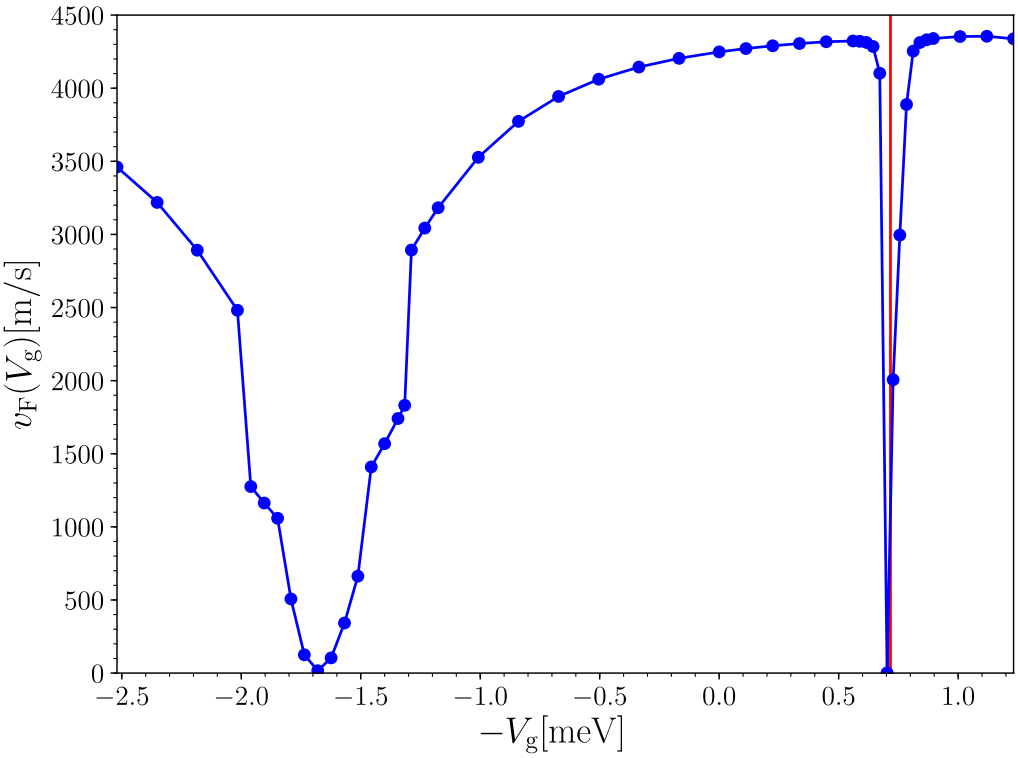

Figure 3.33: Fermi velocity v_{F} of the right-moving edge states as a function of the gate voltage V_{g} changing only the energy offset of the bays, see Fig. 3.29(a). The parameters are $B = 0.25\,\mathrm{T}, L_{x\mathrm{p}} = 3\ell_B \approx 153\,\mathrm{nm}$, $L_y = 6\ell_B \approx 306\,\mathrm{nm}$, $L_{\mathrm{b}} = 2\ell_B \approx 102\,\mathrm{nm}$, and $L_{\mathrm{o}} = 0.1\ell_B \approx 5\,\mathrm{nm}$. The ragged dip at about $V_{\mathrm{g}} = -1.7\mathrm{meV}$ results from the discretization of the BZ with 50 points. A finer mesh would lead to a smoother curve, but is computationally demanding. The red lines are guides to the eye to link the resonance estimated from the uncoupled bay spectrum shown in Fig. 3.30(a).

mode in the opening. The ensuing resonance leads to a broader dip due to the larger hybridization of the opening mode to the edge mode. Note that larger absolute values of V_{g} are needed to reach the resonance compared to what can be estimated from the dispersion. This fact can be explained by the level repulsion from the bulk states which are mixed in. Thus, both dips are shifted relative to the energy differences in the uncoupled dispersion, see panel (a) in Fig. 3.30. We conclude that tuning the bay potential is also a suitable knob to control the Fermi velocity. In summary, tuning both gate voltages leads to resonances with local modes so that substantial reductions of the velocity of signal transmission are achieved.

3.3.4. Conclusion

The above results clearly show that substantial tuning of the Fermi velocity in graphene with tailored edges is possible. This can be used to construct tunable delay lines for charge signals: by controlling external parameters such as gate voltages, the temporal delay can be tuned at will by choosing an appropriate velocity of signal transmission through the sample. This may help to control and to switch properties of nanoscale

devices including devices for quantum information processes. The delayed signal itself does not need to have quantum character, but the tuned delay can help to deliver control precisely at suitable time instants.

Another promising idea in the same spirit is to construct interferometers in which two signals are superposed which have propagated along different pathways. One of these pathways contains the graphene sheet with tunable signal velocity. By adjusting the Fermi velocity the delay in this path can be altered such that destructive or constructive interference takes place. If the signal along the other pathway is propagating through a sample of an unknown compound or an unknown device its transmission properties can be investigated. These two suggestions are meant to exemplify promising applications of tunable signal velocities. We emphasize that the tuning can be done very fast on the time scales on which the gate voltages can be changed.

To obtain an idea of the order of magnitude of the delays we assume the conditions used for Fig. 3.32(b), but with only $N_x = 20$. Note that samples with less units are also eligible. However, 20 units maintain a certain periodicity and thus are related to our framework with a discretized BZ. For simplicity, estimated values are used. The sample length is $L_x \approx 3\,\mu$m and we consider the broader dip because its less susceptible to imperfections. For $\mu = 8\,$meV the undecorated strip of graphene displays a velocity $v_\mathrm{F} = 12\,000\,$m/s. It will be reduced by a factor of 20 down to $v_\mathrm{F} = 600\,$m/s in the minimum of the dip. The time required by a signal to propagate along the edge is delayed from 0.25 ns to 5 ns. This change of transmission time is readily detectable.

We are aware that the calculations presented in this thesis assume idealized conditions. For instance, zero temperature and small samples without imperfections or disorder. So further research is called for to address these points as we did already for the non-relativistic IQHE, see Sec. 3.1.4. Nevertheless, the origin of the predicted effect is clearly elucidated and does not rely on subtleties of the model, for instance the shape of the bays does not matter as long as the bays host local modes. With state-of-the-art techniques, the IQHE can be detected in graphene samples which are not smaller than $3 \times 3\,\mu\mathrm{m}^2$. For smaller samples, imperfections and disorder spoil the Hall states. As long as the IQHE can be observed and the properties of at least one of the edges can be externally controlled, tuning of the signal velocity will be within reach.

The key message is that graphene represents a promising material to realize the IQHE with externally tunable dispersions of the edge states on the basis of today's technology. Tailoring of the edges is an exacting prerequisite. These results should trigger further studies, including experimental ones, paving the way towards tunable signal velocities. As an outlook we point out that further work on the influence of imperfections, disorder, and the presence of the spin degree of freedom are in order. The latter opens up particular applications in spintronics.

4. Topological properties of $BiCu_2PO_6$

Parts of this chapter are submitted for publication [161]. Leanna Müller and I used a directly evaluated enhanced perturbative continuous unitary transformation (deepCUT) program, which has been developed by Holger Krull and Nils A. Drescher, in order to describe $BiCu_2PO_6$. Leanna Müller contributed to the manuscript and to the interpretation of the results. I wrote the main part of the submitted manuscript. Furthermore, I created all figures, dispersions and calculated the shown data.

4.1. General context

Recently, quantum magnets received much attention, in particular magnetically ordered systems [162–167]. But also a disordered valence bond crystal in a dimerized quantum magnet displayed topologically non-trivial behavior [99, 168, 169]. Still, the number of established compounds displaying topologically non-trivial magnetic excitations is extremely limited and therefore novel topological compounds are of great interest. In particular, no candidate for a magnetic system displaying a quantized Zak phase in one dimension has been put forward yet.

Hence, the first of two key goals of the present chapter is to establish the existence of such a non-trivial topological phase in $BiCu_2PO_6$, which represents a quasi-1D quantum antiferromagnet [170–172]. The second goal is a general one reaching beyond the particular material $BiCu_2PO_6$ since it concerns the existence of localized edge states. Often, the bulk-boundary correspondence is interpreted such that topological non-trivial invariants imply the existence of localized modes. We show that for the localization of edge modes generically the existence of an *indirect* gap, i.e., a finite energy difference independent of momentum, is necessary. In contrast, the existence of a topological phase only requires the bands to be separated, i.e. the existence of a *direct* gap at each momentum is sufficient.

Since $BiCu_2PO_6$ is essentially a one-dimensional system, the Berry phase qualifying for a topological invariant is the Zak phase Ω [37]. It can take any value between 0 and 2π ($\Omega \in [0, 2\pi)$) because it measures the scalar product $\exp(\mathrm{i}\Omega) = \langle 2|1\rangle$ between a quantum state $|1\rangle$ at wave vector 0 and the quantum state $|2\rangle$ taken to wave vector 2π by parallel transport. For inversion symmetric systems the direction of parallel transport does not matter so that $\langle 1|2\rangle = \langle 2|1\rangle$ holds and Ω can be either 0 or π. Importantly, the Zak phase has been related to edge modes in strips of graphene [96]. It has been measured in systems of ultracold atoms in 1D optical lattices [87] and in twisted photons [173]. A related, but different topological invariant is the winding number, which is discussed in Sec. 4.5.

4.2. Structure and model of $BiCu_2PO_6$

The crystal structure of $BiCu_2PO_6$ is displayed in Fig. 4.1. The orthorhombic unit cell is classified by the Pnma space group with the lattice parameters $x = 11.776\,\text{Å}$, $y = 5.1776\,\text{Å}$, $z = 7.7903\,\text{Å}$. From the crystal structure we can see with the naked eye the zigzag ladder structure formed by the copper ions which host spin momenta $S = 1/2$. The magnetic properties are primarily described by the copper ions. There are two types of copper ions Cu_A and Cu_B alternating along the ladders due to differing positions relative to the surrounding bismuth ions [174]. If this inequality is taken into account, the mirror-symmetry along the ladders is broken. The absence of an inversion symmetry about the midpoint between the copper sites allows the presence of anisotropic couplings, see below.

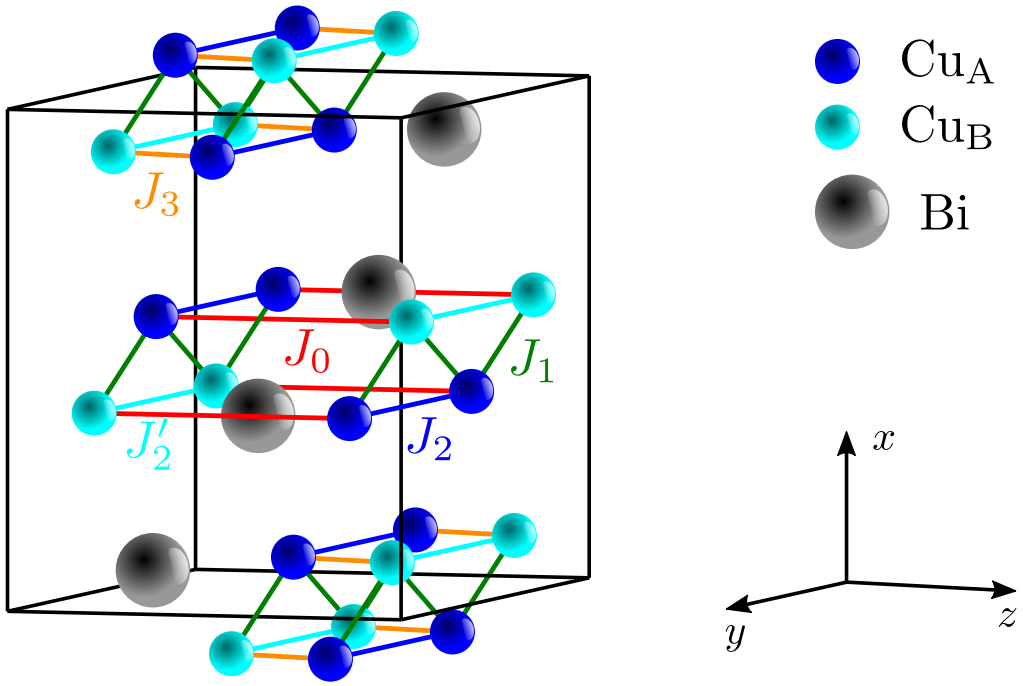

Figure 4.1: Crystal structure of $BiCu_2PO_6$. The unit cell is shown by black lines and has an orthorhombic structure type. The inequivalent copper ions Cu_A and Cu_B form coupled spin ladders. For clarity the phosphorus and oxygen ions are neglected.

The compound $BiCu_2PO_6$ is a low-dimensional quantum antiferromagnet of which the ground state is a valence bond solid. The valence bond solid and the quantum spin liquid are paramagnetic ground states. $BiCu_2PO_6$ does not show magnetic order, but it has a finite spin gap, a finite spin-spin correlation length and elementary spin-1 excitations which are clear pieces of evidence for a valence bond solid states. The spins are coupled antiferromagnetically in dimers interacting via further couplings [170–172, 174, 175]. All couplings are considered to be antiferromagnetic. The coupled dimers form a tube-like, frustrated spin-1/2 Heisenberg ladder as shown in Fig. 4.2(a). The 1D spin ladders form stacked layers with weak, but still measurable interladder couplings in each layer, see Fig. 4.2(b). The couplings between layers are negligible [175]. The dominating couplings are those along the spin ladders. The large atomic number ($Z = 83$) of bismuth

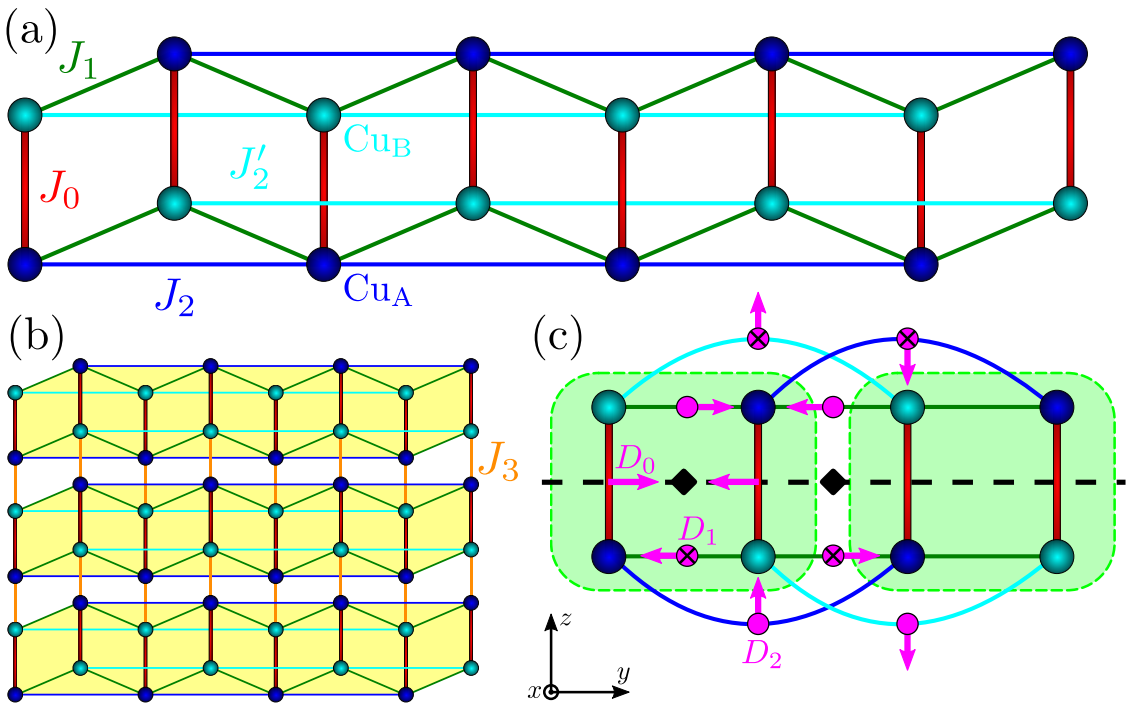

Figure 4.2: Spin model of $BiCu_2PO_6$. (a) The tube-like structure realizes 1D frustrated spin ladders with two copper sites Cu_A and Cu_B. The different bonds represent different isotropic Heisenberg couplings. In the case of the minimal model the difference of copper sites is neglected so that $J_2 = J_2'$ holds. (b) Interladder isotropic Heisenberg coupling J_3 between adjacent spin ladders forming a weakly coupled two-dimensional system. (c) Dzyaloshinskii-Moriya couplings of $BiCu_2PO_6$. Short violet arrows display the orientation of the DM vectors in $\boldsymbol{D}_{ij}(\boldsymbol{S}_i \times \boldsymbol{S}_j)$ where the sites i and j are primarily ordered with ascending y-coordinate and secondarily along z-coordinate; their length is not to scale. Inversion symmetry exists about the centers (black diamonds) of the plaquettes; reflection about the black dashed center line is a symmetry of the isolated, isotropic spin ladder.

induces a strong SOC so that the resulting magnetic exchange coupling is anisotropic with an important antisymmetric Dzyaloshinskii–Moriya (DM) coupling [176] and concomitant symmetric coupling Γ [177, 178]. The antisymmetric DM coupling results in first order from the SOC, whereas the symmetric coupling is of second order. Note that bismuth does not host a spin, but it is part of the superexchange path between the copper ions.

The Hamilton operator reads

$$\mathcal{H} = \sum_{i<j} (J_{ij} \boldsymbol{S}_i \cdot \boldsymbol{S}_j + \boldsymbol{D}_{ij} \cdot (\boldsymbol{S}_i \times \boldsymbol{S}_j) + \sum_{\alpha,\beta} \Gamma_{ij}^{\alpha\beta} S_i^{\alpha} S_j^{\beta}) \quad , \tag{4.1}$$

where bold symbols represent vectors and $\boldsymbol{S}$ denotes the spin vector operator. The couplings J_{ij} are equal to J_0, J_1, J_2, and J_3 as shown in Fig. 4.2(a). Experimentally, it is confirmed that $J_0 \gg J_3$ so that the spins coupled with J_0 form dimers. Hence, J_0 is the dominating intradimer coupling while J_3 describes the interladder coupling. The intraladder couplings J_1 and J_2 or J_2' are the NN and NNN interdimer couplings,

respectively. The J_1 couplings from a zigzag leg while the J_2 couplings form straight legs. The combination of J_1, J_2 and J_2' realizes a triangular structure on the lattice which is responsible for the frustration in the antiferromagnetic spin system. The difference between J_2 and J_2' stems from the coupling between the inequivalent copper ions. Further possible Heisenberg interactions of equivalent copper ions between neighboring legs J_5 and J_6 were also taken into account, where we assume the coupling strengths J_5 and J_6 from first-principles density-functional theory calculations [179]. However the J_5 and J_6 couplings are neglected in the following due to the vanishingly small contribution.

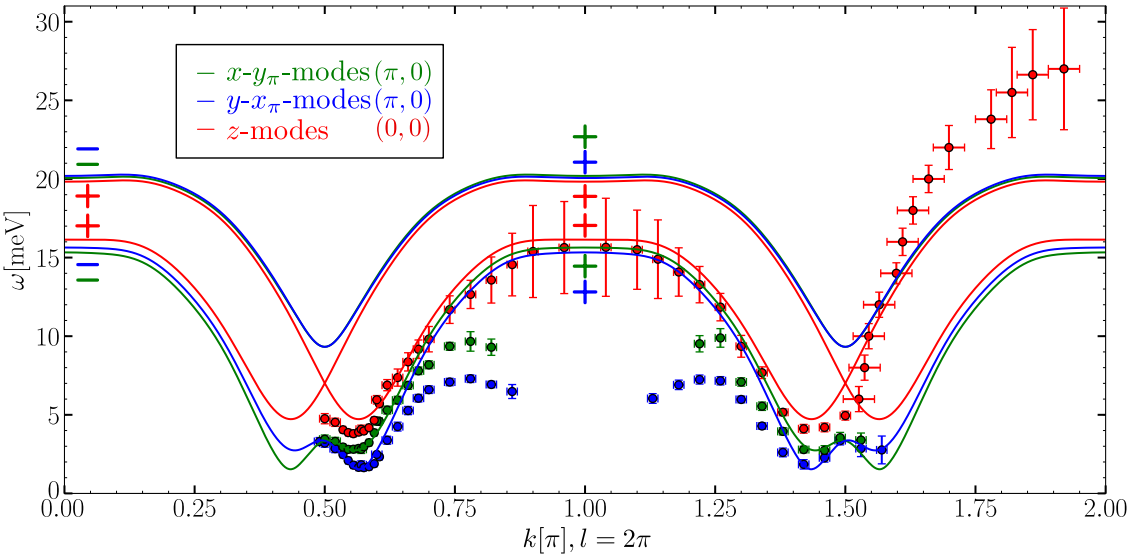

Figure 4.3: Best fit of the one-triplon dispersions obtained for $J_0 = 9.4\,\text{meV}$, $J_3 = 1.5\,\text{meV}$, $J_1 = 1.2J_0$, $J_2 = 1.09J_0$, $D_1^x = 0.58J_0$, $D_1^y = 0.73J_0$, $D_{2,a}^z = -0.02J_0$, and $D_3^y = 0.02J_0$. Components not listed are zero. The symbols with error bars show the inelastic neutron scattering data [170]. The legend denotes the Zak phases $(\pi, 0)$ and $(0, 0)$ of the modes in k- and l-directions, see main text. The plus and minus signs at the time-reversal invariant wave numbers 0 and π indicate the parities of the modes with respect to the inversion symmetry.

The elementary excitations of the spin isotropic ladder are dispersive triplons, i.e., hardcore $S = 1$ quasi-particles [180] with the bilinear Hamiltonian

$$\mathcal{H}^{\text{iso. ladder}} = \sum_{k,\alpha} \omega_0(k) t_k^{\alpha,\dagger} t_k^{\alpha} \quad , \tag{4.2}$$

where $t_k^{\alpha,\dagger}$ creates and t_k^{α} annihilates a triplon with wave vector k and flavor $\alpha \in \{x, y, z\}$, respectively [181]. The dispersion $\omega_0(k)$ is determined systematically by continuous unitary transformations in real space [182] and Fourier transformation. The basic concept of continuous unitary transformations (CUTs) is to simplify a complex initial Hamiltonian by applying continuous unitary transformations, i.e., gradual basis changes [183]. This goal is achieved by setting up a set of differential flow equations with renormalizing properties for running coupling constants. We use this approach to systematically derive Hamiltonians expressed in terms of creation and annihilation operators of elementary excitations, here triplons.

This isotropic model leads to a six-fold degenerate triplon spectrum with six modes due to spin degeneracy and two dimers per unit cell which is at odds with experiment. This discrepancy with the experimental data emphasizes the importance of the DM terms breaking the spin isotropy. In order to include spin anisotropic terms and the interladder terms we transform not only the isotropic Hamiltonian from the representation by spin operators to the representation by triplon operators, but also the spin operators [171]. This allows us to express also the remaining parts of the Hamiltonian, the DM couplings and the interladder couplings, in terms of triplon operators. The resulting expressions are normal-ordered and the bilinear terms are kept yielding a mean-field description of the elementary magnetic excitations of $BiCu_2PO_6$. A discussion of trilinear and quadrilinear interaction terms is provided below.

The anisotropic spin couplings are vital for lifting the spin degeneracy of the triplon modes [170–172]. It is established that the antisymmetric DM and the symmetric Γ coupling have to be considered together [177, 178]. In leading order we use

$$\Gamma_{ij}^{\alpha\beta} = \frac{D_{ij}^{\alpha} D_{ij}^{\beta}}{2J_{ij}} - \frac{\delta^{\alpha\beta}(\boldsymbol{D}_{ij})^2}{6J_{ij}} \quad , \tag{4.3}$$

which results from deriving the anisotropic exchange from a Hubbard model with SOC. The parametrization is chosen such that $\Gamma_{ij}^{\alpha\beta}$ does not comprise an isotropic component because it is included in the Heisenberg coupling J_{ij}. The possible directions of the DM vectors are constrained by the point group symmetries of the lattice, see App. A. The symmetry of $BiCu_2PO_6$ is higher if we neglect the difference between the two copper sites, see Fig. 4.2, dealing with a slightly simplified model which we call the minimal model [171]. In this minimal model, the DM vectors can have components as shown in Fig. 4.2(c) compatible with the Moriya symmetry rules [176]. If the difference between the Cu sites is taken into account, the symmetry is reduced [174]; the possible DM vectors are given in App. A. But the additionally possible DM components are rather small because the copper sites are not very different electronically. Hence, we focus on the minimal model in the following.

The complete bilinear triplon Hamiltonian in momentum space is represented in a generalized Nambu notation (up to unimportant constants) as

$$\mathcal{H} = \frac{1}{2} \sum_{k,l} \boldsymbol{a}_{k,l}^{\dagger} H_{k,l} \boldsymbol{a}_{k,l} \quad , \tag{4.4}$$

where the wave number k corresponds to the direction along the ladders while l corresponds to the perpendicular direction, see Fig. 4.2(b). For brevity of notation, we combined the bosonic triplon operators into a column vector

$$\boldsymbol{a}_{k,l} = (\boldsymbol{t}_{k,l}^{\top}, \boldsymbol{t}_{k+\pi,l}^{\top}, \boldsymbol{t}_{-k,-l}^{\dagger}, \boldsymbol{t}_{-k-\pi,-l}^{\dagger})^{\top} \tag{4.5}$$

with twelve components. Each bold face symbol stands for the three-dimensional vector $\boldsymbol{t}_{k,l} = (t_{k,l}^x, t_{k,l}^y, t_{k,l}^z)^{\top}$ and $\boldsymbol{t}_{k,l}^{\dagger} = (t_{k,l}^{x,\dagger}, t_{k,l}^{y,\dagger}, t_{k,l}^{z,\dagger})$. In this way, the Hamiltonian is described by a Hermitian 12×12 matrix

$$H_{k,l} = \begin{bmatrix} A(k,l) & B(k,l) \\ B^{\dagger}(k,l) & A^{\top}(-k,-l) \end{bmatrix} \tag{4.6}$$

where the matrices $A(k,l) = A^\dagger(k,l)$ and $B(k,l) = B^\top(-k,-l)$ are 6×6 matrices. Note that $\boldsymbol{a}_{k,l}$ and thus $H_{k,l}$ are modified relative to Ref. [184] in order to consider momentum conservation. Further simplifications are discussed in App. B.

The eigenenergies and eigenmodes are obtained by a bosonic Bogoliubov transformation [184] leading to $\mathcal{H} = \sum_{n,k,l} \omega_n(k,l) b^\dagger_{n,k,l} b_{n,k,l}$ where the index n labels the six different modes at a given wave vector (k,l). The Bogoliubov transformation is based on usual bosons without the hardcore property. This is justified because the essential hardcore effects are considered in the transformation of the isolated spin ladder [171, 182]. The one-triplon dispersions $\omega_n(k,l)$ are used to fit the inelastic neutron scattering (INS) data by adjusting the couplings (J_0, D^α_{ij}) keeping the ratios $J_1/J_0 = 1.2$, $J_2/J_1 = 0.9$ and $J_3/J_0 = 0.16$ fixed, because these ratios are determined by the experimentally determined wave number k, where the gap Δ occurs and by the ratio between the measured lower maximum $\omega(k = \pi, l = 2\pi)$ and the gap Δ of the z-mode [171].

The dispersions in k-direction in Fig. 4.3 agree very well with the experimental data at low energies. There are discrepancies at higher energies, in particular the downturns of the modes given by the blue and green symbols. They can be explained qualitatively by hybridization of the single modes with two-triplon states, i.e., by decay processes [170] which would appear as trilinear triplon terms in the Hamiltonian. This appears to be a serious caveat, but the description on the one-particle level in the minimal models can be justified by the following arguments: (i) The energetically low-lying bosonic modes are protected by the finite energy gap so that perturbation theory is valid. Hence any coupling not considered in the single-particle description will only distort the states continuously so that discrete topological invariants will not be altered. (ii) The topological twist causing the finite Zak phase computed below stems essentially from the region in k-space, namely the vicinity of $k = \pi/2$ and $3\pi/2$, see Sec. 4.4, where the single bosonic modes are energetically low-lying, well-defined and provide a reliable description of the experimental data without trilinear or quadrilinear terms in the Hamiltonian. Hence, the calculation of the Zak phase within the minimal, bilinear model stands on a firm basis. In addition, it is computed in two ways, namely by direct computation of the phases of quantum states and by consideration of the parity of states with respect to inversion, see next section.

4.3. Berry phases in bosonic systems

To assess the topological properties of bosonic bands the Berry connection needs to be generalized to bosonic systems. Even for non-interacting bosons this is not trivial. While for fermions the scalar product of quantum states can be naturally transferred to fermionic operators because a fermionic Bogoliubov transformation is unitary, this does not hold for bosonic operators and transformations. For bosonic systems a symplectic product $\langle\langle \boldsymbol{k}_1, n_1 | \, \boldsymbol{k}_2, n_2 \rangle\rangle$ is required. We define the generalized ket by the complex prefactors u and v (see App. B) of the normal bosonic operators

$$|\boldsymbol{k}, n\rangle\rangle := (\boldsymbol{u}^\top_{n,k,l}, \tilde{\boldsymbol{u}}^\top_{n,k,l}, \boldsymbol{v}^\top_{n,k,l}, \tilde{\boldsymbol{v}}^\top_{n,k,l})^\top \quad , \tag{4.7}$$

where each bold symbol corresponds to a 3D vector such as $\boldsymbol{u} = (u^x, u^y, u^z)^\top$. Using the generalized notation, we can then define the symplectic product (see App. C for more

details) for a bosonic system by

$$\begin{aligned}&\langle\langle \boldsymbol{k}_1, n_1 |\, \boldsymbol{k}_2, n_2\rangle\rangle \\ :=\ & \boldsymbol{u}^\dagger_{n_1,k_1,l_1}\boldsymbol{u}_{n_2,k_2,l_2} + \tilde{\boldsymbol{u}}^\dagger_{n_1,k_1,l_1}\tilde{\boldsymbol{u}}_{n_2,k_2,l_2} - \boldsymbol{v}^\dagger_{n_1,k_1,l_1}\boldsymbol{v}_{n_2,k_2,l_2} - \tilde{\boldsymbol{v}}^\dagger_{n_1,k_1,l_1}\tilde{\boldsymbol{v}}_{n_2,k_2,l_2} \quad . \end{aligned} \tag{4.8}$$

Based on this symplectic product, the standard relations [27] for the Berry connection

$$\boldsymbol{\mathcal{A}}_{n,\mathrm{sym}}(\boldsymbol{k}) = \mathrm{i}\langle\langle \boldsymbol{k}, n |\, \nabla_{\boldsymbol{k}}\, |\boldsymbol{k}, n\rangle\rangle \tag{4.9}$$

and the Berry phase

$$\gamma_n = \oint \boldsymbol{\mathcal{A}}_n(\boldsymbol{k})\mathrm{d}\boldsymbol{k} = \mathrm{i}\oint \langle\langle \boldsymbol{k}, n |\, \nabla_{\boldsymbol{k}}\, |\boldsymbol{k}, n\rangle\rangle \mathrm{d}\boldsymbol{k} \tag{4.10}$$

can be kept. If the closed path in the above equation encompasses the BZ, $\Omega_n/(2\pi)$ defines the Chern number. The Chern number in $BiCu_2PO_6$ remains trivially zero even if magnetic fields are included because the material is essentially one-dimensional.

The characteristic Berry phase for one-dimensional systems is the Zak phase [37, 96]. It is computed in one direction in the periodic BZ [37]. Due to the periodicity in k- and l-space the closed loops $k \to k + 2\pi$ or $l \to l + 2\pi$ both allow us to define Berry phases. They can be averaged over the respective other wave vector yielding the vector [185]

$$\boldsymbol{P} = \frac{1}{2\pi}\int \boldsymbol{\mathcal{A}}_{n,\mathrm{sym}}\,\mathrm{d}k\,\mathrm{d}l \quad . \tag{4.11}$$

Its value for each triplon band is given in the legend of Fig. 4.3. The z-mode remains topologically trivial $\boldsymbol{P} = (0, 0)$ while the coupled x-y_π- and x_π-y-modes display the Zak phase $\boldsymbol{P} = (\pi, 0)$, for computational technicalities see App. D. The numerical calculations result a non-trivial phase in the ladder direction, but not perpendicular to it.

One may worry that the dispersion branches of x-y_π- and y-x_π-modes are not separated, and even intersect at $k = \pi/2$ and $k = 3\pi/2$. These intersections are clear crossings so that one can track the states easily by following the differentiably evolving dispersions. As a result, the Zak phases are well-defined. In addition, we studied what happens if a small perturbation, here a magnetic field, lifts the degeneracy at the intersections and converts the crossings to anti-crossings. But since the modes all have the same Zak phase this braiding is trivial and does not make a difference. Thus the Zak phases are robust and remain unaltered.

The l-dependence in the investigated minimal model mainly enters via the isotropic term $J_3\cos(l)$, which does not alter the eigenmodes since this term is proportional to unity. The small D_3^y and the even smaller $\Gamma_3^{\alpha\alpha}$ barely have an impact on the dispersion and on the eigenmodes so that they do not influence the topology. We checked that even larger values of D_3^y and $\Gamma_3^{\alpha\alpha}$ do not induce a non-trivial Zak phase in l-direction or a finite Chern number. So they not influence the topology. The Zak phase is constant for all values of l, being either zero or π. It is pinned to these particular values in $BiCu_2PO_6$ because the system is inversion symmetric, see Fig. 4.2(c). The transformation operator of inversion is given by the matrix $\mathcal{I} = \mathrm{diag}(1, 1, 1, -1, -1, -1, 1, 1, 1, -1, -1, -1)$ with $\mathcal{I}^2 = \mathbb{1}$, which transforms $\mathcal{I}H_{k,l}\mathcal{I} = H_{-k,-l}$ and hence ensures the quantization of the Zak phase as multiples of π.

We stress that the Zak phase is robust, i.e., small changes of the model do not alter it. For instance, it remains the same if we pass from the minimal model to the extended model accounting for different copper sites. This can be done by including couplings which are allowed for different copper sites. Similarly, one may reduce the values of D_1^x and D_1^y even by a factor of 2, cf. Ref. [170], and still obtains the same Zak phase. Moreover, the substantial twist leading to the non-trivial Zak phase stems from the vicinity of the minima of the dispersions, i.e., the low-lying modes matter most. It is crucial that the DM components $D_1^x \neq D_1^y$ are different in order to have a non-trivial Zak phase. If they are equal, the topological bands are no longer separated so that either no Zak phase can be defined or it is trivial. But $D_1^x \neq D_1^y$ is required in order to fit the experimental data. This becomes clear upon analyzing the effects of D_1^x and D_1^y mediated by their symmetric couplings Γ_1^{xx} and Γ_1^{yy} on the dispersion [171]. If both parameters were equal, the corresponding dispersions would be the same as well. This is the crucial point: the experimental data shows that the two lowest-lying modes differ. Hence the values of the components D_1^x and D_1^y must be different. Furthermore, the quantized Zak phase persists in the presence of applied magnetic fields which do not close the spin gap above the ground state. This insensitivity results from the fact that the Zak phase is generated by the coupling between the k and $k+\pi$ wave vectors. Thus, terms coupling at the same wave vectors such as uniform magnetic fields do not destroy it. As mentioned above, even lifted crossings do not change the Zak phases.

The wave vectors with $k, l \in \{0, \pi\}$ are invariant under inversion so that states at these values have a well-defined inversion parity denoted by "+" and by "–" in Fig. 4.3. The product of the parities at $k = 0$ and $k = \pi$, both at $l = 2\pi$, equals the exponential of the corresponding Zak phase [85] in perfect agreement with the direct computation of the Zak phase in k-direction. This alternative route to the Zak phase strongly corroborates our finding that $BiCu_2PO_6$ is the first low-dimensional quantum magnet with a finite non-trivial Zak phase.

4.4. Berry curvature in $BiCu_2PO_6$

The Zak phase is computed from an integral of the Berry connection $\boldsymbol{\mathcal{A}}_{n,\mathrm{sym}}(\boldsymbol{k})$ in Eq. (4.9) which depends on the gauge used for the normal bosonic operators. Changing the gauge changes the Berry connection in its dependence on the wave vector $\boldsymbol{k}$ without changing the integral, i.e., the Zak phase. Hence, it is a priori not clear from which regions in the BZ the topological behavior results. Two arguments, however, show that the topological non-trivial Zak phase results from the vicinity of the minima of the triplon dispersions.

First, we consider the process of switching on the DM interactions. Without them there is no finite Zak phase. The DM terms couple the x-mode at k with the y-mode at $k+\pi$ and vice versa. The degeneracy between the two modes of the x-y_π-modes at $k = \pi/2$ and at $k = 3\pi/2$ is lifted by the DM terms (see green lines in Fig. 4.3). The same holds for the two modes of the y-x_π-modes (see blue lines in Fig. 4.3). The significant band mixing and splitting at $k = \pi/2$ and at $k = 3\pi/2$ is the driving mechanism of the finite Zak phase. Hence, the vicinity of these points in the BZ is decisive for the topologically non-trivial behavior.

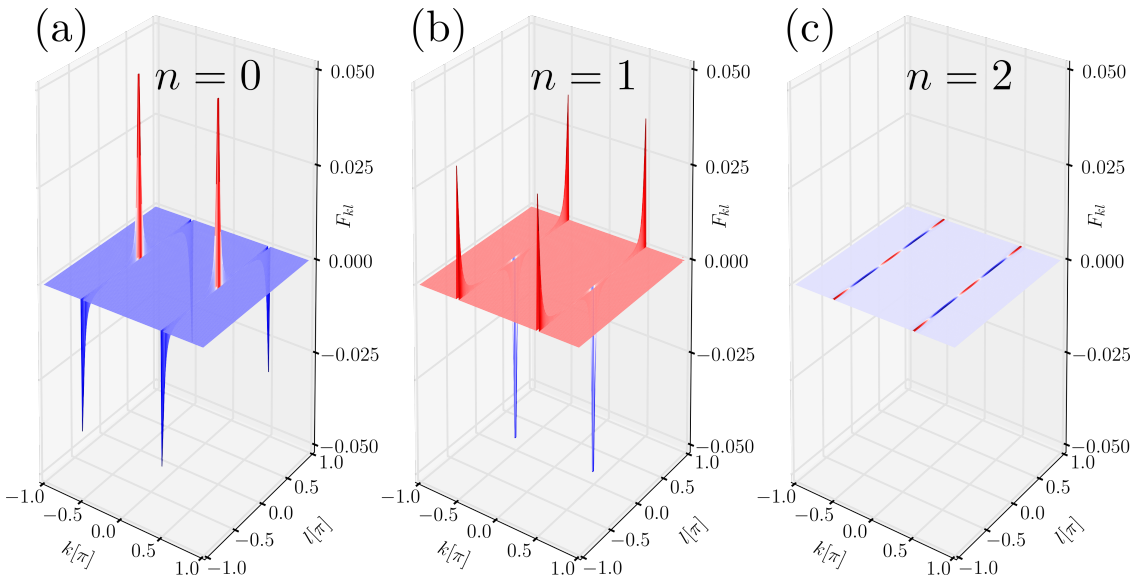

Figure 4.4: The Berry curvatures of the three lowest triplon dispersions calculated for $J_0 = 9.4\,\mathrm{meV}$, $J_3 = 1.5\,\mathrm{meV}$, $J_1 = 1.2J_0$, $J_2 = 1.09J_0$, $D_1^x = 0.58J_0$, $D_1^y = 0.73J_0$, $D_{2,a}^z = -0.02J_0$, $D_3^y = 0.02J_0$, $h_x = 0.1\,\mathrm{T}$, and $h_y = 0.1\,\mathrm{T}$. The curvatures in the panels (a) and (b) show high peaks which are located in the vicinity of $k = \pm\pi/2$ and corresponds to the mixed xy-bands. In contrast, panel (c) shows only a small curvature which corresponds to the topologically trivial z-mode.

Second, we study the Berry curvature

$$F_n(k,l) = \mathrm{i}\left[\left(\partial_k\langle\langle k,l,n|\right)\left(\partial_l\,|k,l,n\rangle\rangle\right)\left(\partial_l\langle\langle k,l,n|\right)\left(\partial_k\,|k,l,n\rangle\rangle\right)\right] \quad , \tag{4.12}$$

which is a gauge-independent quantity and thus suitable to investigate from which region non-trivial behavior results. All modes in the calculated dispersion of $BiCu_2PO_6$ show degenerate crossing points at $k = \pi/2$ and $k = 3\pi/2$. These degeneracies prevent the unambiguous definition of the Berry curvature. In order to be able to define a unambiguous curvature we add a small magnetic field in x- and y-direction $\boldsymbol{h} = h(1,1,0)^\top$ which lifts the degeneracies leading to six well-separated bands. Mathematically, the required magnetic field can be chosen infinitesimally small; for computational stability we chose $h = 0.1\,\mathrm{T}$. The Zak phases do not change upon adding this small magnetic field. The Berry curvatures of the three lowest bands $n = \{0,1,2\}$ are shown in Fig. 4.4. While the summation over the whole BZ vanishes so that the Chern number is zero, it is evident that the strong topological twists result from the vicinity of the original degeneracy points around $k = \pi/2$ and $k = 3\pi/2$. This is the region where the triplon dispersions are low and the agreement with experiment is very good. This piece of evidence supports the validity of the minimal model for the determination of topological phases in spite of missing features such as the downturns in the dispersions close to two-triplon continua [170].

4.5. Winding number w

In Sec. 4.3, we focused on the Zak phase because it is based on a Berry phase and can be defined for any one-dimensional system regardless the preserved symmetries. But there is another often considered topological invariant in one-dimensional systems, namely the winding number [36, 96, 186, 187].

The winding number counts the number of windings around a point in a two-dimensional plane of parameters. For this concept to make sense, the Hamiltonian must have an additional symmetry, conventionally called chiral symmetry, so that in the eigenbasis of the chiral symmetry the Hamiltonian matrix becomes block off-diagonal. The presence of a chiral symmetry is an elementary requirement for the definition of a winding number. A pseudo-spin representation can be used to illustrate the winding tracking the endpoint of the pseudo-spin vector upon varying the wave vector from $k = 0$ to $k = 2\pi$. The chiral symmetry pins the vector to a two-dimensional plane of parameters, see Refs. [96, 186, 187].

Such a chiral symmetry can be found for the minimal model of $BiCu_2PO_6$, i.e., ignoring the difference between the copper sites. But we were not able to find a chiral symmetry for the extended model accounting for different copper sites. The winding numbers w found for the x-y_π- and x_π-y-modes both take the non-trivial value $w = -1$ with respect to the k-dependence. This is in accordance with the calculated Zak phases. We emphasize, however, that the Zak phase is a far more general concept because its definition and computation do not require an additional symmetry.

In the case of the established minimal model for $BiCu_2PO_6$, the Hamiltonian shows the above discussed additional chiral symmetry allowing us to calculate the winding number if we make harmless approximations. Here we discuss the details of this calculation.

In the minimal model with $D_3^y = 0$, the 12×12 matrix in Eq. (4.6) or in Eq. (B.1a) in App. B can be split into 4×4 matrices, simplifying the subsequent analysis which is performed similarly to the one in Ref. [187]. To this end, we focus on the x-mode and its coupling to the y_π-mode. Since all couplings which are proportional to the 4×4 identity matrix do not alter the eigenmodes, they do not alter the topological properties and are therefore omitted. The contributions proportional to $\sigma_x \otimes \mathbb{1}$ only lead to small variations of the energy dispersion and we neglect them in a simplifying approximation. We checked that their omission has no impact on the Zak phase. We expect that the winding number similarly is not changed by the couplings proportional to $\sigma_x \otimes 1$, because their effect on the dispersion is small compared to the gap between the x-y_π-modes (see green lines in Fig. 4.3). Thus the topological invariants have to remain since no gap has closed. The same is assumed for the inclusion of small values of D_3^y.

Thus, for simplicity, we consider the Hamiltonian of a single ladder

$$\mathcal{H} = \frac{1}{2} \sum_k \boldsymbol{a}_k^\dagger H_k \boldsymbol{a}_k \tag{4.13}$$

with the Nambu spinor $\boldsymbol{a}_k = (t_k^x, t_{k+\pi}^y, t_{-k}^{x,\dagger}, t_{-k-\pi}^{y,\dagger})^\top$ and the 4×4 matrix

$$H_k = \begin{bmatrix} C(k) & C(k) \\ C(k) & C(k) \end{bmatrix} \quad , \tag{4.14}$$

where the 2×2 matrix C is parametrized by Pauli matrices $\boldsymbol{\sigma} = (\sigma_x, \sigma_y, \sigma_z)$ according

to

$$C(k) = \boldsymbol{d}(k) \cdot \boldsymbol{\sigma} \tag{4.15a}$$

$$d_x(k) = 0 \ , \quad d_y(k) = \Gamma_1^{xy}(k) - D_2^z(k) \tag{4.15b}$$

$$d_z(k) = \frac{1}{2}\sum_{i=0}^{2}(\Gamma_i^{xx}(k) - \Gamma_i^{yy}(k+\pi)) \quad . \tag{4.15c}$$

Then, the chiral symmetry operator is easy to identify as $\mathbb{1} \otimes \sigma_x$. It fulfils the anticommutator $\{\mathbb{1} \otimes \sigma_x, H_k\} = 0$. In order to calculate the winding number we transform the Hamiltonian into the eigenbasis of the chiral symmetry operator. This is achieved by the unitary transformation

$$U = \frac{1}{\sqrt{2}} \begin{pmatrix} 1 & 0 & 1 & 0 \\ 1 & 0 & -1 & 0 \\ 0 & 1 & 0 & 1 \\ 0 & 1 & 0 & -1 \end{pmatrix} \quad . \tag{4.16}$$

In this basis, the Hamiltonian matrix ηH_k with the metric $\eta = \sigma_z \otimes \mathbb{1}$ has a block off-diagonal form

$$\widetilde{H}_k = U^\dagger(\eta H_k)U \tag{4.17a}$$

$$= \begin{bmatrix} 0 & D_1(k) \\ D_1^*(k) & 0 \end{bmatrix} \quad . \tag{4.17b}$$

The matrix $D_1(k)$ is given by

$$D_1(k) = \begin{pmatrix} d_z(k) + \mathrm{i}d_y(k) & d_z(k) + \mathrm{i}d_y(k) \\ -d_z(k) - \mathrm{i}d_y(k) & -d_z(k) - \mathrm{i}d_y(k) \end{pmatrix} \tag{4.18}$$

and the winding number [188] is calculated by

$$w = \frac{1}{8\pi\mathrm{i}} \oint_{\mathrm{BZ}} \mathrm{d}k \mathrm{Tr}_2 \left(D^{-1}\partial_k D - (D^\dagger)^{-1}\partial_k D^\dagger \right) \tag{4.19}$$

with $D = (D_1(k) + D_1^\top(k))/2$. By construction, the winding number is quantized to integer values $w \in \mathbb{Z}$. For the investigated mode we find $w = -1$.

The same analysis can be performed for the y-mode coupled to the x_π-mode yielding the same winding number. In contrast, the z-mode only displays the trivial winding number $w = 0$, because it does not couple with another mode. Hence, it cannot be twisted or wound in any way.

A chiral symmetry of the general 12×12 matrix including all possible contributions could not be identified so that we could not define a winding number in general.

4.6. (Non-)Existence of edge states

We are looking for a smoking gun signature of a non-trivial Zak phase. The important bulk-boundary correspondence [27] in its conventional interpretation states that at the

boundaries between topologically non-trivial and trivial phases localized states must exist closing the gaps between the topologically distinct bands. Otherwise, the abrupt change of discrete topological invariants cannot be accounted for. These so-called edge states should exist at the ends of strips with a finite discrete Zak phase or a finite winding number [96, 186, 187] in the bulk. Hence, we are looking for localized edge states at the ends of finite strips of the minimal model for $BiCu_2PO_6$. Much to our surprise, we did not find any localized edge states.

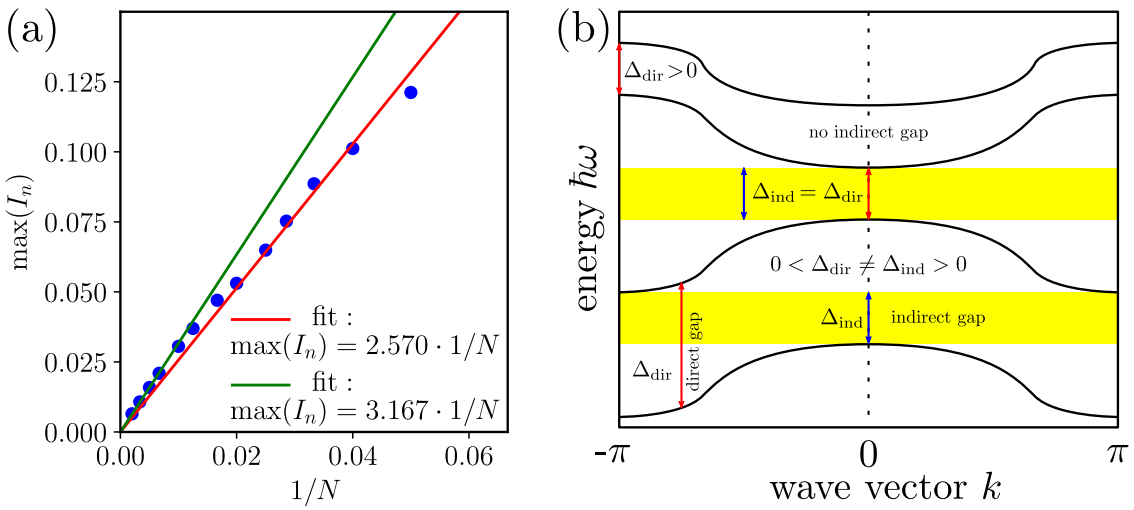

Figure 4.5: (a) Extrapolation of the largest IPR in the minimal model for $BiCu_2PO_6$ clearly indicating that all states are extended and no localized edge states are present. (b) Sketch of a direct gap Δ_{dir} at the red arrows and of an indirect gap Δ_{ind} at the blue arrows. A direct gap is the minimal difference between the maximal energy of a lower mode and the minimal energy of an upper mode at the *same* momentum. In contrast, the indirect gap is given by a forbidden energy interval (shown in yellow) between two modes irrespective of momentum conservation.

We studied the localization of all states quantitatively by computing the inverse participation ratio (IPR) [189, 190], which is a standard measure for localization. To this end, we calculate the eigenstates of a finite piece of chain with open boundaries in y-direction while we maintain the periodic boundary conditions in z-direction so that the IPR can be determined for each of them. We assume the same coupling constants as used for the fit of the INS shown in Fig. 4.3. If the IPR tends to zero for increasing system size the state is extended; if it stays finite the corresponding state is localized. We use the definition

$$I_n = \sum_i p_{n,i}^2 = \sum_i |\langle\langle n,i|\, n,i\rangle\rangle|^2 \tag{4.20}$$

adapted to the bosonic symplectic product and find that all $I_n \to 0$, see Fig. 4.5(a). This is shown by studying the largest IPR in a finite chain segment. Fig. 4.5(a) extrapolates this largest IPR by a linear function of the inverse system size. Obviously, the largest IPR decreases monotonically to zero and hence all IPRs vanish in the thermodynamic limit.

This puzzling fact can be explained by three arguments. First, the usual argument of bulk-boundary correspondence [27] requires the existence of states within the band gaps

of the topologically non-trivial bulk systems; let us call them in-gap states [191]. But there is no argument which requires that these states are *localized*. The localization is plausible because their energy lies within a gap and they are induced by the boundary, but there is no compelling reason for their localization.

Second, the energy of most localized edge states lies in an indirect gap, i.e., independently of momentum conservation they are protected by energy conservation, for an illustration of direct and indirect gaps see Fig. 4.5(b). If there is an indirect gap, the energetic protection persists even if we sum over all wave vectors, for instance to compute local densities of states. In contrast, in absence of an indirect gap the energetic separation of the in-gap states from the bulk states is only ensured by the conserved momentum $\hbar k$. We stress that introducing boundaries, for instance in y-direction, lifts the conservation of momentum so that generically the momenta hybridize and the in-gap states mix with scattering states in the continua and thereby the in-gap states delocalize. Even at this stage, one may wonder whether the in-gap states are localized or not. If the boundary had only the effect to reflect the incident triplon it would only mix k and $-k$ and a direct energy gap were still sufficient to induce localization. Yet this is not the case in $BiCu_2PO_6$ where the bands are separated by direct gaps, but not by indirect gaps. It is known that this mechanism weakens localization in ordinary quantum systems [192, 193] and the localization length has been linked to the precise momentum dependence of the dispersion in topological insulators with direct gaps [194]. Recently, it has been shown that localization of edge states may persist in a topological system if the hybridization is sufficiently suppressed by various symmetries [195, 196]. We emphasize, however, that the outstanding significance of indirect gaps has not been mentioned in the literature.

The third argument resides in the independence of the topological invariants in the bulk on the eigenenergies. The vector potential (4.9) and hence the Berry phase (4.10) depend on the *eigenmodes* only. But they are blind to their eigenenergies, i.e., to the dispersions. Thus, one can modify the Hamiltonian leaving the eigenmodes and the topology completely unaltered while shifting the dispersion energies arbitrarily. But such changes have an effect on the edge modes if boundaries are introduced [191]. We illustrate this point in the next section in a particularly transparent and well-established model, the SSH model [197].

4.7. (De-)Localization in the Su–Schrieffer–Heeger model

Since the topology of bosonic systems is still less known and the model for $BiCu_2PO_6$ is rather intricate we want to support our hypothesis on the delocalization of edge states by a transparent calculation for an established and well-known fermionic model, the SSH model [197]. In this paradigmatic model, we show explicitly that adding a coupling which does *not* alter the eigenstates can delocalize the edge modes. If the indirect gap vanishes, the edge modes become extended, i.e., they are no longer modes at the edge in the proper sense.

We consider the SSH model and extend it slightly by the coupling u between NNNs, see Fig. 4.6. Its Hamiltonian reads

$$\mathcal{H}_{\mathrm{SSH}} = \sum_i^N \left(v c_{i,\mathrm{B}}^\dagger c_{i,\mathrm{A}} + w c_{i+1,\mathrm{A}}^\dagger c_{i,\mathrm{B}} + u c_{i+1,\mathrm{A}}^\dagger c_{i,\mathrm{A}} + u c_{i+1,\mathrm{B}}^\dagger c_{i,\mathrm{B}} \right) + \mathrm{h.c.} \qquad (4.21)$$

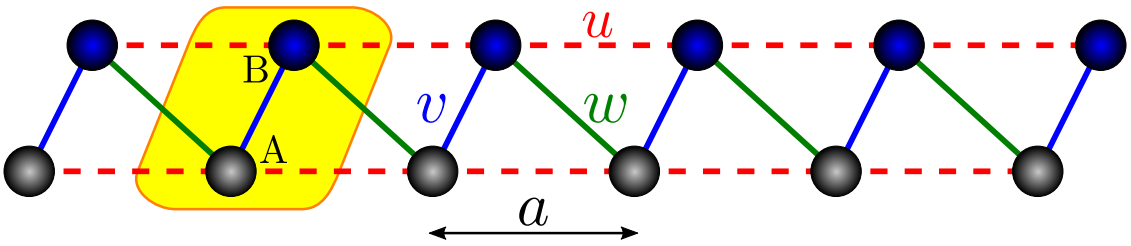

Figure 4.6: Lattice of the extended SSH model with intracell coupling v, intercell coupling w between NNs and intercell coupling u between NNNs. The unit cell comprising sites A and B is displayed by the yellow area.

where $c_{i,\mathrm{A}}$ is the fermionic annihilation operator at site A of unit cell i and $c_{i,\mathrm{B}}$ the corresponding fermionic annihilation operator at site B. The creation operators are the respective Hermitian conjugates. All three couplings are real and shown in Fig. 4.6. The Hamiltonian $\mathcal{H}_{\mathrm{SSH}}$ is particle-conserving.

In the bulk or for periodic boundary conditions Fourier transformation yields

$$\mathcal{H}_{\mathrm{SSH}} = \sum_k \begin{pmatrix} c^\dagger_{k,\mathrm{A}}, & c^\dagger_{k,\mathrm{B}} \end{pmatrix} H_k \begin{pmatrix} c_{k,\mathrm{A}} \\ c_{k,\mathrm{B}} \end{pmatrix} \tag{4.22a}$$

$$H_k = \begin{pmatrix} 2u\cos(k) & v + w\mathrm{e}^{\mathrm{i}k} \\ v + w\mathrm{e}^{-\mathrm{i}k} & 2u\cos(k) \end{pmatrix} \quad , \tag{4.22b}$$

where the lattice constant a is set to unity. The ensuing dispersion is

$$E_n(k) = 2u\cos(k) \pm \sqrt{v^2 + w^2 + 2vw\cos(k)} \tag{4.23}$$

with $n \in \{1, 2\}$ corresponding to the $\pm$ sign in front of the square root. The dispersion branches are depicted in the upper row of Fig. 4.7 for $v = 0$ and the indicated ratios u/w.

On the one hand, the eigenstates are the same as in the usual SSH model without NNN coupling u since the additional coupling leads to a modification of the matrix H_k proportional to the 2×2 identity matrix $2u\cos(k)\mathbb{1}_2$. For this reason, we call the coupling u isotropic. The induced modification does not change the eigenstates at all. Hence, the extended SSH model shows the same Zak phase and the same winding number as the non-extended SSH model.

On the other hand, however, the numerical analysis of a finite piece of chain with open boundary condition reveals that the localization of the edge states is *not* protected against the isotropic coupling despite the fact that the direct gap does not close so that the two bands remain separated, see Fig. 4.7. By the naked eye one already discerns that the wave function with the largest value of the IPR defined in Eq. (4.20), see also Refs. [189, 190], is localized if the energy of the edge modes lies well within the indirect gap. But upon decreasing the indirect gap to zero for $u \to w/2$ the IPR also drops to zero in the thermodynamic limit $N \to \infty$. Then, it is obvious that the corresponding states are no longer localized. These findings are in agreement with the investigation of the localization length shown in App. E. We emphasize that this does not contradict the logic of the bulk-boundary correspondence which requires that the *energy gap* has to close at the boundary to another phase with a different quantized topological invariant [27].

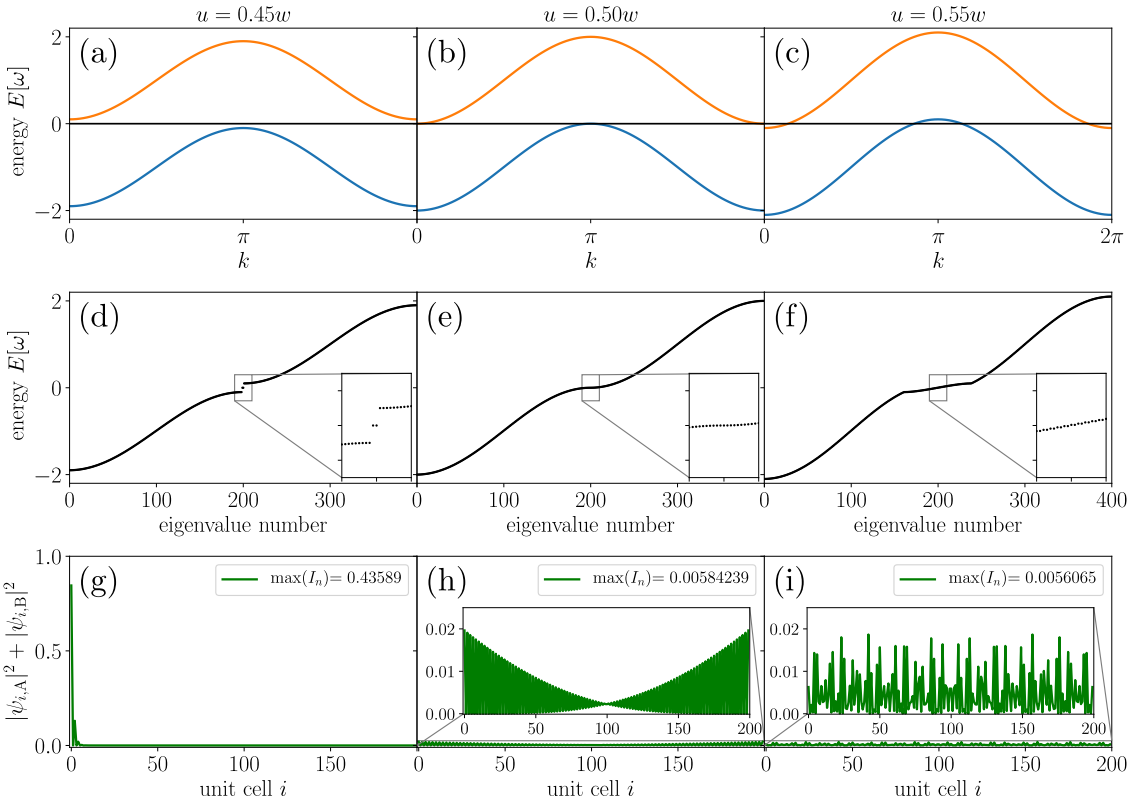

Figure 4.7: Delocalization of the edge states illustrated for $v = 0$. The three rows show from top to bottom: the bulk dispersion, the eigenvalues of a finite piece of chain with open boundaries consisting of 200 unit cells and the probability density $|\psi_{i,\mathrm{A}}|^2 + |\psi_{i,\mathrm{B}}|^2$ of the eigenstate ψ with the highest IPR given in the legend of the lower panels (g)-(i). The three columns refer to different ratios u/w. For $u = 0.45w$, the two edge modes lie within the indirect gap and are well localized. The case $u = 0.50w$ is marginal and for $u = 0.55w$ no indirect gap exists anymore. Concomitantly, no localized modes exist. But the two bands continue to be clearly separated and hence well-defined.

The IPR is the standard measure of localization in perfect agreement with the computed eigenstates shown in the lower row of Fig. 4.7. But it may be argued that remnants of localization persist in local spectral properties to which many eigenstates contribute. The local density of states at the ends of finite chain pieces is a promising candidate to display fingerprints of localized edge states. Three representative results for the local density of states at the chain ends of the SSH model are displayed in Fig. 4.8. In the regime of finite indirect energy gaps where the IPR confirmed a localized edge state a clear resolution-limited peak, a δ-peak, is found, see upper panel. But it is obvious that the delocalization of this in-gap state is accompanied by the broadening of this δ-peak which reduces to a diverging singularity in the marginal case $u = 0.5w$, where the indirect gap has just closed. In the region where the indirect gap does not exist (or is negative, depending on the definition) no divergence occurs, but only a broad feature is present, which is reminiscent of the density of states of a miniband due to its Van Hove singularities at the edges. Hence our conclusion is corroborated that the bulk-boundary correspondence

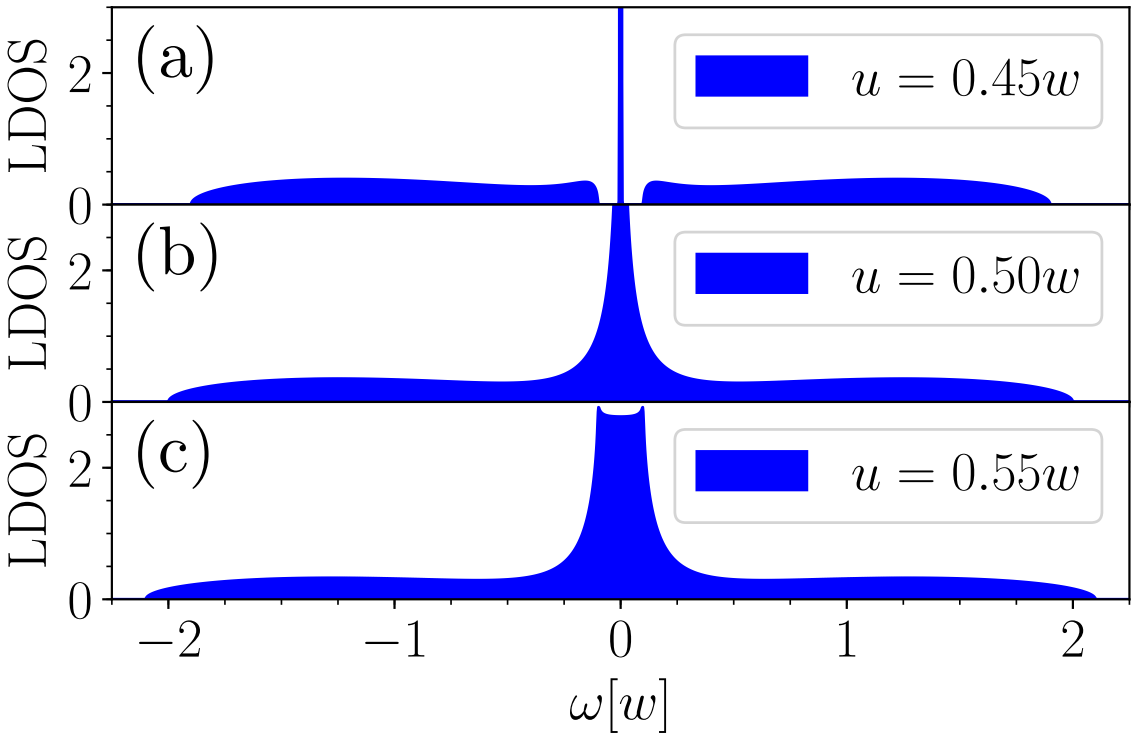

Figure 4.8: Local density of states at one end of a finite piece of chain of the SSH model in (4.21). Panel (a) displays the case where the indirect gap is still finite: a clear resolution-limited δ-peak occurs at zero energy. Panel (b) displays the marginal case where the indirect gap has just vanished. Clearly, no δ-peak is present, but there is still a prominent peak which is no longer resolution limited, i.e., it has an intrinsic width. Panel (c) displays a case where no indirect gap is present. Interestingly, a broad feature occurs, which is reminiscent of a one-dimensional miniband with slightly broadened Van Hove singularities at the edges.

does not imply localization. Peak-like structures may persist in local spectral quantities, but they differ qualitatively from the δ-peak for positive indirect energy gaps.

4.8. Local dynamic structure factor in $BiCu_2PO_6$

In the preceding section, we illustrated and supported our scenario by an analysis of the (de-)localization of the edge modes in the paradigmatic fermionic SSH model for simplicity and transparency. This analysis comprised the IPR and a local spectral property, the local density of states.

Here we return to the quantum magnet $BiCu_2PO_6$. The IPR is analyzed and shown in Fig. 4.5(a). It is the suitable measure for the localization of a single state [189, 190]. Yet we want to extend the analysis to local behavior in spectral properties. To this end, the local dynamic structure factor (local DSF) at the end of a spin ladder suggests itself. It displays a δ-function if there is a localized edge state. It vanishes if the edge state delocalizes. But a certain residual peak made from many eigenstates could remain, see Sec. 4.7 on the SSH model.

To study potential spectral peaks, Fig. 4.9 displays the local DSF at the end of a finite piece of spin ladder with 1000 dimers, i.e., 1000 sites for triplons, where the model for $BiCu_2PO_6$ is varied. At zero temperature, the DSF equals the imaginary part of the spin correlation function χ. The result for the actual model for $BiCu_2PO_6$ is shown in panels (c) and (f). No sharp peak is discernible which could be related to a localized edge mode. But it is a priori unclear where such a peak should be and whether a less specific broad feature represents the remnant of localization, see previous section on the SSH model. Thus, it is instructive to study the DSF of a modified model which has localized edge modes and which can be continuously tuned to the minimal model of $BiCu_2PO_6$.

To this end, we consider the following variation of the Hamiltonian. The dispersion of the isotropic spin ladder in Eq. (B.4) is replaced by

$$\omega_0(k) = 1.55 + u\cos(k) \quad . \tag{4.24}$$

This choice leads to a finite indirect gap for which we expect localized edge modes. For the Hamiltonian with $u = 0$, Fig. 4.9(a) shows the (resolution-limited) δ-peak as it results from the existing localized edge state. In contrast, setting $u = 0.013554$ as in Fig. 4.9(b) leads to the marginal case of an indirect gap which has just vanished. Then, the DSF still displays a peak even though it is not a resolution limited δ-peak anymore. Clearly, it has acquired a certain intrinsic width. If the dispersion is changed further to the realistic one of the isotropic spin ladder so that $BiCu_2PO_6$ is described, all traces of a peak are completely gone, see Figs. 4.9(c) and (f). In order to be able to compare the various DSFs and to assess their evolution, the three cases are shown in Fig. 4.9 (d)-(f) with the same scale.

In essence, we conclude that in $BiCu_2PO_6$, a quantized Zak phase is present, but no signatures of localized edge modes occur.

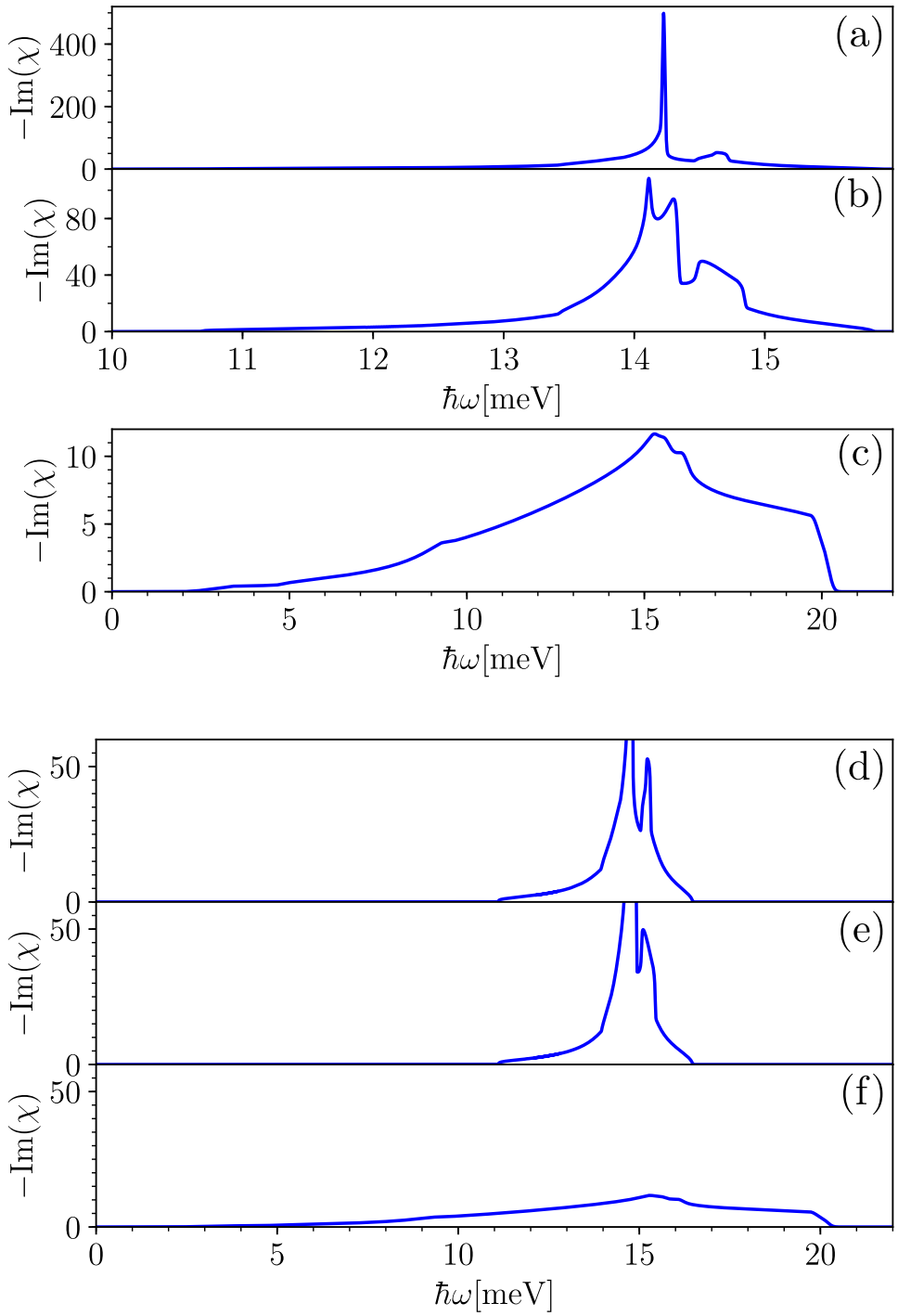

Figure 4.9: The local dynamic structure factor (DSF) as a function of transferred energy. Panels (a) and (d) show the case of localized edge states while panels (b) and (e) show the marginal DSF for a closed indirect energy gap. Panels (c) and (f) correspond to the expected local DSF in $BiCu_2PO_6$ with negative indirect gap and without any traces of localization. The difference between the panels (a)-(c) and the panels (d)-(f) consists in the scales. The upper panels have adapted scales to show the details, in particular the δ-peak, while the lower panels use the same scale and thus show the total evolution of the DSF.

4.9. Conclusion

Two key results are presented in this chapter: One is material-specific while the other is general.

The material-specific result is that we analyzed the INS data of $BiCu_2PO_6$ quantitatively on the basis of a model of non-interacting triplons. This model describes the low-lying magnetic modes very well. Discrepancies at higher energies are attributed to decay and interaction processes which do not change the robust, quantized topological properties. Due to the inversion symmetry of the system, the Zak phase is quantized in multiples of π. We found that $BiCu_2PO_6$ is the first disordered one-dimensional quantum magnet displaying a finite, non-trivial Zak phase of π. This result was obtained by two approaches: (i) direct calculation of the Zak phase and (ii) the study of the parity of the modes at inversion symmetric momenta. In addition, the computation of the winding number in Sec. 4.5 corroborates the conclusion of a non-trivial magnetic topology. The finite Zak phase is a robust result since it essentially depends on the difference of the DM couplings D_1^x and D_1^y. This difference is required in order to describe the slightly asymmetric dispersion around the crossing point at $(k = \pi/2, l = 2\pi)$ and $(k = 3\pi/2, l = 2\pi)$ [171].

The general result concerns the bulk-boundary correspondence which constitutes a fundamental concept in topological systems. We found no localized edge states in $BiCu_2PO_6$ in spite of the non-trivial Zak phase and the winding number. We explained this unexpected behavior by the delocalization of the edge modes due to a negative *indirect* energy gap between excitation modes while the direct gap remains positive so that the bands are well separated. Adding momentum dependent terms to the Hamiltonian which are proportional to the identity does not change the the topology in the bulk, but they strongly influence the localization in confined geometries. From this observation we deduced the generic importance of a positive indirect gap in order to have localized edge modes. This claim was supported by the analysis of an extended SSH model. We view this scenario as generic because it occurs without particular interactions in typical, standard models without any fine-tuning. To this end, we extend our observation of the vital importance of a finite, positive indirect gap for the existence of localized edge modes in two-dimensional Chern insulators as well. This is studied in the next chapter.

We stress that delocalization due to a negative indirect gap is generic although in particular situations localization may be protected in spite of vanishing gaps. This is known from systems without topological properties [192, 193] and from systems with topological properties where further symmetries, e. g., conservation of momentum and energy, can preserve localization although the edge state is coupled to gapless scattering states in the bulk [195, 196].

The crucial conceptual insight into the significance of a positive indirect gap has not been appreciated before. It puts the bulk-boundary correspondence into perspective. While the direct gap protects the topological properties in the bulk, it is not sufficient to protect the localization of edge modes in confined geometries. Hence, the edge states are extended and cease to exist as edge states in the proper sense of the word. Still, they are in-gap states and as such in accordance with the derivation of the established bulk-boundary correspondence [27].

5. Delocalization of topological edge states

Parts of this chapter have been published in Europhysics Letters as a letter [191]. Götz S. Uhrig contributed to the manuscript and the interpretation of the results. I created all figures and calculated all the data.

5.1. General context

The emergence of edge states in non-interacting topological systems is described by the bulk-boundary correspondence [24–27] which relates finite discrete topological invariants of the energy bands in the bulk to the existence of edge states at the boundaries of finite systems. The underlying idea is as follows. The transition between two bulk systems (one could be the vacuum) with different discrete topological invariants cannot be continuous because of the discrete nature of the invariants. Thus there must be in-gap states which link the bands of different topological invariants so that they can no longer be defined for each band separately. Since this argument hinges on the existence of the boundary, it is assumed that these in-gap states are localized at the boundaries, hence represent edge states [27]. For certain Hamiltonians this can be rigorously shown [24–26].

Such topological edge states can be found in topological insulators [27, 198], topological semi-metals [199], and topological crystalline insulators [200]. Higher-order topological insulators in 3D may not display surface states, but so-called hinge states[1] [201]. In one-dimension, there can be localized states at the chain ends [187, 202]. Recently, however, we found in 1D that localized end states do not represent the generic scenario if the indirect energy gap between the bands of different topological invariants vanishes [44]. While the direct gap Δ_{dir} measures the energetic separation of two bands at a given fixed momentum, the indirect gap Δ_{indir} measures this separation if momentum changes are admitted. Clearly, $\Delta_{\text{indir}} \leq \Delta_{\text{dir}}$ and a finite Δ_{dir} are sufficient for the bands to be well-defined. This surprising finding qualifies the bulk-boundary correspondence in the sense that a finite direct gap does not suffice to guarantee the existence of localized edge states.

Since 1D topological systems differ significantly from their higher-dimensional counterparts, the question arises to which extent the delocalization of edge states occurs in 2D as well as if the indirect gap vanishes. The goal of the present chapter is to answer this question by a representative proof-of-principle study.

5.2. Delocalization of edge states in the Haldane model

The fermionic tight-binding model proposed by Haldane [51] as a first example of non-trivial topological behavior without a magnetic field is a well-established model of a Chern

[1] Hinge states are gapless states at the hinges of a 3D system, while the surfaces are gapped and the bulk states provides a topological invariant.

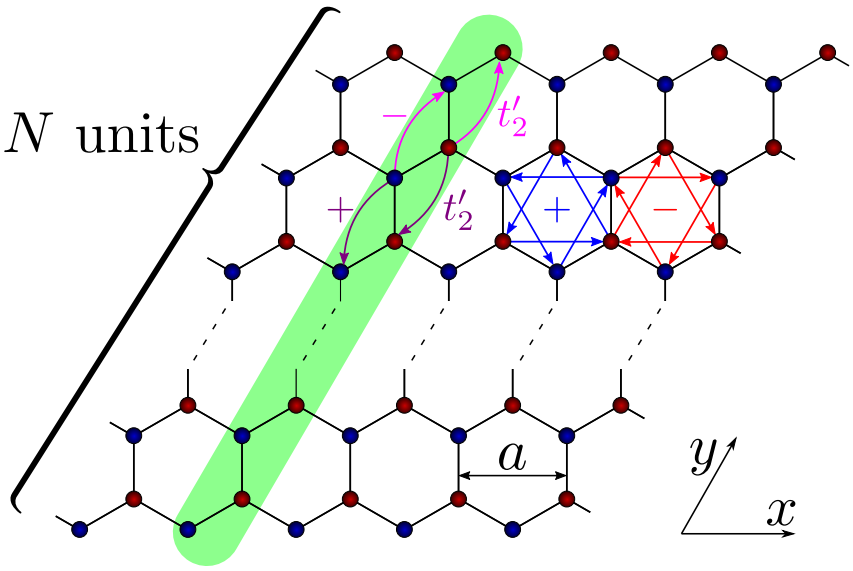

Figure 5.1: Infinite honeycomb strip in x-direction. NN hopping is depicted in black. A unit cell consists of $2N$ sites in y-direction, shown in green. The sign of the phase in NNN hopping is given by arrows, e.g., red arrows stand for $-\phi$ and magenta arrows for $+\varphi$. The lattice constant a is set to unity.

insulator due to its simplicity. Hence, we choose it as our starting point. By adding a spatially anisotropic hopping, it is possible to close the indirect gap while leaving the topological properties of the bands completely untouched. The Hamiltonian reads

$$\mathcal{H} = \mathcal{H}_{\text{Haldane}} + \mathcal{H}_{\text{diag}} \tag{5.1a}$$

$$\mathcal{H}_{\text{Haldane}} = t \sum_{\langle i,j \rangle} c_i^\dagger c_j + t_2 \sum_{\langle\langle i,j \rangle\rangle} \mathrm{e}^{\pm \mathrm{i}\phi} c_i^\dagger c_j \tag{5.1b}$$

$$\mathcal{H}_{\text{diag}} = t_2' \sum_{\overline{\langle\langle i,j \rangle\rangle}} \mathrm{e}^{\pm \mathrm{i}\varphi} c_i^\dagger c_j \quad , \tag{5.1c}$$

where $c_i^\dagger$ and c_i correspond to the creation and annihilation operators at site i, respectively. The hoppings on the honeycomb lattice are shown in Fig. 5.1. A pair of NN and NNN sites is denoted by $\langle i,j \rangle$ and by $\langle\langle i,j \rangle\rangle$, respectively. The hopping elements t, t_2 and t_2' are real and t serves as the energy unit. The sign of the complex phase ϕ for the t_2-hopping is positive for anti-clockwise hopping and negative for clockwise hopping, see blue and red arrows in the plaquettes in Fig. 5.1.

The notation $\overline{\langle\langle i,j \rangle\rangle}$ in the additional Hamiltonian $\mathcal{H}_{\text{diag}}$ restricts the hopping to NNN in the y-direction. Therefore, it breaks the point group symmetry C3 of the bulk system. The sign of its phase φ is positive in y-direction and negative in $-y$-direction. This additional term may seem artificial, but it is suitable for the intended proof-of-principle consideration. Its realization in ultracold atom systems appears feasible [68].

In reciprocal space the bulk Hamiltonian reduces to a 2×2 matrix due to the two sites in a unit cell; it can be expressed in terms of Pauli matrices. One finds that $\mathcal{H}_{\text{diag}}$ is given by $2t_2' \cos(k_y + \varphi)\sigma_0$ where σ_0 is the identity matrix. Hence the t_2'-hopping only induces

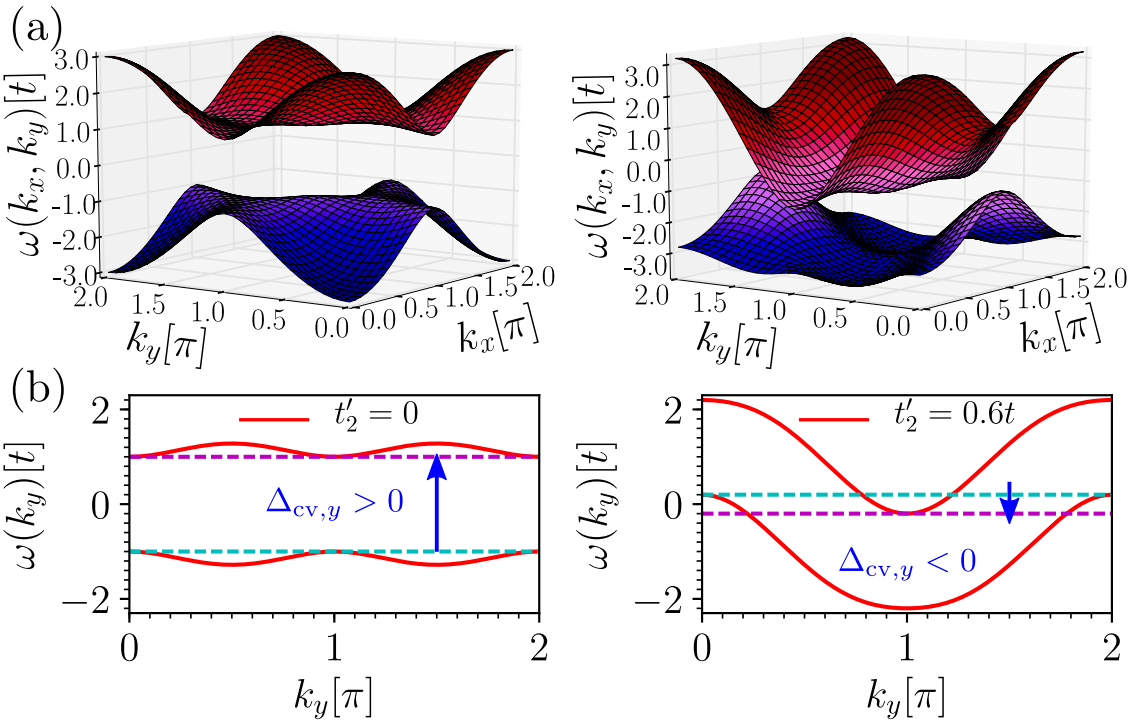

Figure 5.2: (a) Dispersion for $t_2 = 0.2t$, $\phi = \pi/2$, $\varphi = 0$, and $t_2' = 0$ in the left panel and for $t_2' = 0.6t$ in the right panel. (b) Dispersions as in (a) at $k_x = \pi$. The magenta and cyan dotted lines indicate $\varepsilon_{\mathrm{bu,c}}$ and $\varepsilon_{\mathrm{bu,v}}$, respectively.

an energy shift without having any effect on the eigenstates at a given momentum. The topological properties derived from the eigenstates such as the Berry curvature and the concomitant Chern number [97] are preserved. The bulk dispersion, however, is altered due to t_2'.

On the left hand side of Fig. 5.2, we illustrate the dispersion for $t_2 = 0.2t$ and $\phi = \pi/2$ without t_2'. If t_2' is switched on at $\varphi = 0$ the dispersion changes significantly as shown on the right hand side of Fig. 5.2. The direct energy gap at each given k-value does not change so that the two bands stay well-separated. But the indirect gap is given by the energy difference between the magenta and the cyan dashed line and hence vanishes and becomes even negative as displayed clearly in Fig. 5.2(b) at fixed $k_x = \pi$.

To take the orientation of the boundary into account, we define the indirect gap $\Delta_{\mathrm{cv},y}(k_x)$ as the smallest energy difference between the conduction and valence band at a fixed k_x, but for varied momentum k_y. The relevant band edge for the conduction band $\varepsilon_{\mathrm{bu,c}}(k_x) \coloneqq \min_{k_y} \omega_{\mathrm{bu,c}}(k_x, k_y)$ is displayed in Fig. 5.2 as magenta dotted line. For the valence band $\varepsilon_{\mathrm{bu,v}}(k_x) \coloneqq \max_{k_y} \omega_{\mathrm{bu,v}}(k_x, k_y)$ it is marked by the cyan dotted line. Thus one has

$$\Delta_{\mathrm{cv},y}(k_x) = \varepsilon_{\mathrm{bu,c}}(k_x) - \varepsilon_{\mathrm{bu,v}}(k_x) \quad . \tag{5.2}$$

This gap can take negative values formally. Tuning t_2' from 0 to $0.5t$ at $\varphi = 0$ closes the indirect gap at $k_x = \pi$.

Next, we pass from the bulk to a finite, confined system considering a strip with zigzag edges as shown in Fig. 5.1. We investigate the existence of localized edge states. The boundaries are chosen to run in x-direction and thus k_x continues to be preserved, but k_y

does not. Upon turning on the diagonal t_2'-hopping, the topological properties in the bulk remain completely unaffected, but we find a significant impact on the system with boundaries: the exponentially localized edge states at $t_2' = 0$ become less and less localized till they delocalize completely. We want to explore this phenomenon here.

In order to measure the localization of states, the IPR [189, 190] is most suitable. We want to quantify the localization to the edges of the strip, so we define the IPR of a normalized eigenstate by

$$\begin{aligned} I_n(k_x) &= \sum_i p_{n,i}^2(k_x) \\ &= \sum_i |\langle n,i|n,i\rangle|^2(k_x) \quad \in [0,1] \quad , \end{aligned} \tag{5.3}$$

where $p_{n,i}$ is the probability of finding a particle at site i in the unit cell in Fig. 5.1, if the system is in the n-th eigenstate at momentum k_x. The IPR of localized states is finite, even for $N \to \infty$, while it converges towards zero for delocalized, extended states in this limit. Hence, in numerics an IPR of $O(1/N)$ indicates a delocalized state while larger values indicate localization.

First, we focus on the case $k_x = \pi$ being the crossing point of the dispersion of the right and left moving in-gap states. Its energy lies precisely in the middle between the conduction and valence bands rendering the spectrum at this value of k_x similar to the spectrum of the 1D case [44] studied previously in Sec. 4.7. Fig. 5.3(a) depicts the IPR as a function of t_2'. For comparison, the indirect gap $\Delta_{\mathrm{cv},y}$ is shown in Fig. 5.3(b). As in 1D, the IPR at $k_x = \pi$ decreases monotonically to its minimum value $O(1/N)$ upon increasing t_2'. The IPR reaches this value at the same value t_2' where the indirect gap $\Delta_{\mathrm{cv},y}$ vanishes. This delocalized in-gap state remains extended for $\Delta_{\mathrm{cv},y} < 0$.

If k_x takes other values the situation is more complex because the energy of the in-gap states is closer to one of the two bands, conduction or valence, respectively. We observe that the delocalization $I \approx 0$ occurs for smaller values of t_2' than the zero of the indirect gap $\Delta_{\mathrm{cv},y}$, see Fig. 5.3(a) and (b). So we conclude that the existence of an indirect gap and delocalization are linked, but not in a straightforward manner, see discussion below.

In order to achieve a better understanding we define a specific indirect gap Δ_y referring to the energy of the in-gap state. This piece of information is available once the strip geometry is analyzed quantitatively. Let the in-gap energies be denoted by $\omega_{\mathrm{in},\alpha}$ where α denotes the different in-gap branches. Then Δ_y is the smallest energy difference of $\omega_{\mathrm{in},\alpha}$ to one of the bands at fixed k_x

$$\Delta_y(k_x,\alpha) := \min\left\{\omega_{\mathrm{in},\alpha} - \varepsilon_{\mathrm{bu,v}}, \varepsilon_{\mathrm{bu,c}} - \omega_{\mathrm{in},\alpha}\right\} \quad . \tag{5.4}$$

If the in-gap states enter the continua of either the conduction or the valence band we set $\Delta_y(k_x,\alpha) = 0$. Thus, $\Delta_y(k_x,\alpha)$ measures the energy distance of in-gap states to the extended bulk modes. It is to be expected that it is closely related to delocalization.

The indirect gap Δ_y as a function of t_2' is shown in Fig. 5.3 (c). For $k_x = \pi$, Δ_y behaves like $\Delta_{\mathrm{cv},y}$ since in this particular, symmetric case both quantities are proportional to each other. For other momenta, however, differences appear. In contrast to $\Delta_{\mathrm{cv},y}$, Δ_y at $k_x \neq \pi$ vanishes exactly at the value of t_2' where the IPR essentially vanishes. This shows that localization can be attributed to a finite Δ_y. Note also the possible non-monotonic behavior of IPR and Δ_y as a function of t_2', e.g., at $k_x = 0.3\pi$, see Fig. 5.3.

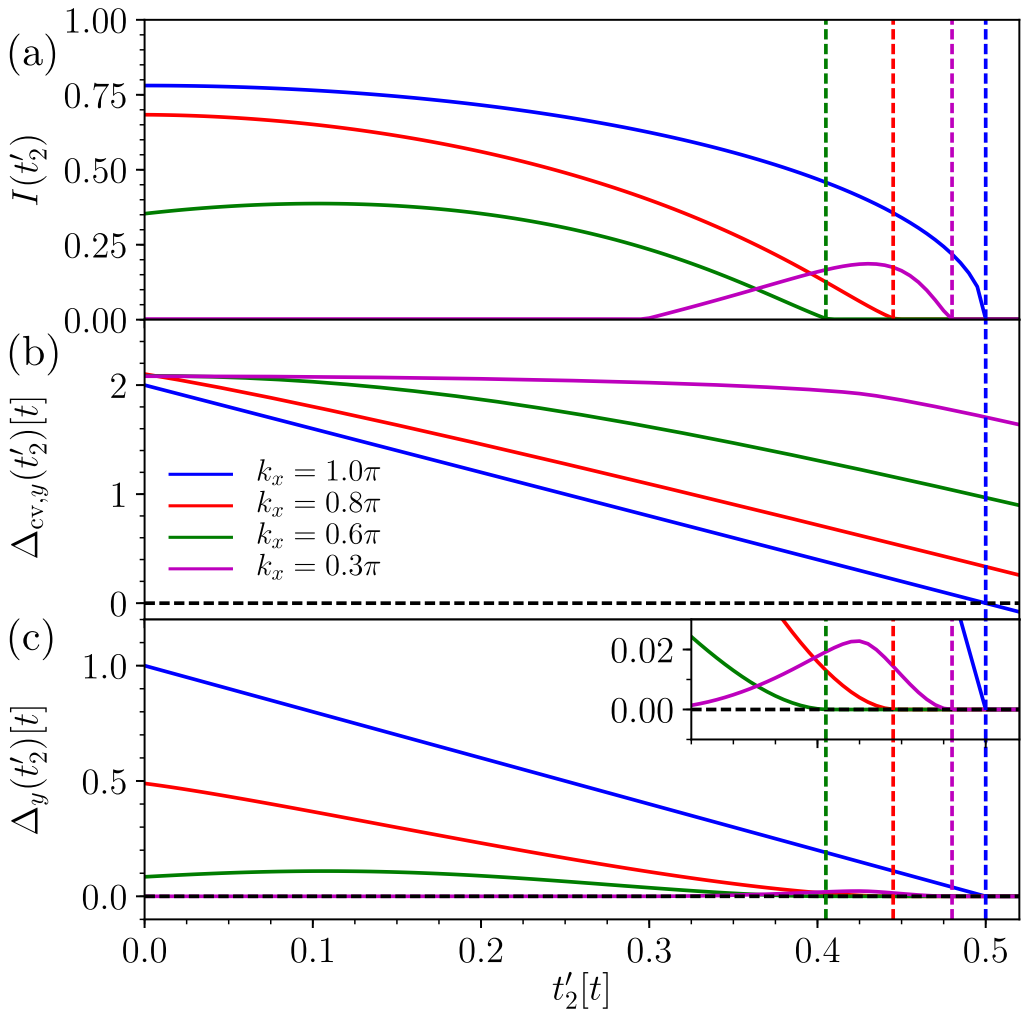

Figure 5.3: (a)-(c) The IPR, $\Delta_{\mathrm{cv},y}$, and Δ_y of the right-moving edge state vs. diagonal hopping t_2' are shown for various momenta k_x as computed for $N = 500$.

For the sake of comprehensibility, we visualize the evolution of the band structure as a function of the hopping amplitude t_2'. In Fig. 5.4 we depict four representative cases $t_2' = \{0, 0.25t, 0.5t, 0.75t\}$. On increasing t_2' the conduction and valence bulk bands approach each other and the edge states become energetically overlapped by them more and more, see Fig. 5.4(a) and (b). At the marginal value $t_2' = 0.5t$ shown in Fig. 5.4(c), all in-gap states are energetically overlapped by bulk states and are therefore delocalized. This coincides with the closing of the indirect gap $\Delta_{\mathrm{cv},y} = 0$ at $k_x = \pi$. Increasing t_2' further, see Fig. 5.4(d), the range of k_x-values increases where $\Delta_{\mathrm{cv},y}$ is zero or negative.

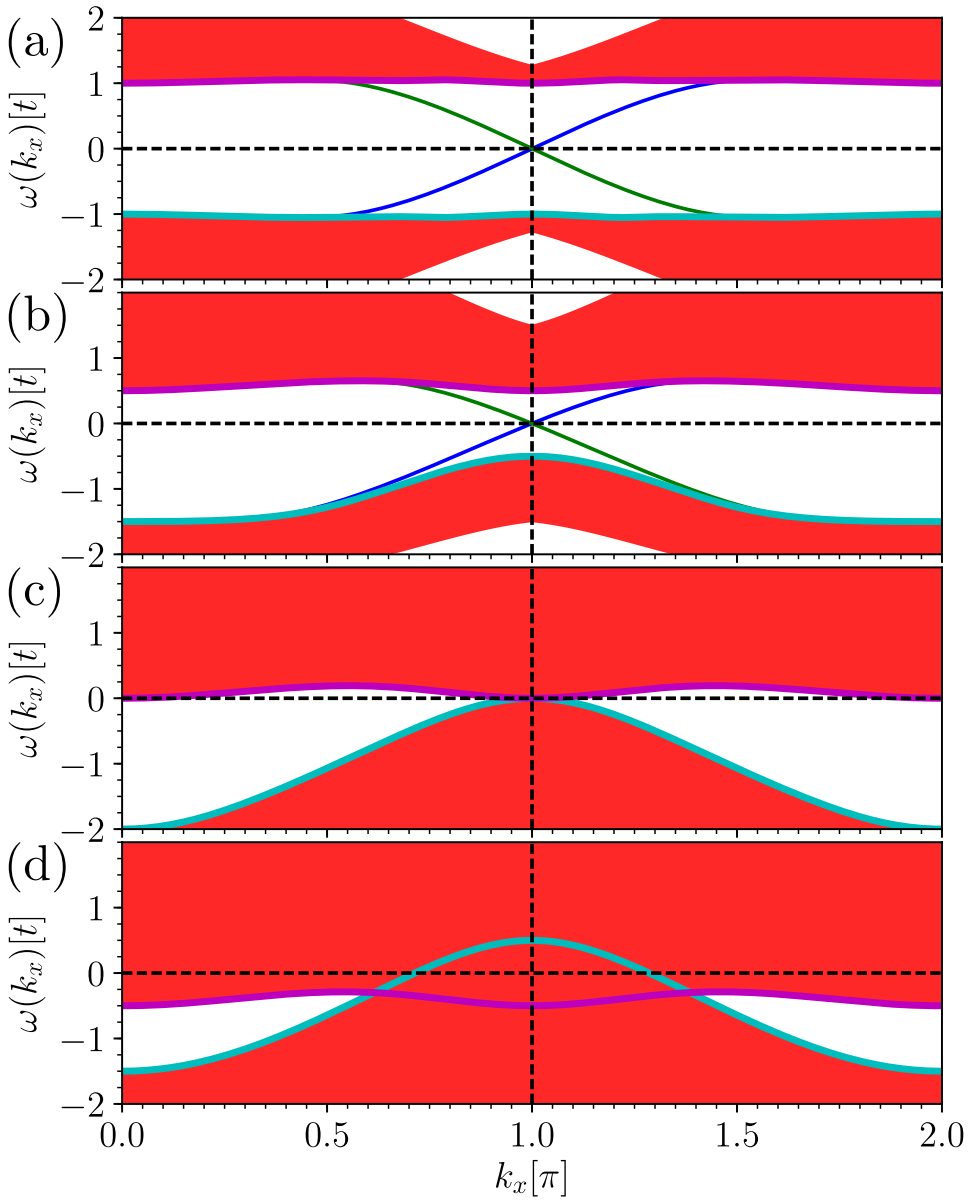

Figure 5.4: (a)-(d) Continua of the two bulk bands and dispersions of the two in-gap states (right-mover in blue, left-mover in green) for $t_2 = 0.2t$, $\phi = \pi/2$, $\varphi = 0$, and $t_2' = \{0, 0.25t, 0.5t, 0.75t\}$. Due to the absence of an indirect gap the continua overlap in panels (c) and (d) and no in-gap states can be identified. The magenta and cyan lines indicate the band edges $\varepsilon_{\mathrm{bu,c}}$ and $\varepsilon_{\mathrm{bu,v}}$, respectively.

5.2.1. Further insights into delocalization

Here we study the effect of the additional diagonal hopping term on the (de-)localization of edge states in more detail. The dispersion of the original Haldane model as given in Eq. (5.1a) in a strip geometry with zigzag edge is shown in Fig. 5.5(a). The two dispersion branches marked in blue and green connect the valence and conduction bands. They belong to the right and left-moving in-gap states with energies $\omega_{\mathrm{in},\alpha}$ where α labels the two branches. In the same range of parameters where the energy of the in-gap states is clearly distinct from the bulk continua (shown in red) the IPR [189, 190] is finite indicating well-localized edge states, see Fig. 5.5(b). The energy separation of the in-gap states from the closest bulk energies is described by the specific indirect gap Δ_y defined in Eq. (5.4). It is displayed in Fig. 5.5(c).

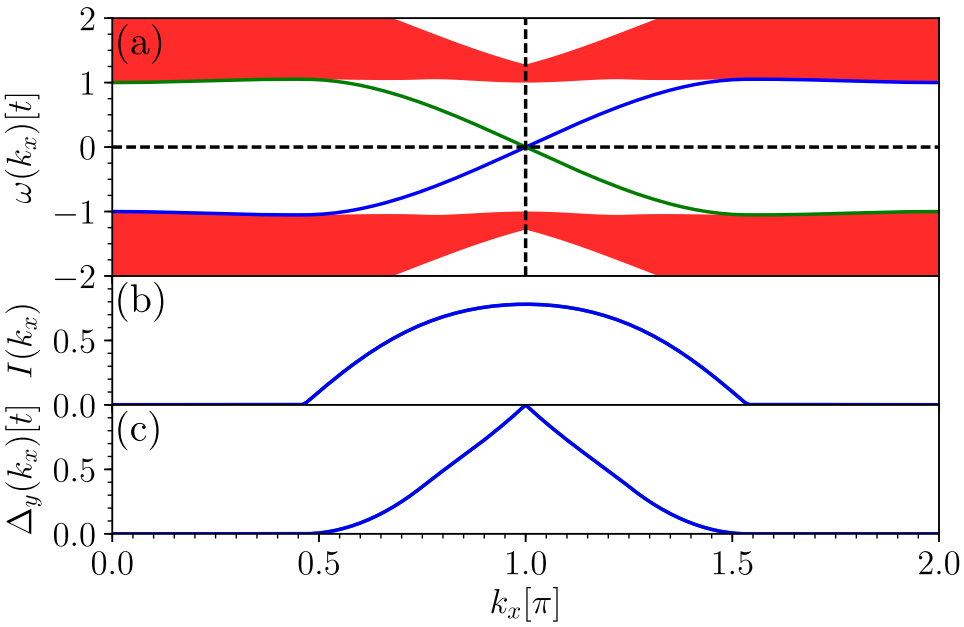

Figure 5.5: (a) Continua of the two bulk bands and dispersions of the in-gap states (right-mover in blue, left-mover in green) for $t_2 = 0.2t$, $\phi = \pi/2$, and $t_2' = 0$. The continua of the bulk bands are marked by filled red areas. (b) The IPR of both edge states as a function of wave vector k_x. (c) The indirect gap of the edge states Δ_y vs. wave vector k_x.

In all three panels, the blue curve refers to the right-mover and the green curve to the left-mover. Clearly, a finite value of Δ_y and a finite value of the IPR go along with each other. Hence the corresponding in-gap states are truly localized edge states, one at the top and one at the bottom of the strip. Due to reflection symmetry both edge states show the same IPR dependence. As a result, the blue and green curves in Fig. 5.5(b) and (c) lie on top of each other. We see that the IPR increases for increasing Δ_y upon variation of k_x, hence the localization length decreases.

Next, we study the effect of changing the indirect gap by turning on t_2' for real hopping, i.e., for $\varphi = 0$, see Fig. 5.6, and for imaginary hopping, i.e., $\varphi = \pi/2$, see Fig. 5.7. Since t_2' breaks the particle-hole symmetry, the left- and right-moving edge states differ from each

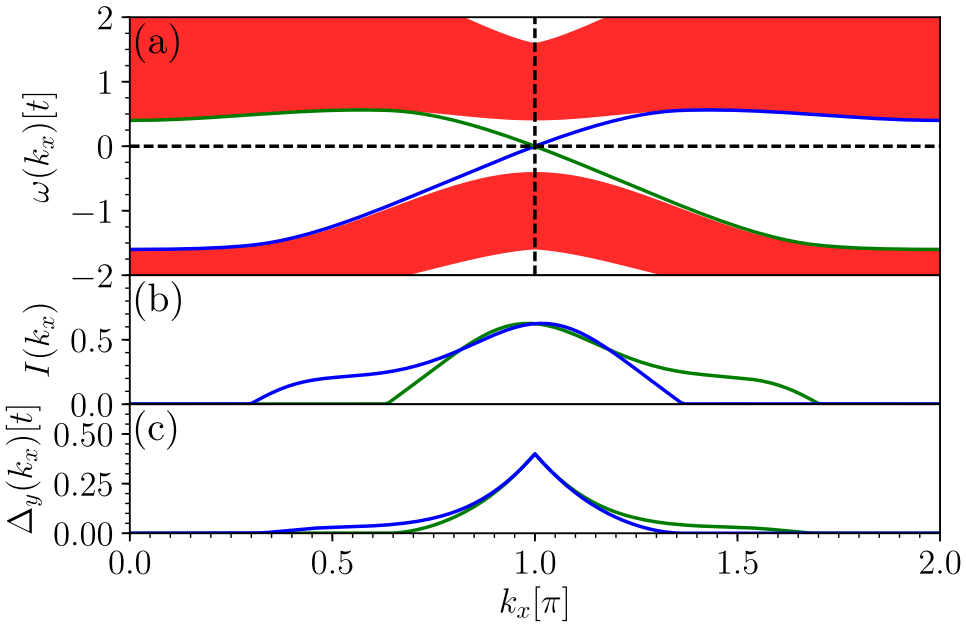

Figure 5.6: (a) Continua of the two bulk bands and dispersions of the two in-gap states (right-mover in blue, left-mover in green) for $t_2 = 0.2t$, $\phi = \pi/2$, $t_2' = 0.3t$, and $\varphi = 0$, i.e., real NNN hopping. The continua of the bulk bands are marked by filled red areas. (b) The IPR of both edge states as a function of wave vector k_x. (c) The indirect gap of the edge states Δ_y vs. wave vector k_x.

other for $t_2' \neq 0$.

Figure 5.6(a) depicts exemplary results which show that the conduction band edge is lowered such that the indirect gap Δ_y and the IPR vanish earlier for the right-movers for $k_x > \pi$ and for the left-movers for $k_x < \pi$. In contrast, the valence band is lowered such that the energy range for distinct edge states is increased. Thus, Δ_y becomes finite in additional regions, namely for smaller k_x for the right-movers and for larger k_x for the left-movers. This is particularly evident in comparison to Fig. 5.5. As a consequence, the curves for the IPR and for the indirect gaps no longer have axial symmetry about $k_x = \pi$ or $k_x = 0$, see Fig. 5.6(b) and (c). But reflection about one of these axes interchanges right- and left-movers. Consequently, the localization analysis of one edge state as shown in Fig. 5.3 is still sufficient.

For completeness, we illustrate the delocalization of edge states as a result of imaginary diagonal hopping for $\varphi = \pi/2$. This hopping alters the edges of the bulk continua considerably spoiling, their axial symmetry. The dispersions and the bulk edges are inversion symmetric with respect to $(\pi, 0)$ as can be seen in Fig. 5.7(a). Thus, the IPR of an edge state is axial symmetric with respect to $k_x = \pi$ or $k_x = 0$. As for the case of real hopping, only a finite indirect gap Δ_y yields a finite value of the IPR in the thermodynamic limit $N \to \infty$. We point out that the imaginary hopping has a different impact on the localization than the real hopping. For instance, the IPRs for the edge states at $k_x = \pi$ are different while their indirect gaps are the same. Hence it is clear that there is no general relation between both quantities. Of course, this was to be expected since the IPR is dimensionless while the indirect gap has the unit of an energy. Clearly,

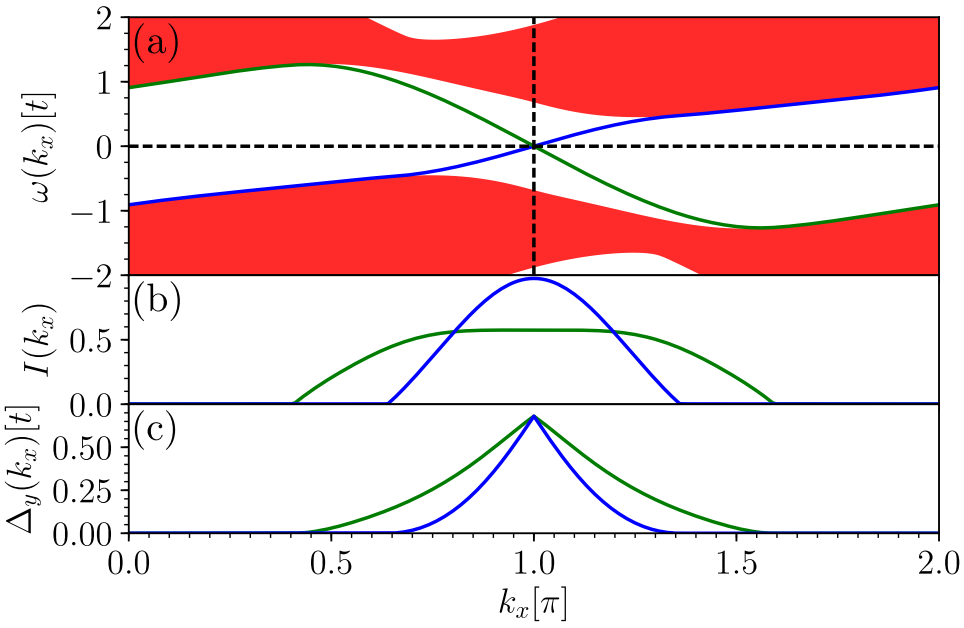

Figure 5.7: (a) Continua of the two bulk bands and dispersions of the two in-gap states (right-mover in blue, left-mover in green) for $t_2 = 0.2t$, $\phi = \pi/2$, $t_2' = 0.3t$, and $\varphi = \pi/2$, i.e., imaginary NNN hopping. The continua of the bulk bands are marked by filled red areas. (b) The IPR of both edge states as a function of the wave vector k_x. (c) The indirect gap of the edge states Δ_y vs. wave vector k_x.

a velocity v and the lattice constant a must enter in a quantitative relation between IPR and Δ_y.

Due to the broken reflection symmetry of the dispersion, the two edge states display different dependencies. The IPR of the edge states as a function of t_2' is shown in Fig. 5.8. Inspecting the IPR of the right-moving edge state at $k_x = \pi$, one discerns that the IPR first increases for increasing t_2' despite the decrease of the indirect gap Δ_y. Thus, it is corroborated that the localization does not only depend on the indirect gap Δ_y. But, just as in the case of real hopping, the vanishing of the indirect gap induces delocalization. Note that the eigenstates at $k_x = \pi$ are doubly degenerate; nonetheless their IPRs are different. In addition, the IPRs of both edge states depending on t_2' are presented in Fig. 5.8. Qualitatively, the relations between the IPRs and the indirect gaps Δ_y are similar to the relations in the case of a real hopping.

The case of $\varphi = \pi/2$ confirms our conclusion that the vanishing of the indirect gap Δ_y goes along with delocalized in-gap states. Both quantities are not linked by a simple monotonic relation because better localized states may have a smaller Δ_y.

In addition, we find that if the additional hopping runs along x and not along y, the additional term reads $2t_2' \cos(k_x + \varphi)\sigma_0$ and changes neither the bulk topology nor the localization in the strip in Fig. 5.1. Thus due to the anisotropy, we clearly see that the choice of different directions for the boundary with respect to the t_2'-hopping has fundamentally different effects.

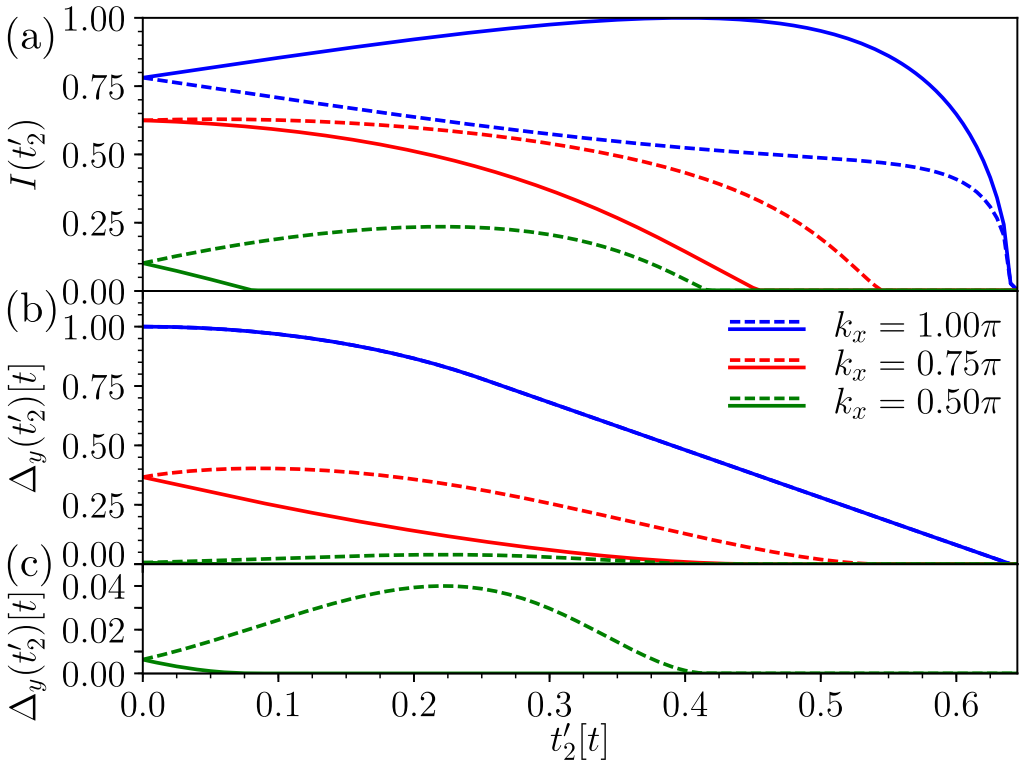

Figure 5.8: (a)-(b) The IPR and Δ_y of both edge states vs. hopping parameter t_2' for various wave vectors k_x. The values of the right-moving edge state are shown as solid lines while the dashed lines belongs to the left-moving edge state. For Δ_y at $k_x = \pi$, they lie on top of each other. Panel (c) shows the function Δ_y at $k_x = 0.5\pi$ with an adapted scale for the sake of a clear presentation.

We point out that different boundaries imply different edge state dispersions. For instance, a bearded boundary[2] [113] in the Haldane model has its crossing point at $k_x = 0$ implying a different $\Delta_y(k_x)$ so that the localization persists up to larger values of t_2'.

5.3. Delocalization in the topological checkerboard model

The standard lattice studied above has provided a proof-of-principle result allowing us to establish the importance of indirect gaps for the localization of in-gap states so that they represent true edge states. In order to corroborate that this scenario is generic and experimentally relevant, we next address the topological checkerboard lattice, see Fig. 5.9, which has been realized by optical lattices [203–205].

[2] A bearded boundary corresponds to a zigzag boundary where each outermost site is coupled to one additonal site, see for instance Fig. 3.1.

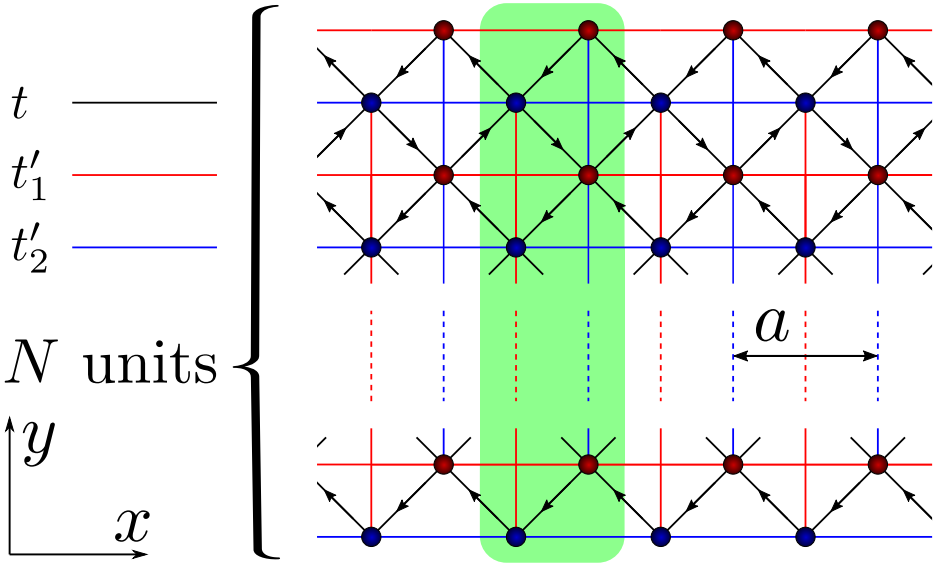

Figure 5.9: Checkerboard strip with NN hopping (black bonds). Hopping in the direction of the arrows has a positive sign. The red (blue) line represents t_1' (t_2') hopping. The lattice constant a is set to unity.

The topological checkerboard lattice is described by a two-band model [206] with NN (t) and NNN (t_1', t_2') hoppings

$$\mathcal{H} = -t \sum_{\langle i,j \rangle} \mathrm{e}^{\pm \mathrm{i}\phi} c_i^\dagger c_j - \sum_{\langle\langle i,j \rangle\rangle} t_{ij}' c_i^\dagger c_j \quad . \tag{5.5}$$

For the bulk, Fourier transformation yields a representation in terms of Pauli matrices

$$\begin{aligned} \mathcal{H} = & -s(\cos(k_x) + \cos(k_y))\sigma_0 \\ & -d(\cos(k_x) - \cos(k_y))\sigma_z \\ & -4t\cos(\phi)\cos(k_x/2)\cos(k_y/2)\sigma_x \\ & -4t\sin(\phi)\sin(k_x/2)\sin(k_y/2)\sigma_y \quad , \end{aligned} \tag{5.6}$$

where we use $s := t_1' + t_2'$ and $d := t_1' - t_2'$ for brevity and t as energy unit. A topological phase occurs for $\phi \neq n\pi$ and $d \neq 0$ [206]. Investigating the strip sketched in Fig. 5.9, one clearly sees the left- and right-moving in-gap states shown in panel (a) of Fig. 5.10. Tuning s while keeping d constant, the bulk topology is not changed, but the dispersion changes, just as for the Hamiltonian (5.1). Indeed, we find the same scenario as in Fig. 5.3, see panels (b) to (d) in Fig. 5.10. This strongly corroborates our findings and paves the way to their experimental verification.

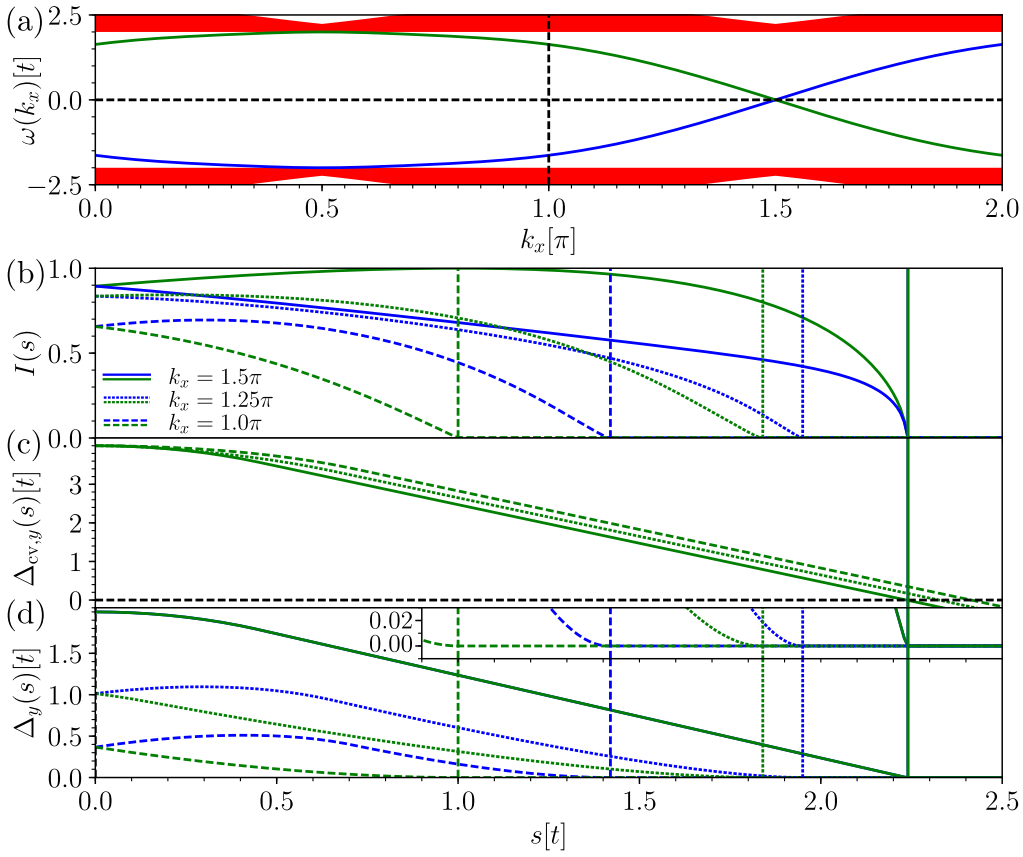

Figure 5.10: (a) Dispersions for $s = 0$, $d = -t$, and $\phi = \pi/4$. The continua of the bulk bands are shown as red areas. (b)-(d) The IPR, $\Delta_{\mathrm{cv},y}$, and Δ_y of the right-moving and left-moving edge states vs. the parameter s are shown for various wave vectors k_x as computed for $N = 500$. The Δ_y of both edge states at $k_x = 1.5\pi$ lie on top of each other.

For completeness, we present the localization behavior of the checkerboard model as a function of k_x. As complement to the plots shown above, Fig. 5.11 displays the continua, the dispersions, the IPR, and the indirect gap for the case where localized edge states are present for $s = 0$, $d = -t$, and $\phi = \pi/4$. The bulk continua are depicted in Fig. 5.11(a) by the red shaded areas, while the dispersions of the right- and left-moving in-gap states are displayed in blue and green. The corresponding IPRs of the in-gap states are shown in Fig. 5.11(b). The IPR is finite over almost the entire BZ. This is consistent with the finite values of the related indirect gap Δ_y in panel (c). As a result of the reflection symmetry, the blue and green curves in Fig. 5.10(b) and (c) lie on top of each other as in the original Haldane model.

By tuning s from 0 to $2.5t$ the indirect gap is closed. The continua and dispersions for $s = 2.5t$, $d = -t$, and $\phi = \pi/4$ are plotted in Fig. 5.12. The upper and lower bands overlap everywhere in the BZ. As a result, the indirect gap is closed and the in-gap states are delocalized for all wave vectors k_x. Hence, there are no edge states in the proper sense of the word.

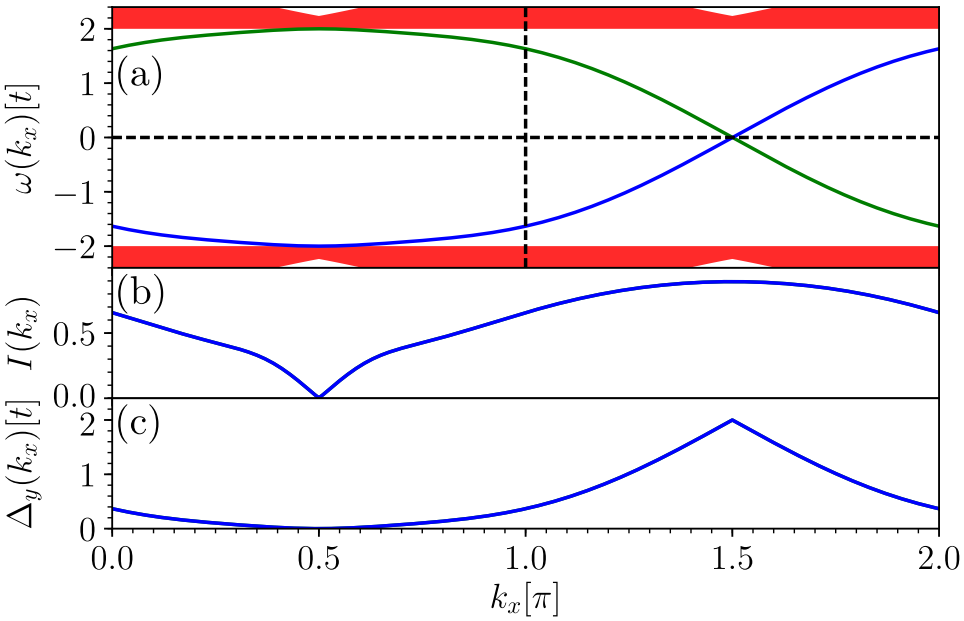

Figure 5.11: (a) Continua of the two bulk bands and dispersions of the two in-gap states for $s = t$, $d = -t$, and $\phi = \pi/4$. The continua of the bulk bands are marked by filled red areas. (b) The IPRs of both edge states as a function of the wave vector k_x. (c) The indirect gap of the edge states Δ_y vs. the wave vector k_x.

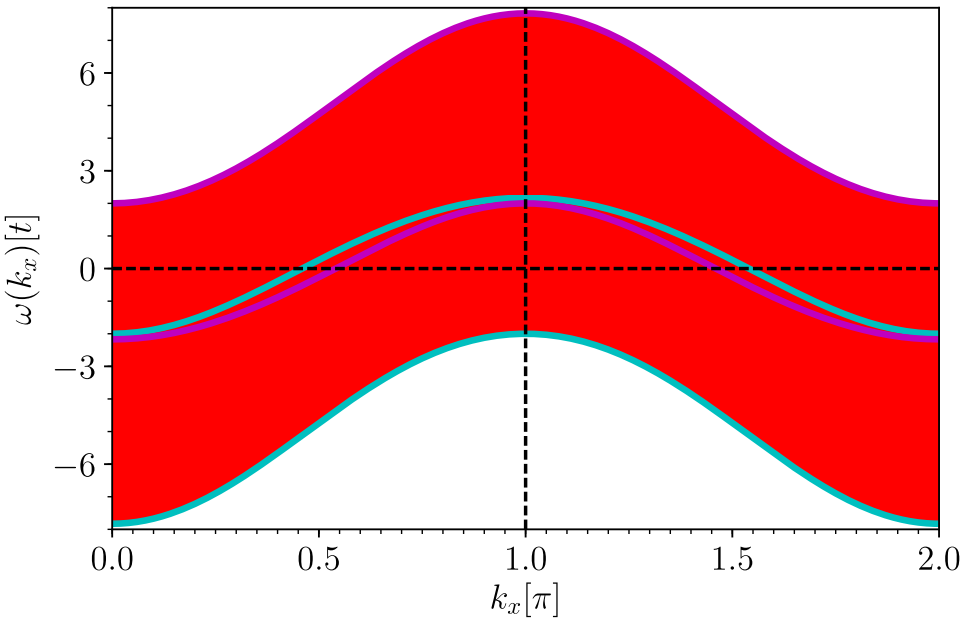

Figure 5.12: Continua of the two bulk bands for $s = 2.5t$, $d = -t$, and $\phi = \pi/4$; they are marked by filled red areas. The band edges of the continua are displayed in magenta for the conduction band and in cyan for the valence band.

5.4. Delocalization of chiral edge states

Edge modes are mostly considered and computed for infinite strip geometries because they allow one to consider models which preserve one translational symmetry. The edge modes can be identified easily by looking for gapless dispersion branches between two bulk bands. For finite samples which are confined in all directions the analysis becomes more intricate because the lack of any momentum conservation makes it difficult to identify the energies of edge modes in the energy spectrum.

A possible solution is to deduce the indirect energy gap in the bulk allowing for changes of all wave vectors if it is finite. Energies of the finite sample lying within the energy window given by the finite indirect gap are associated to edge modes. This method can be used for topological insulators with appropriate finite indirect gaps, but it fails if the indirect gap closes or if the system enters the phase of a topological metal [207].

The edge mode in a finite sample is localized along the entire boundary and the particle in such a state is propagating only in one direction as shown in Fig. 5.13. Such edge modes are called chiral edge modes. The number of sites close to the boundary relative to the total number of sites N_{tot} is small for large samples and tends to zero for $N_{\mathrm{tot}} \to \infty$. This fact opens up the possibility to identify edge modes by their IPR: the states with the largest IPRs are the best localized ones which are to be found along the boundary. Note, however, that this approach does not work for disordered samples where fully localized states may exist in the bulk.

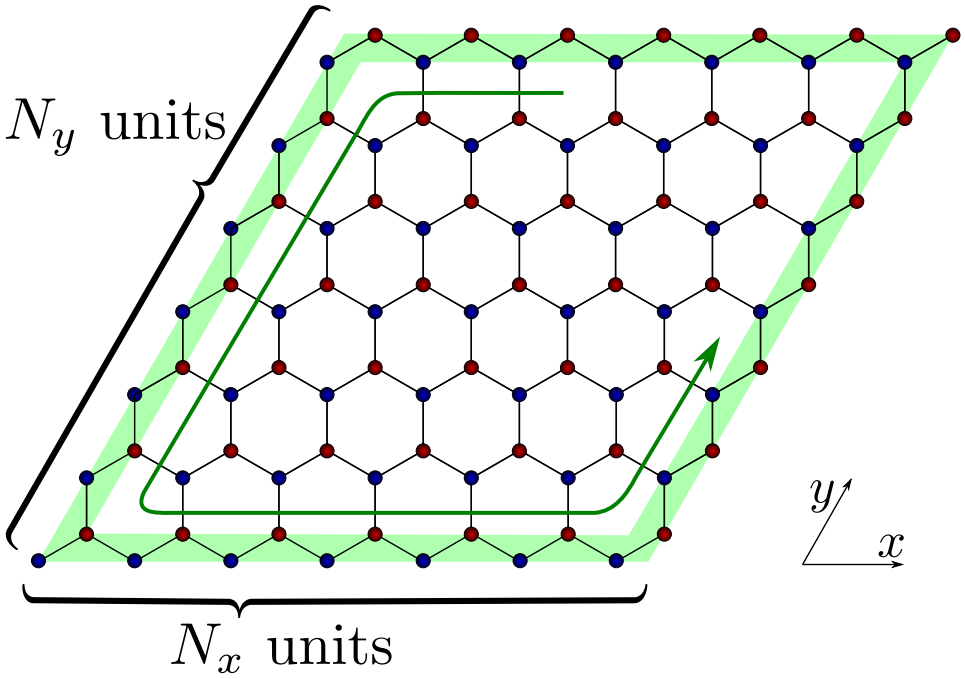

Figure 5.13: Sketch of a finite sample geometry. The localization area of a chiral edge state is highlighted in green. A possible orientation of the chirality is indicated by the green arrow.

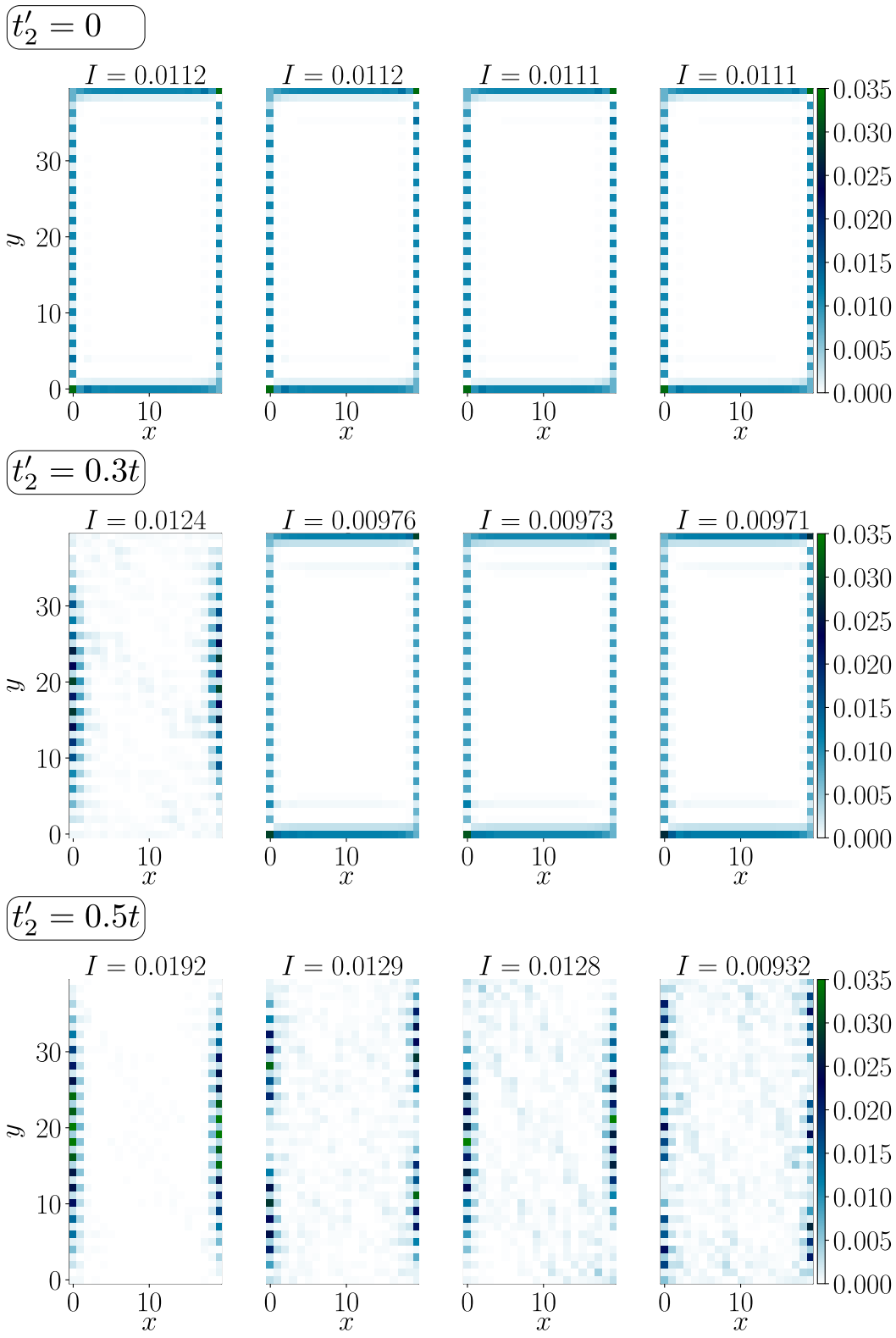

Figure 5.14: Probabilities in a 2D sample with $2N_x \times N_y = 2 \cdot 20 \times 20 = 800$ sites. The four eigenstates with the largest IPRs are depicted in each row at $t_2 = 0.2t, \phi = \pi/2, \varphi = 0$ for $t_2' = \{0, 0.3t, 0.5t\}$, respectively.

Here, the IPR of an eigenstate is defined as

$$I_n = \sum_i p_{n,i}^2 \tag{5.7a}$$

$$= \sum_i |\langle n, i | n, i \rangle|^2 \quad \in [0,1] \quad , \tag{5.7b}$$

where the sum runs over *all* sites of the sample. Fig. 5.14 depicts the probabilities of the four eigenstates with the highest IPRs for $t_2' = \{0, 0.3t, 0.5t\}$ in a finite 2D sample. The case $t_2' = 0$ corresponds to the original Haldane model with its known topological characteristics. As expected, all four eigenstates display localization along the complete boundary indicating that they are indeed chiral states. Increasing t_2' implies that less and less eigenstates show finite probabilities along the complete boundary. But as long as there is a finite indirect gap between the conduction and the valence band chiral edge states exist.

At $t_2' = 0.5t$, the indirect gap has vanished. Indeed, no chiral edge states can be found anymore. The displayed eigenstates in Fig. 5.14 are localized at edges running along the y-direction because this localization is not altered by the diagonal hopping t_2' as we observed already with the roles of x and y interchanged in Sec. 5.2. But we stress that the localization at the edges running in x-direction is completely eradicated due to the diagonal hopping t_2' as expected from the calculations for the strip geometry. Thus, we find that chiral edge states become extended precisely if the in-gap states delocalize along one of the edges.

In addition, we want to mention that the IPR is only used to identify the eigenstates with the strongest localization. However, the IPR in finite samples which are confined in all directions cannot be used to distinguish between the existence or non-existence of chiral edge states. Because if we increase the size of these samples the boundary and their chiral edge states will increase as well. Thus the IPR of chiral edge states vanishes for increasing system sizes, $I_n \to 0$ for $N_{\text{tot}} \to \infty$.

5.5. Conclusion

Summarizing, non-trivial topological properties of the bulk imply the existence of in-gap states. Often, they are supposed to be localized at the boundaries of the sample. But in generic one-particle models we showed that these edge states can delocalize if they are not protected by finite indirect gaps. This can be demonstrated mostly clearly by adding terms to the Hamiltonians proportional to the identity matrix. They change the dispersions but leave the eigenstates and hence the topological properties unchanged. We stress that this holds true independently of the number of bands. This result also implies the most important message that the omission of terms proportional to the identity matrix is acceptable for the bulk, but not for confined geometries.

For in-gap states of which the energy is protected by additional symmetries, it is sufficient to consider the bulk indirect gap $\Delta_{\text{cv},y}$. Generally, this gap is not sufficient to decide on localization and one has to consider the indirect gap Δ_y which measures the energetic distance of the in-gap states to the closest bulk band. Generically, if Δ_y is finite the states are localized and thus true edge states. If Δ_y vanishes, delocalization is to be expected.

While the described scenario is the generic one it can vary in special cases. Baum et al. [195] pointed out that further symmetries such as momentum and energy conservation can prevent delocalization in topological states of matter in spite of coupling edge states to a gapless bulk. Similarly, Verresen and co-workers [196] discovered edge states at the ends of critical chains. Independent of topological properties, it was noted that localization can persist notwithstanding hybridization with continua in especially designed systems [192]. The localization may be weak in the sense that it is not exponential, but algebraic [193].

Yet, the results presented here for standard one-particle topological models illustrate that delocalization of edge states is the generic phenomenon if indirect gaps vanish and hybridization with bulk continua occurs. To the best of our knowledge, this fact has not yet been appreciated in literature even though it has important consequences for realizations of topological phases and their experimental detection. The key message is that the lack of localized edge modes does not preclude the existence of non-trivial topology characterized by discrete topological invariants. Then, however, direct techniques to detect topological invariants are required [87, 208, 209].

To pave the way towards experimental verifications by ultracold atoms in optical lattices, we considered the topological checkerboard model explicitly. Further preliminary results show that the advocated scenario also occurs in the Kane–Mele model including Rashba couplings as a prototypical model with a $\mathbb{Z}_2$ topological invariant.

6. Topological magnon bands in the ferromagnetic Shastry–Sutherland model

Parts of this chapter have been published in Physical Review B [210]. Götz S. Uhrig contributed to the manuscript and the interpretation of the results. I created all figures and calculated all the data.

6.1. General context

Topological phases [29, 30] exist in both fermionic and bosonic systems and constitute a fast developing research area. Although the theoretical understanding of fermionic topological systems has made impressive progress, topological bosonic excitations have gained considerable attention only in the past few years. Despite the increasing conceptual knowledge of topological matter, just very few materials have been identified with topological properties compared to the large number of potential topological materials [3]. Even less is known about potential applications. This is, in particular, true for topological bosonic signatures [163]. Thus, it is a major challenge to theoretically predict and experimentally verify topological bosonic fingerprints in order to move towards useful applications.

In the research on topological properties in condensed matter, the magnetic degrees of freedom have attracted more and more attention. Magnetic data storage is already a ubiquitous everyday technology [211] as for instance hard disk drivers. Recently, magnetic spin waves, so-called magnons, themselves are used to carry and to process information which is called "magnonics" [165, 212, 213]. Adding topological aspects, the field of magnonics [214] considerably enhances the possibilities to build efficient devices for which we will make a proposal below in this section.

The inclusion of DM interaction terms are often proposed to identify the topological properties in magnetic systems. Because DM couplings play an important role in topological excitations in magnetic systems similar to SOC in fermionic systems. However, the challenge in finding topological signatures in magnetically ordered spin systems are the small DM interactions [176, 215] which induce only small Berry curvatures. The size of the DM terms relative to the isotropic coupling is roughly as large as $|g-2|/2$, i.e., the deviation of the g factor from 2, because both result from SOC. Thus, the DM terms are generically too small to induce experimental detectable topological effects. In strongly frustrated systems, however, the relative size of the DM terms can indeed be comparable to the isotropic couplings [171].

Another issue is the localization of edge modes. Employing the wording of semiconductor physics, one must distinguish direct (at fixed wave vector) and indirect gaps (allowing for changes in the wave vector). The existence of direct gaps throughout the BZ is sufficient to separate bands so that their topological properties are well defined. But the vanishing of the indirect gap generically implies that the edge states are not localized

anymore, i.e., the bulk-boundary correspondence with respect to localization does not hold anymore [191]. This was one of the main findings of the previous chapter.

In magnetic systems, three types of elementary excitations occur. Long-range ordered magnets display magnons (or spin waves) [216], valence-bond crystals mostly feature triplons [180], whereas quantum spin liquids may display fractional excitations [217], for instance spinons [218]. For triplons, topological behavior, i.e., non-zero Chern numbers [1], were predicted in Shastry–Sutherland lattices [99, 168] and in spin ladders [187]. The topological triplon excitations in the Shastry–Sutherland lattice have been verified in the sense that the theoretical calculations coincide with the experimentally measured inelastic neutron scattering data [169]. For ferromagnetically ordered systems, topological magnons are theoretically suggested in kagome lattices [162, 167], pyrochlore lattices [166], and in honeycomb lattices [219, 220]. For antiferromagnets, they are proposed in pyrochlore lattices [221], square, and cubic lattices exploiting the Aharonov–Casher effect [214]. In analogy to the QHE [19], the magnon Hall effect [163] as well as the triplon Hall effect [99] arise since the topological Berry curvature acts analogously to a magnetic field. So far, only the magnon Hall effect was observed [163, 222]. Topologically non-trivial spinons are discussed in Mott insulators [223, 224] as well as in quantum spin liquids [162, 225, 226].

The Shastry–Sutherland model [227] is commonly studied with antiferromagnetic couplings leading to triplon excitations [228]. Including DM interactions combined with a transverse magnetic field induces topological properties [99, 168] where the magnetic field is also used as a control parameter to tune a topological phase transition. The Shastry–Sutherland lattice with purely ferromagnetic couplings also serves as a good platform for topological magnon excitations. To show this, is the first of the two main objectives in this chapter. The second one is to discuss compounds which are likely to realize this model and to point out possible applications.

6.2. Topological magnon excitations

This section is structured as follows. By exact spin wave theory we show that the ferromagnetic Shastry–Sutherland model with DM couplings has topological bands with non-trivial Chern numbers. The occurrence of a ferromagnetic ground state represents the spontaneous breaking of TRS. In combination with the DM interactions a finite Berry curvature is induced which can lead to finite Chern numbers. The degeneracy at the quadratic band crossing point (QBCP) is lifted, and a gap opens. The expected topologically protected edge states [45] are retrieved in strip geometry [44]. In order to guide the experimental verification of the magnon Hall effect, we compute the thermal Hall effect.

6.2.1. Possible compounds for realization

Real materials are always three-dimensional; so we look for the ferromagnetic Shastry–Sutherland model realized in layers of 3D materials. If the interlayer coupling is not too strong, the 3D quantum Hall system can be considered to be an ensemble of layered 2D quantum Hall systems so that it is sufficient to investigate 2D models. This statement will be supported later by discussing the effects of interlayer coupling, see Sec. 6.2.3.

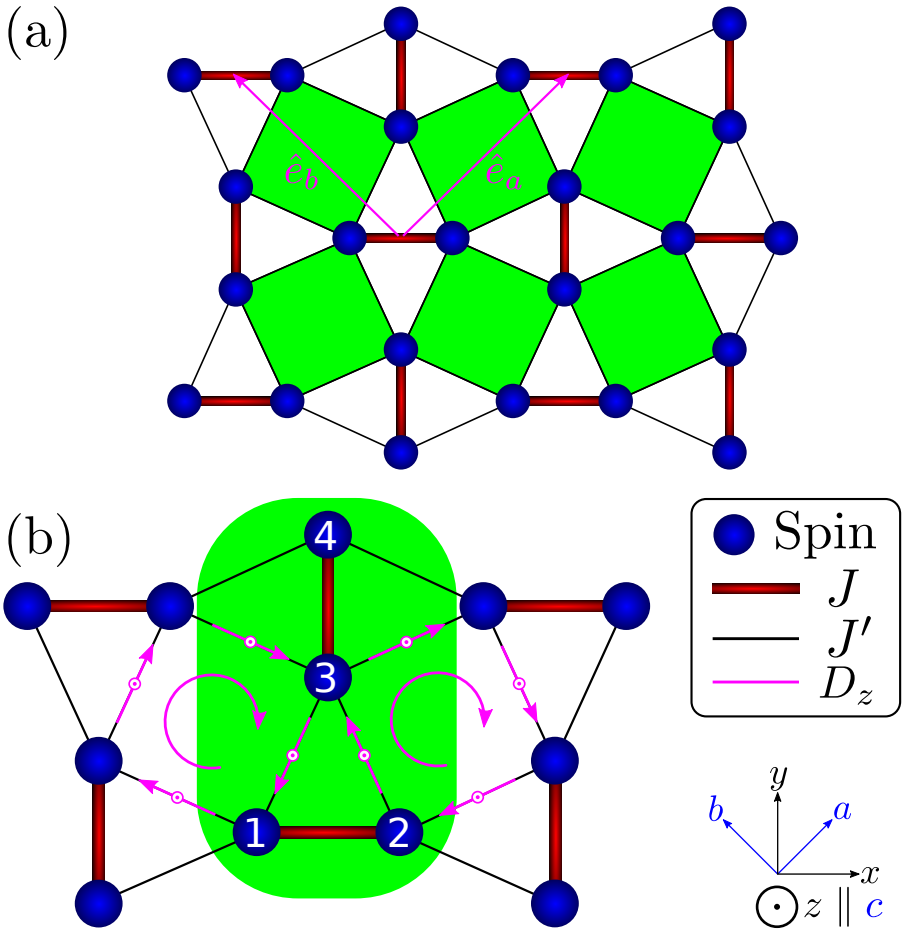

Figure 6.1: (a) Illustration of the 2D Shastry–Sutherland lattice. The NN couplings are shown as thick red lines, whereas the squares are highlighted in green. (b) The model studied comprises the Heisenberg couplings J and J' as well as the DM interaction D_z. The unit cell is highlighted in green. The sequence of the spins in the term $\boldsymbol{D} \cdot \boldsymbol{S}_i \times \boldsymbol{S}_j$ with $\boldsymbol{D} = D_z \hat{e}_z$ is shown by the arrow pointing from i to j. The DM couplings follow a clockwise rotation, see the circular arrows.

Layers of the Shastry–Sutherland lattice are found in various insulating magnetic materials since it is easily constructed from corner-sharing squares. The squares are not aligned parallel or perpendicular to one another so that dimers are formed, see Fig. 6.1(a). Due to the lack of inversion symmetry about the midpoints of the bonds, DM interactions are possible and generically occur from spin-orbit interactions. To reach large values of the DM couplings it is necessary to include atoms with large atomic number, because large electron velocities favor relativistic effects and hence SOC. Moreover, the couplings should be ferromagnetic so that it is advantageous to avoid linear bonds which would favor antiferromagnetic superexchange according to the Goodenough–Kanamori rules. Hence the Shastry–Sutherland lattice depicted in Fig. 6.1 appears promising if superexchange via larger subgroups does not occur which is what happens in $SrCu_2(BO_3)_2$ [228].

The following materials appear to be particularly interesting: RE_5Si_4 or RESi [229, 230] (RE=Gd, Dy, Ho, Er, Y). The compounds RE_5Si_4 have a Sm_5Ge_4-type structure, and

RESi has a FeB-type structure which both comprise planes of Shastry–Sutherland lattices. These compounds display a macroscopic magnetization $\boldsymbol{M}$ indicating dominant ferromagnetic couplings [229, 230]. In addition, the macroscopic magnetization clearly shows that one of the two degenerate ground states dominates, i.e., one domain prevails.

We compute the four bands from the unit cell with four sites shown in Fig. 6.1(b) in green. The DM couplings of the Shastry–Sutherland lattice can be directed in-plane or out-of-plane [99]. Usually, however, the out-of-plane couplings are assumed to dominate in 2D [99, 231]. In order to focus on a minimal model, we thus constrain the DM coupling to a uniform direction perpendicular to the plane $\boldsymbol{D} = D_z\hat{e}_z$ as shown in Fig. 6.1(b). Obviously, this introduces a chiral orientation. Single-ion anisotropy (SIA) $A^{\alpha\beta}$ ($\alpha, \beta \in \{x, y, z\}$) is typically present in ferromagnets with spins $S > 1/2$. For the minimal model, we consider it to favor easy-axis alignment along the z-axis, so that $A^{zz} = A \geq 0$. The SIA and the DM coupling compete because the latter profits from tilts away from the z-axis. Therefore we estimate cautiously up to which value of the DM interaction the collinear, fully polarized ferromagnetic order favored by the SIA represents the ground state of the model.

To obtain such an estimate we study two NNN spins coupled by J' as classical vectors of length S with polar angles θ_1 and θ_2 and relative azimuthal angle $\varphi := \varphi_1 - \varphi_2$ which takes the value $\tan\varphi = d := D_z/J'$ at the energy minimum E

$$2E/(J'S^2) = -a(1+xy)/2 - x - y - |x-y|\sqrt{1+d^2} \quad , \tag{6.1}$$

where $a := A/J'$, $x := \cos(\theta_1 + \theta_2)$, and $y := \cos(\theta_1 - \theta_2)$ with $|x|, |y| \leq 1$. The full derivation for this equation and its minimization are given in App. F. As long as $1 + a/2 \geq \sqrt{1+d^2}$, full polarization is optimal, i.e., a canted state can occur for $d \geq \sqrt{a + a^2/4}$ only, which is a conservative estimate because the effects of J, of quantum fluctuations, and of the geometric constraints in the lattice are not included. Hence, for small SIA and DM coupling the SIA wins and the fully polarized state is generic.

6.2.2. Topological magnons

The complete Hamiltonian of the minimal model consists of three parts

$$\mathcal{H} = \mathcal{H}_{\mathrm{H}} + \mathcal{H}_{\mathrm{DM}} + \mathcal{H}_{\mathrm{SIA}} \quad , \tag{6.2a}$$

where

$$\mathcal{H}_{\mathrm{H}} = -J \sum_{\langle ij \rangle} \left[\frac{1}{2}(S_i^+ S_j^- + S_i^- S_j^+) + S_i^z S_j^z \right]$$

$$-J' \sum_{\langle\langle ij \rangle\rangle} \left[\frac{1}{2}(S_i^+ S_j^- + S_i^- S_j^+) + S_i^z S_j^z \right] \tag{6.2b}$$

$$\mathcal{H}_{\mathrm{DM}} = -\frac{\mathrm{i}D_z}{2} \sum_{\langle\langle ij \rangle\rangle} (S_i^+ S_j^- - S_i^- S_j^+) \tag{6.2c}$$

$$\mathcal{H}_{\mathrm{SIA}} = -A \sum_i (S_i^z)^2 \tag{6.2d}$$

with ferromagnetic couplings $J, J' > 0$; J serves as the energy unit henceforth. A pair of NNs and of NNNs is denoted by $\langle ij \rangle$ and by $\langle\langle ij \rangle\rangle$, respectively.

We use the Dyson–Maleev representation of the spin operators [232, 233] which is exact as long as a single magnon above the fully polarized ground state is considered. But even for a macroscopic fraction of magnons, spin wave theory is well justified due to the large spins involved ($S \approx 4-5$ for {RE=Gd, Dy, Ho, Er, Y}). Note that large spins generically lead to large energy ranges with considerable gaps which are favorable for application. The bilinear Hamiltonian in momentum space reads

$$\mathcal{H} = \sum_{\boldsymbol{k}} \sum_{n,m} b^\dagger_{n,\boldsymbol{k}} H_{nm}(\boldsymbol{k}) b_{m,\boldsymbol{k}} \tag{6.3}$$

where $b^\dagger_n$ and b_n are the bosonic creation and annihilation operators, respectively, at the site $n \in \{1, 2, 3, 4\}$, see Fig. 6.1(b). The 4×4 Hamiltonian matrix is given by

$$H(\boldsymbol{k}) = \begin{pmatrix} A & B(\boldsymbol{k}) \\ B^\dagger(\boldsymbol{k}) & A \end{pmatrix} \tag{6.4}$$

with the 2×2 matrices

$$A = \begin{pmatrix} JS + 4J'S + A(2S-1) & -JS \\ -JS & JS + 4J'S + A(2S-1) \end{pmatrix} \tag{6.5a}$$

$$B = \begin{pmatrix} -C\ (1 + \mathrm{e}^{\mathrm{i}k_a}) & -C^*(\mathrm{e}^{\mathrm{i}k_a} + \mathrm{e}^{\mathrm{i}(k_a+k_b)}) \\ -C^*(1 + \mathrm{e}^{\mathrm{i}k_b}) & -C\ (\mathrm{e}^{\mathrm{i}k_b} + \mathrm{e}^{\mathrm{i}(k_a+k_b)}) \end{pmatrix} \quad , \tag{6.5b}$$

where $C := S(J' + \mathrm{i}D_z)$. We set the lattice constant to unity so that the wave vectors become dimensionless. Diagonalizing $H(\boldsymbol{k})$ yields four distinct magnon bands $\mathcal{H} = \sum_{n,\boldsymbol{k}} \omega_n(\boldsymbol{k}) \tilde{b}^\dagger_{n,\boldsymbol{k}} \tilde{b}_{n,\boldsymbol{k}}$ depicted in Fig. 6.2. The four bands form pairs p of two bands which are degenerate at the boundary of the BZ. We strongly presume that this degeneracy is linked to the point group symmetry of the Shastry–Sutherland lattice which consists of a vertical or horizontal translation shifting vertical dimers to horizontal ones and vice versa combined with a rotation by 90°. But unfortunately we did not find an analytic proof for this hypothesis. The whole lattice is C_4 symmetric considering rotations about the centers of the squares so that dispersions display the same symmetry.

Ferromagnetic Heisenberg models without spin anisotropic couplings such as SIA or DM coupling display gapless Goldstone bosons [234] with a quadratic dispersion at low energies at the Γ point. As soon as the SIA (A>0) is turned on, the continuous spin rotation symmetry is no longer broken spontaneously but externally, and a finite spin gap $A(2S-1)$ appears. Note the offset energy axis in panel (c) of Fig. 6.2. Spontaneously, the system chooses one of the two degenerate fully polarized ground states. The external symmetry breaking stabilizes the fully polarized ground state since it becomes energetically isolated from the remaining spectrum.

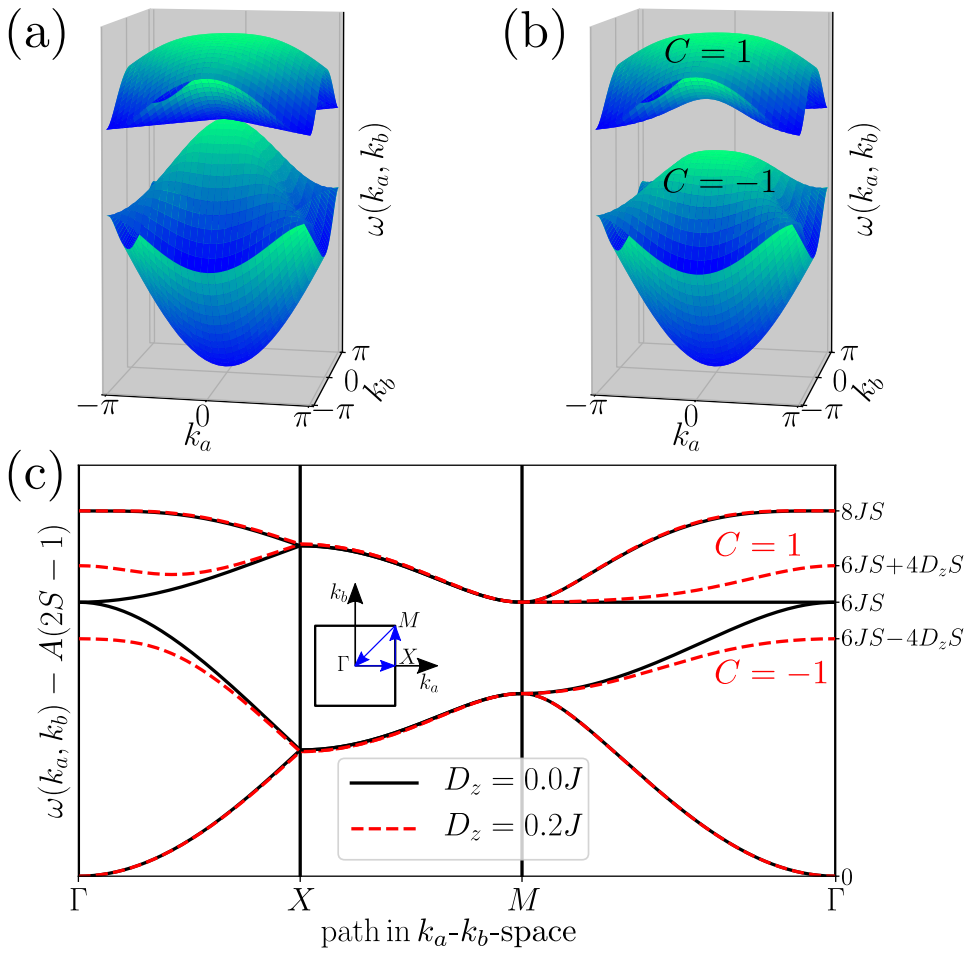

Figure 6.2: One-magnon dispersions for $J = J'$ for two values of the DM coupling. The critical case is $D_z = 0$ (panel (a) and black lines in panel (c)) where the QBCP at the Γ point is clearly visible. The degeneracy of the quadratic bands is lifted for finite $D_z > 0$ (panel (b) and red lines in panel (c)) so that distinct bands appear which show non-trivial topological Chern numbers $C = \pm 1$.

For vanishing DM coupling, two magnon bands cross quadratically at the Γ point at finite energies. Hence, the model displays an unusual QBCP. Generically, one can assign a Berry phase of π (or multiples of π) to them [235]. The QBCP is stable and can be interpreted as a pair of Dirac cones [236] which are superimposed due to the C_4 symmetry [235]. As a result, a QBCP can have a Berry flux of 0 or $\pm 2\pi$. The QBCP can either be removed by breaking the C_4 symmetry which splits it into an even number of Dirac cones or by lifting its degeneracy, e.g., by opening a gap leading to topologically non-trivial bands. Turning on the DM interaction ($D_z \neq 0$) induces the latter scenario. But, as shown in Fig. 6.2, the degeneracy of the upper pair of bands and of the lower pair of bands at the boundary of the BZ persists so that no Chern number of a single band can be defined. Hence, we define the Chern number of subspaces by taking the sum over the Berry curvatures in each subspace [168, 237] which derives from the Berry phase of the determinants of unitary transformations along closed paths [49]. Denoting the Chern

number of a pair of bands by $C^{(p)}$ where p stands for "upper" or "lower" one has

$$C^{(p)} = \frac{1}{2\pi} \iint_{\mathrm{BZ}} \sum_{n \in p} F_{n,ab}(\boldsymbol{k}) \, \mathrm{d}k_a \, \mathrm{d}k_b \quad , \tag{6.6}$$

where $F_{n,ab}$ is the Berry curvature of band n defined by

$$F_{n,ab}(\boldsymbol{k}) = \frac{\partial A_{n,b}(\boldsymbol{k})}{\partial k_a} - \frac{\partial A_{n,a}(\boldsymbol{k})}{\partial k_b} \tag{6.7a}$$

$$\text{with} \quad A_{n,\mu}(\boldsymbol{k}) = \langle \boldsymbol{k}, n | \, \nabla_{k_\mu} \, | \boldsymbol{k}, n \rangle \quad . \tag{6.7b}$$

The numerical robust calculation of the Berry curvature is performed by discretization of the BZ [97] avoiding the eigenstates precisely at the boundaries of the BZ. This is possible because the relevant curvature occurs in the vicinity of the Γ point anyway. The calculated Chern numbers of the pairs of magnon bands are $C^{(\text{upper/lower})} = \pm 1$ as shown in Fig. 6.2. Changing the sign of D_z reverses the sign of the Chern numbers. The non-zero Chern numbers can be attributed to the complex hopping stemming from the DM coupling leading to fluxes of fictitious fields [162, 222]. The direct gap between both pairs of bands occurs at Γ and is given by $8D_zS$ as long as $4D_z < J$. Otherwise, the direct gap is located at the M point and takes the value $2JS$. These relations highlight the importance of large spins and DM couplings for large gaps.

According to the bulk-boundary correspondence [1, 45], the existence of non-trivial Chern numbers implies topologically protected edge states [238]. For verification, we analyze a finite strip of $N = 50$ unit cells in b-direction and periodic boundaries in a-direction, see panel (c) in Fig. 6.3. The energy eigenvalues as a function of the well-defined wave vector k_a are depicted in panel (a) of Fig. 6.3. One can easily see two chiral edge states moving right and left according to the slope of their dispersion branches which connect the two continua shown in red. Additionally, panel (b) illustrates the localization of these modes at the lower (yellow curve and sites) and upper (blue curve and sites) edges of the strip.

6.2.3. Effects of interlayer couplings

In absence of detailed information about the structure and the magnetic couplings in the proposed three-dimensional materials we discuss that the effects of weak interlayer couplings do not destroy the topological properties put forward in the analyzed 2D model.

In our case, we assume that the system consists of stacked parallel planes, where each plane realizes a two-dimensional ferromagnetic Shastry–Sutherland model. The distinct planes are connected by a perpendicular interlayer coupling J_c. Since there is no detailed data on magnetic exchange paths for the proposed classes of materials [229, 230] we restrict the calculations to vertical couplings between the layers because they usually have the largest impact. As a result, the Hamiltonian in Eq. (6.2a) is extended by the additional term

$$\mathcal{H}_{\text{inter}} = -J_c \sum_{\langle ij \rangle} \left[\frac{1}{2} (S_i^+ S_j^- + S_i^- S_j^+) + S_i^z S_j^z \right] \tag{6.8}$$

with the ferromagnetic coupling $J_c > 0$. The notation $\langle ij \rangle$ indicates a coupling between NNs from adjacent layers. We apply the Dyson–Maleev representation [232, 233] and

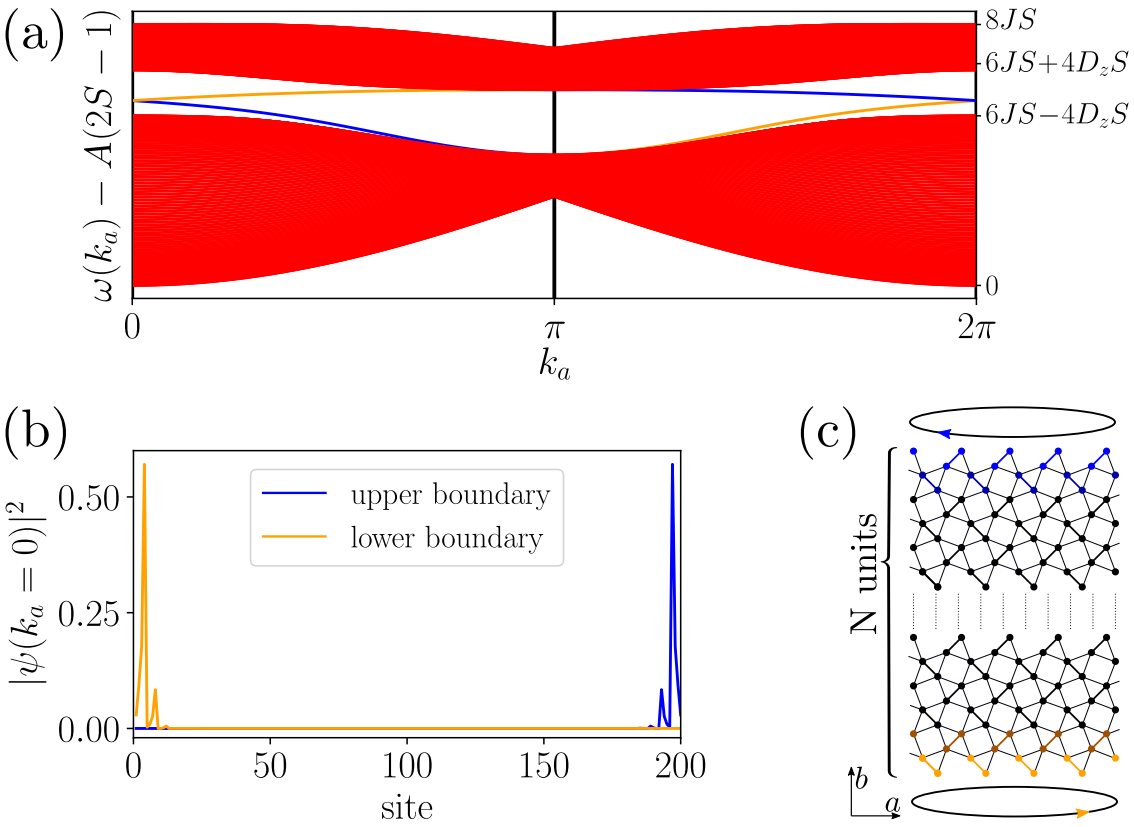

Figure 6.3: (a) Eigenenergies of a strip geometry, see panel (c), with $N = 50$, $J = J'$, $D_z = 0.2J$, and $A = 0.2J$. (b) Probability density $|\psi(k_a = 0, r_b)|^2$ as a function of the site r_b of both edge modes; the colors of their curves corresponds to the colors of the boundary sites in panel (c).

the Fourier transform to calculate the dispersion of the bosonic one-particle excitations within spin wave theory which is exact for single-excitations above the fully polarized ferromagnetic state. In this way, the interlayer term $\mathcal{H}_{\text{inter}}$ leads to to an additional 4×4-matrix given by $4J_cS\sin^2(k_c^2/2)\mathbb{1}$, i.e., proportional to the identity matrix.

From this we conclude that the ground states remains fully polarized since the finite spin gap remain at its value $A(2S-1)$ created by the SIA. The topological properties in the bulk remain the same as well, because terms proportional to the identity matrix obviously do not change the eigenstates. Since only the eigenstates determine the topological properties, the same Chern number in the k_a-k_b-plane will ensue, regardless of the strength of J_c, at each value of k_c. Note that only the k_a-k_b-plane in the 3D parameter space given by $\{k_a, k_b, k_c\}$ results in a quantized non-trivial Chern number. Thus the magnons realize a 3D quantum Hall system which can be considered as layered 2D quantum Hall system. Thus they are primarily described by their 2D properties, since only one of the planes has a topological character.

Concomitantly, we find edge states in the corresponding strip geometry for arbitrary k_c. The resulting dispersion is the same as shown in Fig. 6.3 with an additional overall shift proportional to $4J_cS\sin^2(k_c^2/2)$. The localization of the 3D edge states is identical to the one of the 2D eigenstates. The set of all localized edge states depending on k_a and k_c

represents the surface states.

Furthermore, indirect gaps can vanish due to the interlayer coupling. Note that the direct gap remains always finite which guarantees isolated bands in the bulk. The disappearance of the indirect gap can lead to delocalized in-gap states as discussed in Chap. 5 for 2D systems. The additional variation of the momentum k_c can close the indirect gap to the edge states which is denoted by Δ_c[1]. In this context, we ask the question whether the edge state stay localized or not by investigating a finite, confined system in two dimensions (b- and c-direction) and periodic in one dimension (a-direction), where the indirect gap Δ_c is closed. If the system is additionally confined in c-direction, the edge states could hybridize with bulk states which leads to delocalization. However, the vanishing of the indirect gap Δ_c does not lead to a delocalization in this case. This is explained by the direction of the interlayer coupling to the edge states. In Sec. 5.2.1 we mentioned that the direction of the couplings are crucial for the localization of edge states. This scenario represents a further example where the direction of the coupling preserves the localization while the edge states are energetically overlapped with other bulk states. In order to show this, we analyze a layered strip with $N_b = 25$ and $N_c = 4$ (film system with four layers thickness) while the momentum k_a remains conserved.

The localization of one edge state is determined by the IPR [189]

$$I_n(k_a) = \sum_{\delta,b,c} = |\langle n, \delta, b, c | n, \delta, b, c \rangle|^2(k_a) \in [0, 1] \quad , \tag{6.9}$$

where δ denotes the site within a unit cell and (b, c) the unit cell itself. Since we couple four layers with each other and each layer has two boundaries, we assume the presence of eight edge states. Therefore, we highlight the eight eigenstates in Fig. 6.4(a) with blue lines which have the largest IPR at each k_a. As a result, we can emphasize the localized in-gap states which are mostly covered by bulk states. Nonetheless, the edge states remain localized at the boundary in b-direction as shown for instance in panel (b) of Fig. 6.4. We can understand this localization behavior by considering the vertical couplings between the layers with the edge states. The couplings are perpendicular to the layers but they do not point into the bulk. Since this vertical coupling is parallel to the boundary, the edge states primarily hybridize with each other and not with bulk states which therefore leads to surface states. Such a surface state corresponds to a superposition of all edge states in each layer which can be seen for instance Fig. 6.4(b). This explanation is in accordance with our investigation in Sec. 5.2. Note that in an small interval around $k_a = \pi$ in Fig. 6.4(a) it is not possible to find localized edge states. The same interval does not provide edge states in the single layer case, see dispersion in Fig. 6.3(a). Thus this interval only provides bulk states and thus the IPR fails to find a localized state which therefore leads to this strange behavior in the interval around $k_a = \pi$ shown in Fig. 6.4(a).

In conclusion, the investigation of an additional 3D perpendicular interlayer coupling shows that the topological edge modes persist and are not altered as long as the fully polarized ground state is preserved. Hence, for weak interlayer couplings the topological properties found in the 2D model also hold in three dimensions and thus the proposed materials are good candidates to search for realizations of 2D physics.

[1] We use the same convention as in Chap. 5, where the variation of k_y leads to the notion of Δ_y. Here we denote Δ_c for the indirect gap to the edge states with respect to the variation of k_c.

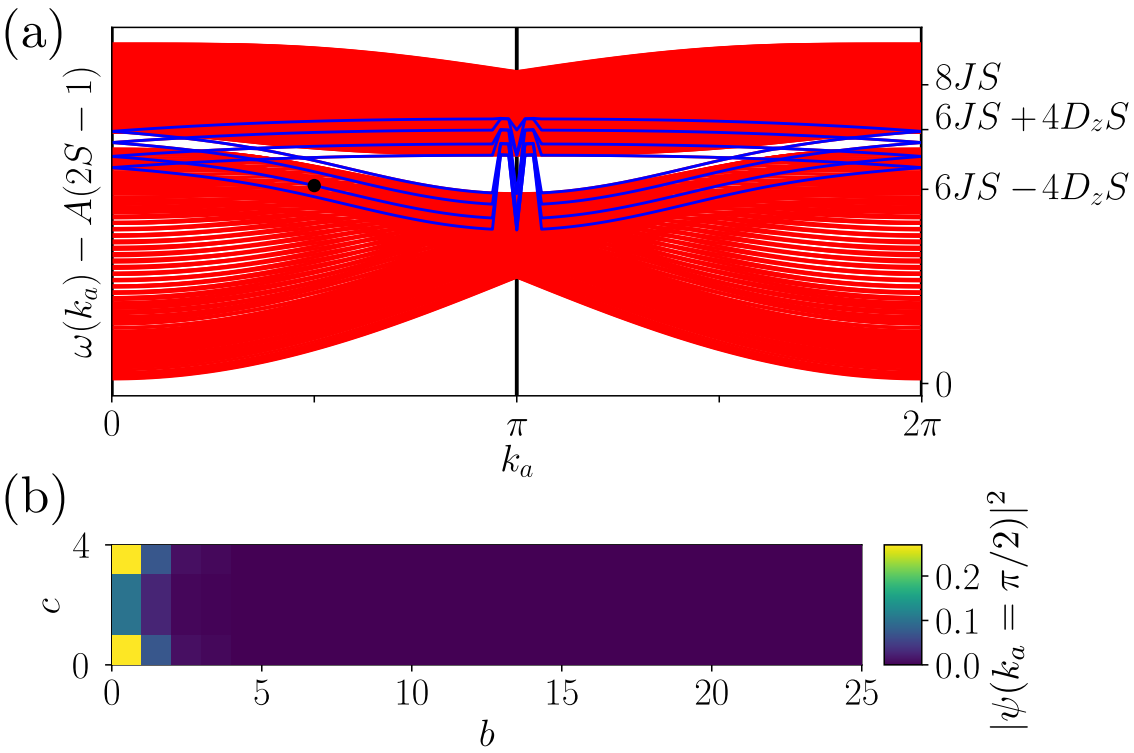

Figure 6.4: (a) Eigenenergies of a layered strip geometry with $N_b = 25$, $N_c = 4$, $J = J'$, $D_z = 0.2J$, $J_c = 0.3J$, and $A = 0.2J$. The eight eigenstates with the largest IPRs are highlighted in blue. (b) Probability density $\sum_{\delta\in\{1,2,3,4\}} |\psi_{\delta,b,c}(k_a = \pi/2)|^2$ as a function of the unit cell at (b, c); The probability density corresponds to the state of which the energy is depicted by the black circle in the dispersion in panel (a).

6.2.4. Thermal Hall effect

Next, we address possible experimental signatures. Since magnons do not carry charge, usual electric conductivity measurements do not make sense. The thermal Hall effect offers a way to detect non-trivial Berry curvatures in real materials. The thermal Hall effect consists of a finite gradient of the temperature perpendicular to a heat current. The expression for the transversal heat conductivity κ_{ab} [164] is given by

$$\kappa_{ab} = -\frac{k_\mathrm{B}^2 T}{\hbar} \sum_{n,\boldsymbol{k}} c_2(\rho_n) F_{n,ab}(\boldsymbol{k}) \quad , \tag{6.10}$$

where we sum over all magnon bands and set $k_\mathrm{B} = 1$ and $\hbar = 1$. The weight $c_2(\rho_n)$ is given by

$$c_2(\rho) = \int_{\varepsilon_n}^{\infty} \mathrm{d}\varepsilon\, (\beta\varepsilon)^2 \left(-\frac{\mathrm{d}\rho}{\mathrm{d}\varepsilon}\right)\Bigg|_{\mu=0} \tag{6.11a}$$

$$= -2\,\mathrm{Li}_2(-\rho) + \rho \log^2(\rho^{-1}+1) - \log^2(\rho+1) + 2\log(\rho+1)\log(\rho^{-1}+1)\ , \tag{6.11b}$$

where ρ is the Bose–Einstein distribution $(\exp(\beta\omega) - 1)^{-1}$ and Li_m is the dilogarithm for $m = 2$ (Spence's integral, in general). Equation (6.10) clearly shows that the transversal

heat conductivity κ_{ab} depends directly on the Berry curvature, thus it represents an ideal fingerprint of non-trivial topological properties. Figure 6.5 displays the results of Eq. (6.10) as a function of temperature for various values of D_z. For the topological phase ($D_z \neq 0$), the conductivity first slightly decreases to negative values before it strongly increases as a function of temperature. For high temperatures, κ_{ab} approaches a finite value. In comparison, the topologically trivial bands for $D_z = 0$ may have a finite curvature, but such that it cancels in the sum over the BZ so that κ_{ab} vanishes.

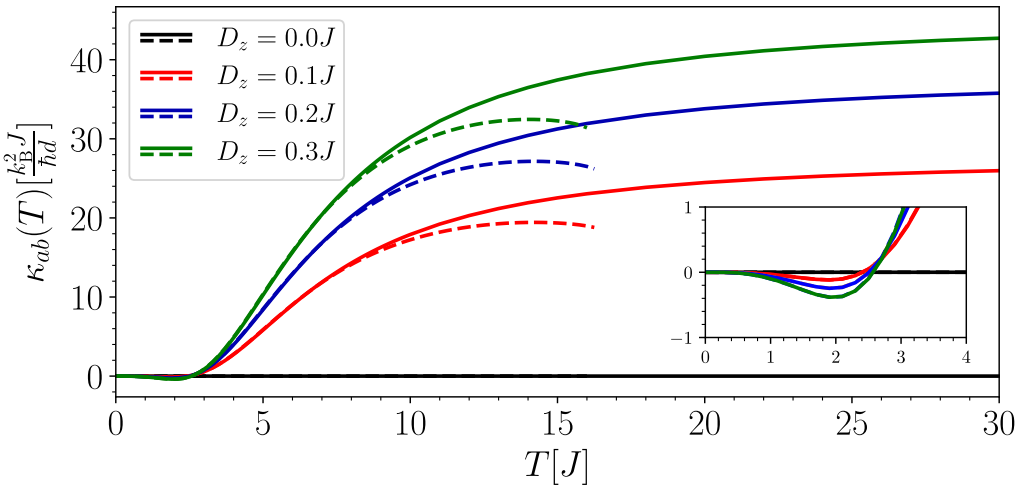

Figure 6.5: Thermal Hall conductivity κ_{ab} as a function of temperature for various values of the DM coupling D_z at $J = J'$, $A = 0.2J$, and $S = 4$. The solid lines correspond to the bilinear calculations whereas the dashed lines correspond to the mean-field calculations.

Since the magnetization generally decreases with increasing temperature until eventually the ferromagnetic phase ceases to exist at T_c, κ_{ab} should also decrease until it disappears at T_c. The temperature dependency of the static calculation of the transversal heat conductivity κ_{ab} stems only from the weight $c_2(\rho_n)$ and its contribution to κ_{ab} which is proportional to the Berry curvature $F_{n,ab}(\boldsymbol{k})$. This curvature, however, is independent of the temperature. In order to make quantitative statements, it is appropriate to improve the results for finite temperatures, i.e., to partly include the effects of finite T by applying self-consistent spin wave theory.

Here we use the Dyson–Maleev representation of the spin operators which leads to an exact description at the quartic level of operators and is given by

$$S_i^+ = \sqrt{2S}\left(b_i - \frac{1}{2S} b_i^\dagger b_i b_i\right) \tag{6.11a}$$

$$S_i^- = \sqrt{2S}\; b_i^\dagger \tag{6.11b}$$

$$S_i^z = b_i^\dagger b_i - S \quad . \tag{6.11c}$$

The complete Hamiltonian in bosonic representation is given by

$$\mathcal{H} = \mathcal{H}_{\mathrm{H}} + \mathcal{H}_{\mathrm{DM}} + \mathcal{H}_{\mathrm{SIA}} \tag{6.12a}$$

$$\mathcal{H}_{\mathrm{H}} = -J \sum_{\langle ij \rangle} S(b_i^\dagger b_j + b_j^\dagger b_i - b_i^\dagger b_i - b_j^\dagger b_j) \tag{6.12b}$$

$$+J \sum_{\langle ij \rangle} \frac{1}{2}(b_i^\dagger b_i^\dagger b_i b_j + b_j^\dagger b_j^\dagger b_j b_i) - b_i^\dagger b_j^\dagger b_i b_j$$

$$-J' \sum_{\langle\langle ij \rangle\rangle} S(b_i^\dagger b_j + b_j^\dagger b_i - b_i^\dagger b_i - b_j^\dagger b_j) \tag{6.12c}$$

$$+J' \sum_{\langle\langle ij \rangle\rangle} \frac{1}{2}(b_i^\dagger b_i^\dagger b_i b_j + b_j^\dagger b_j^\dagger b_j b_i) - b_i^\dagger b_j^\dagger b_i b_j$$

and with

$$\mathcal{H}_{\mathrm{DM}} = -\mathrm{i}D_z \sum_{\langle\langle ij \rangle\rangle} S(b_i^\dagger b_j + b_j^\dagger b_i)$$

$$+\frac{\mathrm{i}D_z}{2} \sum_{\langle\langle ij \rangle\rangle} (b_i^\dagger b_i^\dagger b_i b_j + b_j^\dagger b_j^\dagger b_j b_i) \tag{6.12d}$$

$$\mathcal{H}_{\mathrm{SIA}} = -A \sum_i (2S-1) b_i^\dagger b_i + b_i^\dagger b_i^\dagger b_i b_i \quad , \tag{6.12e}$$

where we neglected all constant terms. Applying a mean-field approximation reduces the quartic terms to bilinear terms. For this purpose, we introduce the expectation values

$$n = \left\langle b_i^\dagger b_i \right\rangle \in \mathbb{R} \tag{6.13a}$$

$$a = \left\langle b_i^\dagger b_j \right\rangle \in \mathbb{R} \quad \text{for } \langle ij \rangle \tag{6.13b}$$

$$c = \left\langle b_i^\dagger b_j \right\rangle \in \mathbb{C} \quad \text{for } \langle\langle ij \rangle\rangle \quad , \tag{6.13c}$$

where a corresponds to NNs and c to NNNs. The Fourier transformation of the mean-field Hamiltonian yields

$$\mathcal{H} = \sum_{\boldsymbol{k}} \sum_{n,m} b_{n,\boldsymbol{k}}^\dagger H_{nm}(\boldsymbol{k}, n, a, c)\, b_{m,\boldsymbol{k}} \tag{6.14}$$

with the bosonic creation $b_n^\dagger$ and annihilation operators b_n at the site $n \in \{1,2,3,4\}$. The Hamiltonian becomes implicitly temperature-dependent since the expectation values depend on the temperature. The 4×4 Hamilton matrix reads

$$H(\boldsymbol{k}) = \begin{pmatrix} A & B(\boldsymbol{k}) \\ B^\dagger(\boldsymbol{k}) & A \end{pmatrix} \tag{6.15}$$

with the 2×2 matrices

$$A = \begin{pmatrix} A_{11} & A_{12} \\ A_{21} & A_{22} \end{pmatrix} \qquad B = \begin{pmatrix} B_{11} & B_{12} \\ B_{21} & B_{22} \end{pmatrix} \quad , \tag{6.16}$$

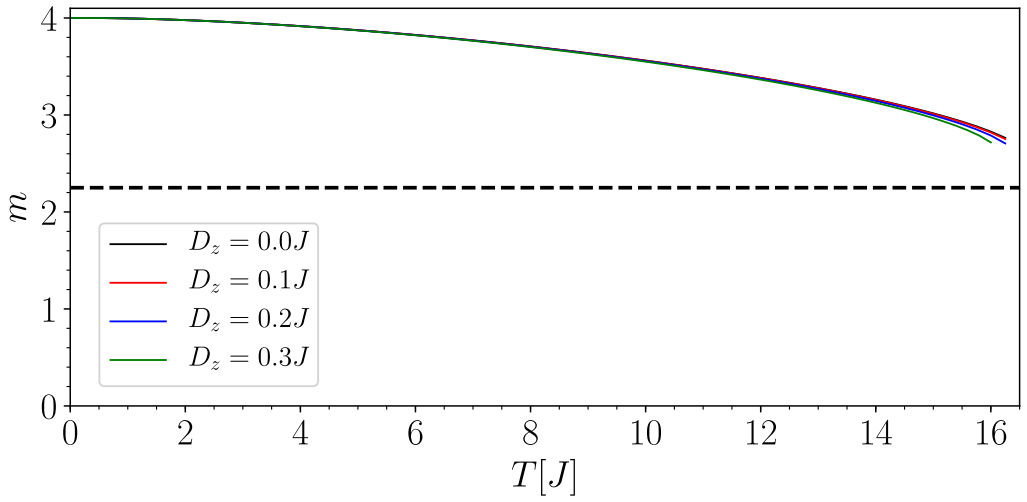

Figure 6.6: Magnetization as a function of temperature T for various values of D_z at $J = J'$, $A = 0.2J$, and $S = 4$. The horizontal dashed line indicates the value at which the spin gap closes.

where the matrix elements are given by

$$A_{11} = A_{22} = J(S - n + a) + 4J'(S - n + \mathrm{Re}(c)) + A(2S - 4n - 1) + 4D_z\mathrm{Im}(c) \quad (6.17a)$$

$$A_{12} = A_{21} = -J(S - n + a) \quad (6.17b)$$

$$B_{11} = -J'(S - n + c^*) - J'(S - n + c)\mathrm{e}^{\mathrm{i}k_a} - \mathrm{i}D_z(S - n)(1 + \mathrm{e}^{\mathrm{i}k_a}) \quad (6.17c)$$

$$B_{21} = -J'(S - n + c^*) - J'(S - n + c)\mathrm{e}^{\mathrm{i}k_b} + \mathrm{i}D_z(S - n)(1 + \mathrm{e}^{\mathrm{i}k_b}) \quad (6.17d)$$

$$B_{12} = -J'(S - n + c)\mathrm{e}^{\mathrm{i}k_a} - J'(S - n + c^*)\mathrm{e}^{\mathrm{i}(k_a + k_b)} + \mathrm{i}D_z(S - n)(\mathrm{e}^{\mathrm{i}k_a} + \mathrm{e}^{\mathrm{i}(k_a + k_b)}) \quad (6.17e)$$

$$B_{22} = -J'(S - n + c)\mathrm{e}^{\mathrm{i}k_b} - J'(S - n + c^*)\mathrm{e}^{\mathrm{i}(k_a + k_b)} - \mathrm{i}D_z(S - n)(\mathrm{e}^{\mathrm{i}k_b} + \mathrm{e}^{\mathrm{i}(k_a + k_b)})\,. \quad (6.17f)$$

By expressing the expectation values using the Bose–Einstein distribution, we are able to determine the renormalized dispersion self-consistently and the corresponding magnetization m at a specific temperature. The magnetization is given by the simple relation $m = S - n$. The renormalized spin gap Δ is purely determined by the SIA, which is given by

$$\Delta = A(2S - 4n - 1) \quad . \quad (6.18)$$

Obviously, the spin gap closes before the magnetization vanishes, so that in this approximation a Curie temperature cannot be determined. The spin gap closes for $2S - 4n - 1 = 0$. For the magnetization, this implies that the spin gap closes if the magnetization reaches the value $m = (2S + 1)/4$ as indicated by the horizontal dashed line in Fig. 6.6.

The self-consistently calculated magnetization shows the unexpected problem that no solution can be found for small values of the spin gap or the magnetization vanishes. It appears that the phase transition from the ordered phase induced by the SIA to the disordered phase cannot be captured by self-consistent spin wave theory. This issue deserves further investigations, but it is beyond the scope of this thesis.

The improved calculations by applying self-consistent spin wave theory show that the signature starts to decrease for higher temperatures before no self-consistent solution is

found anymore as depicted by the dashed lines (see Fig. 6.6).

6.3. Conclusion

The study of the Shastry–Sutherland lattice with purely ferromagnetic couplings shows that topological magnon bands are achievable if finite DM interactions are taken into account. The DM couplings lifts the QBCP which result in separated excitation bands with non-trivial Chern number. Due to bulk-boundary correspondence chiral edge modes occur. To this end, we proposed compounds as possible realizations of the investigated model.

A finite thermal Hall conductivity κ_{ab} can serve as a smoking gun signature in experiments to verify topological properties of a magnetic material under study. In order to obtain large signals, we recommend the experimental preparation of a single-domain crystal in order to avoid cancellation effects.

In view of the above findings, we suggest characterizing the magnetic properties of the putative realizations [229, 230] of ferromagnetic Shastry–Sutherland lattices in detail, for instance by inelastic neutron scattering. This will help to determine the relevant microscopic model which, in turn, will render the calculation of the Berry curvature possible. In parallel, measurements of the thermal Hall conductivity can provide evidence [163, 222] for finite Berry curvatures.

The usage of topological magnon excitations represents a promising approach to improve magnonic devices. The field of magnonics attempts to create devices in magnetic nanostructures which are able to carry and process informations. To this end, the application of topological magnon excitations can take magnonics to the next level since bosonic topological excitations have a chiral nature and are assumed to be robust against disorder. Hence, less dissipation will occur if topological properties are included.

Most concepts for processing magnonic excitations are based on interference effects [239]. To this reason, we propose to tailor the edges of strips of the system by decorating them similarly to what we proposed and computed for fermionic models in Chap. 3. In this way, largely different group velocities can be achieved depending on the direction in which signals of packets of magnons travel. The key is to structure upper and lower boundaries of a strip in a different manner so that the group velocities of the right- and of the left-moving packets are very different. Ideally, the group velocities should be tunable by moderate changes of the model controlled by external parameters, such as magnetic fields or pressure. The realization of this phenomenon will pave the way for fascinating devices in magnonics, such as delay lines and interference devices.

7. Summary

In this thesis we followed different paths in order to investigate the variation and the robustness of signal transmission in low-dimensional topological systems. Here we give a short summary of the results regarding all topics in this thesis.

Tunable edge states and their robustness towards disorder

We reported on the tunability of edge states of topologically non-trivial phases. To this end, we investigated the decorated Haldane model as well as the decorated Kane–Mele model. By adjusting the spectrum of local states with a gate voltage the dispersion of the edge states and thus the Fermi velocity as well is changed as desired. Helical edge states can be made depending on direction and on spin. The tunability is also possible in the case of a broken S^z spin symmetry.

Furthermore, the effect of local disorder in the decorated Haldane model was addressed. The maximization of the transition probability is applied to reassign the momenta to edge modes in presence of disorder and thus reconstructed the dispersion of edge states. The possibility to reconstruct the dispersion depends on the strength of the disorder and the distance to other energies. Hence, flat dispersions of decorated edge states are prone to perturbations and therefore only reconstructable for moderate disorder. Hence, in contrast to the naive expectation of complete robustness against perturbations due to the topological origin of the edge states disorder changes the dispersion of edge modes and therefore can deteriorate signal transmission beyond the DC conductivity.

Tunable dispersion of the edge states in the integer quantum Hall effect

We considered the integer quantum Hall effect of a 2D electron gas as the next step towards the application of a tunable Fermi velocity. As a result, we additionally proved that the main principles are not based on lattice models. We discretized the Hamilton operator for a free 2D electron gas subjected to a magnetic field. The discretization mesh was chosen fine enough, so that various continuous geometries could be described reliably. Attaching bays to the boundaries of a Hall sample result in local modes which can be energetically tuned by gate voltages. A weak coupling between the periodic bays and the bulk of the quantum Hall sample leads to narrow and steep dips in the Fermi velocity. Thus the local modes can be tuned into resonance and the Fermi velocity can be reduced by up to two orders of magnitude. The implementation with the state-of-the-art techniques turned out to be difficult, unfortunately.

Tunable signal velocity in the integer quantum Hall effect of tailored graphene

The investigation of graphene showed that the requirements in order to realize the tuning of the Fermi velocity with the state-of-the-art techniques are fulfilled. Thus novel devices such as delay lines and interferometers based on a tunable Fermi velocity are

feasible. The integer quantum Hall effect in graphene provides topological edge states for fast signal transmission which persist even at low magnetic fields. As a result, the magnetic length corresponds to experimentally available dimensions for tailored bays at the boundary. Additional gate voltages can be used to tune the local modes into resonance with the edge state at the Fermi energy which reduces the signal velocity remarkably.

Topological properties of $BiCu_2PO_6$

The dispersion of the triplon excitations of $BiCu_2PO_6$ has unique characteristics and we additionally found special topological properties. We calculated the dispersion of the triplon modes with a directly evaluated enhanced perturbative continuous unitary transformation method and a bosonic Bogoliubov transformation. By fitting the dispersion to the inelastic neutron scattering data, we determined the strengths of the couplings. The investigation of the resulting effective model showed that $BiCu_2PO_6$ is the first gapful, disordered quantum antiferromagnet with a non-trivial Zak phase for the triplon excitations. The four x- and y-modes display a non-trivial Zak phase of $\boldsymbol{P} = (\pi, 0)$. We calculated the Zak phase numerically by extending the formula to Bogoliubov quasiparticles. The quantization of the Zak phase is guaranteed by the inversion symmetry so that we could additionally determine the Zak phase through the inversion parity.

A finite winding number confirmed the topological triplon modes. The calculation of a finite chain revealed the surprising fact that no localized edge states are present in $BiCu_2PO_6$ despite the bulk-boundary correspondence. We explained that the absence of an indirect gap leads to delocalized in-gap states in $BiCu_2PO_6$. The absence of localization in $BiCu_2PO_6$ is supported by the investigation of the local dynamic structure factor. The examination of a generalized Su–Schrieffer–Heeger model clearly illustrates the process of delocalization. Thus the bulk-boundary correspondence is set into perspective. The bulk properties are preserved by the direct gap while the localization of edge states is related to the presence of an indirect gap.

Delocalization of edge states in topological phases

In order to prove the generality of our conclusion that the indirect gap is important for localized edge states regardless of dimension, we explored 2D Chern insulators. The investigation of a Haldane model in a strip geometry showed that the lack of an indirect gap to the edge states leads to delocalization. However, the indirect gap regarding the direction parallel to the boundary does not affect the localization which emphasizes the importance of the directions. The topological checkerboard model displayed a similar scenario. The study of the Haldane model which describes a sample finite in both directions showed that the chirality is lost as soon as an indirect gap is closed regardless of the direction. In summary, we concluded that the indirect gap generally is an essential ingredient for localized edge states.

Topological magnon bands for magnonics

The investigation of the ferromagnetic Shastry–Sutherland lattices showed the emergence of topological magnon excitations which represent promising candidates for applications in magnonics. The single-ion anisotropy coupling should generate a finite spin gap while Dzyaloshinskii-Moriya couplings lift the quadratic band crossing point. Each

pair of bands possesses a non-trivial Chern number leading to topological edge states. As a smoking gun experiment we proposed to measure the thermal Hall conductivity. To this end, we discussed some compounds as possible physical realizations of ferromagnetic Shastry–Sutherland lattices. These materials are promising for magnonics due to the large spin and the likelihood of large Dzyaloshinskii-Moriya couplings.

Appendix[1]

A. Symmetry analysis of $BiCu_2PO_6$

The directions of the DM vectors $\boldsymbol{D}_m, m \in \{0,1,2,3\}$ are restricted due to the symmetries of the system. These restrictions are formulated by the five selection rules of Moriya [176] which relate the different couplings based on the point group symmetries of the system. For the sake of completeness, we present these five selection rules here briefly. Moriya established them by considering two interacting ions with spins whose positions we label with A and B. The center of the connecting line $\overline{\mathrm{AB}}$ is denoted by C. The five selection rules of Moriya are given by:

- 1^{st} If C presents a center of inversion, then $\boldsymbol{D} = 0$ holds.
- 2^{nd} If there is a mirror plane perpendicular to $\overline{\mathrm{AB}}$ and passing through C, then $\boldsymbol{D} \perp \overline{\mathrm{AB}}$ is valid.
- 3^{rd} If a mirror plane including the positions A and B is present, the vector $\boldsymbol{D}$ is perpendicular to this mirror plane.
- 4^{th} In the case of a two-fold rotation axis perpendicular to the line $\overline{\mathrm{AB}}$ and passing through C, then $\boldsymbol{D}$ is perpendicular to this two-fold rotation axis.
- 5^{th} If there is an n-fold axis ($n \geq 2$) passing along $\overline{\mathrm{AB}}$, the relation $\boldsymbol{D} \parallel \overline{\mathrm{AB}}$ is valid.

Besides the information that specific $\boldsymbol{D}_{ij}$ components are forbidden due to point group symmetries of the single bonds, one can additionally obtain information on the signs of the possible $\boldsymbol{D}_{ij}$ along the ladder by considering translations and glide reflections. Likewise the parity of the components relative to the reflection about the center line, see Fig. 4.2 in Chap. 4, can be elucidated. This parity determines whether a term contributes to the dispersions on the level of bilinear Hamiltonians or not [240].

If we neglect the difference between the two copper ions Cu_A and Cu_B, we arrive at the minimal model of $BiCu_2PO_6$ with the possible DM components shown in Fig. 4.2 in Chap. 4. Taking into account the difference between the two copper sites [174] the symmetry of the lattice is lower so that more $\boldsymbol{D}_{ij}$ components are allowed. Then only the following two symmetries of the crystal structure are present:

1. RS_y: Rotation by π around the y-axis located in the middle of the spin ladder and a shift by half a unit cell.
2. S_{xz}: Reflection at the xz-plane located at a dimer.

[1] Parts of this appendix are submitted for publication [161] or have been published in Physical Review B [210].

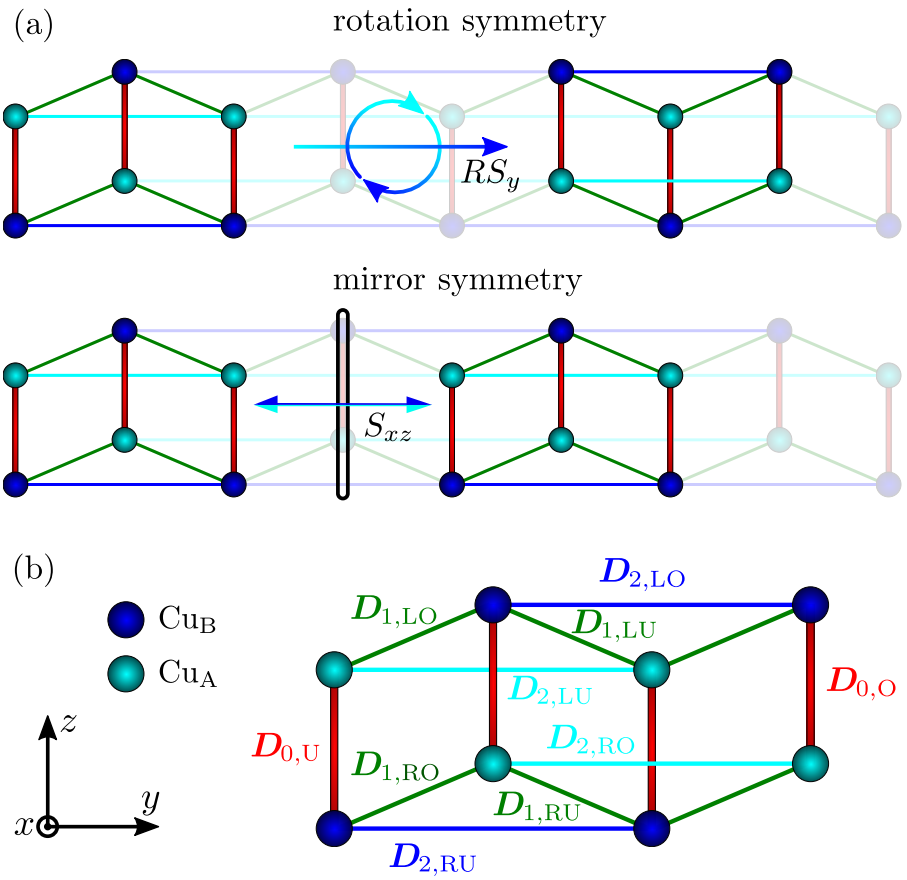

Figure A.1: Symmetry analysis. (a) Illustration of the two symmetry operations RS_y and S_{xz} leaving the model of $BiCu_2PO_6$ invariant. (b) Notation of the various $\boldsymbol{D}$ vectors in $BiCu_2PO_6$.

These two symmetry operations are shown in Fig. A.1(a). The notation of the various DM vectors are shown in Fig. A.1(b).

The determined symmetries imply the following constraints. The vector $\boldsymbol{D}_0$ only has a y-component due to the third selection rule based on the symmetry S_{xz}. The RS_y symmetry yields the relation

$$RS_y(\boldsymbol{D}_{0,\mathrm{U}}) = -\boldsymbol{D}_{0,\mathrm{O}} \quad . \tag{A.1}$$

After a RS_y rotation, the stipulated sequence of the spin operators within the term $\boldsymbol{D}_{ij}(\boldsymbol{S}_i \times \boldsymbol{S}_j)$ (according to ascending y- and z-coordinates) must be recovered by swapping the spin operators. Thus, Eq. (A.1) shows the alternating behavior of D_0^y along the legs. The symmetry analysis of the $\boldsymbol{D}_1$ bond leads to the relations

$$S_{xz}(\boldsymbol{D}_{1,\mathrm{LU}}) = \boldsymbol{D}_{1,\mathrm{LO}} \tag{A.2a}$$

$$S_{xz}(\boldsymbol{D}_{1,\mathrm{LO}}) = \boldsymbol{D}_{1,\mathrm{LU}} \tag{A.2b}$$

$$S_{xz}(\boldsymbol{D}_{1,\mathrm{RU}}) = \boldsymbol{D}_{1,\mathrm{RO}} \tag{A.2c}$$

$$S_{xz}(\boldsymbol{D}_{1,\mathrm{RO}}) = \boldsymbol{D}_{1,\mathrm{RU}} \tag{A.2d}$$

$$RS_y(\boldsymbol{D}_{1,\mathrm{LU}}) = \boldsymbol{D}_{1,\mathrm{RO}} \tag{A.2e}$$
$$RS_y(\boldsymbol{D}_{1,\mathrm{LO}}) = \boldsymbol{D}_{1,\mathrm{RU}} \tag{A.2f}$$
$$RS_y(\boldsymbol{D}_{1,\mathrm{RU}}) = \boldsymbol{D}_{1,\mathrm{LO}} \tag{A.2g}$$
$$RS_y(\boldsymbol{D}_{1,\mathrm{RO}}) = \boldsymbol{D}_{1,\mathrm{LU}} \quad . \tag{A.2h}$$

To clarify the properties of $\boldsymbol{D}_1$ we start with an arbitrary vector

$$\boldsymbol{D}_{1,\mathrm{LU}} = c_x\hat{\boldsymbol{e}}_x + c_y\hat{\boldsymbol{e}}_y + c_z\hat{\boldsymbol{e}}_z \quad , \tag{A.3}$$

where $\hat{\boldsymbol{e}}_\mu$ are unit vectors in the directions indicated by the subscript and c_μ are real coefficients. Applying Eqs. (A.2a) and (A.2e) to this ansatz for $\boldsymbol{D}_{1,\mathrm{LU}}$, we obtain

$$\boldsymbol{D}_{1,\mathrm{LO}} = \quad c_x\hat{\boldsymbol{e}}_x - c_y\hat{\boldsymbol{e}}_y + c_z\hat{\boldsymbol{e}}_z \tag{A.4a}$$
$$\boldsymbol{D}_{1,\mathrm{RO}} = -c_x\hat{\boldsymbol{e}}_x + c_y\hat{\boldsymbol{e}}_y - c_z\hat{\boldsymbol{e}}_z \quad . \tag{A.4b}$$

The first condition determines that the x- and z-components are uniform while the y-component alternates along the ladder. The second condition indicates that all three components have odd-parity since the translation to $\boldsymbol{D}_{1,\mathrm{RU}}$ changes the sign of the y-component as well so that all coefficients acquire a negative sign.

In the same way, we investigate $\boldsymbol{D}_2$. Applying both symmetry operations to $\boldsymbol{D}_2$ yields

$$S_{xz}(\boldsymbol{D}_{2,\mathrm{LU}}) = \boldsymbol{D}_{2,\mathrm{LU}} \tag{A.5a}$$
$$S_{xz}(\boldsymbol{D}_{2,\mathrm{LO}}) = \boldsymbol{D}_{2,\mathrm{LO}} \tag{A.5b}$$
$$S_{xz}(\boldsymbol{D}_{2,\mathrm{RU}}) = \boldsymbol{D}_{2,\mathrm{RU}} \tag{A.5c}$$
$$S_{xz}(\boldsymbol{D}_{2,\mathrm{RO}}) = \boldsymbol{D}_{2,\mathrm{RO}} \tag{A.5d}$$
$$RS_y(\boldsymbol{D}_{2,\mathrm{LU}}) = \boldsymbol{D}_{2,\mathrm{RO}} \tag{A.5e}$$
$$RS_y(\boldsymbol{D}_{2,\mathrm{LO}}) = \boldsymbol{D}_{2,\mathrm{RU}} \tag{A.5f}$$
$$RS_y(\boldsymbol{D}_{2,\mathrm{RU}}) = \boldsymbol{D}_{2,\mathrm{LO}} \tag{A.5g}$$
$$RS_y(\boldsymbol{D}_{2,\mathrm{RO}}) = \boldsymbol{D}_{2,\mathrm{LU}} \quad . \tag{A.5h}$$

Again, we start from the general ansatz

$$\boldsymbol{D}_{2,\mathrm{LU}} = d_x\hat{\boldsymbol{e}}_x + d_y\hat{\boldsymbol{e}}_y + d_z\hat{\boldsymbol{e}}_z \quad . \tag{A.6}$$

Using Eq. (A.5a) we easily see that the y-component has to vanish. In contrast, using Eq. (A.5e) does not lead to an unambiguous solution because we obtain

$$\boldsymbol{D}_{2,\mathrm{RO}} = -d_x\hat{\boldsymbol{e}}_x - d_z\hat{\boldsymbol{e}}_z \quad . \tag{A.7}$$

Each component can fulfill this condition in two different ways. Either the component alternates along the ladder with even-parity or it is uniform along the ladder with

couplings	along the legs	parity
D_0^y	alternating	odd
D_1^x	uniform	odd
D_1^y	alternating	odd
D_1^z	uniform	odd
$D_{2,\mathrm{a}}^x$	alternating	even
$D_{2,\mathrm{u}}^x$	uniform	odd
$D_{2,\mathrm{a}}^z$	alternating	even
$D_{2,\mathrm{u}}^z$	uniform	odd
D_3^y	alternating	N/A

Table A.1: Behavior of the sign of the D-components along the legs of the spin ladder and their parity with respect to the symmetry S_{xy} (reflection with respect to the center line of the spin ladder, see Fig. 4.2 in Chap. 4). Components which are not listed are forbidden due to the selection rules of Moriya [176].

odd-parity. Thus, the $\boldsymbol{D}_2$-vector is generally expressed by the superposition of both possibilities

$$D_2^x = D_{2,\mathrm{a}}^x + D_{2,\mathrm{u}}^x \tag{A.8a}$$

$$D_2^z = D_{2,\mathrm{a}}^z + D_{2,\mathrm{u}}^z \quad , \tag{A.8b}$$

where subscript a stands for "alternating" and u for "uniform".

Considering the fact that the differences between the copper ions are small [174], we may neglect them altogether which allows us to conclude [171] $D_2^x = D_{2,\mathrm{u}}^x$ and $D_2^z = D_{2,\mathrm{a}}^z$. Thus, we conclude that the uniform x-component and the alternating z-component predominate. Arbitrary components as in Eq. (A.8) are allowed, but decisive contributions only come from the alternating even-parity z-component and the uniform odd-parity x-component.

Note that we neglect potential differences between $\boldsymbol{D}_2$ on the J_2 bond and $\boldsymbol{D}_2'$ on the J_2' bond because they have odd-parity and do not contribute on the bilinear level anyway. The potential differences in the ensuing symmetric Γ-terms are neglected as well because of their barely measurable impact.

The results of the symmetry analysis are collected in Tab. A.1. Since the Γ-couplings result from the D-couplings according to Eq. (4.3) in Sec. 4.2, one can establish a similar table for the Γ-components based on Tab. A.1. The property of being alternating/odd corresponds to a minus sign while uniform/even corresponds to a plus sign in the DM components. Thus by multiplying the DM components by ± 1 in Eq. (4.3) one arrives at the resulting properties of the Γ-components.

Finally, we remark that the orientation of the $\boldsymbol{D}_3$-vector, which belongs to the interladder coupling, is analogous to the $\boldsymbol{D}_0$-vector. The $\boldsymbol{D}_3$-vector couples two adjacent ladders, contributing to the transversal dispersion. No parity can be defined because the reflection about the center line refers to a symmetry within each ladder separately.

B. Matrix representation of the bilinear Hamilton operator

The general expression in the Nambu representation of the complete bilinear Hamiltonian in momentum space is given up to unimportant constants by

$$\mathcal{H} = \frac{1}{2}\sum_{k,l} \boldsymbol{a}_{k,l}^{\dagger} H_{k,l} \boldsymbol{a}_{k,l} \quad \text{with} \tag{B.1a}$$

$$H_{k,l} = \begin{bmatrix} A(k,l) & B(k,l) \\ B^{\dagger}(k,l) & A^{\top}(-k,-l) \end{bmatrix} = H_{k,l}^{\dagger} \tag{B.1b}$$

and the twelve-dimensional Nambu spinor $\boldsymbol{a}_{k,l} = (\boldsymbol{t}_{k,l}^{\top}, \boldsymbol{t}_{k+\pi,l}^{\top}, \boldsymbol{t}_{-k,-l}^{\dagger}, \boldsymbol{t}_{-k-\pi,-l}^{\dagger})^{\top}$, as shown in Eq. (4.5) in Sec. 4.2, using $\boldsymbol{t}_{k,l} = (t_{k,l}^{x}, t_{k,l}^{y}, t_{k,l}^{z})^{\top}$ and $\boldsymbol{t}_{k,l}^{\dagger} = (t_{k,l}^{x,\dagger}, t_{k,l}^{y,\dagger}, t_{k,l}^{z,\dagger})$. Note that the sum in (B.1a) runs over all values of $l \in [0, 2\pi)$ (lattice constant set to unity) in the BZ while it runs only over the values $k \in [0, \pi)$, i.e., over half the BZ. The reason is that the above Nambu spinor addresses k and $k + \pi$ simultaneously.

The 12×12 matrix $H_{k,l}$ is composed of the two 6×6 matrices A and B which are again made up by 3×3 matrices

$$A(k,l) = \begin{pmatrix} A_1(k) + B_1(k,l) & B_2(k,l) \\ B_2^{\dagger}(k,l) & A_1(k+\pi) + B_1(k+\pi,l) \end{pmatrix} \tag{B.2a}$$

$$B(k,l) = \begin{pmatrix} B_1(k,l) & B_2(k,l) \\ B_2^{\dagger}(k,l) & B_1(k+\pi,l) \end{pmatrix} \quad . \tag{B.2b}$$

The 3×3 matrices are derived to be

$$A_1(k) = \begin{pmatrix} \omega_0(k) & \mathrm{i}h_z & -\mathrm{i}h_y \\ -\mathrm{i}h_z & \omega_0(k) & \mathrm{i}h_x \\ \mathrm{i}h_y & -\mathrm{i}h_x & \omega_0(k) \end{pmatrix} \tag{B.3a}$$

$$B_1(k,l) = \begin{pmatrix} F^x(k,l) & 0 & \Gamma_1^{xz}(k) + \Gamma_2^{xz}(k) \\ 0 & F^y(k,l) & 0 \\ \Gamma_1^{xz}(k) + \Gamma_2^{xz}(k) & 0 & F^z(k,l) \end{pmatrix} \tag{B.3b}$$

$$B_2(k,l) = \begin{pmatrix} 0 & -\mathrm{i}(\Gamma_1^{xy}(k) - D_2^z(k)) & -\mathrm{i}D_3^y(k,l) \\ -\mathrm{i}(\Gamma_1^{xy}(k) + D_2^z(k)) & 0 & -\mathrm{i}(\Gamma_1^{yz}(k) - D_2^x(k)) \\ \mathrm{i}D_3^y(k,l) & -\mathrm{i}(\Gamma_1^{yz}(k) + D_2^x(k)) & 0 \end{pmatrix} \quad . \tag{B.3c}$$

The dispersion of the isotropic spin ladder is calculated by the deepCUT method [176, 182] yielding

$$\omega_0(k) = \sum_{\delta=0}^{13} \omega_\delta \cos(\delta k) \quad . \tag{B.4}$$

The coefficients ω_δ are given in Tab. B.1. Similarly, the transformation of the spin operators to triplon operators

$$S_{0,\mathrm{L}}^{\mu} = -S_{0,\mathrm{R}}^{\mu} \tag{B.5a}$$

$$= \sum_{\delta=-12}^{12} a_{|\delta|}(t_{\delta}^{\mu} + t_{\delta}^{\mu,\dagger}) + \begin{matrix}\text{bilinear and} \\ \text{higher terms}\end{matrix} \tag{B.5b}$$

δ	ω_δ	a_δ
0	1.5499384208488	0.3874491109155713
1	0.358817770492231	-0.05165001704799924
2	0.524739087510573	-0.08095884805094124
3	-0.209722209664048	0.03713614889687351
4	-0.160344853773972	0.0219291397751164
5	0.0967516245738429	-0.01719462494862808
6	0.010462389004026	-0.004727305201296136
7	-0.0347043572019398	0.01024208259455439
8	0.000112462598212057	-0.001628782296091526
9	0.0139297388647789	-0.00497492501969249
10	-0.00637707478352971	0.002315960919757644
11	-0.00403742286524941	0.001621270078823474
12	0.00429559542625067	-0.001835116321222724
13	0.000461321168694168	

Table B.1: The coefficients ω_δ used to describe the dispersion of the isotropic spin ladder as well as the prefactors a_δ to transform the spin operators are calculated by using the deepCUT method for the ratios $J_1/J_0 = 1.2$ and $J_2/J_1 = 0.9$. The values for higher δ are small enough to be neglected.

yields the amplitudes a_δ also given in Tab. B.1. The spin operators are labeled with subscripts left (L) and right (R) spin in a dimer referring to the two legs of each ladder. Bilinear or higher products of triplon operators are neglected in our approach to the transformation of the spin operator. The Fourier transform

$$a(k) := \sum_{\delta=-12}^{12} a_{|\delta|} \cos(\delta k) \tag{B.6}$$

yields the momentum-dependent amplitude $a(k)$ which appears generically in effective triplon Hamiltonians [171, 241, 242]. The Hamiltonian also includes a general uniform magnetic field $\boldsymbol{h} = (h_x, h_y, h_z)^\top$ given by $\mathcal{H}_{\text{Zeeman}} = -\boldsymbol{h} \sum_i \boldsymbol{S}_i$.

Further variables introduced for clarity are

$$F^\mu(k,l) = d(k,l) + \Gamma_0^{\mu\mu}(k) + \Gamma_1^{\mu\mu}(k) + \Gamma_2^{\mu\mu}(k) + \Gamma_3^{\mu\mu}(k,l) \tag{B.7}$$

with $\mu \in \{x, y, z\}$ and

$$d(k,l) = -2J_3 \cos(l) a^2(k) \tag{B.8a}$$

$$\Gamma_0^{\mu\mu}(k) = -2\Gamma_0^{\mu\mu} a^2(k) \tag{B.8b}$$

$$\Gamma_1^{\mu\mu}(k) = \quad 4\Gamma_1^{\mu\mu} a^2(k) \cos(k) \tag{B.8c}$$

$$\Gamma_2^{\mu\mu}(k) = \quad 4\Gamma_2^{\mu\mu} a^2(k) \cos(2k) \tag{B.8d}$$

$$\Gamma_3^{\mu\mu}(k,l) = -2\Gamma_3^{\mu\mu} a^2(k) \cos(l) \tag{B.8e}$$

$$\Gamma_1^{xy}(k) = \quad 4\Gamma_1^{xy} a(k) a(k+\pi) \sin(k) \tag{B.8f}$$

$$\Gamma_1^{yz}(k) = 4\Gamma_1^{yz} a(k)a(k+\pi)\sin(k) \tag{B.8g}$$

$$\Gamma_1^{xz}(k) = 4\Gamma_1^{xz} a(k)^2\cos(k) \tag{B.8h}$$

$$\Gamma_2^{xz}(k) = 4\Gamma_2^{xz} a(k)^2\cos(2k) \tag{B.8i}$$

$$D_{2,a}^{z}(k) = 4D_{2,a}^{z} a(k)a(k+\pi)\sin(2k) \tag{B.8j}$$

$$D_{2,a}^{x}(k) = 4D_{2,a}^{x} a(k)a(k+\pi)\sin(2k) \tag{B.8k}$$

$$D_{3}^{y}(k,l) = -2D_{3}^{y} a(k)a(k+\pi)\sin(l) \quad . \tag{B.8l}$$

Inspecting the above matrices one realizes that for zero magnetic field the slightly simpler form

$$H_{k,l} = \begin{bmatrix} A(k,l) & B(k,l) \\ B(k,l) & A(k,l) \end{bmatrix} \tag{B.9}$$

holds. The eigenenergies and eigenmodes are obtained by a bosonic Bogoliubov transformation [184] from the t-operators to the normal b-operators. This requires the diagonalization of the matrix

$$\widetilde{H}_{k,l} := \eta H_{k,l}, \tag{B.10}$$

where the metric η is the diagonal matrix

$$\eta = \mathrm{diag}(1_1, \ldots, 1_6, -1_7, \ldots, -1_{12}) \quad . \tag{B.11}$$

The resulting Hamiltonian reads $\mathcal{H} = \sum_{n,k,l} \omega_n(k,l) b_{n,k,l}^\dagger b_{n,k,l}$, where the index n labels the six different modes at a given wave vector (k,l). The normal bosonic operators read

$$b_{n,k,l}^\dagger = \sum_{\mu=x,y,z} \left(u_{n,k,l}^\mu t_{k,l}^{\mu,\dagger} + \tilde{u}_{n,k,l}^\mu t_{k+\pi,l}^{\mu,\dagger} - v_{n,k,l}^\mu t_{-k,-l}^\mu - \tilde{v}_{n,k,l}^\mu t_{-k-\pi,-l}^\mu \right) \quad , \tag{B.12}$$

where u and v with and without tilde are generally complex prefactors. The annihilation operator follows by Hermitian conjugation.

C. Symplectic product and Berry phase for bosons

The Berry phase in quantum mechanics is defined by the complex phase of the scalar product between two quantum states [50]. Thus, the key ingredient is an appropriate scalar product. In order to be independent of a particular basis for quantum states we aim at lifting the definition of topological phases from the level of quantum states to operators in second quantization. In App. B, we obtained the normal bosonic creation operator (B.12). With the prefactors occurring in this equation we define a generalized ket by these prefactors

$$|\boldsymbol{k}, n\rangle\rangle := (\boldsymbol{u}_{n,k,l}^\top, \tilde{\boldsymbol{u}}_{n,k,l}^\top, \boldsymbol{v}_{n,k,l}^\top, \tilde{\boldsymbol{v}}_{n,k,l}^\top)^\top \quad , \tag{C.1}$$

which is a column vector with twelve components. The bold face symbols such as $\boldsymbol{u}$ represent three-dimensional column vectors with components u^x, u^y and u^z. Then, we

define the symplectic product by

$$\langle\langle \boldsymbol{k}_1, n_1 |\, \boldsymbol{k}_2, n_2 \rangle\rangle \tag{C.2a}$$

$$:= (\boldsymbol{u}^\dagger_{n_1,k_1,l_1}, \tilde{\boldsymbol{u}}^\dagger_{n_1,k_1,l_1}, \boldsymbol{v}^\dagger_{n_1,k_1,l_1}, \tilde{\boldsymbol{v}}^\dagger_{n_2,k_2,l_2})\ \eta\ (\boldsymbol{u}^\top_{n_2,k_2,l_2}, \tilde{\boldsymbol{u}}^\top_{n_2,k_2,l_2}, \boldsymbol{v}^\top_{n_2,k_2,l_2}, \tilde{\boldsymbol{v}}^\top_{n_2,k_2,l_2})^\top \tag{C.2b}$$

$$= \boldsymbol{u}^\dagger_{n_1,k_1,l_1}\boldsymbol{u}_{n_2,k_2,l_2} + \tilde{\boldsymbol{u}}^\dagger_{n_1,k_1,l_1}\tilde{\boldsymbol{u}}_{n_2,k_2,l_2} - \boldsymbol{v}^\dagger_{n_1,k_1,l_1}\boldsymbol{v}_{n_2,k_2,l_2} - \tilde{\boldsymbol{v}}^\dagger_{n_1,k_1,l_1}\tilde{\boldsymbol{v}}_{n_2,k_2,l_2} \quad . \tag{C.2c}$$

We highlight the so far unnoted fact that $\widetilde{H}_{k,l}$, in contrast to $H_{k,l}$, see Eq. (B.10), is self-adjoint with respect to this symplectic product implying the well-known facts that its eigenvalues are real and that creation and annihilation operators of different eigenvalues commutate.

The above formalism is presented at the level of second quantization. Here we want to elucidate its formal properties further. To be as general as possible, we consider a set of bosonic annihilation operators a_j and creation operators $a_j^\dagger$ with $j \in \{1, 2, \dots m\}$. A general linear combination c reads

$$c := \sum_{j=1}^{m} (u_j a_j^\dagger - v_j a_j) \quad , \tag{C.3}$$

where c is not normalized and it is not specified whether it is a creation or annihilation operator. Then, we define the corresponding generalized ket by the column vector

$$|c\rangle\rangle := (u_1, \dots, u_m, v_q, \dots, v_m)^\top = \underline{c} \quad . \tag{C.4}$$

Sometimes the vector notation $\underline{c}$ is more convenient than the ket notation. Axiomatically, we can define the symplectic product between two kets $|c\rangle\rangle$ and $|c'\rangle\rangle$ by

$$\langle\langle c|c'\rangle\rangle := \sum_{j=1}^{m} (u_j^* u'_j - v_j^* v'_j) \tag{C.5a}$$

$$= \underline{c}^\dagger \eta \underline{c}' \quad , \tag{C.5b}$$

where the diagonal $2m \times 2m$ matrix $\eta = \mathrm{diag}(1_1, \dots, 1_m, -1_{m+1}, \dots, -1_{2m})$ is used as a metric with $\eta^2 = \mathbb{1}$. This sort of "generalized scalar product" runs under several names in the literature such as "quasi-scalar product" or "para-scalar product" and the conserving transformation as "quasi-unitary" or "para-unitary". [165, 243, 244]. We prefer to avoid the term "scalar product" completely because it suggests semi-positivity, but use "symplectic" which is the established attribute for a metric with equal number of positive and negative directions, see for instance the symplectic structure of phase space in analytical mechanics.

It is easy to verify that a conventional Hermitian matrix $H = H^\dagger$ is not self-adjoint with respect to Eqs. (C.5). But ηH is self-adjoint due to

$$\langle\langle c|\eta H c'\rangle\rangle = \underline{c}^\dagger \eta\eta H \underline{c}' \tag{C.6a}$$

$$= \underline{c}^\dagger H \underline{c}' \tag{C.6b}$$

$$\langle\langle \eta H c|c'\rangle\rangle = \underline{c}^\dagger H \eta\eta \underline{c}' \tag{C.6c}$$

$$= \underline{c}^\dagger H \underline{c}' \quad . \tag{C.6d}$$

Alternatively, one can also start from

$$\langle\langle c|c'\rangle\rangle := [c^\dagger, c'] \quad , \tag{C.7}$$

which obviously yields an expression identical to Eqs. (C.5). The inequality $\langle\langle c|c\rangle\rangle > 0$ tells us that c is an unnormalized creation operator while $\langle\langle c|c\rangle\rangle < 0$ tells us that it is an unnormalized annihilation operator.

The following question is imminent at this stage: Can one relate Eq. (C.5) and Eq. (C.7) to the conventional scalar product between quantum states? The answer is ambiguous: it depends. If there is a general ground state, i.e., a vacuum $|0\rangle$ annihilated by all annihilation operators b considered (here the linear combinations b have to be annihilation operators), then the following relation between the standard scalar product $\langle 0|\, b'b^\dagger\, |0\rangle$ in Fock space for two one-particle states and the above defined symplectic product holds

$$\langle 0|\, b'b^\dagger\, |0\rangle = \langle 0|\, (b'b^\dagger - b^\dagger b')\, |0\rangle \tag{C.8a}$$

$$= [b', b^\dagger] \quad , \tag{C.8b}$$

where the last line is precisely the definition (C.7) equivalent to (C.5). Indeed, this situation is a very common one in multi-band systems where $|0\rangle$ is the vacuum with respect to all bosons at all values of $\boldsymbol{k}$. Then one retrieves the Berry connection (4.9) and the Berry phase (4.10) for paths through the BZ shown in Sec. 4.3.

But we stress that the identity (C.8) does not hold if an external control parameter λ is varied which changes the vacuum as well. Then the Berry phase for a path from $\lambda = 0$ to $\lambda = \lambda_1$ reads

$$\gamma = \mathrm{i}\int_0^{\lambda_1} \langle 0(\lambda)|\, b(\lambda)\partial_\lambda b^\dagger(\lambda)\, |0(\lambda)\rangle \, \mathrm{d}\lambda \tag{C.9a}$$

$$= \mathrm{i}\int_0^{\lambda_1} \left[\langle 0(\lambda)|\, b(\lambda)\left(\partial_\lambda b^\dagger(\lambda)\right)|0(\lambda)\rangle + \langle 0(\lambda)|\, b(\lambda)b^\dagger(\lambda)\left(\partial_\lambda\, |0(\lambda)\rangle\right)\right] \mathrm{d}\lambda \tag{C.9b}$$

$$= \mathrm{i}\int_0^{\lambda_1} \left[\langle 0(\lambda)|\, [b(\lambda), \left(\partial_\lambda b^\dagger(\lambda)\right)]\, |0(\lambda)\rangle + \langle 0(\lambda)|\, \left(\partial_\lambda\, |0(\lambda)\rangle\right)\right] \mathrm{d}\lambda \tag{C.9c}$$

$$= \gamma_{\mathrm{exc}}(\lambda_1) + \gamma_{\mathrm{vac}}(\lambda_1) \quad , \tag{C.9d}$$

where two contributions are identified

$$\gamma_{\mathrm{exc}}(\lambda_1) := \mathrm{i}\int_0^{\lambda_1} \langle 0(\lambda)|\, [b(\lambda), \left\{\partial_\lambda b^\dagger(\lambda)\right\}]\, |0(\lambda)\rangle \, d\lambda \tag{C.10a}$$

$$\gamma_{\mathrm{vac}}(\lambda_1) := \mathrm{i}\int_0^{\lambda_1} \langle 0(\lambda)|\, \{\partial_\lambda\, |0(\lambda)\rangle\}\, d\lambda \quad . \tag{C.10b}$$

One contribution, γ_{exc}, results from the bosonic excitation and equals what one obtains using the symplectic product. The other contribution, γ_{vac}, is the Berry phase of the vacuum. For paths in the BZ, the analogous result has been derived in Ref. [245] where, however, the vacuum contribution should not occur because the global vacuum of the system does not depend on the momentum.

The bottom line is that for topological properties defined in the BZ the symplectic product yields a Berry phase identical to the conventional definition. In more general cases, however, the variation of the vacuum matters as well.

We corroborate this conclusion by repeating Berry's original adiabatic approach in the bosonic Fock space. Let us assume that the bilinear Hamiltonian depends on the parameter λ, which may parametrize a path in the BZ or may be an external control parameter. It is varied slowly from 0 to 1, i.e., $\lambda = t/T$ for $t \in [0, T]$ with $T \to \infty$. The Hamiltonian is generally given by the matrix $H(\lambda)$ [184]; for an example see Eq. (4.4) in Sec. 4.3. At each value of λ the ket $|n(\lambda)\rangle$ parameterizes the creation of a boson in the nth eigenmode. Hence the equation

$$\eta H(\lambda) |n(\lambda)\rangle = \omega_n(\lambda) |n(\lambda)\rangle \tag{C.11}$$

is fulfilled. We assume the eigenmodes to be non-degenerate for clarity. The adiabatic ansatz, see for instance Ref. [49], for the solution $|\psi_n(t)\rangle$ close to the instantaneous eigenstate $|\phi_n(\lambda)\rangle := b_n^\dagger(\lambda) |0(\lambda)\rangle$ reads

$$|\psi_n(t)\rangle = \exp(-\mathrm{i}\Theta(t)) \left(|\phi_n(\lambda(t))\rangle + (1/T) |\perp\rangle \right) \quad , \tag{C.12}$$

where the correction $(1/T) |\perp\rangle$ is small in $1/T$ and perpendicular to $|\phi_n(\lambda(t))\rangle$. Inserting this ansatz in the Schrödinger equation $\mathrm{i}\partial_t |\psi_n(t)\rangle = H |\psi_n(t)\rangle$ yields

$$\begin{aligned} H |\psi_n(t)\rangle = (\partial_t \Theta) |\psi_n(t)\rangle + \exp(-\mathrm{i}\Theta(t)) \frac{\mathrm{i}}{T} \partial_\lambda |\phi_n(\lambda)\rangle \\ + \text{perpendicular terms} \quad . \end{aligned} \tag{C.13}$$

Next, we multiply with $\langle \phi_n(\lambda)|$ from the left to obtain

$$\omega_n(\lambda) + E_0(\lambda) = \partial_t \Theta + \frac{1}{T} \partial_\lambda (\gamma_{\mathrm{exc}}(\lambda) + \gamma_{\mathrm{vac}}(\lambda)) \quad , \tag{C.14}$$

where E_0 is the ground state energy and we used the result of the calculation (C.9). Integrating from $\Theta(t = 0) = 0$ to $t = T$ yields

$$\Theta(T) = T \int_0^1 (\omega_n(\lambda) + E_0(\lambda)) \, \mathrm{d}\lambda - \gamma_{\mathrm{exc}}(1) - \gamma_{\mathrm{vac}}(1) \quad . \tag{C.15}$$

This is the usual result for Berry phases in an adiabatic setting. The first term on the right hand side of Eq. (C.15) represents the dynamic phase and the second term $\gamma_{\mathrm{exc}}(1) + \gamma_{\mathrm{vac}}(1)$ is the Berry phase. Clearly, there is a contribution from the excitation and potentially from the ground state, i.e., the bosonic vacuum. Again, if the ground state is a global vacuum applying to all bosons it does not change as a function of λ. Then there is no vacuum Berry phase, i.e., $\gamma_{\mathrm{vac}} = 0$. This is the case for topological phases determined in the BZ.

D. Numerical calculation of the Zak phase

Only in rare cases, the analytical determination of the Zak phase is possible. In particular for higher-dimensional problems, for instance the twelve-dimensional extended model considered for $BiCu_2PO_6$, a numerical approach is needed. The first step is to discretize the contour of integration. As an example for determining the phase from $k = 0$ to $k = 2\pi$ we use $k_i = \frac{2\pi i}{N}$ with $i = 0, 1, \cdots, N-1$ (lattice constant is set to unity). It

is straightforward to determine the eigenmodes $|n, k_i\rangle\rangle$ numerically[2]. But the numerical choice of phase at each momentum k_i is arbitrary so that we cannot rely on a continuous evolution and hence an approximation of

$$\gamma_n = \mathrm{i} \int_0^{2\pi} \langle\langle n, k| \, \partial_k \, |n, k\rangle\rangle \, \mathrm{d}k \tag{D.1}$$

does not work. A well-established solution [75, 246] consists in using the Wilson loop

$$\gamma_n = -\mathrm{Im} \sum_{i=0}^{N-1} \ln \left(\langle\langle n, k_i | n, k_{i+1} \rangle\rangle \right) \mod 2\pi \tag{D.2}$$

instead, where $|n, k_0\rangle\rangle = |n, k_N\rangle\rangle$ holds because the loop is closed. We stress that in the above formula the gauge, i.e., the choice of the phase, of each eigenmode does not matter because it cancels out. Re-gauging each eigenmode arbitrarily

$$|n, k_j\rangle\rangle \to \widetilde{|n, k_j\rangle\rangle} = \exp(\mathrm{i}\varphi_j) \, |n, k_j\rangle\rangle \tag{D.3}$$

does not alter the outcome of Eq. (D.2) because each eigenmode appears once as ket and once as bra.

An alternative variant of the above approach relies on the idea of parallel transport. The eigenmode $|n, k_j\rangle\rangle$ serves as a reference state for $|n, k_{j+1}\rangle\rangle$. If their symplectic product reads

$$\langle\langle n, k_j | n, k_{j+1} \rangle\rangle = z = |z| \exp(-\mathrm{i}\varphi_{j+1}) \tag{D.4}$$

we re-gauge $|n, k_{j+1}\rangle\rangle$ such that it becomes as parallel as possible to $|n, k_j\rangle\rangle$. Obviously, this is achieved by

$$|n, k_{j+1}\rangle\rangle \to \widetilde{|n, k_{j+1}\rangle\rangle} = \exp(\mathrm{i}\varphi_{j+1}) \, |n, k_{j+1}\rangle\rangle \quad . \tag{D.5}$$

This procedure is iterated recursively from $j = 0$ to $j = N - 2$. The next and final step for $j = N - 1$ yields φ_N, but the corresponding re-gauging (D.5) is not possible because the phase of $|n, k_0\rangle\rangle = |n, k_N\rangle\rangle$ is fixed already. Then the total sum (D.2) simply reduces to

$$\gamma_n = -\mathrm{Im} \ln \left(\langle\langle n, k_{N-1} | n, k_0 \rangle\rangle \right) \quad , \tag{D.6}$$

since all re-gauged products are real and positive so that the Zak phase corresponds to

$$\gamma_n = \varphi_N \quad . \tag{D.7}$$

The attractive feature of this second variant is that it reveals the geometric character of the Berry phase. It stems from the parallel transport in the U(1) principal fiber bundle of the manifold given by the eigenmodes as a function of momentum.

D.1. Exemplary calculation of the Zak phase

Here we want to elucidate the numerical calculations for an analytically solvable problem in order to get insights into the methods. As already discussed in Sec. 2.3.3, the SSH

[2] Since this appendix is referred in Sec. 4.3, we use the generalized notation for the eigenmodes which is applied for $BiCu_2PO_6$. In constrast, the numerical example in App. D.1 uses the normal ket notation due to the presented calculation in the standard SSH model.

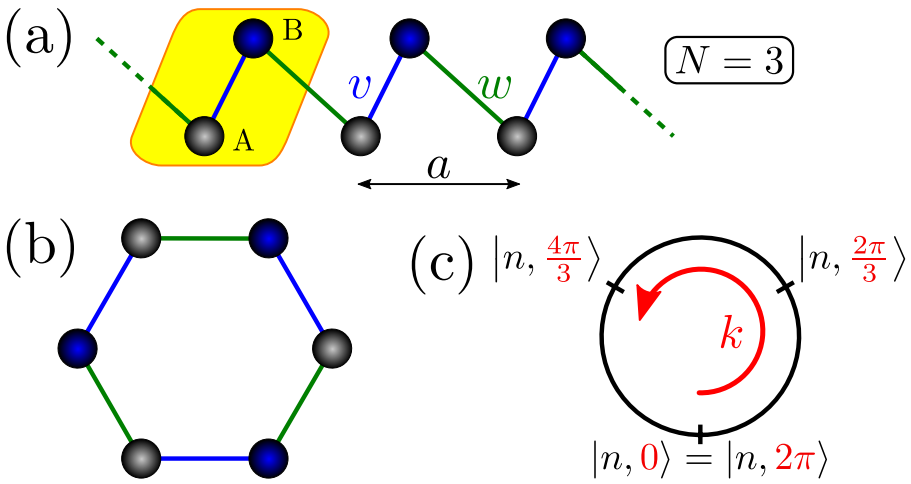

Figure D.1: (a) Lattice structure of SSH model with periodic boundary conditions and $N = 3$ unit cells which can also be represented by a six-site loop as in panel (b). The corresponding discretized BZ is shown in panel (c).

model serves as a standard example for a quantized Zak phase. We recall[3] that the Hamiltonian is given by

$$\mathcal{H}_{\mathrm{SSH}} = \sum_i \left(v c^\dagger_{i,\mathrm{B}} c_{i,\mathrm{A}} + w c^\dagger_{i+1,\mathrm{A}} c_{i,\mathrm{B}} \right) + \mathrm{h.c.} \quad , \tag{D.8}$$

where we focus on the fully dimerized limit $v = 0$ and we set the lattice constant $a = 1$. Thus, the pseudo-spin representation is given by $\boldsymbol{d}(k) = (w\cos(k), w\sin(k), 0)$. The Berry connection can be calculated with Eq. (2.35)

$$A_\pm = \mathrm{i} \langle \pm | \, \partial_k \, | \pm \rangle = \frac{-1}{2d(d \pm d3)} (d_2 \partial_k d_1 - d_1 \partial_k d_2) = -\frac{1}{2} \quad , \tag{D.9}$$

where $\pm$ denotes the two bands, respectively. In this special case, the Berry connection is momentum-independent and therefore contributes uniformly over the complete BZ. Thus the Zak phase is analytically determined by

$$\gamma_\pm = \int_0^{2\pi} A_\pm \, \mathrm{d}k = -\pi \quad , \tag{D.10}$$

which is equivalent to π modulo 2π.

Now we want to reproduce the same result with the numerical approach. We assume periodic boundary condition with $N = 3$ which form a six-site loop, see Fig. D.1. Therefore, the momentum can take on values $k_i = \frac{2\pi i}{N}$ with $i = \{0, 1, 2\}$. We trace the parallel transport of the eigenstate with a positive eigenvalue

$$|+, k\rangle = \frac{1}{\sqrt{2}} \begin{pmatrix} 1 \\ \mathrm{e}^{\mathrm{i}k} \end{pmatrix} \tag{D.10a}$$

$$\Rightarrow \quad |+, 0\rangle = \frac{1}{\sqrt{2}} \begin{pmatrix} 1 \\ 1 \end{pmatrix}, \quad |+, \frac{2\pi}{3}\rangle = \frac{1}{\sqrt{2}} \begin{pmatrix} 1 \\ \mathrm{e}^{\mathrm{i}2\pi/3} \end{pmatrix}, \quad |+, \frac{4\pi}{3}\rangle = \frac{1}{\sqrt{2}} \begin{pmatrix} 1 \\ \mathrm{e}^{\mathrm{i}4\pi/3} \end{pmatrix} \quad . \tag{D.10b}$$

[3] A more detailed description of the SSH model is given in Sec. 2.3.

Performing the numerical calculation according to Eq. (D.2), we obtain

$$\gamma_+ = -\mathrm{Im}\ln\left[\langle +,0|+,2\pi/3\rangle\,\langle +,2\pi/3|+,4\pi/3\rangle\,\langle +,4\pi/3|+,0\rangle\right] \tag{D.11a}$$

$$= -\mathrm{Im}\ln\left[\left(\frac{\mathrm{e}^{\mathrm{i}\pi/3}}{2}\right)^3\right] = -\pi \quad . \tag{D.11b}$$

For the alternative approach, we re-gauge the eigenstates to

$$|+,0\rangle = \frac{1}{\sqrt{2}}\begin{pmatrix}1\\1\end{pmatrix},\quad |+,\frac{2\pi}{3}\rangle = \frac{1}{\sqrt{2}}\begin{pmatrix}\mathrm{e}^{-\mathrm{i}\pi/3}\\ \mathrm{e}^{\mathrm{i}\pi/3}\end{pmatrix},\quad |+,\frac{4\pi}{3}\rangle = \frac{1}{\sqrt{2}}\begin{pmatrix}\mathrm{e}^{-\mathrm{i}2\pi/3}\\ \mathrm{e}^{\mathrm{i}2\pi/3}\end{pmatrix} \quad . \tag{D.12}$$

As a result, the inner products $\langle +,0|+,2\pi/3\rangle = \langle +,2\pi/3|+,4\pi/3\rangle = \cos(\pi/3) = 0.5$ are real and positive so that do not contribute to the phase except the last inner product. Note that the magnitude of one inner product is always smaller than unity and can be interpreted as the amount of change in one iteration step of the parallel transport. The last inner product $\langle +,4\pi/3|+,0\rangle = \cos(2\pi/3) = -0.5 = 0.5\mathrm{e}^{\mathrm{i}\pi}$ provides the Zak phase $\gamma_+ = -\pi$ accumulated over all steps. So by re-gauging, the phase was always shifted to the next inner product until all contributions to the complex phase are summed in the last term.

E. Investigation of the localization length in the Su–Schrieffer–Heeger model

The fact that topological in-gap states delocalize by closing the indirect gap can be observed by investigating confined geometries. The disappearence of the indirect gap, however, can also be read off the energy dispersion in the bulk. This leads to the question if there is also the possibility to observe the delocalization process in the bulk properties. To this end, we investigate the localization/correlation length ξ.

The conventional relation $\xi = s/\Delta$ is only valid for the relativistic free fermionic dispersion $E(q) = \sqrt{\Delta^2 + (sq)^2}$. A generalized approach relates the whole dispersion curve with the localization length [247]. This universal relation is given by

$$E(\mathrm{i}\kappa) = 0 \quad \text{with} \quad \kappa = -\mathrm{i}k' + 1/\xi \quad , \tag{E.1}$$

where k' is determined by the minimum of the dispersion curve above the ground state. According to the example shown in Sec. 4.7, we determine the localization length in the topological phase of the SSH model with $v = 0$. The dispersion is described by

$$E(k) = w + 2u\cos(k) \quad . \tag{E.2}$$

Hence, inserting $k = \mathrm{i}\kappa = \pi + \mathrm{i}/\xi$ leads to

$$E(\mathrm{i}\kappa) = w - 2u\cosh(1/\xi) = 0 \tag{E.2a}$$

$$\Rightarrow 1/\xi = \mathrm{acosh}\left(\frac{w}{2u}\right) \quad . \tag{E.2b}$$

At the transition point $w = 2u$ where the indirect gap closes, the localization length diverges. The parameter range $w > 2u$ leads to finite values for ξ, whereas $w < 2u$ leads

to an invalid imaginary solution for ξ, which corresponds to the range of values with delocalized in-gap states. Thus, this argument supports our result that a finite indirect gap leads to a finite localization length for the in-gap states while the closing of the indirect gap is connected to an infinite ξ.

In order to confirm the correctness of the universal approach we numerically calculate the localization length of the eigenstate with zero energy at the left boundary. As above, we consider the SSH model with $v = 0$. We assume exponentially localized wave function with $\psi = a\mathrm{e}^{-x/\xi}$ so that the probability density is given by

$$|\psi|^2 = a^2\mathrm{e}^{-2x/\xi} \quad , \tag{E.3}$$

where a^2 is real and positive.

In Fig. E.1(a) we plot an exemplary probability density of the investigated zero-mode with $u/w = 0.49$. The probability density alternates and decreases by going from the left boundary to the right. To this end, we use the function from Eq. (E.3) to fit the envelop function of the probability density which is shown by a blue line in Fig. E.1(a). The used fit function works very well to describe the envelop function of the probability density. We use a least square fit method which leads to errors below the tenth digit and are therefore neglected.

Figure E.1(b) shows the analytical solution for the localization length using the universal approach as a function of u/w as well as the numerical calculations. The analytical function coincides very well with the numeric and thus supports the validity of the universal relation.

As a complement, we additionally calculate the localization length with the conventional relation. To do so, we describe the minimum of the dispersion with a Taylor expansion up to the second order

$$E(k = \pi + q) = w - 2u(1 - \frac{q^2}{2} + \mathcal{O}(q^4)) \quad . \tag{E.4}$$

The square of the Eq. (E.4) is described by

$$E^2(q) = (w - 2u)^2 + (w - 2u)2uq^2 + \mathcal{O}(q^4) \quad . \tag{E.5}$$

The comparison with $E^2(q) = \Delta^2 + (sq)^2$ leads to

$$\Delta = w - 2u \quad \text{and} \quad s^2 = (w - 2u)2u \quad . \tag{E.6}$$

Thus the localization length with the conventional approach is given by

$$\xi = \frac{s}{\Delta} = \sqrt{\frac{2u}{w - 2u}} \quad . \tag{E.7}$$

This relation for ξ also diverges for $w = 2u$ and is finite for $w > 2u$ which also coincides with our results. However the discrepancy to the numerical values is clearly shown in Fig. E.1(b). Therefore we conclude that the universal approach is more suitable to calculate the localization length.

For the sake of completeness, the localization length has also been determined in general for the extended SSH model [248] and is described by

$$1/\xi = \operatorname{acosh}\left(\frac{v}{w} - \frac{vw}{4u^2} + \frac{1}{4u^2}\sqrt{4u^2(w^2 - v^2) + w^2v^2}\right) \quad . \tag{E.8}$$

The delocalization of in-gap states is a general phenomena and also occurs in two-dimensional topological systems as well, see Chap. 5. Thus it may be possible to extend the one-dimensional approach to find a localization length in two dimensions. This task is left to future research.

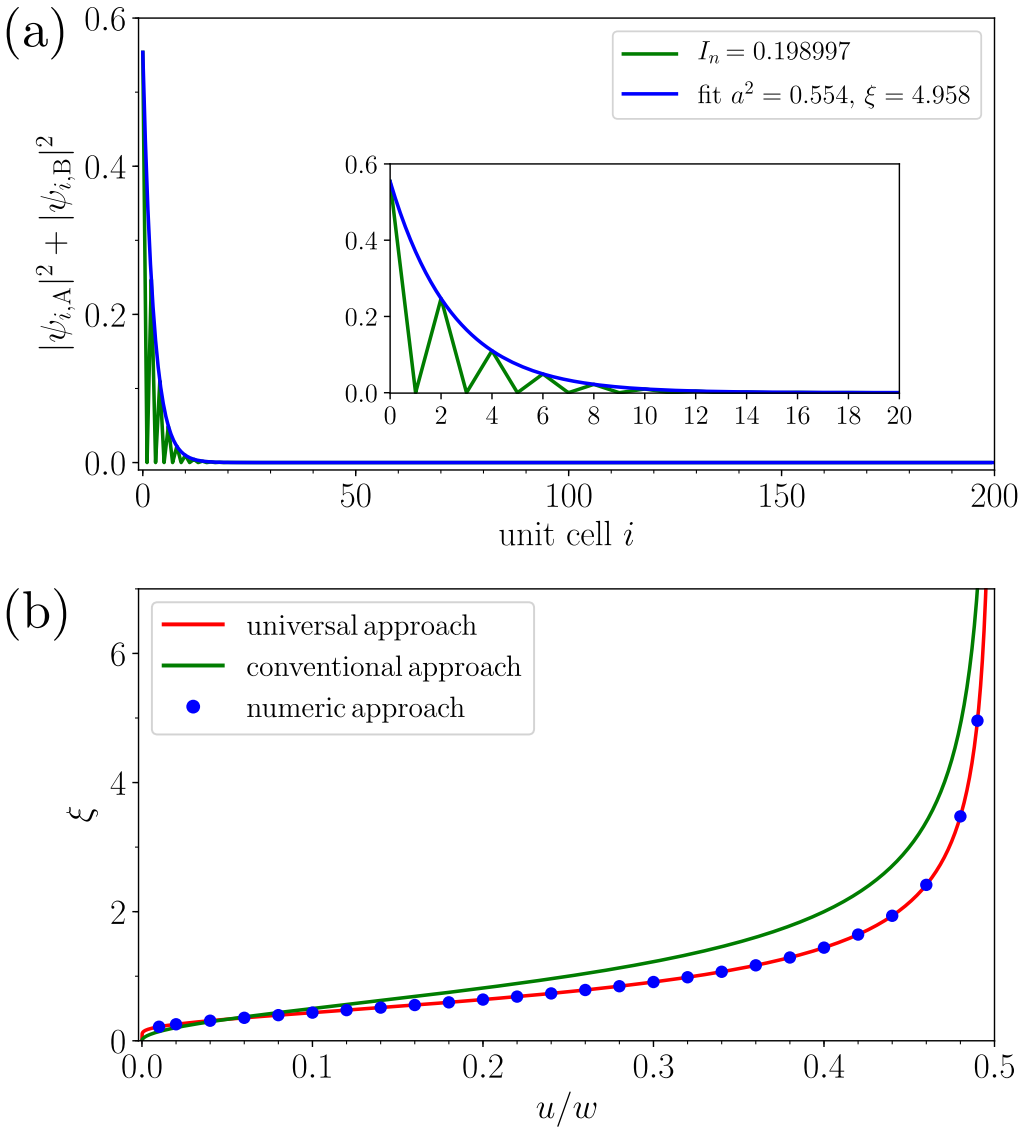

Figure E.1: (a) Fit of the envelop probability function with an exponentially localized function in the SSH model at $v = 0$ and $u/w = 0.49$. The IPR of the eigenstate and the fit parameters are given in the legend. (b) The localization length for the universal and conventional approach as a function of u/w are shown by red and green lines, respectively. The numerical calculated values are depicted by blue circles.

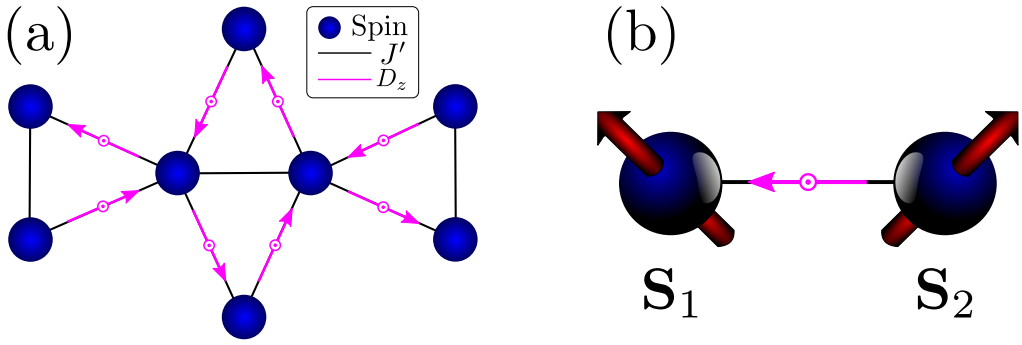

Figure F.1: (a) Cutout of two nearest neighbor spins in the Shastry–Sutherland lattice including their Dzyaloshinskii–Moriya coupling to the next-nearest neighbor. (b) Coupling of two classical spins.

F. Estimation of the ground state with two classical spins

The ground state of the spin system determines the character of the spin excitations, which are the subject of the investigation, and therefore represents the basis of our spin calculation in Chap. 6. The single-ion anisotropy (SIA) and the Dzyaloshinskii–Moriya (DM) coupling favor different ground state alignments. While the SIA favors an easy-axis alignment along the z-axis for $A^{zz} = A \geq 0$, the DM coupling benefits from tilted spins. To find the energetically optimum alignment, we estimate the condition for the transition from a polarized state to a tilted ground state by investigating two classical spins of length S, see Fig. F.1(b). For the correct embedding of the spin pair in the Shastry–Sutherland lattice, the SIA term is split into four parts $A/4$ because each site has four J' and D_z bonds, see Fig. F.1(a). The Hamiltonian of the two spins reads

$$\mathcal{H} = -J'\boldsymbol{S}_1\boldsymbol{S}_2 - \frac{A}{4}\left((S_1^z)^2 + (S_2^z)^2\right) - D_z(S_1^x S_2^y - S_1^y S_2^x) \quad . \tag{F.1}$$

The two classical spins are parameterized by two paris of angels

$$\boldsymbol{S_1} = S\begin{pmatrix}\sin(\theta_1)\cos(\varphi_1)\\ \sin(\theta_1)\sin(\varphi_1)\\ \cos(\theta_1)\end{pmatrix} \quad \text{and} \quad \boldsymbol{S_2} = S\begin{pmatrix}\sin(\theta_2)\cos(\varphi_2)\\ \sin(\theta_2)\sin(\varphi_2)\\ \cos(\theta_2)\end{pmatrix} \quad , \tag{F.2}$$

where φ_1 and φ_2 set the azimuthal angles whereas θ_1 and θ_2 set the polar angles. Hence, the classical energy is given by

$$\begin{aligned} E(\theta_1,\theta_2,\varphi_1,\varphi_2) = &-J'S^2(\cos(\theta_1)\cos(\theta_2) + \sin(\theta_1)\sin(\theta_2)\cos(\varphi_1-\varphi_2)) \\ &-\frac{A}{4}S^2(\cos(\theta_1)^2 + \cos(\theta_2)^2) - D_zS^2\sin(\theta_1)\sin(\theta_2)\sin(\varphi_1-\varphi_2)) \,, \end{aligned} \tag{F.3}$$

where only the difference of the azimuthal angels matters. Thus, we define the relative azimuthal angle $\varphi := \varphi_1 - \varphi_2$. The aim is to find the lowest energy. First, we minimize the energy by finding the extrema with respect to φ:

$$\frac{\partial E(\theta_1,\theta_2,\varphi)}{\partial\varphi} = -\sin(\theta_1)\sin(\theta_2)S^2(D_z\cos(\varphi) - J'\sin(\varphi)) = 0 \quad , \tag{F.4}$$

which is given for all polar angles by fulfilling $d := D_z/J' = \tan(\varphi)$. Furthermore, we introduce $a := A/J'$, $x := \cos(\theta_1 + \theta_2)$, and $y := \cos(\theta_1 - \theta_2)$ with $|x|, |y| \leq 1$, so that we can simplify the Eq. (F.3) to

$$\frac{2E(x,y,\varphi)}{S^2 J'} = -x - y - (y-x)\cos(\varphi) - \frac{a}{2}(1+xy) - (y-x)\frac{\sin(\varphi)^2}{\cos(\varphi)} \tag{F.4a}$$

$$= -x - y - \frac{a}{2}(1+xy) - \frac{(y-x)}{\cos(\varphi)} \quad . \tag{F.4b}$$

Without loss of generality, we choose that $\mathrm{sgn}(\cos(\varphi)) = -\mathrm{sgn}(x-y)$. Using

$$\left|\frac{1}{\cos(\varphi)}\right| = \sqrt{1+\tan(\varphi)^2} = \sqrt{1+d^2} \tag{F.5}$$

leads to the final equation

$$\frac{2E(x,y)}{S^2 J'} = -x - y - \frac{a}{2}(1+xy) - |x-y|\sqrt{1+d^2} \quad . \tag{F.6}$$

This expression is invariant under the exchange of x with y so that we restrict the considered range of parameters to $1 \geq x \geq y \geq -1$ so that $|x-y| \to x-y$. As a result, Eq. (F.6) can be recast to

$$\frac{2E(x,y)}{S^2 J'} = x\left(-1 - \frac{ay}{2} - \sqrt{1+d^2}\right) - \frac{a}{2} + y\left(-1 + \sqrt{1+d^2}\right) \quad . \tag{F.7}$$

The term proportional to x in Eq. (F.7) is negative

$$-(1 + \frac{ay}{2} + \sqrt{1+d^2}) < 0 \quad , \tag{F.8}$$

so that $x = 1$ is the best value to lower the energy. The classical energy can now be interpreted as a function of y:

$$\frac{2E(y)}{S^2 J'} = -\left(\frac{a}{2} + 1 + \sqrt{1+d^2}\right) + y\left(-\frac{a}{2} - 1 + \sqrt{1+d^2}\right) \quad , \tag{F.9}$$

where the function has a minimal value at the boundary $y = 1$ in the case of a negative slope. Hence the sign changes at

$$\frac{a}{2} + 1 = \sqrt{1+d^2} \tag{F.10}$$

which determines the phase transition. We conclude that as long as $\frac{a}{2}+1 \geq \sqrt{1+d^2}$ holds, one of the two possible polarized ground states is spontaneously chosen since $x = y = 1$ corresponds to $\theta_1 = \theta_2 = \{0, \pi\}$.

Bibliography

[1] D. J. Thouless, M. Kohmoto, M. P. Nightingale, and M. Den Nijs, *Quantized Hall conductance in a two-dimensional periodic potential*, Physical Review Letters **49**, 405 (1982).

[2] K. v. Klitzing, *The quantized Hall effect*, Reviews of Modern Physics **58**, 519 (1986).

[3] B. Bradlyn, L. Elcoro, J. Cano, M. G. Vergniory, Z. Wang, C. Felser, M. I. Aroyo, and B. A. Bernevig, *Topological quantum chemistry*, Nature **547**, 298 (2017).

[4] T. Bartels-Rausch, V. Bergeron, J. H. E. Cartwright, R. Escribano, J. L. Finney, H. Grothe, P. J. Gutiérrez, J. Haapala, W. F. Kuhs, J. B. C. Pettersson, et al., *Ice structures, patterns, and processes: A view across the icefields*, Reviews of Modern Physics **84**, 885 (2012).

[5] T. M. Gasser, A. V. Thoeny, L. J. Plaga, K. W. Köster, M. Etter, R. Böhmer, and T. Loerting, *Experiments indicating a second hydrogen ordered phase of ice vi*, Chemical Science **9**, 4224–4234 (2018).

[6] J. M. Kosterlitz and D. J. Thouless, *Long range order and metastability in two dimensional solids and superfluids.(Application of dislocation theory)*, Journal of Physics C: Solid State Physics **5**, L124 (1972).

[7] J. M. Kosterlitz and D. J. Thouless, *Ordering, metastability and phase transitions in two-dimensional systems*, Journal of Physics C: Solid State Physics **6**, 1181 (1973).

[8] A. Kitaev and J. Preskill, *Topological entanglement entropy*, Physical Review Letters **96**, 110404 (2006).

[9] M. Levin and X.-G. Wen, *Detecting topological order in a ground state wave function*, Physical Review Letters **96**, 110405 (2006).

[10] X.-G. Wen, *Topological orders in rigid states*, International Journal of Modern Physics B **4**, 239–271 (1990).

[11] X. Chen, Z.-C. Gu, and X.-G. Wen, *Local unitary transformation, long-range quantum entanglement, wave function renormalization, and topological order*, Physical Review B **82**, 155138 (2010).

[12] Z.-C. Gu and X.-G. Wen, *Tensor-entanglement-filtering renormalization approach and symmetry-protected topological order*, Physical Review B **80**, 155131 (2009).

[13] M. Levin and Z.-C. Gu, *Braiding statistics approach to symmetry-protected topological phases*, Physical Review B **86**, 115109 (2012).

[14] X.-G. Wen and Q. Niu, *Ground-state degeneracy of the fractional quantum Hall states in the presence of a random potential and on high-genus Riemann surfaces*, Physical Review B **41**, 9377 (1990).

[15] R. B. Laughlin, *Anomalous quantum Hall effect: An incompressible quantum fluid with fractionally charged excitations*, Physical Review Letters **50**, 1395 (1983).

[16] G. Gregory and N. Read, *Nonabelions in the fractional quantum Hall effect*, Nuclear Physics B **360**, 362–396 (1991).

[17] C. Nayak, S. H. Simon, A. Stern, M. Freedman, and S. Das Sarma, *Non-Abelian anyons and topological quantum computation*, Reviews of Modern Physics **80**, 1083 (2008).

[18] X.-G. Wen, *Topological orders and edge excitations in fractional quantum Hall states*, Advances in Physics **44**, 405–473 (1995).

[19] K. v. Klitzing, G. Dorda, and M. Pepper, *New method for high-accuracy determination of the fine-structure constant based on quantized Hall resistance*, Physical Review Letters **45**, 494 (1980).

[20] D. C. Tsui, H. L. Stormer, and A. C. Gossard, *Two-dimensional magnetotransport in the extreme quantum limit*, Physical Review Letters **48**, 1559 (1982).

[21] L. Savary and L. Balents, *Quantum spin liquids: A review*, Reports on Progress in Physics **80**, 016502 (2016).

[22] L. Fidkowski and A. Kitaev, *Topological phases of fermions in one dimension*, Physical Review B **83**, 075103 (2011).

[23] M. Ezawa, Y. Tanaka, and N. Nagaosa, *Topological phase transition without gap closing*, Scientific Reports **3**, 2790 (2013).

[24] R. S. K. Mong and V. Shivamoggi, *Edge states and the bulk-boundary correspondence in Dirac Hamiltonians*, Physical Review B **83**, 125109 (2011).

[25] L. Fidkowski, T. S. Jackson, and I. Klich, *Model characterization of gapless edge modes of topological insulators using intermediate Brillouin-zone functions*, Physical Review Letters **107**, 036601 (2011).

[26] T. Fukui, K. Shiozaki, T. Fujiwara, and S. Fujimoto, *Bulk-edge correspondence for Chern topological phases: A viewpoint from a generalized index theorem*, Journal of the Physical Society of Japan **81**, 114602 (2012).

[27] B. A. Bernevig and H. L. Hughes, *Topological insulators and topological superconductors* (Princeton university press, 2013).

[28] M. König, S. Wiedmann, C. Brüne, A. Roth, H. Buhmann, L. W. Molenkamp, X.-L. Qi, and S.-C. Zhang, *Quantum spin Hall insulator state in HgTe quantum wells*, Science **318**, 766–770 (2007).

[29] M. Z. Hasan and C. L. Kane, *Colloquium: Topological insulators*, Reviews of Modern Physics **82**, 3045 (2010).

[30] X.-L. Qi and S.-C. Zhang, *Topological insulators and superconductors*, Reviews of Modern Physics **83**, 1057 (2011).

[31] Y. Ando, *Topological insulator materials*, Journal of the Physical Society of Japan **82**, 102001 (2013).

[32] C.-Z. Chang, J. Zhang, X. Feng, J. Shen, Z. Zhang, M. Guo, K. Li, Y. Ou, P. Wei, L.-L. Wang, et al., *Experimental observation of the quantum anomalous Hall effect in a magnetic topological insulator*, Science **340**, 167–170 (2013).

[33] A. Kitaev, "Periodic table for topological insulators and superconductors", in AIP Conference Proceedings, Vol. 1134, 1 (AIP, 2009), pp. 22–30.

[34] M. R. Zirnbauer, *Riemannian symmetric superspaces and their origin in random-matrix theory*, Journal of Mathematical Physics **37**, 4986–5018 (1996).

[35] A. Altland and M. R. Zirnbauer, *Nonstandard symmetry classes in mesoscopic normal-superconducting hybrid structures*, Physical Review B **55**, 1142 (1997).

[36] A. P. Schnyder, S. Ryu, A. Furusaki, and A. W. W. Ludwig, *Classification of topological insulators and superconductors in three spatial dimensions*, Physical Review B **78**, 195125 (2008).

[37] J. Zak, *Berry's phase for energy bands in solids*, Physical Review Letters **62**, 2747 (1989).

[38] C.-K. Chiu, J. C. Y. Teo, A. P. Schnyder, and S. Ryu, *Classification of topological quantum matter with symmetries*, Reviews of Modern Physics **88**, 035005 (2016).

[39] M. Kohmoto, *Topological invariant and the quantization of the Hall conductance*, Annals of Physics **160**, 343–354 (1985).

[40] L. Fu and C. L. Kane, *Time reversal polarization and a $\mathbb{Z}_2$ adiabatic spin pump*, Physical Review B **74**, 195312 (2006).

[41] C. Wu, B. A. Bernevig, and S.-C. Zhang, *Helical liquid and the edge of quantum spin Hall systems*, Physical Review Letters **96**, 106401 (2006).

[42] C. Xu and J. E. Moore, *Stability of the quantum spin Hall effect: Effects of interactions, disorder, and $\mathbb{Z}_2$ topology*, Physical Review B **73**, 045322 (2006).

[43] A. M. Essin and J. E. Moore, *Topological insulators beyond the Brillouin zone via Chern parity*, Physical Review B **76**, 165307 (2007).

[44] M. Malki and G. S. Uhrig, *Tunable edge states and their robustness towards disorder*, Physical Review B **95**, 235118 (2017).

[45] Y. Hatsugai, *Chern number and edge states in the integer quantum Hall effect*, Physical Review Letters **71**, 3697 (1993).

[46] M. Nakahara, *Differentialgeometrie, Topologie und Physik* (Springer-Verlag, 2015).

[47] J. E. Avron, R. Seiler, and B. Simon, *Homotopy and quantization in condensed matter physics*, Physical Review Letters **51**, 51 (1983).

[48] Q. Niu, D. J. Thouless, and Y.-S. Wu, *Quantized Hall conductance as a topological invariant*, Physical Review B **31**, 3372 (1985).

[49] G. S. Uhrig, *Ohm's law in the quantum Hall effect*, Zeitschrift für Physik B Condensed Matter **82**, 29–36 (1991).

[50] M. V. Berry, "Quantal phase factors accompanying adiabatic changes", in Proceedings of the Royal Society of London A: Mathematical, Physical and Engineering Sciences, Vol. 392, 1802 (The Royal Society, 1984), pp. 45–57.

[51] F. D. M. Haldane, *Model for a quantum Hall effect without Landau levels: Condensed-matter realization of the parity anomaly*, Physical Review Letters **61**, 2015 (1988).

[52] H. Weng, R. Yu, X. Hu, X. Dai, and Z. Fang, *Quantum anomalous Hall effect and related topological electronic states*, Advances in Physics **64**, 227–282 (2015).

[53] C.-X. Liu, S.-C. Zhang, and X.-L. Qi, *The quantum anomalous Hall effect: Theory and experiment*, Annual Review of Condensed Matter Physics **7**, 301–321 (2016).

[54] Y. Ren, Z. Qiao, and Q. Niu, *Topological phases in two-dimensional materials: A review*, Reports on Progress in Physics **79**, 066501 (2016).

[55] C. L. Kane and E. J. Mele, *Quantum spin Hall effect in graphene*, Physical Review Letters **95**, 226801 (2005).

[56] C. L. Kane and E. J. Mele, $\mathbb{Z}_2$ *topological order and the quantum spin Hall effect*, Physical Review Letters **95**, 146802 (2005).

[57] B. A. Bernevig and S.-C. Zhang, *Quantum spin Hall effect*, Physical Review Letters **96**, 106802 (2006).

[58] B. A. Bernevig, T. L. Hughes, and S.-C. Zhang, *Quantum spin Hall effect and topological phase transition in HgTe quantum wells*, Science **314**, 1757–1761 (2006).

[59] A. Roth, C. Brüne, H. Buhmann, L. W. Molenkamp, J. Maciejko, X.-L. Qi, and S.-C. Zhang, *Nonlocal transport in the quantum spin Hall state*, Science **325**, 294–297 (2009).

[60] I. Knez, R.-R. Du, and G. Sullivan, *Evidence for helical edge modes in inverted InAs/GaSb quantum wells*, Physical Review Letters **107**, 136603 (2011).

[61] L. Du, I. Knez, G. Sullivan, and R.-R. Du, *Robust helical edge transport in gated InAs/GaSb bilayers*, Physical Review Letters **114**, 096802 (2015).

[62] C.-C. Liu, W. Feng, and Y. Yao, *Quantum spin Hall effect in silicene and two-dimensional germanium*, Physical Review Letters **107**, 076802 (2011).

[63] X. Kou, S.-T. Guo, Y. Fan, L. Pan, M. Lang, Y. Jiang, Q. Shao, T. Nie, K. Murata, J. Tang, et al., *Scale-invariant quantum anomalous Hall effect in magnetic topological insulators beyond the two-dimensional limit*, Physical Review Letters **113**, 137201 (2014).

[64] C.-Z. Chang, W. Zhao, D. Y. Kim, H. Zhang, B. A. Assaf, D. Heiman, S.-C. Zhang, C. Liu, M. H. W. Chan, and J. S. Moodera, *High-precision realization of robust quantum anomalous Hall state in a hard ferromagnetic topological insulator*, Nature Materials **14**, 473 (2015).

[65] S.-C. Wu, G. Shan, and B. Yan, *Prediction of near-room-temperature quantum anomalous Hall effect on honeycomb materials*, Physical Review Letters **113**, 256401 (2014).

[66] Y. Han, J.-G. Wan, G.-X. Ge, F.-Q. Song, and G.-H. Wang, *High-temperature quantum anomalous Hall effect in honeycomb bilayer consisting of Au atoms and single-vacancy graphene*, Scientific Reports **5**, 16843 (2015).

[67] A. V. Krasheninnikov and R. M. Nieminen, *Attractive interaction between transition-metal atom impurities and vacancies in graphene: A first-principles study*, Theoretical Chemistry Accounts **129**, 625–630 (2011).

[68] G. Jotzu, M. Messer, R. Desbuquois, M. Lebrat, T. Uehlinger, D. Greif, and T. Esslinger, *Experimental realization of the topological Haldane model with ultracold fermions*, Nature **515**, 237–240 (2014).

[69] D. Xiao, M.-C. Chang, and Q. Niu, *Berry phase effects on electronic properties*, Reviews of Modern Physics **82**, 1959 (2010).

[70] S. Pancharatnam, "Generalized theory of interference and its applications", in Proceedings of the Indian Academy of Sciences-Section A, Vol. 44, 6 (Springer, 1956), pp. 398–417.

[71] T. Kato, *On the adiabatic theorem of quantum mechanics*, Journal of the Physical Society of Japan **5**, 435–439 (1950).

[72] M. Fruchart and D. Carpentier, *An introduction to topological insulators*, Comptes Rendus Physique **14**, 779–815 (2013).

[73] N. Fläschner, B. S. Rem, M. Tarnowski, D. Vogel, D.-S. Lühmann, K. Sengstock, and C. Weitenberg, *Experimental reconstruction of the Berry curvature in a Floquet Bloch band*, Science **352**, 1091–1094 (2016).

[74] A. A. Soluyanov and D. Vanderbilt, *Smooth gauge for topological insulators*, Physical Review B **85**, 115415 (2012).

[75] F. Wilczek and A. Zee, *Appearance of gauge structure in simple dynamical systems*, Physical Review Letters **52**, 2111 (1984).

[76] W. P. Su, J. R. Schrieffer, and A. J. Heeger, *Soliton excitations in polyacetylene*, Physical Review B **22**, 2099 (1980).

[77] A. J. Heeger, S. Kivelson, J. Schrieffer, and W.-P. Su, *Solitons in conducting polymers*, Reviews of Modern Physics **60**, 781 (1988).

[78] E. P. Wigner, *Gruppentheorie und ihre anwendung auf die quantenmechanik der atomspektren*, (1931) 10.1007/978-3-663-02555-9.

[79] M. J. Rice and E. J. Mele, *Elementary excitations of a linearly conjugated diatomic polymer*, Physical Review Letters **49**, 1455 (1982).

[80] J. K. Asbóth, L. Oroszlány, and A. Pályi, *A short course on topological insulators*, Lecture Notes in Physics **919** (2016) 10.1007/978-3-319-25607-8.

[81] H. Guo and S. Chen, *Kaleidoscope of symmetry-protected topological phases in one-dimensional periodically modulated lattices*, Physical Review B **91**, 041402 (2015).

[82] R. Resta, *Macroscopic polarization in crystalline dielectrics: The geometric phase approach*, Reviews of Modern Physics **66**, 899 (1994).

[83] R. Resta, *Theory of the electric polarization in crystals*, Ferroelectrics **136**, 51–55 (1992).

[84] R. D. King-Smith and D. Vanderbilt, *Theory of polarization of crystalline solids*, Physical Review B **47**, 1651 (1993).

[85] T. L. Hughes, E. Prodan, and B. A. Bernevig, *Inversion-symmetric topological insulators*, Physical Review B **83**, 245132 (2011).

[86] R. Resta and D. Vanderbilt, "Theory of polarization: A modern approach", in *Physics of Ferroelectrics* (Springer, 2007), pp. 31–68.

[87] M. Atala, M. Aidelsburger, J. T. Barreiro, D. Abanin, T. Kitagawa, E. Demler, and I. Bloch, *Direct measurement of the Zak phase in topological Bloch bands*, Nature Physics **9**, 795 (2013).

[88] D. J. Thouless, *Quantization of particle transport*, Physical Review B **27**, 6083 (1983).

[89] Q. Niu and D. J. Thouless, *Quantised adiabatic charge transport in the presence of substrate disorder and many-body interaction*, Journal of Physics A: Mathematical and General **17**, 2453 (1984).

[90] Q. Niu, *Towards a quantum pump of electric charges*, Physical Review Letters **64**, 1812 (1990).

[91] J. P. Pekola, O.-P. Saira, V. F. Maisi, A. Kemppinen, M. Möttönen, Y. A. Pashkin, and D. V. Averin, *Single-electron current sources: Toward a refined definition of the ampere*, Reviews of Modern Physics **85**, 1421 (2013).

[92] R. B. Laughlin, *Quantized Hall conductivity in two dimensions*, Physical Review B **23**, 5632 (1981).

[93] B. I. Halperin, *Quantized Hall conductance, current-carrying edge states, and the existence of extended states in a two-dimensional disordered potential*, Physical Review B **25**, 2185 (1982).

[94] D. R. Hofstadter, *Energy levels and wave functions of Bloch electrons in rational and irrational magnetic fields*, Physical Review B **14**, 2239 (1976).

[95] P. G. Harper, *Single band motion of conduction electrons in a uniform magnetic field*, Proceedings of the Physical Society. Section A **68**, 874 (1955).

[96] P. Delplace, D. Ullmo, and G. Montambaux, *Zak phase and the existence of edge states in graphene*, Physical Review B **84**, 195452 (2011).

[97] T. Fukui, Y. Hatsugai, and H. Suzuki, *Chern numbers in discretized Brillouin zone: Efficient method of computing (spin) Hall conductances*, Journal of the Physical Society of Japan **74**, 1674–1677 (2005).

[98] S. Heinze, K. Von Bergmann, M. Menzel, J. Brede, A. Kubetzka, R. Wiesendanger, G. Bihlmayer, and S. Blügel, *Spontaneous atomic-scale magnetic skyrmion lattice in two dimensions*, Nature Physics **7**, 713 (2011).

[99] J. Romhányi, K. Penc, and R. Ganesh, *Hall effect of triplons in a dimerized quantum magnet*, Nature Communications **6**, 6805 (2015).

[100] X.-L. Qi, Y.-S. Wu, and S.-C. Zhang, *Topological quantization of the spin Hall effect in two-dimensional paramagnetic semiconductors*, Physical Review B **74**, 085308 (2006).

[101] Y. A. Bychkov and E. I. Rashba, *Oscillatory effects and the magnetic susceptibility of carriers in inversion layers*, Journal of Physics C: Solid State Physics **17**, 6039 (1984).

[102] H. A. Kramers, *Théorie générale de la rotation paramagnétique dans les cristaux*, Proc. Acad. Amst **33**, 959–972 (1930).

[103] J. E. Moore and L. Balents, *Topological invariants of time-reversal-invariant band structures*, Physical Review B **75**, 121306 (2007).

[104] L. Fu and C. L. Kane, *Topological insulators with inversion symmetry*, Physical Review B **76**, 045302 (2007).

[105] T. Fukui and Y. Hatsugai, *Quantum spin Hall effect in three dimensional materials: Lattice computation of $\mathbb{Z}_2$ topological invariants and its application to Bi and Sb*, Journal of the Physical Society of Japan **76**, 053702–053702 (2007).

[106] D. N. Sheng, Z. Y. Weng, L. Sheng, and F. D. M. Haldane, *Quantum spin-Hall effect and topologically invariant Chern numbers*, Physical Review Letters **97**, 036808 (2006).

[107] E. Prodan, *Robustness of the spin-Chern number*, Physical Review B **80**, 125327 (2009).

[108] M. Malki and G. S. Uhrig, *Tunable dispersion of the edge states in the integer quantum Hall effect*, SciPost Physics **3**, 032 (2017).

[109] M. Malki and G. S. Uhrig, *Tunable signal velocity in the integer quantum Hall effect of tailored graphene*, arXiv:1909.03520 (2019).

[110] J. S. Van Dyke and D. K. Morr, *Controlling the flow of spin and charge in nanoscopic topological insulators*, Physical Review B **93**, 081401(R) (2016).

[111] Z. Qiao, Y. Han, L. Zhang, K. Wang, X. Deng, H. Jiang, S. A. Yang, J. Wang, and Q. Niu, *Anderson localization from the Berry-curvature interchange in quantum anomalous Hall systems*, Physical Review Letters **117**, 056802 (2016).

[112] C. H. Redder and G. S. Uhrig, *Topologically nontrivial Hofstadter bands on the kagome lattice*, Physical Review A **93**, 033654 (2016).

[113] G. S. Uhrig, *Tunable and direction-dependent group velocities in topologically protected edge states*, Physical Review B **93**, 205438 (2016).

[114] S. A. Wolf, D. D. Awschalom, R. A. Buhrman, J. M. Daughton, S. Von Molnar, M. L. Roukes, A. Y. Chtchelkanova, and D. M. Treger, *Spintronics: A spin-based electronics vision for the future*, Ccience **294**, 1488–1495 (2001).

[115] I. Žutić, J. Fabian, and S. D. Sarma, *Spintronics: Fundamentals and applications*, Reviews of Modern Physics **76**, 323 (2004).

[116] Z. Jiang, C.-Z. Chang, C. Tang, J.-G. Zheng, J. S. Moodera, and J. Shi, *Structural and proximity-induced ferromagnetic properties of topological insulator-magnetic insulator heterostructures*, AIP Advances **6**, 055809 (2016).

[117] T. Jungwirth, J. Sinova, J. Mašek, J. Kučera, and A. H. MacDonald, *Theory of ferromagnetic (III, Mn) V semiconductors*, Reviews of Modern Physics **78**, 809 (2006).

[118] Z. Qiao, S. A. Yang, W. Feng, W.-K. Tse, J. Ding, Y. Yao, J. Wang, and Q. Niu, *Quantum anomalous Hall effect in graphene from Rashba and exchange effects*, Physical Review B **82**, 161414(R) (2010).

[119] T.-W. Chen, Z.-R. Xiao, D.-W. Chiou, and G.-Y. Guo, *High Chern number quantum anomalous Hall phases in single-layer graphene with Haldane orbital coupling*, Physical Review B **84**, 165453 (2011).

[120] S. Bauer and C. A. Bobisch, *Nanoscale electron transport at the surface of a topological insulator*, Nature Communications **7**, 11381 (2016).

[121] A. Altland and B. D. Simons, *Condensed matter field theory* (Cambridge University Press, 2010).

[122] M. Büttiker, Y. Imry, R. Landauer, and S. Pinhas, *Generalized many-channel conductance formula with application to small rings*, Physical Review B **31**, 6207 (1985).

[123] C. W. J. Beenakker and H. van Houten, "Quantum transport in semiconductor nanostructures", in *Solid State Physics*, Vol. 44 (Elsevier, 1991), pp. 1–228.

[124] J. Weis and K. v. Klitzing, *Metrology and microscopic picture of the integer quantum Hall effect*, Philosophical Transactions of the Royal Society A: Mathematical, Physical and Engineering Sciences **369**, 3954–3974 (2011).

[125] M. Aidelsburger, M. Lohse, C. Schweizer, M. Atala, J. T. Barreiro, S. Nascimbène, N. Cooper, I. Bloch, and N. Goldman, *Measuring the Chern number of Hofstadter bands with ultracold bosonic atoms*, Nature Physics **11**, 162 (2015).

[126] G. Fève, A. Mahé, J.-M. Berroir, T. Kontos, B. Placais, D. C. Glattli, A. Cavanna, B. Etienne, and Y. Jin, *An on-demand coherent single-electron source*, Science **316**, 1169–1172 (2007).

[127] S. W. Hwang, H. P. Wei, L. W. Engel, D. C. Tsui, and A. M. M. Pruisken, *Scaling in spin-degenerate Landau levels in the integer quantum Hall effect*, Physical Review B **48**, 11416 (1993).

[128] N. Paradiso, S. Heun, S. Roddaro, L. N. Pfeiffer, K. W. West, L. Sorba, G. Biasiol, and F. Beltram, *Selective control of edge-channel trajectories by scanning gate microscopy*, Physica E: Low-dimensional Systems and Nanostructures **42**, 1038–1041 (2010).

[129] L. D. Landau, *Diamagnetismus der Metalle, Z. Physik, 64, 629–637*, 1930.

[130] E. Polizzi, *Density-matrix-based algorithm for solving eigenvalue problems*, Physical Review B **79**, 115112 (2009).

[131] D. Yoshioka, *The quantum Hall effect*, Vol. 133 (Springer Science & Business Media, 2013).

[132] D. Venturelli, V. Giovannetti, F. Taddei, R. Fazio, D. Feinberg, G. Usaj, and C. A. Balseiro, *Edge channel mixing induced by potential steps in an integer quantum Hall system*, Physical Review B **83**, 075315 (2011).

[133] D. B. Chklovskii, B. I. Shklovskii, and L. I. Glazman, *Electrostatics of edge channels*, Physical Review B **46**, 4026 (1992).

[134] L. Brey and H. A. Fertig, *Edge states and the quantized Hall effect in graphene*, Physical Review B **73**, 195408 (2006).

[135] D. A. Abanin, P. A. Lee, and L. S. Levitov, *Charge and spin transport at the quantum Hall edge of graphene*, Solid state communications **143**, 77–85 (2007).

[136] P. Delplace and G. Montambaux, *Wkb analysis of edge states in graphene in a strong magnetic field*, Physical Review B **82**, 205412 (2010).

[137] W. Wang and Z. S. Ma, *Edge states and distributions of edge currents in semi-infinite graphene*, The European Physical Journal B **81**, 431–439 (2011).

[138] T. Stegmann and A. Lorke, *Edge magnetotransport in graphene: A combined analytical and numerical study*, Annalen der Physik **527**, 723–736 (2015).

[139] K. Kadel, L. Kumari, W. Z. Li, J. Y. Huang, and P. P. Provencio, *Synthesis and thermoelectric properties of Bi_2Se_3 nanostructures*, Nanoscale Research Lett **6**, 57 (2011).

[140] D. L. Perry, *Handbook of inorganic compounds* (CRC press, 2016).

[141] Y. Zhang, Y.-W. Tan, H. L. Stormer, and P. Kim, *Experimental observation of the quantum Hall effect and Berry's phase in graphene*, Nature **438**, 201 (2005).

[142] A. H. C. Neto, F. Guinea, N. M. R. Peres, K. S. Novoselov, and A. K. Geim, *The electronic properties of graphene*, Reviews of Modern Physics **81**, 109 (2009).

[143] K. S. Novoselov, A. K. Geim, S. V. Morozov, D. Jiang, M. I. Katsnelson, I. V. Grigorieva, S. V. Dubonos, and A. A. Firsov, *Two-dimensional gas of massless Dirac fermions in graphene*, Nature **438**, 197 (2005).

[144] A. K. Geim and K. S. Novoselov, *The rise of graphene*, Nature Materials **6**, 183 (2007).

[145] D. P. DiVincenzo and E. J. Mele, *Self-consistent effective-mass theory for intralayer screening in graphite intercalation compounds*, Physical Review B **29**, 1685 (1984).

[146] G. W. Semenoff, *Condensed-matter simulation of a three-dimensional anomaly*, Physical Review Letters **53**, 2449 (1984).

[147] C. Hwang, D. A. Siegel, S.-K. Mo, W. Regan, A. Ismach, Y. Zhang, A. Zettl, and A. Lanzara, *Fermi velocity engineering in graphene by substrate modification*, Scientific Reports **2**, 590 (2012).

[148] M.-H. Liu, P. Rickhaus, P. Makk, E. Tóvári, R. Maurand, F. Tkatschenko, M. Weiss, C. Schönenberger, K. Richter, et al., *Scalable tight-binding model for graphene*, Physical Review Letters **114**, 036601 (2015).

[149] V. P. Gusynin and S. G. Sharapov, *Unconventional integer quantum Hall effect in graphene*, Physical Review Letters **95**, 146801 (2005).

[150] K. I. Bolotin, K. J. Sikes, Z. Jiang, M. Klima, G. Fudenberg, J. Hone, P. Kim, and H. L. Stormer, *Ultrahigh electron mobility in suspended graphene*, Solid State Communications **146**, 351–355 (2008).

[151] C. R. Dean, A. F. Young, I. Meric, C. Lee, L. Wang, S. Sorgenfrei, K. Watanabe, T. Taniguchi, P. Kim, K. L. Shepard, et al., *Boron nitride substrates for high-quality graphene electronics*, Nature Nanotechnology **5**, 722 (2010).

[152] W. Han, R. K. Kawakami, M. Gmitra, and J. Fabian, *Graphene spintronics*, Nature Nanotechnology **9**, 794 (2014).

[153] S. Roche, J. Åkerman, B. Beschoten, J.-C. Charlier, M. Chshiev, S. P. Dash, B. Dlubak, J. Fabian, A. Fert, M. Guimarães, et al., *Graphene spintronics: the European Flagship perspective*, 2D Materials **2**, 030202 (2015).

[154] F. Lafont, R. Ribeiro-Palau, D. Kazazis, A. Michon, O. Couturaud, C. Consejo, T. Chassagne, M. Zielinski, M. Portail, B. Jouault, et al., *Quantum Hall resistance standards from graphene grown by chemical vapour deposition on silicon carbide*, Nature Communications **6**, 6806 (2015).

[155] Y. Zheng and T. Ando, *Hall conductivity of a two-dimensional graphite system*, Physical Review B **65**, 245420 (2002).

[156] J. W. McClure, *Diamagnetism of graphite*, Physical Review **104**, 666 (1956).

[157] Y. Aharonov and D. Bohm, *Significance of electromagnetic potentials in the quantum theory*, Physical Review **115**, 485 (1959).

[158] Z. Chen, Y.-M. Lin, M. J. Rooks, and P. Avouris, *Graphene nano-ribbon electronics*, Physica E: Low-dimensional Systems and Nanostructures **40**, 228–232 (2007).

[159] E. W. Hill, A. K. Geim, K. Novoselov, F. Schedin, and P. Blake, *Graphene spin valve devices*, IEEE Transactions on Magnetics **42**, 2694–2696 (2006).

[160] L. C. Campos, V. R. Manfrinato, J. D. Sanchez-Yamagishi, J. Kong, and P. Jarillo-Herrero, *Anisotropic etching and nanoribbon formation in single-layer graphene*, Nano Letters **9**, 2600–2604 (2009).

[161] M. Malki, L. Müller, and G. S. Uhrig, *Absence of localized edge modes in spite of a non-trivial Zak phase in $BiCu_2PO_6$*, Physical Review Research **1**, 033197 (2019).

[162] H. Katsura, N. Nagaosa, and P. A. Lee, *Theory of the thermal Hall effect in quantum magnets*, Physical Review Letters **104**, 066403 (2010).

[163] Y. Onose, T. Ideue, H. Katsura, Y. Shiomi, N. Nagaosa, and Y. Tokura, *Observation of the magnon Hall effect*, Science **329**, 297–299 (2010).

[164] R. Matsumoto and S. Murakami, *Theoretical prediction of a rotating magnon wave packet in ferromagnets*, Physical Review Letters **106**, 197202 (2011).

[165] R. Shindou, R. Matsumoto, S. Murakami, and J.-i. Ohe, *Topological chiral magnonic edge mode in a magnonic crystal*, Physical Review B **87**, 174427 (2013).

[166] L. Zhang, J. Ren, J.-S. Wang, and B. Li, *Topological magnon insulator in insulating ferromagnet*, Physical Review B **87**, 144101 (2013).

[167] R. Chisnell, J. S. Helton, D. E. Freedman, D. K. Singh, R. I. Bewley, D. G. Nocera, and Y. S. Lee, *Topological magnon bands in a kagome lattice ferromagnet*, Physical Review Letters **115**, 147201 (2015).

[168] M. Malki and K. P. Schmidt, *Magnetic Chern bands and triplon Hall effect in an extended Shastry–Sutherland model*, Physical Review B **95**, 195137 (2017).

[169] P. A. McClarty, F. Krüger, T. Guidi, S. F. Parker, K. Refson, A. W. Parker, D. Prabhakaran, and R. Coldea, *Topological triplon modes and bound states in a Shastry–Sutherland magnet*, Nature Physics **13**, 736 (2017).

[170] K. W. Plumb, K. Hwang, Y. Qiu, L. W. Harriger, G. E. Granroth, A. I. Kolesnikov, G. J. Shu, F. C. Chou, Ch. Rüegg, Y. B. Kim, et al., *Quasiparticle-continuum level repulsion in a quantum magnet*, Nature Physics **12**, 224 (2016).

[171] L. Splinter, N. A. Drescher, H. Krull, and G. S. Uhrig, *Minimal model for the frustrated spin ladder system $BiCu_2PO_6$*, Physical Review B **94**, 155115 (2016).

[172] K. Hwang and Y. B. Kim, *Theory of triplon dynamics in the quantum magnet $BiCu_2PO_6$*, Physical Review B **93**, 235130 (2016).

[173] F. Cardano, A. D'Errico, A. Dauphin, M. Maffei, B. Piccirillo, C. de Lisio, G. De Filippis, V. Cataudella, E. Santamato, L. Marrucci, et al., *Detection of Zak phases and topological invariants in a chiral quantum walk of twisted photons*, Nature Communications **8**, 15516 (2017).

[174] A. A. Tsirlin, I. Rousochatzakis, D. Kasinathan, O. Janson, R. Nath, F. Weickert, C. Geibel, A. M. Läuchli, and H. Rosner, *Bridging frustrated-spin-chain and spin-ladder physics: Quasi-one-dimensional magnetism of $BiCu_2PO_6$*, Physical Review B **82**, 144426 (2010).

[175] K. W. Plumb, Z. Yamani, M. Matsuda, G. J. Shu, B. Koteswararao, F. C. Chou, and Y.-J. Kim, *Incommensurate dynamic correlations in the quasi-two-dimensional spin liquid $BiCu_2PO_6$*, Physical Review B **88**, 024402 (2013).

[176] T. Moriya, *Anisotropic superexchange interaction and weak ferromagnetism*, Physical Review **120**, 91 (1960).

[177] L. Shekhtman, O. Entin-Wohlman, and A. Aharony, *Moriya's anisotropic superexchange interaction, frustration, and Dzyaloshinsky's weak ferromagnetism*, Physical Review Letters **69**, 836 (1992).

[178] L. Shekhtman, A. Aharony, and O. Entin-Wohlman, *Bond-dependent symmetric and antisymmetric superexchange interactions in La_2CuO_4*, Physical Review B **47**, 174 (1993).

[179] O. Mentré, E. Janod, P. Rabu, M. Hennion, F. Leclercq-Hugeux, J. Kang, C. Lee, M.-H. Whangbo, and S. Petit, *Incommensurate spin correlation driven by frustration in $BiCu_2PO_6$*, Physical Review B **80**, 180413 (2009).

[180] K. P. Schmidt and G. S. Uhrig, *Excitations in one-dimensional $S = \frac{1}{2}$ quantum antiferromagnets*, Physical Review Letters **90**, 227204 (2003).

[181] S. Sachdev and R. N. Bhatt, *Bond-operator representation of quantum spins: Mean-field theory of frustrated quantum Heisenberg antiferromagnets*, Physical Review B **41**, 9323 (1990).

[182] H. Krull, N. A. Drescher, and G. S. Uhrig, *Enhanced perturbative continuous unitary transformations*, Physical Review B **86**, 125113 (2012).

[183] F. Wegner, *Flow-equations for Hamiltonians*, Annalen der Physik **506**, 77–91 (1994).

[184] J.-P. Blaizot and G. Ripka, *Quantum theory of finite systems*, Vol. 3, 9 (MIT press Cambridge, MA, 1986).

[185] F. Liu and K. Wakabayashi, *Novel topological phase with a zero Berry curvature*, Physical Review Letters **118**, 076803 (2017).

[186] L. Li, C. Yang, and S. Chen, *Winding numbers of phase transition points for one-dimensional topological systems*, EPL (Europhysics Letters) **112**, 10004 (2015).

[187] D. G. Joshi and A. P. Schnyder, *Topological quantum paramagnet in a quantum spin ladder*, Physical Review B **96**, 220405(R) (2017).

[188] D. G. Joshi, K. Coester, K. P. Schmidt, and M. Vojta, *Nonlinear bond-operator theory and 1/d expansion for coupled-dimer magnets. I. Paramagnetic phase*, Physical Review B **91**, 094404 (2015).

[189] B. Kramer and A. MacKinnon, *Localization: Theory and experiment*, Reports on Progress in Physics **56**, 1469 (1993).

[190] M. Calixto and E. Romera, *Inverse participation ratio and localization in topological insulator phase transitions*, Journal of Statistical Mechanics: Theory and Experiment **2015**, P06029 (2015).

[191] M. Malki and G. S. Uhrig, *Delocalization of edge states in topological phases*, Europhysics Letters **127**, 27001 (2019).

[192] M. I. Molina, A. E. Miroshnichenko, and Y. S. Kivshar, *Surface bound states in the continuum*, Physical Review Letters **108**, 070401 (2012).

[193] G. Corrielli, G. Della Valle, A. Crespi, R. Osellame, and S. Longhi, *Observation of surface states with algebraic localization*, Physical Review Letters **111**, 220403 (2013).

[194] M. Wada, S. Murakami, F. Freimuth, and G. Bihlmayer, *Localized edge states in two-dimensional topological insulators: Ultrathin Bi films*, Physical Review B **83**, 121310 (2011).

[195] Y. Baum, T. Posske, I. C. Fulga, B. Trauzettel, and A. Stern, *Coexisting edge states and gapless bulk in topological states of matter*, Physical Review Letters **114**, 136801 (2015).

[196] R. Verresen, N. G. Jones, and F. Pollmann, *Topology and edge modes in quantum critical chains*, Physical Review Letters **120**, 057001 (2018).

[197] W. P. Su, J. R. Schrieffer, and A. J. Heeger, *Solitons in polyacetylene*, Physical Review Letters **42**, 1698 (1979).

[198] N. Goldman, J. Dalibard, A. Dauphin, F. Gerbier, M. Lewenstein, P. Zoller, and I. B. Spielman, *Direct imaging of topological edge states in cold-atom systems*, Proceedings of the National Academy of Sciences **110**, 6736–6741 (2013).

[199] X. Wan, A. M. Turner, A. Vishwanath, and S. Y. Savrasov, *Topological semimetal and Fermi-arc surface states in the electronic structure of pyrochlore iridates*, Physical Review B **83**, 205101 (2011).

[200] L. Fu, *Topological crystalline insulators*, Physical Review Letters **106**, 106802 (2011).

[201] F. Schindler, A. M. Cook, M. G. Vergniory, Z. Wang, S. S. P. Parkin, B. A. Bernevig, and T. Neupert, *Higher-order topological insulators*, Science Advances **4**, eaat0346 (2018).

[202] A. Y. Kitaev, *Unpaired Majorana fermions in quantum wires*, Physics-Uspekhi **44**, 131 (2001).

[203] M. Ölschläger, G. Wirth, T. Kock, and A. Hemmerich, *Topologically induced avoided band crossing in an optical checkerboard lattice*, Physical Review Letters **108**, 075302 (2012).

[204] M. Aidelsburger, M. Atala, M. Lohse, J. T. Barreiro, B. Paredes, and I. Bloch, *Realization of the Hofstadter Hamiltonian with ultracold atoms in optical lattices*, Physical Review Letters **111**, 185301 (2013).

[205] H. Miyake, G. A. Siviloglou, C. J. Kennedy, W. C. Burton, and W. Ketterle, *Realizing the Harper Hamiltonian with laser-assisted tunneling in optical lattices*, Physical Review Letters **111**, 185302 (2013).

[206] K. Sun, Z. Gu, H. Katsura, and S. D. Sarma, *Nearly flatbands with nontrivial topology*, Physical Review Letters **106**, 236803 (2011).

[207] X. Ying and A. Kamenev, *Symmetry-protected topological metals*, Physical Review Letters **121**, 086810 (2018).

[208] J. M. Zeuner, M. C. Rechtsman, Y. Plotnik, Y. Lumer, S. Nolte, M. S. Rudner, M. Segev, and A. Szameit, *Observation of a topological transition in the bulk of a non-Hermitian system*, Physical Review Letters **115**, 040402 (2015).

[209] S. Mittal, S. Ganeshan, J. Fan, A. Vaezi, and M. Hafezi, *Measurement of topological invariants in a 2D photonic system*, Nature Photonics **10**, 180 (2016).

[210] M. Malki and G. S. Uhrig, *Topological magnon bands for magnonics*, Physical Review B **99**, 174412 (2019).

[211] A. Fert, *Nobel lecture: Origin, development, and future of spintronics*, Reviews of Modern Physics **80**, 1517 (2008).

[212] V. V. Kruglyak, S. O. Demokritov, and D. Grundler, *Magnonics*, Journal of Physics D: Applied Physics **43**, 264001 (2010).

[213] S. O. Demokritov and A. N. Slavin, *Magnonics: From fundamentals to applications*, Vol. 125 (Springer Science & Business Media, 2012).

[214] K. Nakata, S. K. Kim, J. Klinovaja, and D. Loss, *Magnonic topological insulators in antiferromagnets*, Physical Review B **96**, 224414 (2017).

[215] I. Dzyaloshinsky, *A thermodynamic theory of "weak" ferromagnetism of antiferromagnetics*, Journal of Physics and Chemistry of Solids **4**, 241–255 (1958).

[216] F. Bloch, *Zur Theorie des Ferromagnetismus*, Zeitschrift für Physik **61**, 206–219 (1930).

[217] D. J. P. Morris, D. A. Tennant, S. A. Grigera, B. Klemke, C. Castelnovo, R. Moessner, C. Czternasty, M. Meissner, K. C. Rule, J.-U. Hoffmann, et al., *Dirac strings and magnetic monopoles in the spin ice $Dy_2Ti_2O_7$*, Science **326**, 411–414 (2009).

[218] L. D. Faddeev and L. A. Takhtajan, *What is the spin of a spin wave?*, Physics Letters A **85**, 375–377 (1981).

[219] S. A. Owerre, *A first theoretical realization of honeycomb topological magnon insulator*, Journal of Physics: Condensed Matter **28**, 386001 (2016).

[220] S. K. Kim, H. Ochoa, R. Zarzuela, and Y. Tserkovnyak, *Realization of the Haldane–Kane–Mele model in a system of localized spins*, Physical Review Letters **117**, 227201 (2016).

[221] F.-Y. Li, Y.-D. Li, Y. B. Kim, L. Balents, Y. Yu, and G. Chen, *Weyl magnons in breathing pyrochlore antiferromagnets*, Nature Communications **7**, 12691 (2016).

[222] T. Ideue, Y. Onose, H. Katsura, Y. Shiomi, S. Ishiwata, N. Nagaosa, and Y. Tokura, *Effect of lattice geometry on magnon Hall effect in ferromagnetic insulators*, Physical Review B **85**, 134411 (2012).

[223] D. Pesin and L. Balents, *Mott physics and band topology in materials with strong spin–orbit interaction*, Nature Physics **6**, 376 (2010).

[224] S. Rachel and K. Le Hur, *Topological insulators and Mott physics from the Hubbard interaction*, Physical Review B **82**, 075106 (2010).

[225] A. Rüegg and G. A. Fiete, *Topological order and semions in a strongly correlated quantum spin Hall insulator*, Physical Review Letters **108**, 046401 (2012).

[226] G. Y. Cho, Y.-M. Lu, and J. E. Moore, *Gapless edge states of background field theory and translation-symmetric $\mathbb{Z}_2$ spin liquids*, Physical Review B **86**, 125101 (2012).

[227] B. S. Shastry and B. Sutherland, *Exact ground state of a quantum mechanical antiferromagnet*, Physica B+C **108**, 1069–1070 (1981).

[228] S. Miyahara and K. Ueda, *Theory of the orthogonal dimer Heisenberg spin model for $SrCu_2(BO_3)_2$*, Journal of Physics: Condensed Matter **15**, R327 (2003).

[229] J. Roger, V. Babizhetskyy, T. Guizouarn, K. Hiebl, R. Guérin, and J.-F. Halet, *The ternary RE–Si–B systems (RE= Dy, Ho, Er and Y) at 1270 K: Solid state phase equilibria and magnetic properties of the solid solution $REB_{2-x}Si_x$ (RE= Dy and Ho)*, Journal of Alloys and Compounds **417**, 72–84 (2006).

[230] Y. I. Spichkin, V. K. Pecharsky, and K. A. Gschneidner Jr, *Preparation, crystal structure, magnetic and magnetothermal properties of $(Gd_x\ R_{5-x})\ Si_4$, where R= Pr and Tb, alloys*, Journal of Applied Physics **89**, 1738–1745 (2001).

[231] A. L. Chernyshev and P. A. Maksimov, *Damped topological magnons in the kagome-lattice ferromagnets*, Physical Review Letters **117**, 187203 (2016).

[232] F. J. Dyson, *General theory of spin-wave interactions*, Physical Review **102**, 1217 (1956).

[233] S. V. Maleev, Zh. Eksp. Teor. Fiz. **33**, 1010 (1957).

[234] J. Goldstone, *Field theories with «Superconductor» solutions*, Il Nuovo Cimento (1955-1965) **19**, 154–164 (1961).

[235] K. Sun, H. Yao, E. Fradkin, and S. A. Kivelson, *Topological insulators and nematic phases from spontaneous symmetry breaking in 2d Fermi systems with a quadratic band crossing*, Physical Review Letters **103**, 046811 (2009).

[236] Y. D. Chong, X.-G. Wen, and M. Soljačić, *Effective theory of quadratic degeneracies*, Physical Review B **77**, 235125 (2008).

[237] A. A. Soluyanov and D. Vanderbilt, *Wannier representation of $\mathbb{Z}_2$ topological insulators*, Physical Review B **83**, 035108 (2011).

[238] A. Mook, J. Henk, and I. Mertig, *Edge states in topological magnon insulators*, Physical Review B **90**, 024412 (2014).

[239] A. V. Chumak, A. A. Serga, and B. Hillebrands, *Magnon transistor for all-magnon data processing*, Nature Communications **5**, 4700 (2014).

[240] K. P. Schmidt and G. S. Uhrig, *Spectral properties of magnetic excitations in cuprate two-leg ladder systems*, Modern Physics Letters B **19**, 1179–1205 (2005).

[241] G. S. Uhrig, K. P. Schmidt, and M. Grüninger, *Unifying magnons and triplons in stripe-ordered cuprate superconductors*, Physical Review Letters **93**, 267003 (2004).

[242] G. S. Uhrig, K. P. Schmidt, and M. Grüninger, *Magnetic excitations in bilayer high-temperature superconductors with stripe correlations*, Journal of the Physical Society of Japan **74**, 86–97 (2005).

[243] J. H. P. Colpa, *Diagonalization of the quadratic boson Hamiltonian*, Physica A: Statistical Mechanics and its Applications **93**, 327–353 (1978).

[244] Y. Kawaguchi and M. Ueda, *Spinor Bose–Einstein condensates*, Physics Reports **520**, 253–381 (2012).

[245] V. Peano, M. Houde, C. Brendel, F. Marquardt, and A. A. Clerk, *Topological phase transitions and chiral inelastic transport induced by the squeezing of light*, Nature Communications **7**, 10779 (2016).

[246] F. Grusdt, D. Abanin, and E. Demler, *Measuring $\mathbb{Z}_2$ topological invariants in optical lattices using interferometry*, Physical Review A **89**, 043621 (2014).

[247] K. Okunishi, Y. Akutsu, N. Akutsu, and T. Yamamoto, *Universal relation between the dispersion curve and the ground-state correlation length in one-dimensional antiferromagnetic quantum spin systems*, Physical Review B **64**, 104432 (2001).

[248] B. Pérez-González, M. Bello, Á. Gómez-León, and G. Platero, *Interplay between long-range hopping and disorder in topological systems*, Physical Review B **99**, 035146 (2019).

List of Figures

1.1. Overview of topological phases . . . 3
1.2. Distinction of topological phases by invariants . . . 5

2.1. Accumulation of the Berry phase during a cyclic adiabatic evolution . . . 13
2.2. Lattice structure of the SSH model . . . 18
2.3. Thouless pump cycle . . . 26
2.4. Lattice structure of the Haldane model . . . 28
2.5. Schematic illustration of the mass term in honeycomb lattices . . . 30
2.6. Phase diagram of the Haldane model . . . 31
2.7. Strip geometry of the Haldane model and the corresponding dispersion . . . 32

3.1. Site decoration of the honeycomb strip lattice . . . 39
3.2. Dispersion of chiral edge states in the Haldane model with decorated boundaries . . . 40
3.3. Dispersion of helical edge states in the Kane–Mele model with decorated boundaries . . . 42
3.4. Dispersion of helical edge states in the Kane–Mele model including Rashba coupling with decorated boundaries . . . 43
3.5. Fermi velocity in the decorated Kane–Mele model as a function of the Rashba coupling . . . 44
3.6. Dispersion of the edge states with a spin-dependent decoration . . . 45
3.7. Finite honeycomb sheet with local disorder . . . 47
3.8. Reconstruction of the dispersion of the edge states in the Haldane model with local disorder . . . 48
3.9. Approximation of the gap closing due to disorder compared to inversion symmetry breaking terms . . . 49
3.10. Transition probability as a function over the BZ . . . 50
3.11. Transition probability as a function of the disorder strength . . . 51
3.12. Transition probability as a function of the strip width . . . 52
3.13. Linear fit of logarithm of the transition probability . . . 53
3.14. Reconstruction of the dispersion of the edge states in a decorated system 55
3.15. Proposal for a decorated quantum Hall sample realizing a tunable Fermi velocity . . . 59
3.16. Sketch of the considered quantum Hall geometries . . . 61
3.17. Improvement of the boundary approximation . . . 63
3.18. Sketches of the gradually increased quantum Hall meshes . . . 64
3.19. Dispersions of the LLs of a finite strip . . . 67
3.20. Investigation of edge states in the IQHE . . . 68
3.21. Extended and reduced zone schemes for edge states in the IQHE . . . 70
3.22. Discrete energy spectra of isolated bays as a function of their size . . . 71

3.23. Illustration of the avoided level crossing in a quantum Hall sample by increasing the bay opening 72
3.24. Probability densities of the decorated quantum Hall sample 73
3.25. Fermi velocity as a function of the bay size and bay opening 75
3.26. Fermi velocity as a function of the distance between the bays 76
3.27. Fermi velocity as a function of the gate voltage for $L_\mathrm{b} = 2\,\mu\mathrm{m}$ 77
3.28. Fermi velocity as a function of the gate voltage for $L_\mathrm{b} = 3\,\mu\mathrm{m}$ 78
3.29. Sketch of the proposed graphene samples 82
3.30. Illustration of the avoided level crossing in graphene by increasing the bay opening 85
3.31. Probability densities of graphene samples 86
3.32. Fermi velocity as a function of the chemical potential in graphene 88
3.33. Fermi velocity as a function of the gate voltage in graphene 89

4.1. Crystal structure of $BiCu_2PO_6$ 92
4.2. Spin model of $BiCu_2PO_6$ 93
4.3. Fit of the one-triplon dispersions of $BiCu_2PO_6$ 94
4.4. Berry curvature of the three lowest triplon dispersions of $BiCu_2PO_6$ with a small magnetic field 99
4.5. Extrapolation of the largest IPR of a finite piece of chain in the minimal model for $BiCu_2PO_6$ and a sketch illustrating the direct and indirect gaps 102
4.6. Extended SSH model 104
4.7. Delocalization of the edge states in the extended SSH model 105
4.8. Local density of states at one end of a finite chain in the extended SSH model 106
4.9. Local dynamic structure factor as a function of transferred energy 108

5.1. Haldane model including spatially anisotropic hopping 112
5.2. Dispersion of the Haldane model with and without an indirect gap 113
5.3. IPR and indirect gap investigation as a function of real diagonal hopping in the Haldane model 115
5.4. Evolution of the two bulk bands and dispersions of the two in-gap states in the Haldane model for increasing diagonal hopping 116
5.5. Edge state investigation regarding IPR and indirect gap of the initial Haldane model 117
5.6. Edge state investigation regarding IPR and indirect gap of the Haldane model with real diagonal hopping 118
5.7. Edge state investigation regarding IPR and indirect gap of the Haldane model with imaginary diagonal hopping 119
5.8. IPR and indirect gap investigation as a function of imaginary diagonal hopping in the Haldane model 120
5.9. Strip of the topological checkerboard model with NN hopping 121
5.10. Dispersion of the checkerboard model. IPR and indirect gap investigation as a function of diagonal parameter term 122
5.11. Edge state investigation regarding IPR and indirect gap of the topological checkerboard model 123

5.12. Bulk bands of the topological checkerboard model with no indirect gap over the complete BZ 123
5.13. Sketch of a finite honeycomb sample geometry with a chiral edge state . . 124
5.14. Loss of chirality shown by probabilities in a 2D Haldane sample 125

6.1. Illustration of the 2D ferromagnetic Shastry–Sutherland model 131
6.2. One-magnon dispersions of the ferromagnetic Shastry–Sutherland model . 134
6.3. Edge states of the ferromagnetic Shastry–Sutherland model 136
6.4. Edge states of a layered strip geometry in the ferromagnetic Shastry–Sutherland model 138
6.5. Thermal Hall conductivity of the ferromagnetic Shastry–Sutherland model 139
6.6. Magnetization of the ferromagnetic Shastry–Sutherland model 141

A.1. Symmetry analysis of $BiCu_2PO_6$ 148
D.1. SSH model of a six-sited loop 158
E.1. Localization length of the extended SSH model 161
F.1. Ground state approximation for the Shastry–Sutherland lattice 162

List of Tables

1.1. Periodic table of topological insulators and topological superconductors from one up to three dimensions 6

2.1. Important discrete symmetry properties of topological phases 21

3.1. Linear fit parameters of $\ln \left|\langle\psi|\psi_{\mathrm{cl}}\rangle\right|^2 (N_x) \approx a - \gamma\, N_x$ 54

A.1. Behavior of DM couplings for $BiCu_2PO_6$ 150
B.1. Resulting deepCUT coefficients for $BiCu_2PO_6$ 152

Danksagung

An dieser Stelle möchte ich allen danken, die mir während meiner Promotionszeit geholfen haben.

An erster Stelle möchte ich mich besonders bei Prof. Dr. Götz S. Uhrig für die hervorragende Betreuung und tolle Zusammenarbeit bedanken. Die intensiven Diskussionen waren sehr hilfreich und seine Bereitschaft, mich bei jeglichen Herausforderungen zu unterstützen, war vorbildlich.

Bei Prof. Dr. Kai P. Schmidt möchte ich mich für die langjährige Zusammenarbeit sowie der Erstellung einer gemeinsamen Publikation bedanken. Zusätzlich bedanke ich mich bei ihm und Prof. Dr. Dirk Morr für die Begutachtung der Arbeit. Prof. Dr. Joachim Stolze danke ich für die anregenden Diskussionen und seine Unterstützung.

Bei der Studienstiftung des deutschen Volkes möchte ich mich auch herzlich bedanken für die finanzielle Unterstützung sowie die ideelle Förderung. In diesem Zusammenhang möchte ich meinen Vertrauensdozentinnen Prof. Dr. Ute Ritterfeld und Prof. Dr. Katja Crone danken, die mich zusätzlich betreuten.

Der Wilhelm-und-Else-Heraeus-Stiftung danke ich für das Stipendium, mit dem ich an der 69. Lindauer Nobelpreisträgertagung teilnehmen konnte.

Bei Leanna Müller bedanke ich mich für die Zusammenarbeit und die Erstellung einer gemeinsamen Publikation. Bei Jens Winkelmann bedanke ich mich für seine Unterstützung. Weiterhin möchte ich auch der gesamten Arbeitsgruppe T1a danken, die für ein angenehmes Arbeitsklima sorgte. Meinen Freunden danke ich für die motivierende Worte. Den Personen Christian Gerhorst, Peter Lorenz und Ismo Toijala danke ich für das Korrekturlesen der Arbeit.

Zuletzt möchte ich mich vor allem bei meiner Familie bedanken, die mich zu jeder Zeit förderte und mich in jedem Schritt ermunterte.

Eidesstattliche Erklärung

Hiermit erkläre ich, Maik Malki, an Eides statt, dass ich die vorliegende Dissertation mit dem Titel

Robustness and Variation
of Low-Dimensional
Signal Transmission
in Topological Phases

selbstständig verfasst habe. Alle in Anspruch genommenen Quellen und Hilfen wurden in der Dissertation vermerkt. Teile der Arbeit wurden in Refs. [44, 108, 161, 191, 210] publiziert oder zur Publikation eingereicht [109].

Ich versichere außerdem, dass ich die beigefügte Dissertation nur in diesem und keinem anderen Promotionsverfahren eingereicht habe. Zudem versichere ich, dass diesem Promotionsverfahren keine endgültig gescheiterten Promotionsverfahren vorausgegangen sind.

.....
Ort, Datum

.....
Unterschrift